Measurement of
the Iron Spectrum in Cosmic Rays
with the VERITAS Experiment

D i s s e r t a t i o n

zur Erlangung des akademischen Grades

d o c t o r   r e r u m   n a t u r a l i u m

(Dr. rer. nat.)

im Fach Physik
Spezialisierung Experimentalphysik

eingereicht an der
Mathematisch-Naturwissenschaftlichen Fakultät
der Humboldt-Universität zu Berlin

von
Henrike Fleischhack, M.Sc.

Präsidentin der Humboldt-Universität zu Berlin:
Prof. Dr.-Ing. Dr. Sabine Kunst

Dekan der Mathematisch-Naturwissenschaftlichen Fakultät:
Prof. Dr. Elmar Kulke

Gutachter: 1. Dr. Gernot Maier
2. Prof. Dr. Thomas Lohse
3. Prof. Dr. Markus Risse

Tag der mündlichen Prüfung: 19.01.2017

To coffee. And cats.

Summary

More than a hundred years after their discovery, a lot is already known about cosmic rays. Still, there are many open questions: How does their composition change with energy? Which types of sources dominate in different energy ranges? How long do cosmic rays propagate inside the galaxy?

Cosmic rays have been detected over many decades in energy. Their energy spectrum can provide important clues as to their origin and propagation. Different experimental techniques have to be combined to cover the full energy range: Direct detection experiments at lower energies and indirect detection via air showers at higher energies. In addition to detecting cosmic rays at Earth, we can also study them via the electromagnetic radiation, in particular gamma rays, that they emit in interactions with gas, dust, and electromagnetic fields near the acceleration regions or in interstellar space.

In the following, I will present two studies: First, a measurement of the energy spectrum of iron nuclei in cosmic rays, and second, a search for gamma-ray emission from star-forming galaxies. Both studies use data taken by the imaging air Cherenkov telescope (IACT) VERITAS.

IACTs such as VERITAS image extensive air showers by the Cherenkov light emitted by their charged component. Their main purpose is gamma-ray astronomy in the very-high-energy (VHE, $E > 100\,\mathrm{GeV}$) regime, but they also detect a lot of cosmic-ray induced showers. In this thesis, I present a measurement of the cosmic ray iron spectrum. I use a novel template likelihood method to reconstruct the primary energy and arrival direction, which is for the first time adapted for the use with iron-induced showers. I further use a multi-variate classifier which uses the presence of *direct Cherenkov light* emitted by charged primary particles before the first interaction, as well as other image parameters, to identify iron-induced showers. Their energy spectrum is well described by a power law $\frac{\mathrm{d}F}{\mathrm{d}E} = f_0 \cdot \left(\frac{E}{E_0}\right)^{-\gamma}$ from $20\,\mathrm{TeV}$ to $500\,\mathrm{TeV}$ with $E_0 = 50\,\mathrm{TeV}$, $f_0 = \left(4.82 \pm 0.98(\mathrm{stat.})^{+2.12}_{-2.65}(\mathrm{syst.})\right) \cdot 10^{-7}\,\mathrm{cm}^{-2}\,\mathrm{s}^{-1}\,\mathrm{TeV}^{-1}\,\mathrm{sr}^{-1}$, and $\gamma = 2.82 \pm 0.30(\mathrm{stat.}) \pm^{+0.23}_{-0.25}(\mathrm{syst.})$.

In addition, I present a search for VHE gamma-ray emission from the three star-forming galaxies Arp 220, IRAS 17208-0014, and IC 342 using VERITAS data. Galaxies with high star formation rates contain many young and middle-aged supernova remnants, which accelerate cosmic rays. These cosmic rays are expected to interact with the dense interstellar medium in the star-forming regions to emit gamma-ray photons up to very high energies. No gamma-ray emission is detected from the studied objects and the resulting limits begin to constrain theoretical models of the cosmic ray acceleration and propagation in Arp 220.

Zusammenfassung

Seit ihrer Entdeckung vor über einhundert Jahren fasziniert die kosmische Strahlung die Wissenschaft. Inzwischen ist vieles über ihre Herkunft und Zusammensetzung bekannt. Aber noch immer sind viele Fragen offen: Welche Quellen der kosmischen Strahlung überwiegen in welchem Energiebereich? Wie hängt ihre Zusammensetzung von der Energie ab? Wie lange propagieren die Teilchen der kosmischen Strahlung in der Milchstraße?

Das Energiespektrum der kosmischen Strahlung bietet wichtige Hinweise auf ihren Ursprung und ihre Ausbreitung. Verschiedene Messtechniken müssen kombiniert werden, um den ganzen Energiebereich abdecken zu können: Direkte Messungen mit Teilchendetektoren bei niedrigen Energien, indirekte Messungen von Luftschauern bei hohen Energien. Dazu kommt die Messung von Photonen, hauptsächlich im GeV- und TeV-Bereich, die bei der Wechselwirkung von kosmischer Strahlung mit Materie oder elektromagnetischen Feldern entstehen. Im Folgenden werde ich zwei Studien dazu vorstellen, die beide auf Daten des abbildenden Tscherenkow-Teleskopes VERITAS beruhen.

Abbildende Tscherenkow-Teleskope wie VERITAS werden hauptsächlich für Gammastrahlungsastronomie jenseits von 100 GeV eingesetzt. Allerdings detektieren sie auch eine große Anzahl von Schauern, die durch kosmische Strahlung ausgelöst werden. In dieser Arbeit stelle ich eine Messung das Energiespektrums von Eisenkernen in der kosmischen Strahlung vor. Für die Bestimmung der Energie und Ankunftsrichtung der Primärteilchen benutze ich eine neuartige Template-Likelihood-Methode, die hier erstmals auf Eisenschauer angewendet wird. Dazu kommt eine multivariate Klassifizierungsmethode, um Eisenschauer von Schauern, die durch leichtere Kerne induziert werden, zu trennen. Dafür benutze ich unter anderem das *direkte Tscherenkow-Licht*, welches von geladenen Teilchen vor der ersten Wechselwirkung ausgestrahlt wird. Das so gemessene Energiespektrum wird im Bereich von 20 TeV bis 500 TeV gut durch ein Potenzgesetz $\frac{\mathrm{d}F}{\mathrm{d}E} = f_0 \cdot \left(\frac{E}{E_0}\right)^{-\gamma}$ mit $E_0 = 50$ TeV, Normierungskonstante $f_0 = \left(4.82 \pm 0.98(\text{stat.})^{+2.12}_{-2.65}(\text{syst.})\right) \cdot 10^{-7}\,\mathrm{cm}^{-2}\,\mathrm{s}^{-1}\,\mathrm{TeV}^{-1}\,\mathrm{sr}^{-1}$ und spektralem Index $\gamma = 2.82 \pm 0.30(\text{stat.})^{+0.23}_{-0.25}(\text{syst.})$ beschrieben.

Außerdem beschreibe ich eine Suche nach Gammastrahlung oberhalb von 100 GeV von den drei Galaxien Arp 220, IRAS 17208-0014 und IC 342. Diese drei Galaxien haben hohe Sternentstehungsraten und daher viele Supernova-Überreste, welche kosmische Strahlung erzeugen. Diese wechselwirkt erwartungshalber mit den dichten Staubwolken in den Sternentstehungsgebieten und erzeugt Gammastrahlung. VERITAS konnte keine solche Gammastrahlung messen. Die daraus abgeleitete Höchstgrenze für die Luminosität schränkt theoretische Modelle der Erzeugung und Propagation von kosmischer Strahlung in der Galaxie Arp 220 ein.

Contents

1 Cosmic Rays

1.1 Introduction

Cosmic rays were first discovered in 1912 by V. Hess. Measuring the amount of ionizing radiation in the lower atmosphere, he discovered that above about 1 km, the radiation increases with height. He concluded that there must be a second component to this radiation, in addition to radioactive elements in the earth's crust. He found no correlation with the weather, time of day, or the season, and concluded that this newly discovered radiation must come from space. Soon, the phenomenon became known as 'cosmic rays' (Hess, 1912).

Even though we now know that these 'rays' are indeed particles, the term *cosmic rays* is still used to describe charged particles of cosmic origin. Cosmic rays impinge upon the Earth's atmosphere constantly from all directions. They consist mostly of protons and other nuclei, with a small amount of electrons, positrons and anti-protons (Olive et al., 2014). Sometimes, the term is used to refer only to *hadronic* cosmic rays, i.e., protons and nuclei, as opposed to electrons and positrons. There are also neutral particles impinging upon the Earth such as neutrinos and neutrons, which will not be considered in this thesis.

The energies of cosmic rays that have been observed at Earth cover more than ten orders of magnitude. Particles with energies in the keV to MeV energy range can originate from the Sun (McGuire & Rosenvinge, 1984). It is thought that cosmic rays with energies in the GeV to PeV range are mainly *galactic* cosmic rays, with most of them being accelerated in supernova remnants, while cosmic rays with even higher energies are thought to be of extra-galactic origin, possibly accelerated by active galactic nuclei (Longair, 2011).

Cosmic rays can also be separated into *primary* and *secondary* cosmic rays (Olive et al., 2014). Primary cosmic rays are those that are accelerated by astrophysical sources. Secondary cosmic rays are produced by the interaction of primary or secondary cosmic rays with interstellar matter, photons, or magnetic fields. For example, it is thought that positrons are mostly secondary cosmic rays, while electrons have a primary and a secondary component. Secondary electrons and positrons are the end products of the decays of pions, which are produced abundantly in hadronic interactions. Some nuclei such as lithium and boron have higher abundance in cosmic rays compared to the abundance with which they are produced in stellar fusion. Those secondary elements are produced via spallation processes when heavier cosmic rays interact with the interstellar/intergalactic medium.

As charged particles, cosmic rays are deflected by magnetic fields as they propagate through the Galaxy or even through intergalactic space. This makes it impossible to pinpoint their

sources directly. However, one can learn about their sources by comparing the measured energy spectra and composition of Cosmic Rays to model predictions assuming different source types. Another approach is to use gamma rays, which are produced for example in interactions of cosmic rays with dust or gas in or near the source, to learn more about the sources and acceleration mechanisms. However, gamma rays are also produced in electron accelerators, and there are degeneracies in the spectra which can make it difficult to determine how many hadronic cosmic rays are accelerated in a given source.

After about a century of measurements, our picture of the nature and origin of cosmic rays has become clearer. Still, many unsolved questions remain. In particular, the origin of cosmic rays has not been conclusively established.

This chapter is structured as follows: Section 1.2, gives an introduction to cosmic ray physics, describing possible acceleration mechanisms, cosmic ray propagation, and the interaction of cosmic rays with the Earth's atmosphere. Section 1.4 describe some experimental techniques for the observation of cosmic rays and lists some current experiments. Section 1.5 gives an overview over some recent measurements, and Section 1.6 lists some models that have been proposed to explain the measured cosmic ray fluxes. Finally, Section 1.7 provides some background and motivation for the main topic of this thesis: the measurement of the cosmic ray iron spectrum in the TeV to PeV range.

1.2 Fundamentals of Cosmic Ray Physics

1.2.1 Acceleration of Cosmic Rays

The energy spectrum of cosmic rays follows a power law over many orders of magnitude, with only small deviations (see for example Gaisser et al., 2013; Olive et al., 2014). This means that the cosmic rays must be of non-thermal origin (otherwise they should follow a black-body spectrum). Electric and magnetic fields exert a force on charged particles. However, (static) magnetic fields cannot affect a particle's speed, only its direction. Static electric fields cannot exist in a plasma environment as they would short out quickly. Hence, to accelerate particles, one needs changing magnetic fields, which induce an electric field in the particle's rest frame.

There are several mechanisms that could explain the acceleration of charged particles in magnetized plasma environments. The following paragraphs follow Chapter 17 in Longair, (2011).

Magnetic Reconnection events

Magnetic reconnection occurs when two magnetic fields with opposite polarity meet. The topology of the magnetic field changes rapidly and large electric fields can occur which accelerate charged particles. Magnetic reconnection has been shown to occur in solar outbursts (Tsuneta, 1996) and is likely responsible for particle acceleration during those events. It

is also thought to be a possible mechanism for the acceleration of electrons in pulsar wind nebulae (Cerutti et al., 2014).

Second-order Fermi Acceleration

Fermi described particle acceleration via a stochastic process of inelastic scattering with "magnetic clouds" in the interstellar medium (ISM) (Fermi, 1949). The clouds, which move with characteristic speed $V = c\beta_{cl}$, are assumed to act like mirrors to charged particles which they encounter. For a relativistic test particle which moves with angle θ relative to the cloud, one obtains the following relation for the energy gain (or loss) in the laboratory frame for one single collision:

$$\frac{\Delta E}{E} = 2\beta_{cl} \cdot \cos(\theta) + 2\beta_{cl}^2 + \mathcal{O}\left(\beta_c l^3\right)$$

Neglecting the higher-order terms, the particle's energy always increases for "head-on" collisions ($\cos(\theta) > 0$) and decreases for "head-tail" collisions ($\cos(\theta) < 0$). Taking the first two terms and averaging over the angle θ, the average energy gain is

$$\left\langle \frac{\Delta E}{E} \right\rangle = \frac{8}{3}\beta_{cl}^2$$

Intuitively, there is a net increase in energy because "head-on" collisions are more likely to happen than "head-tail" collisions.

In Fermi's model, the test particle would be able to diffuse out of the accelerating region with some characteristic time τ_{esc}. Neglecting the stochastic nature of the scattering process and assuming a constant rate of energy increase

$$\frac{\mathrm{d}E}{\mathrm{d}t} = \frac{4}{3}\left(\frac{c\beta_{cl}^2}{L}\right) = \alpha E$$

with mean free path L between clouds, the steady-state energy spectrum of particles in this accelerator would follow a power law $\frac{\mathrm{d}N}{\mathrm{d}E} \propto E^{-\gamma}$ with index $\gamma = 1 + \frac{1}{\tau_{esc}\alpha}$.

Considering also the changes to $\langle E^2 \rangle$, one obtains a slightly different expression for the spectral index, but the fundamental results remain. Fermi estimated the characteristic speed of the clouds to be on the order of $\beta_{cl} \lesssim 10^{-4}$. With this assumption, the acceleration proceeds very slowly, with the energy increasing by a factor of e about every 10^8 collisions. Assuming a characteristic propagation time of about 60 million years and a characteristic time between interactions with cloud of about one year, he obtained a spectral index of about -2.9, in accordance with the observations at the time (Fermi, 1949). This approach

assumes that the clouds are distributed relatively evenly throughout the galaxy and all have very similar properties to explain the observed uniform flux of cosmic rays.

First-order Fermi Acceleration

An extension to Fermi's idea considers situations in which the "clouds" have a preferred direction. In this case, one could obtain an energy increase which is *linear* in the cloud speed and hence a faster energy increase. Instead of gas clouds in the interstellar medium, this model considers a strong, non-relativistic shock moving through an ionized medium with speed U. Hence, the process is called *diffusive shock acceleration.*

In this picture, the charged test particles do not interact directly with the shock front. They are assumed to interact with the plasma so that their directions are always isotropic with respect to their surroundings. In this case, the relativistic particle's energy in the laboratory frame *increases* at each shock crossing, independent of the direction in which it crosses the shock, by

$$\frac{\mathrm{d}E}{E} = \frac{3}{4} \cdot \frac{U}{c} \cdot \cos{(\theta)} \rightarrow \left\langle \frac{\Delta E}{E} \right\rangle = \frac{U}{c}.$$

Here, only angles between $0°$ and $180°$ contribute. The average energy increase has been given for a full cycle (two shock crossings).

The probability for the test particle to remain in the vicinity of the shock and undergo another cycle of acceleration is given by

$$P = 1 - \frac{U}{c}.$$

Assume N_0 particles at fixed energy E_0 are injected into the shock. After k cycles, there are $N = N_0 \cdot P^k$ particles with energy $E = E_0 \cdot \left(1 + \frac{U}{c}\right)^k$ still in the vicinity of the shock. From this, one derives that the particles again follow a power law $\frac{\mathrm{d}N}{\mathrm{d}E} \propto E^{-\gamma}$ with index

$$\gamma = 1 - \frac{\ln\left(1 - \frac{U}{c}\right)}{\ln\left(1 + \frac{U}{c}\right)} \approx 1 - \frac{-\frac{U}{c}}{\frac{U}{c}} = 2.$$

This result is promising: For strong shocks, the energy spectrum of the accelerated particles does not depend strongly on the shock velocity. Considering weaker shocks, one obtains qualitatively similar results but different power law indices.

Relativistic shocks (e.g., in the jets of active galactic nuclei) can also accelerate particles in a similar manner. They can also produce power-laws, albeit with a slightly softer index. For relativistic shocks, the spectral shape depends on the assumptions made on the angle between the magnetic field and the shock front (Longair, 2011).

Limits of the Acceleration Process

The calculations above make several assumptions about the accelerated particles, for example that they isotropize through interactions with the plasma before leaving the acceleration region. Also, energy losses through ionization or synchrotron emission are neglected. More detailed calculations lead to deviations from the predicted power law energy spectrum or show that some environments cannot be efficient particle accelerators. In particular, these effects can be used to estimate the maximum energy to which a source can accelerate a particle. Some of these limits are listed below. Here, Ze is the charge of the particle to be accelerated E its energy, B the magnetic field in the acceleration region and L the characteristic size of the accelerator/source.

Size of the acceleration region (Hillas' argument)   Sources can only efficiently accelerate particles which are confined to the source region by the ambient magnetic field, i.e. whose gyro-radius $\frac{E}{ZeB}$ is smaller than the source region. This leads to an upper limit for the energy of $E_{max} = ZeBLc$.

Lifetime of the accelerating object   The expanding shells in supernova remnants are slowed down by the interstellar medium, which makes acceleration less efficient after the first few thousand years. If the speed of the energy increase is given by $\left\langle \frac{\mathrm{d}E}{\mathrm{d}t} \right\rangle = \alpha E$ and the particles are injected with energy E_0, then the maximum energy reached after time T is given by $E_{max} = E_0 \cdot e^{\alpha T}$.

Magnetic flux density   Since the accelerating electric field is generated by changes in the magnetic field, we have $\nabla \times E = -\frac{\partial B}{\partial t}$. For a shock moving with constant speed U and negligible turbulence, we have $\nabla \times E \sim \frac{E}{L}$ and $\frac{\partial B}{\partial t} \sim \frac{BL}{U}$, so $E \sim BU$ to first order. The maximum energy can then be estimated as $E_{max} = Ze \int E \mathrm{d}x = ZeBUL$.

Energy losses   The accelerated particles continually lose energy, for example through synchrotron radiation (in the ambient magnetic field or the fields of nuclei in the plasma), or through interactions with ambient matter or photons. The energy gain must be faster than the energy losses for acceleration to occur. However, these effects provide a means to observe cosmic-ray acceleration by measuring for example the synchrotron emission, or neutrinos and gamma-ray photons which are the secondary products of interactions between nuclei and the surrounding matter.

Lagage & Cesarsky, (1983) estimated the maximum energy up to which nuclei could be accelerated in supernova remnants and obtained upper limits of 10 TeV to 100 TeV per nucleon. Note that all these limits depend on assumptions about the conditions in the acceleration regions. There is evidence that the magnetic fields in supernova remnants can be several orders of magnitude larger than expected from the interstellar medium due to amplification

by different kinds of instabilities. This could increase the energy range over which particles could be accelerated.

Non-linear Diffusive Shock Acceleration

The approaches above considered the accelerated particles as test particles which do not affect their surroundings. However, it turns out that the acceleration process can be so efficient that a significant fraction[1] of the accelerator's energy density can be transferred to highly energetic cosmic rays. In that case, the test particle approach breaks down. The three major components (plasma, accelerated particles, and magnetic fields) and their actions on one another have to be considered separately. See Blasi, (2013) for a good overview of the non-linear effects, focusing on acceleration in supernova remnants. The main effects are the following:

The accelerated particles and the magnetic fields both affect the shape of the shock front, which in turn can change the energy spectra of the accelerated particles and in particular cause deviations from a simple power-law spectrum. Amplifications in the magnetic field, either due to the accelerated particles themselves or due to density fluctuations in the plasma, do not only affect the shock front, but also the accelerated particles directly. The increased magnetic field increases the energy up to which particles are confined close to the shock. It also decreases the average time between shock crossings, making the acceleration process faster and more efficient. Both effects raise the maximum energy up to which particles can be accelerated. On the other hand, increased magnetic fields also lead to an increased synchrotron cooling rate, especially for electrons.

Numerical simulations of the three components are needed to make realistic predictions about the energy spectrum of the accelerated cosmic rays, and in particular the maximum energy that can be generated by a particular source. In addition to non-linear effects, these simulations also need to take into account the environment into which the supernova explodes, which is influenced by the wind emitted by the precursor star. See Telezhinsky et al., (2012) for an example of modeling cosmic ray acceleration in young supernova remnants.

Possible Sites for Cosmic Ray Acceleration

There are many classes of astrophysical objects in which theses types of shock waves occur and which release enough energy to accelerate significant amounts of cosmic rays. Some of these candidates are plotted in Fig. 1.1. In this plot, estimates for the magnetic field strength are plotted against the size of the accelerating region, so that diagonal lines correspond to fixed values of the maximum energy according to Hillas' argument that cosmic rays need to be confined within the acceleration region. Note that this is just a very rough approximation for the energy threshold. The magnetic field may be amplified due to non-linear shock

---

[1]up to 50% according to Longair, (2011)
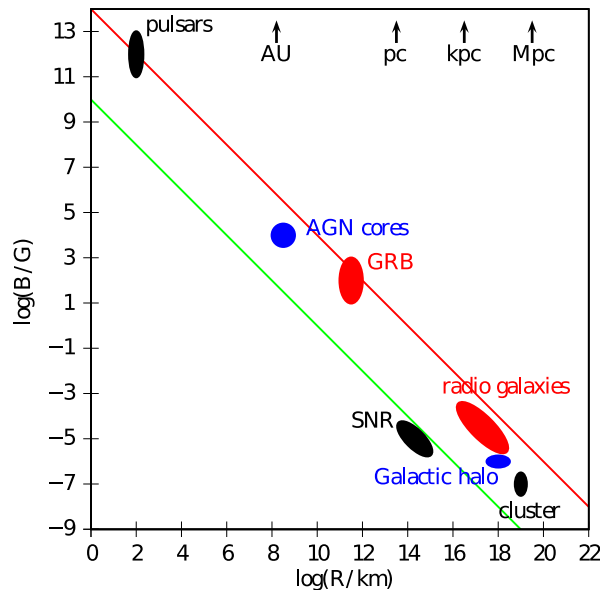
Figure 1.1: Magnetic field strength versus size for possible sources of cosmic rays (Hillas plot). Figure taken from Kachelrieß, (2008). If cooling can be neglected, the maximum energy is proportional to product of the size of the accelerating region and the magnetic field. The red line corresponds to sources able to accelerate protons up to 1 ZeV. The green line corresponds to sources able to accelerate iron nuclei up to 100 EeV.

acceleration effects, increasing the maximum energy. On the other hand, additional factors such as the lifetime of the accelerator affect the maximum energy as well.

The main sources of cosmic rays within our Galaxy are thought to be young or middle aged supernova remnants. The supernova shell expands outward into the interstellar medium at supersonic speed and diffusive shock acceleration is thought to occur near the resulting shock-front. There is plenty of circumstantial evidence which supports the paradigm of SNRs as accelerators of galactic cosmic rays.

Observationally, it has been shown that highly relativistic particles (electrons or cosmic rays) are present at many SNRs (see Section 1.5.5 for more details).

Simulations have shown that particles can be accelerated in SNRs via diffusive shock acceleration as explained above. In fact, SNRs can be quite efficient accelerators, with several percent of the total available energy being converted into cosmic rays. The acceleration efficiency depends on the properties of the SNR, for example Schure & Bell, (2013) find acceleration efficiencies of about 5% for young SNRs.

SNRs appear to release enough cosmic rays into the Galaxy to explain the observed cosmic rays flux. A detailed study of the cosmic ray propagation finds that for reasonable assumptions about the supernova rate, an average acceleration efficiency of $5\% - 10\%$ is sufficient to replenish the losses due to cooling or leakage from the Galaxy (Strong et al., 2010).

It has recently been suggested that OB associations may play a large role in particle accelerations by SNRs (Bykov & Toptygin, 2001; Parizot et al., 2004). OB associations are young stellar associations containing many massive O- and B-type stars. The strong stellar

winds emitted by those stars merge and carve out cavities in the ISM, so called *superbubbles*. There are multiple possible sites for CR acceleration in superbubbles: SNRs expanding into the bubble, interaction zones of the stellar winds from different stars, or interaction of stellar winds with SNRs. Also, it is possible that particles accelerated in one SNR stay confined in the bubble and are further accelerated in a different SNR in the same bubble.

Still, it has not been conclusively shown that SNRs (whether within or outside of super-bubbles) are the only major source for cosmic rays in the Galaxy, nor is it known up to which energy they are able to efficiently accelerate particles.

Other candidates of cosmic ray sources within our Galaxy are pulsars/pulsar wind nebu-lae and micro-quasars. Micro-quasars are compact objects such as stellar-mass black holes accreting matter from a companion star, which forms an accretion disk around the compact object. Some of the matter is not absorbed by the compact object, but ejected in a *jet* perpendicular to the accretion disk. Shocks are thought to occur in these jets as clumps of plasma are injected into the jet at different speeds.

The sources of cosmic rays beyond roughly $1\,\text{EeV}$ are thought to lie outside of the Galaxy. Active Galactic Nuclei (AGNs) are the main candidates (Bykov et al., 2012). These are galaxies with a super-massive black hole at their core which is accreting matter. They have accretion disks and jets similar to the micro-quasars described above, but are much more energetic. The particles in AGN jets move at relativistic speeds; in fact, due to the projection angle between the jet axis and the line of sight, apparent superlumninal motion has been observed in AGN jets. Another class of candidates is given by gamma-ray bursts (Baerwald et al., 2015). These are transient events which release a large amount of energy (about 10^{51} ergs, similar to the energy released in a supernova explosion) within seconds or less. Most of the energy released is tightly beamed an in the form of gamma radiation, making it possible to observe GRBs up to cosmological distances (Piran, 2004).

1.2.2 Interactions between Cosmic Rays and their Environment

As charged particles, cosmic rays (protons, nuclei, and electrons) interact with the ambient matter, magnetic fields, and photon fields through several different processes. These effects occur both at sites of cosmic ray acceleration and as cosmic rays propagate through the Galaxy or intergalactic space. Cosmic rays typically lose energy in such interactions, which changes their energy spectrum. Additionally, the interaction between cosmic rays and their environment is strongly connected to the emission of non-thermal *photons* from the radio to the gamma-ray regime as well as *neutrinos*. Gamma-ray photons with energies above $10\,\text{MeV}$ are of particular interest because they can *only* be produced due to the interactions of charged particles.

Many sites of cosmic rays acceleration tend to have stronger magnetic fields and higher densities of gas/plasma than the interstellar space, and are thus expected to be strong emitters of non-thermal photons. Cosmic rays propagating in the Galaxy give rise to *diffuse* gamma-ray emission as they interact with the interstellar medium, especially denser molecular clouds.

Ionization

Charged particles like protons and electrons can lose energy by ionizing matter, e.g. when they cross clouds of atomic or molecular hydrogen. For ultra-relativistic cosmic rays, ionization is not one of the dominant mechanisms for energy loss. For example, for an electron with an energy of $3\,\mathrm{GeV}$ propagating in the ISM with an average density of $1\,\mathrm{cm}^{-3}$, would lose only about $10\,\mathrm{eV}\,\mathrm{yr}^{-1}$, corresponding to a cooling time scale of about $300\,\mathrm{Myr}$ (Longair, 2011). However, ionization is a stochastic process and occasionally involves a large energy transfer from the ionizing particle to the electron (knock-on process). Thus, it has to be considered as a possible source of secondary electrons.

Hadronic Pion Production

Neutral and charged pions are produced in inelastic interactions of hadronic cosmic rays with interstellar gas (mainly hydrogen). Assuming the target material to be at rest, the center-of-mass energy $\sqrt{s}$ for a proton-proton collision is given by

$$
\begin{aligned}
s &= (p^{\mu}_{CR} + p^{\mu}_T)^2 \\
&= (E_{CR} + m_T)^2 - (\vec{p}_{CR} + 0)^2 \\
&= E_{CR}^2 + m_T^2 + 2 \cdot E_{CR} \cdot m_T - p_{CR}^2 \\
&= m_{CR}^2 + m_T^2 + 2 \cdot E_{CR} \cdot m_T \\
&= 2\left(m_p^2 + E_{CR} \cdot m_p\right)
\end{aligned}
$$

The kinematic threshold for neutral pion production ($pp \rightarrow pp\pi^0$) is given by $\sqrt{s} > 2 \cdot m_p + m_{\pi}^0 = 2.016\,\mathrm{GeV}$, which corresponds to a minimum total energy of $970\,\mathrm{MeV}$ or a kinetic energy of $30\,\mathrm{MeV}$ for the cosmic ray proton. Similarly, the threshold for the production of a charged pion via $pp \rightarrow pn\pi^+$ is given by $\sqrt{s} > m_p + m_n + m_{\pi}^+ = 2.012\,\mathrm{GeV}$, which corresponds to a minimum total energy of $960\,\mathrm{MeV}$ or a kinetic energy of $20\,\mathrm{MeV}$. For higher energies, several pions may be created in the same interaction. Heavier nuclei in cosmic rays also undergo hadronic interactions with ambient gas.

Pions are unstable particles. Neutral pions decay into two gamma-ray photons, while charged pions decay into a neutrino and a muon, which further decays into an electron and two neutrinos. Thus, inelastic hadronic interactions produce both gamma-ray photons and neutrinos in similar amounts.

Photo-Pion Production

Pions can also be produced in interactions between hadronic cosmic rays and photon fields (for example, $p\gamma \rightarrow p\pi^0$, $p\gamma \rightarrow n\pi^+$). The energy threshold for this process is $E_{CR} \geq \frac{m_{\pi} \cdot m_p}{E_{\gamma}}$.

This corresponds to an energy of about $200\,\mathrm{EeV}$ for cosmic rays interacting with the cosmic

microwave background (CMB) with a peak energy of $E_\gamma \approx 600\,\mu\text{eV}$ (Longair, 2011). A more thorough evaluation of the cross section, integrating over the CMB spectrum, shows that protons at about $100\,\text{EeV}$ have a (comparatively) large cross section for interacting with photons from the cosmic microwave background, losing 20% or more of their energy per interaction (Greisen, 1966; Zatsepin & Kuz'min, 1966). This effect is called the *GZK cutoff* and limits the distances that cosmic rays at these energies can propagate through the universe. The energy loss scale length is on the order of $10\,\text{Mpc}$ for protons at $100\,\text{EeV}$ (Greisen, 1966).

In principle, photo-pion production also affects lower-energy cosmic ray protons if they propagate through intense photon fields. However, the product of the cross section and the number of available photons is usually too low to significantly affect the proton spectrum.

Nuclear Interactions

As they propagate through the Galaxy or intergalactic space, cosmic ray nuclei also interact with the interstellar medium or with photons. Cosmic ray nuclei such as iron or carbon interacting with protons in the ISM undergo *spallation* (Silberberg & Tsao, 1990), producing lighter elements as well as neutrons, pions and other mesons, which in turn decay into gamma rays (from neutral pions), as well as neutrinos, electrons, and positrons (from decays of neutrons, charged pions, and their decay products). The spallation products and their decay products are called *secondary cosmic rays*. Due to this process, the elemental abundances in cosmic rays differ significantly from the abundances in the solar system (Longair, 2011).

Heavy nuclei can also be broken up into smaller fragments through interactions with photons via a process called *photo-disintegration*. For example, iron nuclei with energies above $100\,\text{EeV}$ are affected by photo-disintegration with the photons from the CMB (Khan et al., 2005). This effect causes a cutoff in the cosmic ray spectrum at the highest energies, similar to the GZK cutoff described above.

In principle, photo-disintegration or $p\gamma$ scattering via pion production can also affect cosmic rays at all energies if photons with appropriate energies are available. The photon fields need to be very dense for this effect to be significant, but this can happen for example inside or near cosmic ray acceleration regions.

Synchrotron Radiation

Charged particles propagating in a magnetic field are deflected perpendicular to the field lines and their own velocity. Like any acceleration of charged particles, this deflection causes the emission of *synchrotron* radiation. For ultra-relativistic cosmic rays, the median energy of the radiated photons is given by $E_s = \frac{3eBE_{CR}}{m_{CR}^2 c^2}$, where B is the magnetic field strength (Olive et al., 2014). For electrons with energies of hundreds of GeV in the galactic magnetic field ($B \approx 1\,\text{nT}$), this corresponds to radiation in the radio band (GHz).

The average energy loss rate via synchrotron radiation for ultra-relativistic electrons in a turbulent magnetic field is given by $\left\langle -\frac{\mathrm{d}E}{\mathrm{d}t} \right\rangle = \frac{4}{3}\sigma_T \cdot c \cdot \frac{B^2}{2\mu_0} \cdot \gamma$, where $\sigma_T \approx 6.7 \cdot 10^{-29}\,\text{m}^2$ is

the Thomson cross section and $\gamma = \frac{E_{CR}^2}{m_{CR}^2 c^4}$. For a $100\,\text{GeV}$ electron in the galactic magnetic field, this corresponds to an energy loss of $5\,\text{meV}\,\text{s}^{-1}$ and an energy loss scale of about $6\,\text{Myr}$ (Longair, 2011). For protons in the galactic magnetic field, synchrotron radiation is not a dominant mode of energy loss as the radiated power is proportional to $\frac{1}{M_{CR}^4}$.

Bremsstrahlung

Cosmic rays can also be deflected by the electric fields of nuclei (mostly protons) in the ISM, emitting photons referred to as *bremsstrahlung*. Again, this is mode of energy loss is not efficient for protons. For ultra-relativistic electrons, the average energy loss per traversed column depth is given as $\left\langle -\frac{\mathrm{d}E}{\mathrm{d}\chi} \right\rangle = \frac{E}{\chi_0}$. For hydrogen gas, the *radiation length* χ_0 is approximately $58\,\text{g}\,\text{cm}^{-2}$ (Longair, 2011). Assuming an average density of the ISM of $1\,\text{cm}^{-3}$, this corresponds to a fractional energy loss rate of $-\frac{1}{E}\frac{\mathrm{d}E}{\mathrm{d}t} = 3.66 \cdot 10^{-14}\,\text{s}^{-1} = 1.2 \cdot 10^{-8}\,\text{yr}^{-1}$.

(Inverse) Compton Scattering

Elastic interactions between (free) electrons and photons are referred to as Compton scattering. If the electron energy is larger than the photon energy, the electron will lose energy and *upscatter* the photon to higher energies. Thus, the inverse Compton process is both a source of high-energy photons and affects the energy spectrum of cosmic ray electrons.

The energy loss rate via inverse compton scattering is given by $\left\langle -\frac{\mathrm{d}E}{\mathrm{d}t} \right\rangle = \frac{4}{3}\sigma_T \cdot c \cdot U_{rad} \cdot \gamma$, where U_{rad} is the intensity of the radiation field and $\gamma = \frac{E_{CR}^2}{m_{CR}^2 c^4}$. For $100\,\text{GeV}$ electrons scattering off the CMB, this corresponds to a maximum lifetime of $12\,\text{Myr}$ (Longair, 2011).

The average energy of the upscattered photons is roughly $E'_{ph} \approx \frac{4}{3} \cdot \gamma^2 \cdot E_{ph}$. This means that a $100\,\text{GeV}$ electron ($\gamma \approx 2 \cdot 10^5$) would up-scatter optical photons ($E = 2\,\text{eV}$) to gamma-ray photons ($E \approx 70\,\text{GeV}$).

1.2.3 Propagation of Cosmic Rays

Cosmic Rays with energies below some PeV are thought to be confined to the Galaxy due to magnetic fields (Longair, 2011). The galaxy can be modeled as a *leaky box*: Relativistic particles diffuse within the Galaxy, losing energy as described above. If they get to the edge, they have a small probability of leaving the volume, in which case they are "lost" forever. The confinement time in the galaxy, estimated from the ratio of secondary to primary cosmic rays, and from the abundances of long-lived, unstable isotopes, is about $15\,\text{Myr}$ (Mewaldt et al., 2001).

In the most simple picture, cosmic rays undergo Kolmogorov diffusion in the turbulent magnetic fields with an energy-dependent diffusion coefficient $D = D_0 \cdot \left(\frac{E}{E_0}\right)^{-\delta}$, with $\delta \approx 0.4$ (Longair, 2011) This, in addition to the energy loss mechanisms described above leads to a softening of the observed cosmic ray energy spectra with respect to the source spectra.

More realistic approaches try to include the *drift* due to the regular component of the magnetic field, and the actual source distribution in the Galaxy (Ptuskin et al., 1993). This can lead to pronounced features in the cosmic ray spectra.

Cosmic rays with energies above several PeV are not confined in the Galaxy. Hence, we expect that most of the cosmic rays we observe above this energy to originate from sources outside of the Galaxy. However, the exact energy at which this transition occurs is not yet known; it depends on the energy spectra of galactic and extra-galactic sources.

1.3 Cosmic Rays in the Atmosphere

Most cosmic rays do not reach the ground, but are deflected by the geomagnetic field and/or absorbed by the Earth's atmosphere. Cosmic rays with energies of GeV or more will produce an *air shower*, a cascade of relativistic particles. The physics of air showers is quite complex as several different processes contribute. The most important effects are listed and explained below, and are schematically depicted in Fig. 1.2. Understanding the processes in air showers is important because the detection of air showers and measurement of their properties allows us to determine the properties of the primary cosmic rays.

The shower development is often described with respect to the mass overburden or column depth $X = \int_s \rho(s)\mathrm{d}s = \int_s \frac{\rho(h)}{\cos\theta}\mathrm{d}h$ along the particle's path s to be independent of the density profile of the atmosphere and the incidence angle θ.

Unless otherwise marked, all numbers and quantities in the following sections are taken from Grieder, (2010).

1.3.1 Electromagnetic Cascades

Electrons/positrons and photons mainly interact via electromagnetic processes. The two main processes that play a role in the development of air showers are e^+e^- *pair production* by photons in the electric field of air nuclei, and the emission of *bremsstrahlung* by electrons/positrons (also in the electric field of nuclei). These two processes cause the cascade to develop: A photon is 'split' into an electron/positron pair. The electron and positron radiate bremsstrahlung photons, which in turn produce more electron/positron pairs (of lower energy) and so on (cf. the blue component in Fig. 1.2). The particle content of the cascade increases, while the energy per particle decreases. With decreasing energy, the cross sections for pair production and bremsstrahlung decrease, and other processes become important. For photons, the major process is *Compton-scattering* off (quasi-free) electrons. The critical energy (defined as the energy for which the pair production cross section equals the Compton scattering cross section) in air is about 24 MeV. For electrons, ionization and excitation of air molecules becomes the dominant mode of energy loss at low energies. The critical energy (here defined as the energy for which the energy loss by the two processes is equal) is about 84 MeV in air. Below the critical energy, the production of new particle slows down and eventually stops. The shower particles continue to lose energy via Compton scattering and ionization. Eventually, photons are absorbed in atoms/molecules, positrons annihilate with electrons and any remaining electrons are bound into atoms/molecules.

The process of energy loss by bremsstrahlung is often described in terms of the radiation length χ_0. The *average* energy loss per traversed mass overburden is given by the following equation:
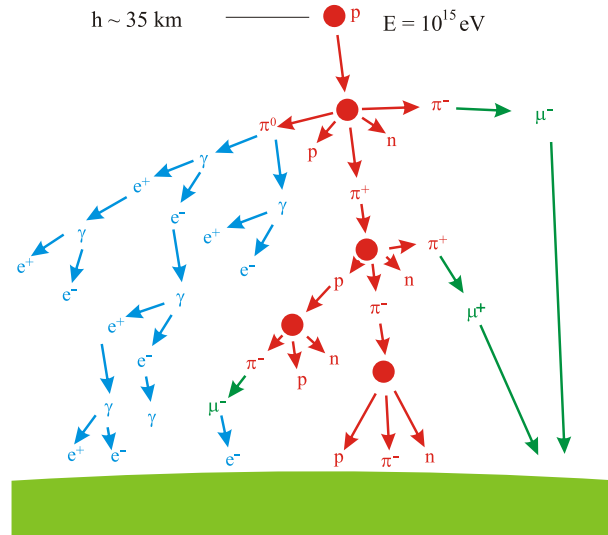
Figure 1.2: Air shower development in the atmosphere (schematic). Image by Mpfiz. Licensed under CC BY 3.0 via Commons. `https://commons.wikimedia.org/wiki/File:AirShower.svg`

$$-\left\langle \frac{\mathrm{d}E}{\mathrm{d}X}\right\rangle_{br} = \frac{E}{\chi_0}.$$

After traveling for one radiation length, the particle has lost on average $(1 - e^{-1})$ of its energy. The radiation length for bremsstrahlung by elecrons/positrons in air is $\chi_0^{br} = 37\,\mathrm{g\,cm^{-2}}$. For ease of comparison, the pair production cross section can be expressed in terms of the interaction length $\chi_0^{e^+e^-} = \frac{m_A}{\sigma^{e^+e^-}}$, where m_A is the atomic mass of the target substance. For e^+e^- pair production in air, the interaction length is about $47\,\mathrm{g\,cm^{-2}}$. The column depth at sea level is about $1\,\mathrm{kg\,cm^{-2}}$, corresponding to more than 20 interaction lengths for electromagnetic showers from zenith.

1.3.2 Hadronic Cascades

Hadronic particles also cause particle cascades or air showers (cf. the red component of Fig. 1.2), but these are more complex than the elecromagnetic showers due to the *inelastic* interactions between hadrons. Let us first consider inelastic nucleon-nucleon scattering. In such interactions, a number of secondary particles (mostly nucleon-antinucleon pairs, pions and kaons) are created. The average particle multiplicity increases the energy of the incoming nucleon. For an incoming proton with an energy of $100\,\mathrm{GeV}$ ($10\,\mathrm{TeV}$), the average number of charged secondaries is 5 (20). Most of the particles produced are mesons, about $90\,\%$ of which are pions. All three kinds of pions (π^+, π^-, π^0) are produced at approximately the same rate. The rest of the mesons are made up of kaons and a very small fraction of heavy mesons. The available kinetic energy is not distributed equally among the secondary

Particle	σ	χ	Interaction Length $L_\chi(h)$ [km]				
	[mb]	[g cm^{-2}]	$h = 2\,\mathrm{km}$	$h = 5\,\mathrm{km}$	$h = 10\,\mathrm{km}$	$h = 20\,\mathrm{km}$	$h = 30\,\mathrm{km}$
$\pi^\pm$	230	105	1.1	1.6	3.0	10	36
K	200	121	1.3	1.8	3.44	12	42
p	300	80	0.84	1.2	2.29	8.0	28
Fe	1700	14	0.15	0.22	0.40	1.4	4.9

Table 1.1: Approximate cross sections and interaction lengths for the inelastic scattering of 10 TeV hadrons with air nuclei (Heck et al., 1998).

particles: On average, the most energetic secondary carries about half of the available energy. However, the energy distribution fluctuates a lot from interaction to interaction. This leads to large fluctuations in the shower development. It also makes the showers less even than purely electromagnetic cascades: Hadronic showers can have several sub-cascades which may be slightly displaced from each other.

Most short-lived resonances produced in hadronic interactions decay quickly into pions, kaons, and nucleons. We will focus here on the main secondary products: Pions, kaons, and nucleons.

Nucleons and anti-nucleons produced in hadronic interactions will propagate through the atmosphere before again interacting with air nuclei and producing more secondary particles. The interaction cross sections and interaction lengths are given in Table 1.1. Kaons and charged pions are unstable particles. They may decay before they have the chance to interact with another nucleus. Characteristic decay lengths and interaction lengths are given in Tables 1.1 and 1.2. The lower the particle's energy and the higher in the atmosphere it is produced, the larger the chance of decaying. Neutral pions have such a short interaction length that they can be considered to always decay, unless produced with energies above 100 TeV (Heck et al., 1998).

The interaction lengths for pions, kaons, and protons in air are longer than the radiation lengths of electromagnetic cascades. This, coupled with the *leading particle effect*, whereby the most energetic secondary carries a significantly larger fraction of the energy than the other particles, means that hadronic showers tend to develop more slowly and penetrate more deeply into the atmosphere than purely electromagnetic cascades with the same primary energy.

The shower development depends on the energy of the primary particle. The higher the energy, the more likely it is for the shower to penetrate deep into the atmosphere and for shower particles to be detected at ground.

Unstable Particles in Hadronic Cascades

As mentioned before, the pions and kaons produced in hadronic cascades are unstable. Decay times and dominant decay products are given in Table 1.2.

Neutral pions decay quickly and almost exclusively into two photons, which will start

Particle	m [MeV]	τ	L_τ ($E=1\,\mathrm{TeV}$)	Decay modes
$\mu^\pm$	106.5	$2.2\,\mu s$	$6226.4\,\mathrm{km}$	$e^\pm \overset{(-)}{\nu_e}$
$\pi^\pm$	139.6	$260\,\mathrm{ns}$	$55.7\,\mathrm{km}$	$\mu^\pm \overset{(-)}{\nu_\mu}$
π^0	135.0	$85\,\mathrm{as}$	$190\,\mu m$	$\gamma\gamma$
$K^\pm$	493.7	$120\,\mathrm{ns}$	$7.5\,\mathrm{km}$	$\mu^\pm \overset{(-)}{\nu_\mu},\ \pi^\pm \pi^0$
K^0_S	497.6	$90\,\mathrm{ps}$	$54.7\,\mathrm{m}$	$\pi^+ \pi^-,\ \pi^0 \pi^0$
K^0_L	497.6	$51\,\mathrm{ns}$	$30.9\,\mathrm{km}$	$\pi^\pm \ell^\mp \overset{(-)}{\nu_\ell},\ 3\pi^0,\ \pi^+ \pi^- \pi^0$

Table 1.2: Characteristic decay times τ and decay lengths L as well as dominant decay modes of some unstable particles that occur in air showers. The decay length $L = \gamma\beta c\tau \approx \gamma c\tau = \frac{Ec\tau}{m}$ is proportional to energy for highly relativistic particles. Masses, decay modes, and life times from Olive et al., (2014). ℓ stands for e or μ.

electromagnetic sub-cascades if their energy is high enough. About one third of the mesons produced in hadronic interactions are neutral pions. Thus, after a few 'generations' of the shower, a significant fraction of the shower's energy will actually be contained in (potentially overlapping) electromagnetic cascades.

Charged pions decay almost exclusively into a muon and muon neutrino. Neutrinos from such decays propagate virtually without interacting with the atmosphere. They reach the ground and even penetrate the Earth. Muons lose some energy via ionization of the atmosphere and Cherenkov radiation, but can also penetrate far into the atmosphere and even reach the ground. Some muons might decay into electrons (which might start another electromagnetic cascade) and more neutrinos before they reach the ground.

Kaons decay into pions and/or a charged lepton and a neutrino, which behave as explained above.

Interactions of Nuclei

So far, only nucleon-nucleon interactions have been considered. However, cosmic-ray induced air showers are more complicated: The target material, air, consists of a mixture of different nuclei, mostly nitrogen, oxygen, and argon (electron shells and molecular structures can be ignored in the treatment of hadronic interactions).

Interactions between two nuclei (or a proton and a nucleus) can be considered as a superposition of one or more nucleon-nucleon interactions (between parts of the incoming nucleus and parts of the target nucleus). The parts of the nuclei which are not directly involved in the interaction are left in an excited, unstable state. They generally decay into one or more heavy nuclear fragments as well as free nucleons (Longair, 2011).

The cross section for interactions with air nuclei increases with increasing mass of the cosmic ray nucleus. For example, a 10 TeV iron nucleus has a roughly six times larger cross section than a proton of the same energy. This means that iron nuclei tend to have their first interaction higher up in the atmosphere than protons or helium nuclei. Also, iron-induced

showers develop differently than proton-induced showers because less energy is available per nucleon, but more nucleons are available to start hadronic cascades. As iron-induced showers start developing higher up, where the atmosphere is thinner, they tend to have more high-energy muons as pions produced high up are more likely to decay rather than to undergo further hadronic interactions.

1.3.3 Air Shower Observables

Kampert & Unger, (2012) gives a good overview of the air shower observables relevant for measuring the energy and charge of the primary particle, focusing on the difference between showers induced by protons and iron nuclei as representatives of light and heavy nuclei. Two important observables are the particles at ground and the shower development in the atmosphere, in particular X_{max}, the location of the shower maximum (where the number of charged particles is largest).

Most of the charged particles reaching the ground are electrons, followed by muons. The number of particles at ground strongly increases with the energy of the primary particle. On average, iron-induced showers have more muons than proton-induced showers of the same energy.

Heavier nuclei have a larger cross section for interacting with a nucleus in the atmosphere than protons, and their showers tend to develop faster. Hence, iron-induced showers have a smaller $\langle X_{max} \rangle$ and $\sigma(X_{max})$ than proton-induced showers.

Measuring the mass and energy of the primary particle using air shower observables is challenging and can only be done on a statistical basis, as both the particle distributions at ground and the shower maximum display large fluctuations between showers. In addition, and the predictions from different models or simulations of hadronic models do not always agree with each other.

1.3.4 Electromagnetic Emission by Air Showers

Air showers emit electromagnetic radiation in several wavelength bands. This radiation can be measured instead of or in addition to detecting the shower particles themselves. In particular, electromagnetic radiation can be used to directly access information about the shower development. There are several effects which lead to the emission of electromagnetic radiation:

Radio waves are emitted dominantly by two processes: The acceleration of charged shower particles by the geomagnetic field, and the net current of negative charges as the shower front propagates through the atmosphere (Askaryan effect). Recent experimental and theoretical efforts have lead to an increased understanding of radio emission by air showers, see Huege, (2016) for details.

Cherenkov radiation is emitted by charged particles traveling faster than the speed of light. In air, the Cherenkov light is emitted in the UV to visible range, and tightly beamed

in the forward direction. Cherenkov emission is treated in more details in Section 1.4.3 and Chapter 3.

Air fluorescence (more precisely, *luminescence*) refers to light which is emitted by excited molecules as they return to a lower-energetic state. Fluorescence emission due to air showers is mostly emitted by nitrogen molecules (N_2) and ions (N_2^+) in the wavelength range from 290 nm to 430 nm. See Keilhauer et al., (2013) for more information.

1.4 Detection of Cosmic Rays

As detailed in the previous section, cosmic rays do not reach the ground. As a result, there are two main approaches to detecting and measuring them. Depending on the energy range, one can either use balloon- and satellite-borne detectors for direct detection, or ground-based instruments which detect air showers induced by cosmic rays, not the primary particles themselves.

1.4.1 Direct Detection

Balloon- and space-borne cosmic ray experiments detect cosmic rays passing through the detector volume and measure their energy/momentum as well as their mass/charge. They generally consist of the same components as the detectors used in high-energy particle physics experiments, but of course condensed to fulfill the space, mass, and power requirements of space or balloon missions. Some recent experiments will be described below.

Direct detection experiments are sensitive in the MeV to TeV energy range. Above TeV energies, direct detection experiments run into their limits. Cosmic rays follow a power law energy spectrum with an index of about -2.5, which means that direct detection experiments eventually run out of statistics due to their limited volume. Additionally, at higher energies it becomes more difficult to measure a particle's momentum and energy via deflection in the magnetic field or via a particle shower in the calorimeter.

AMS-02

AMS, the Alpha Magnetic Spectrometer (Ting, 2013), is a particle detector installed on the international space station. It has a permanent magnet with a 0.15 T magnetic field, enabling it to measure cosmic ray momenta up to the TeV range. AMS has measured the proton spectrum up to 1.8 TeV (Aguilar et al., 2015b) and the helium spectrum up to 6 TeV (Aguilar et al., 2015a).

AMS has a charge resolution of less than 10% of the electron charge for light nuclei (Tomassetti & Oliva, 2015), enabling it to measure for example the boron to carbon ratio up to 700 GeV per nucleon (Oliva & the AMS Collaboration, 2016). AMS is able to identify nuclei up to Z=26 (Ting, 2013), however they have not published any spectra of heavy nuclei.

CREAM

CREAM, the Cosmic Ray Energetics and Mass (Ahn et al., 2007) was a balloon-borne detector designed to measure cosmic ray energy spectra over the energy range from about 1 TeV to 1 PeV, for nuclei from hydrogen to iron. The detector was flown successfully several times. The instrument has a charge resolution of about 20 % of the electron charge for light elements (C,N,O) and about 50% of the electron charge for heavy elements such as iron (Ahn et al., 2009), enabling it to identify the elemental composition of cosmic rays. However, CREAM was statistics limited at high energies and high Z. The iron spectrum was measured up to about 80 TeV, and was statistics-limited at high energies (Ahn et al., 2009).

1.4.2 Indirect Detection via Air Showers

Above TeV energies, direct detection experiments lose sensitivity. However, at these energies, one can use indirect detection techniques to detect cosmic rays, by detecting the air showers induced by the cosmic ray particles. Depending on the energy and direction of the incoming particle, some of the shower's contents, especially muons, can reach the ground and be detected there. In addition, the charged particles in the shower can be detected via Cherenkov light, radio emission, or fluorescence light. Kampert & Unger, (2012) provides a good overview over the experimental techniques employed by ground-based air shower arrays.

Charged particles that reach the ground are detected and counted using, for example, arrays of scintillation detectors or water Cherenkov counters. Muons can be separated from electrons by shielding part of the detectors so that electrons cannot enter. Especially at the highest energies, these air shower arrays can be very sparse and still detect enough particles to determine the shower parameters.

Radio signals are detected by (generally non-imaging) radio antennae. Cherenkov light can be detected either in non-imaging Cherenkov stations or with Imaging Cherenkov telescopes. Fluorescence light is detected by (imaging) fluorescence stations (or telescopes). Both fluorescence and Cherenkov emission is in the visible/UV range and can be detected with sensitive light sensors such as photomultiplier tubes (PMTs) or silicon photomultipliers (SiPMs).

Imaging and non-imaging detectors are sensitive to different observables. Non-imaging detectors can determine the arrival direction from the time profile of the signals they detect (radio, Cherenkov, or particles). In general, the energy is derived from the number of particles in the shower, which is derived from the total signal. Two shower properties are used to measure the charge of the primary particle: The ratio of muons to electrons (heavy primaries have more muons) and the longitudinal shower profile (showers induced by heavy primaries start earlier and develop faster). The longitudinal profile is inferred from the lateral shower profile (on the ground). Imaging Fluorescence detectors on the other hand can measure the longitudinal shower profile directly, but are not sensitive to the muon content of the shower. Some indirect detection experiments are listed below; many of them combine several detection methods. The Imaging Cherenkov method is described in Section 1.4.3.

The shower-to-shower fluctuations are too large to determine the charge of the primary particle on a shower-to-shower basis, but the measured distributions of the shower maxima or the muon content can be used to determine the composition of the cosmic rays at a given energy.

Measurements are compared to simulated air showers for both energy and composition measurements. The description of the hadronic interactions in air showers cannot (yet) be derived from first principles and are not directly accessible with current experimental technologies (for the highest energies at least). The simulation programs use approximations and extrapolations from measurements. There are systematic uncertainties associated with the mismodeling of the shower physics.

Because they use the Earth's atmosphere as a calorimeter, indirect detection experiments have much larger effective collection area and cover more radiation lengths than direct detection experiments. However, as energy and charge reconstruction rely heavily on the modeling of air showers in the atmosphere, the energy and charge resolution is generally much coarser than for direct detection experiments.

KASCADE and KASCADE-Grande

KASCADE (Antoni et al., 2003) was an air shower array in Germany which took data from 1996 to 2009. The initial array covered an area of $40 \, \text{hm}^2$ and was sensitive to air showers induced by cosmic rays with energies between $100 \, \text{TeV}$ and $100 \, \text{PeV}$. In 2003, it received an extension, *KASCADE-Grande*, which covered energies up to $2 \, \text{EeV}$ (Apel et al., 2010). The arrays consisted of several hundred stations with up to five scintillation detectors each. One of the detectors in each station was shielded from electrons using layers of lead and iron. In this way, each detector station could provide information about the total number of charged particles as well as the number of muons passing through the scintillation layers. This made the experiment sensitive to the mass of the primary particle. Additionally, *KASCADE* was equipped with a central detector (hadronic calorimeter) and a muon tracker near the center of the array. Both experiments measured the spectrum of cosmic rays in five elemental groups from $1 \, \text{PeV}$ to $200 \, \text{PeV}$ with large overlap between the two experiments, and the all-particle spectrum to above $1 \, \text{EeV}$(Apel et al., 2013).

Telescope Array and the Auger Observatory

The Pierre Auger Observatory (Abraham et al., 2004) and Telescope Array (Abu-Zayyad et al., 2013) are two hybrid arrays designed to investigate ultra-high energy cosmic rays (UHECR) with energies above $100 \, \text{PeV}$. They both have arrays of particle detectors as well as imaging air fluorescence detectors. The Auger Observatory uses water tanks to detect charged particles via Cherenkov emission in water, whereas Telescope Array uses scintillation detectors. Neither experiment is currently able to separate the muonic and electronic components of air showers. However, their fluorescence telescopes are very well suited to
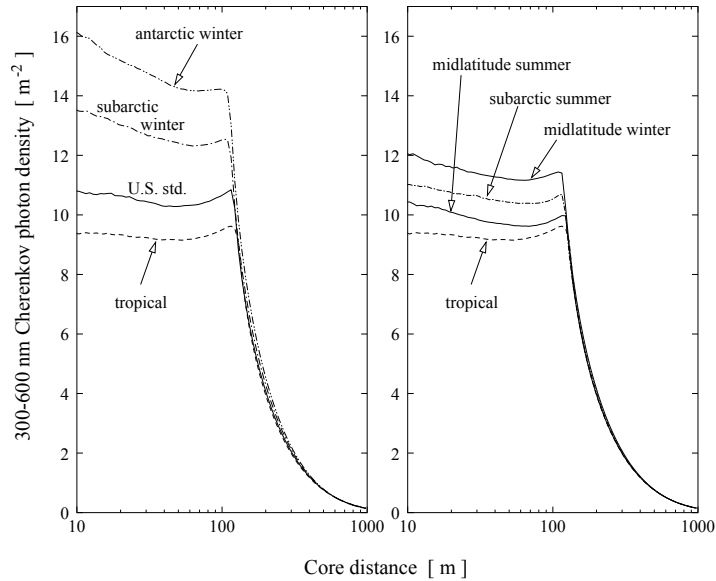
Figure 1.3: Cherenkov light intensity for a 100 GeV gamma-ray induced shower versus distance from the shower core for different atmospheric models, neglecting absorption. Figure taken from Bernlöhr, (2000).

measure the height of the shower maximum, making the experiments sensitive to the mass of the primary particle. The fluorescence telescopes can only take data during dark conditions, however, they can be used to calibrate other observables related to the distribution of particles on the ground measured by the surface detectors. The Auger Observatory also measures radio emission of charged particles in air showers. Both experiments have published measurements of the cosmic ray spectrum, composition and anisotropy above 1 EeV (Tinyakov, 2014; Aab et al., 2014; Aab et al., 2015b).

1.4.3 Cosmic Ray Air Shower Detection with IACTs

Imaging Air Cherenkov Telescopes are mainly used for gamma-ray astronomy. They generally have large mirror areas (roughly ten meter in diameter), focusing light onto a very sensitive, but coarse camera with only a few hundreds or thousands of 'pixels'. These light detectors are usually PMTs or silicon detectors, and are sensitive even to a few photons, with an integration time of a few nanoseconds. IACTs are able to image the Cherenkov light emitted by the charged components of air showers. From the orientation and shape of the image, the energy, arrival direction, and 'species' of the primary particle can be determined. Figure 1.3 shows examples of the Cherenkov intensity on the ground for showers induced by a 100 GeV gamma-ray photon.

As IACTs are optimized for gamma-ray astronomy, their main focus is on determining the energy and arrival direction of gamma-ray induced showers, and on separating them from the background of cosmic-ray induced showers. However, they can also be used to measure the charge and energy of cosmic ray induced showers. They are sensitive to the charge of

the primary particle due to differences in the image shape and the first interaction height, but also through direct Cherenkov (DC) light, emitted by charged primary particles before the first interaction. As the DC light is emitted high up in the atmosphere and under small angles, it can be separated from the light emitted by the rest of the shower.

The use of DC light to measure the charge of the primary particle was first proposed 15 years ago (Kieda et al., 2001). The DC light is concentrated in angular space and separated in time from the light emitted by the shower, so the two contributions to the signal can be separated in the camera of an IACT. Note that unless the telescope optics are isochronous, the time difference between the DC light and the shower light may be washed out by the mirror structure.

The intensity of the DC light is proportional to the square of the primary particle's charge, hence it can be used to measure this charge, especially for heavy primary particles. Aharonian et al., (2007) and Wissel, (2010) applied the DC technique to IACT data to separate showers induced by heavy particles, such as iron, from lighter ones, and measured the iron spectrum.

1.4.4 Astronomy and the Sources of Cosmic Rays

Cosmic rays are deflected by magnetic fields and hence do not point back to their sources. However, photons and neutrinos can be produced in connection with cosmic ray acceleration, making it possible to directly observe the sources of cosmic rays. Protons and nuclei in cosmic rays can interact with nuclei or photons fields in or near the acceleration site, producing pions which decay either into gamma rays (neutral pions) or into electrons and neutrinos (charged pions). Also, they may emit synchrotron radiation in the ambient magnetic field, and they may up-scatter ambient photons to higher energies (inverse Compton scattering). If the source is sufficiently optically transparent, the emitted photons can leave the source and be detected at Earth. From the emitted spectrum, which typically extends over many wavelengths from radio to TeV gamma rays, one can reconstruct the flux and spectrum of the accelerated cosmic rays. One problem with this approach is that in general, the observed spectra are not sufficient to fully characterize the cosmic ray flux in the absence of independent measurements of the magnetic field, plasma densities etc. Another problem is that one can obtain similar spectra from modeling the acceleration of electrons and positrons rather than hadronic cosmic rays (Böttcher et al., 2013). For variable sources, studying correlations between different wavelengths can help making this distinction, so can precise measurements of certain spectral features. For example, the energy spectra of gamma rays emitted from pion decays display a characteristic "bump" around the pion mass. The detection of neutrino emission from one of these sources would be further evidence for the acceleration of cosmic rays.

Cosmic rays can also interact with interstellar matter as they propagate through the galaxy, producing pions and finally gamma-ray photons. This *diffuse galactic emission* can be observed to measure the flux and cosmic ray spectrum elsewhere in our Galaxy.

1.4.5 Cosmic Rays in Star-Forming Galaxies

Star-forming galaxies provide a good way of studying sources of cosmic rays via astronomy and especially gamma-ray astronomy. Galaxies other than the Milky Way are expected to have mechanisms for the acceleration and propagation of cosmic rays that are similar to our own. If SNRs are indeed the main sources of galactic cosmic rays, the cosmic ray flux in other galaxies should correlate with the supernova rate, which in turn correlates with the star formation rate.

Cosmic rays can interact with the material in their galaxies, producing gamma-ray photons up to TeV energies (Torres & Domingo-Santamaría, 2005). The gamma-ray luminosity of galaxies should thus depend on the star formation rate as well as the density of gas and dust inside the galaxy. Observing this emission could help test the models of cosmic ray acceleration and propagation under different conditions.

Star formation rates differ from one galaxy to another, and also change over time. Galaxies with a high rate of star formation are called *starburst galaxies* (SBGs). Periods of high star formation generally only last for a small fraction of the lifetime of the galaxy, and are often triggered by interactions with other galaxies, e.g., mergers.

Due to the high rate of star formation, SBGs contain a large population of bright, massive O- and B-type stars, which burn all of their fuel within a few million years. Eventually, the cores of these massive stars undergo a super-nova explosion, during which their core collapses into a neutron star or a black hole. Most of the star formation takes place in the dense cores of the galaxies, with densities of the interstellar medium (ISM) above $100\,\mathrm{cm}^{-3}$ (Lacki et al., 2011).

Star-forming galaxies are very luminous in many wavelength bands from radio to gamma rays: The massive OB stars have a thermal emission spectrum which peaks in the UV range. The UV photons can be absorbed by the dense dust and gas of the star-forming regions and re-emitted in the far infra-red (FIR). Galaxies that contain enough dust to absorb all of the UV photons are called *complete UV calorimeters*. In those galaxies, the luminosity in the FIR range is expected to be proportional to the number of OB stars, and thus to the star formation rate.

Such a linear relationship indeed describes many galaxies for which the star formation rate can be estimated independently of the FIR luminosity. For example, Kennicutt, (1998) finds the following relation between the star formation rate SFR and the luminosity L^{FIR} in the $8\,\mathrm{\mu m}$ to $1\,\mathrm{mm}$ range:

$$\frac{SFR}{1 M_\odot \mathrm{yr}^{-1}} = \frac{L^{\mathrm{FIR}}}{5.8 \cdot 10^9 L_\odot}$$

This linear relationship only holds as long as the dust heating is dominated by UV emission from young, massive stars. In older galaxies, the FIR emission can also have contributions due to light emitted from older, less massive stars.

Star-forming galaxies also emit non-thermal radio-waves in the GHz regime. This radio emission is due to relativistic electrons and positrons, which are accelerated in SNRs and pulsar-wind nebulae and which cool via synchrotron emission due to the galactic magnetic fields. SNRs and PWNe, the remnants of massive stars, are efficient particle accelerators for roughly $1 \cdot 10^5$ yr. The rate of super-nova explosions is correlated with the star-forming rate. Hence, the number of SNRs/PWNs, the density of relativistic electrons, and the continuum radio emission should all be correlated with the star forming rate, and with the infrared luminosity.

This radio-infrared correlation is well known and has been measured extensively over many orders of magnitudes (Lacki et al., 2010). This result further supports the aforementioned explanation for the radio and infrared emission.

It is thought that SNRs are the main sources of Galactic cosmic rays. If this is indeed true, then this should also be the case in other galaxies. Hence, the density of (hadronic) cosmic rays should scale with the number of SNRs, which is proportional to the star formation rate.

Since star-forming galaxies are more dense compared to our own Galaxy, cosmic rays have a larger chance of interacting with interstellar matter or radiation fields, potentially producing gamma rays in the HE and VHE regime. The spectrum of the gamma-ray emission is expected to follow the energy spectrum of the cosmic ray population. Gamma-ray emission can occur due to hadronic processes (via neutral pions) and leptonic processes (inverse Compton scattering), with hadronic processes dominating above about 1 GeV.

Thus, there should be a GeV-infrared and a TeV-infrared correlation similar to the radio-infrared correlation described above. A linear relation between gamma-ray luminosity and star formation rate is only expected if all galaxies are complete *proton calorimeters*, meaning that protons above the pion production threshold lose all of their energy via inelastic collisions with the ISM. This is refered to as the *calorimetric limit*. For galaxies which are not complete proton calorimeters, the gamma-ray emission scales with the *calorimeter fraction* f_{cal}, which is the ratio of cosmic ray energy converted to pions to the injected energy, for cosmic rays above about 1 GeV (Pohl, 1994). The calorimeter fraction increases with the ISM density (Pohl, 1994).

Detailed simulations of the cosmic-ray production and gamma-ray emission of star-forming galaxies have been conducted by several groups (Torres, 2004; Torres & Domingo-Santamaría, 2005; Lacki et al., 2010; Yoast-Hull et al., 2015) to predict the gamma-ray emission of yet undetected galaxies. The models generally start with the injection spectra of protons and electrons. Energy losses via escape from the galaxy ionization, pion production, synchrotron radiation as well as the production of secondary particles e.g. from pion decays are taken into account to derive the steady-state proton, pion, and electron spectra. Then, the emission at radio and gamma-ray wavelengths is derived from these spectra. Input parameters such as injected spectra, ISM density, and magnetic field strength may be constrained from independent measurements, but with large uncertainties. They are adjusted within the constraints to match the measured radio spectrum.

Due to uncertainties and degeneracies in the fits, there can be large uncertainties on the predicted gamma-ray luminosities. This is illustrated by comparing some of the available predictions. For example, Torres, (2004) had to correct their first predictions, because the parametrization of the proton-proton cross section they used is thought to overestimate the amount of energy going into pion production. Using an updated parametrization of the cross section reduced their flux predictions above 100 GeV by a factor of about 5 (Torres & Domingo-Santamaría, 2005).

The authors of (Lacki et al., 2010) describe a class of models which fit several galaxies at the same time, which each galaxy described in terms of its column density, rate of star formation, and scale height. They found that several models can fit the same set of measurements. For example, in addition to their nominal model, they present a model with an increased magnetic field and increased winds in the galaxies, which predicts twice the gamma-ray flux from Arp 220 compared to the nominal model. Their nominal model agrees well with the updated predictions from (Torres & Domingo-Santamaría, 2005).

The predictions of the gamma-ray flux from Arp 220 by Yoast-Hull et al., (2015) actually span almost an order of magnitude in flux normalization, due to uncertainties in the magnetic field, acceleration efficiency of SNRs, and other parameters. Their predictions are also lower than the older predictions described above by one to two orders of magnitude, despite a similar approach. One marked difference is that (Torres, 2004; Torres & Domingo-Santamaría, 2005; Lacki et al., 2010) actually predict a large component due to emission from the galactic disk, while Yoast-Hull et al., (2015) only models the emission from the nuclei. This shows the large uncertainties in modeling starforming galaxies, and emphasizes the need for measurements in the gamma-ray regime.

Gamma-ray photons may be absorbed due to interactions with matter or radiation inside the galaxy. The two dominant processes are e^+e^- pair production in the electric field of a nucleus in the ISM (with a threshold energy of some MeV) and e^+e^- pair production due to interactions with infrared photons (with a threshold energy of some TeV). Detailed calculations have shown that the first process does not significantly affect the gamma-ray emission of Arp 220. However, $\gamma\gamma$ interactions do lead to a significant photon loss, which is expected to cause a cutoff in the observed spectrum above 2 TeV to 5 TeV (Torres, 2004; Yoast-Hull et al., 2015).

1.5 Experimental Results — Properties of Cosmic Rays

Cosmic rays mostly consist of protons and helium with smaller numbers of heavier elements as well as anti-protons. There are also contributions from electrons and positrons, which will not be treated in detail. The energy spectrum of hadronic cosmic rays approximately follows a power law with an index of -2.7 over a large energy range from several (GeV to several EeV), however several spectral features (deviations from this power law shape) have been identified. The arrival directions are distributed approximately isotropically.

1.5.1 Cosmic Ray Energy Spectra

Below some tens or hundreds of TeV, cosmic rays are detected directly by satellites or balloon-borne detectors. These generally have a fine charge resolution (typically below one electron charge), so that the elemental spectra can be measured. The measured spectra for the eleven most abundant elements are shown in Fig. 1.4. This plot includes measurements from eleven different experiments over seven orders of magnitude. There is good agreement between experiments in overlapping energy ranges. The H.E.S.S. data points correspond to the group of elements between $Z = 25$ and $Z = 28$, of which iron is the most abundant.

All elements show a suppression below a few GeV per nucleon and follow a power law for higher energies. The suppression at low energies is caused by interactions with the solar wind and the interplanetary magnetic field and is modulated with the solar cycle (Longair, 2011). In periods of high solar activity, the cosmic ray flux is suppressed.

At higher energies, the spectra of the intermediate to heavy elements (carbon to iron) can be fitted with a power law with a common spectral index of approximately -2.7. The all-particle spectrum also follows a power law with the same index. For proton and helium, there are indications that the spectrum deviates slightly from a simple power law. The AMS-02 experiment found that the spectra of the two elements become harder at higher energies. For protons, they measured a spectral index of $\gamma = -2.85 \pm 0.01$ below $(340 \pm 100)\,\mathrm{GeV}$, and a hardening of $\Delta\gamma = 0.13 \pm 0.06$ for higher energies (Aguilar et al., 2015b). Helium has a slightly harder spectrum overall, AMS measured a spectral index of $\gamma = -2.78 \pm 0.01$ below $(500 \pm 100)\,\mathrm{GeV}$ and a hardening of $\Delta\gamma = 0.12 \pm 0.04$ for higher energies. Measurements by CREAM confirm the hardening, in fact they find even harder spectra above a few TeV. CREAM found that the proton and helium spectra between 2.5 TeV and 250 TeV follow power-laws with indices 2.66 ± 0.02 for protons and 2.58 ± 0.02 for helium (Yoon et al., 2011).

For energies above the reach of direct detection experiments, the charge resolution is generally worse and only the all-particle spectrum or spectra of elemental groups can be measured. Figure 1.5 shows the all-particle energy spectrum from 100 TeV to 400 EeV. There seem to be significant discrepancies between the different results. However, there has been no cross-calibration between different experiments; Gaisser et al., (2013) show that the measurements can be brought into better agreement by shifting the energy scales within the systematic uncertainties of each experiment.

At about 4 PeV, there is a break in the power law spectrum and the spectral index softens to about -3.1. This break is also called the *knee* and it is thought to mark the transition from galactic to extra-galactic sources. It has been found that each elemental group displays a break or cutoff in the energy spectrum, with the cutoff energy increasing with the charge of the nucleus. The cutoff energy can be approximated as $Z \cdot 4\,\mathrm{PeV}$ (Hörandel, J. R., 2013). The superposition produces the observed break in the all-particle spectrum.

At a few 1 EeV, the all-particle spectrum steepens again. This feature is called the *ankle* and is thought to indicate the onset of a second component, most likely due to extra-galactic
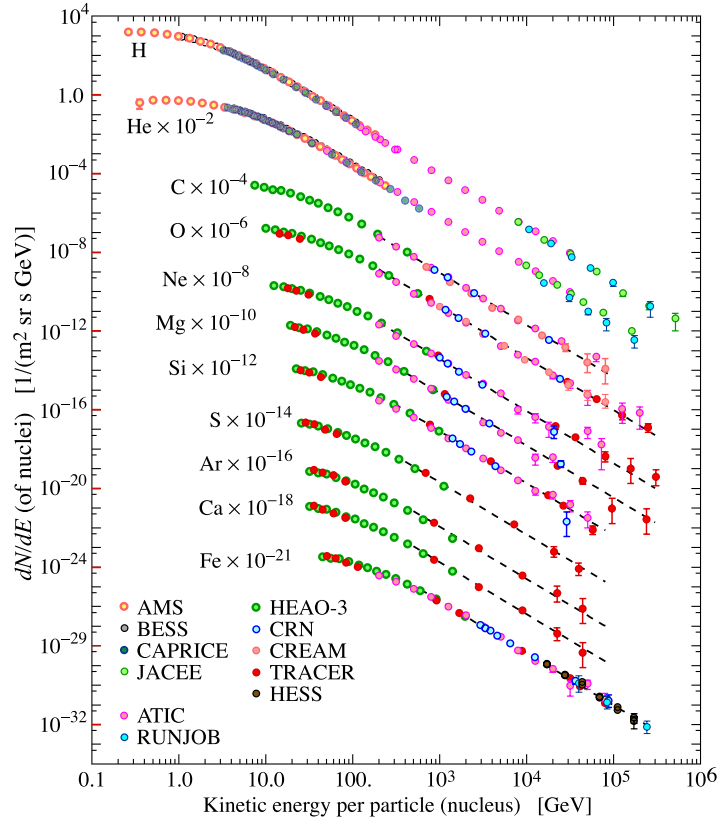
Figure 1.4: Single-element cosmic ray energy spectra below 1 PeV. Figure taken from Olive et al., (2014), see references therein.
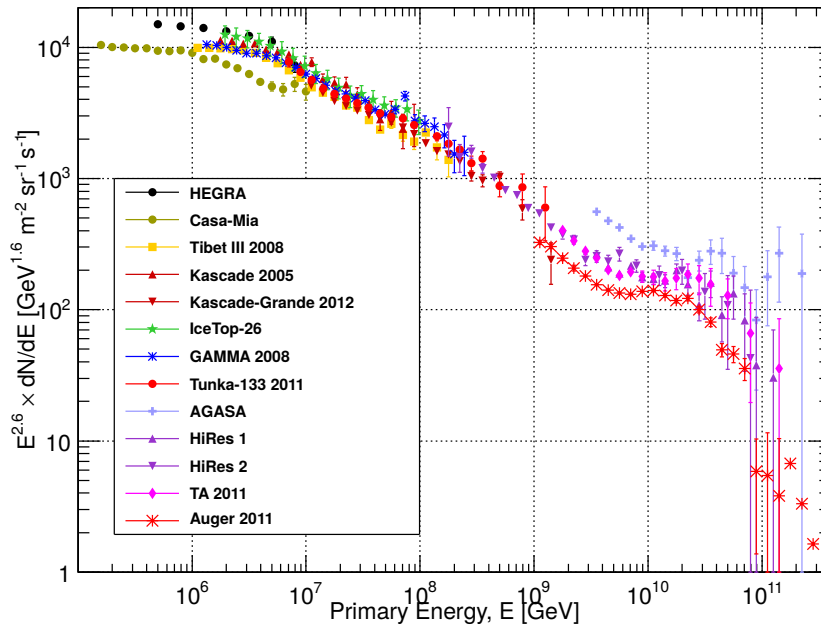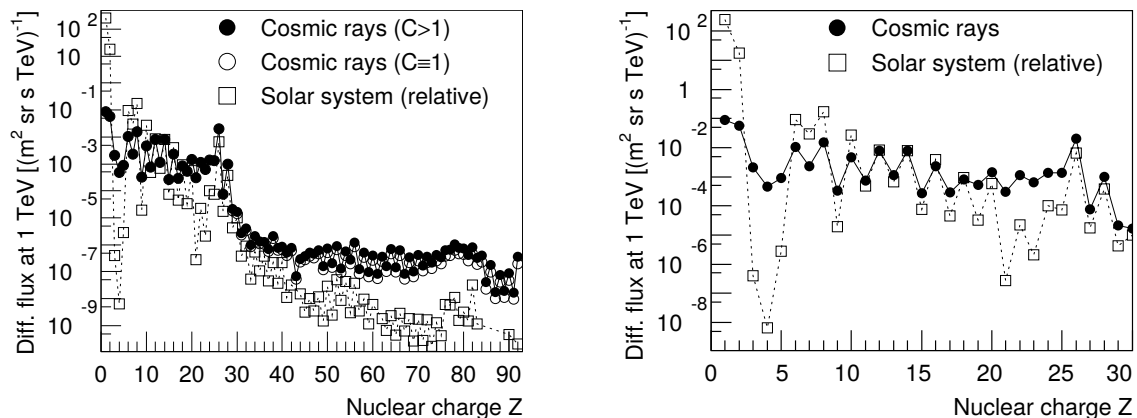

Figure 1.5: All-particle cosmic ray energy spectrum at the knee region and above. Figure taken from Gaisser et al., (2013), see references therein. Note the *knee* at a few PeV, the *ankle* at a few EeV, and a cutoff at a few tens of EeV.

(a) Figure taken from Hörandel, J. R., (2003). Solid and open circles refer to different methods of extrapolating the spectral index to high Z.

(b) Zoom to $Z < 30$. Figure taken from Hörandel, J. R., (2005).

Figure 1.6: Elemental abundances in cosmic rays at 1 TeV compared to the abundances found in the solar system. Solar system abundances are normalized to the silicon flux in cosmic rays. The y-axis refers to cosmic rays only.

cosmic rays. Telescope Array measured the ankle at 6.4 ± 0.3 EeV (Tinyakov, 2014), while Auger reports it to be at 4.2 ± 0.1 EeV (Abreu et al., 2012).

Telescope Array and Auger have both observed a cutoff at the highest energies. Auger measured the cutoff energy to 26 ± 1 EeV (Abreu et al., 2012), while Telescope Array measured it to be 54 ± 6 EeV (Tinyakov, 2014). The reason for the discrepancy is under investigation.

1.5.2 Cosmic Ray Composition

At lower energies (up to the TeV range), the elemental composition of cosmic rays is well sampled. Below a few GeV, protons and helium dominate the flux of cosmic rays as the solar modulation affects heavier elements more. Figure 1.6 shows the elemental abundances in cosmic rays at 1 TeV where solar modulation effects do not play a role, compared to the abundances in the solar system. Heavy elements up to Uranium (Donnelly, 1999) have been detected in cosmic rays, but elements above $Z = 30$ do not contribute significantly to the flux of cosmic rays. The elements with the highest abundance at 1 TeV are protons, helium, and iron.

The relative abundances differ between cosmic rays and the material in the solar system. For example, cosmic rays contain less hydrogen and helium, but more lithium, beryllium, and boron, as well as the elements from potassium to manganese. The reason for the deficit in hydrogen and helium may be that these elements are harder to ionize than heavier elements, which means that fewer of them might be accelerated. The overabundance of light and intermediate elements is explained by spallation processes, see Section 1.2.3. Nuclei produced via spallation are called *secondary cosmic rays*.

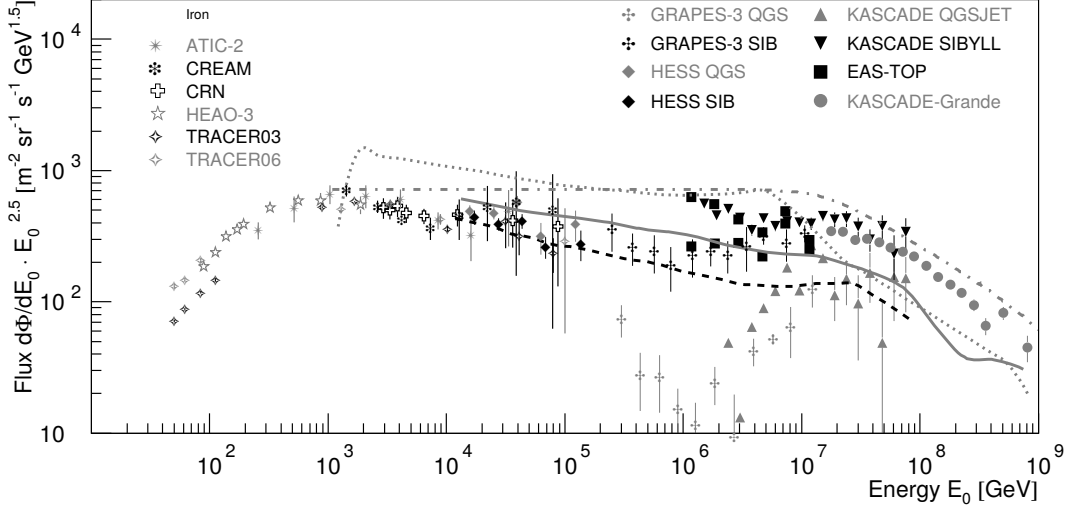At higher energies, the flux is too low for direct detection, and composition measurements

Figure 1.7: Measurements of the energy spectrum of iron nuclei in cosmic rays. Figure taken from Hörandel, J. R., (2013), see references therein for details. Air shower experiments (top right) measured elemental groups whereas direct detection experiments (top left) generally have single-element resolution. The lines refer to predictions from models of different sources/acceleration processes.

are more challenging. The elemental composition can be inferred from the shower shape (showers induced by heavy elements tend to have their maximum higher up in the atmosphere) or from the particle content at ground (shower induced by heavy elements tend to have more muons at ground). However, there is some discrepancy between the shower shapes predicted by different hadronic interaction models, especially at the highest energies, which leads to systematic uncertainties and to discrepancies between experiments. It seems clear now that the composition becomes continually heavier after the knee. This occurs because the proton spectrum drops off first, followed by helium, etc, up to iron (Hörandel, J. R., 2013).

After the iron knee, the composition becomes lighter again and appears to be dominated by helium and the nitrogen-group (Buitink et al., 2016).

At the highest energies, the measurements are less clear. For example, the Auger collaboration found that the flux of cosmic rays is dominated by protons around 1 EeV, whereas for higher energies, heavier components (helium or nitrogen) increase and dominate around 10 EeV (Aab et al., 2014). On the other hand, the Telescope Array collaboration saw no deviation from a proton-dominated composition between 2 EeV and 40 EeV (Abbasi et al., 2014).

1.5.3 The Iron Spectrum

The iron spectrum has been measured over a large energy range by both direct and indirect means. Figure 1.7 shows a compilation of previous results. Measurements were performed using direct detection experiments up from 50 GeV to 100 TeV, IACTs (direct Cherenkov technique) from 13 TeV to 200 TeV, and air shower arrays from 200 TeV to 1 EeV. Above

	E_0/TeV	$\phi_0 \cdot \text{m}^2\,\text{s}\,\text{sr}\,\text{TeV}$	γ
H.E.S.S. (QGSJET)	1	$(2.2 \pm 0.9_{\text{stat.}} \pm 0.6_{\text{sys.}}) \cdot 10^{-2}$	$2.62 \pm 0.11_{\text{stat.}} \pm 0.17_{\text{sys.}}$
H.E.S.S. (SYBILL)	1	$(2.9 \pm 1.1_{\text{stat.}} \pm 0.8_{\text{sys.}}) \cdot 10^{-2}$	$2.76 \pm 0.11_{\text{stat.}} \pm 0.17_{\text{sys.}}$
VERITAS (QGSJET)	50	$(5.8 \pm 0.84_{\text{stat.}} \pm 1.2_{\text{sys.}}) \cdot 10^{-7}$	$2.84 \pm 0.3_{\text{stat.}} \pm 0.3_{\text{sys.}}$

Table 1.3: Previous measurements of the cosmic ray iron spectrum by H.E.S.S. (Aharonian et al., 2007) and VERITAS (Wissel, 2010). Both experiments found the spectrum to be parametrized by a power law $f(E) = \phi_0 \cdot \left(\frac{E}{E_0}\right)^{-\gamma}$, with the parameters given above.

1 TeV, the spectrum seems to follow a power law with a cutoff or break somewhere around 200 PeV. At lower energies, the spectrum is suppressed.

Especially between 100 TeV and 1 PeV, there are not many measurements. The results from the GRAPES-3 array (Tanaka, 2005) have large systematic uncertainties due to differences between the predictions from different hadronic interaction models. This makes it difficult to measure or exclude any deviation from a power law in this energy range.

Measurements using the IACT technique were performed by the H.E.S.S. (Aharonian et al., 2007) and VERITAS (Wissel, 2010) collaborations. H.E.S.S. reported on the iron spectrum from 13 TeV to 200 TeV, using two different hadronic interaction models to reconstruct the energy and determine the selection efficiency. This provides an estimate for the systematic uncertainty due to the interaction model. VERITAS measured the spectrum from 20 TeV to 140 TeV. Both experiments found that the spectrum follows a power law. The fit results can be found in Table 1.3. The results agree with each other within the uncertainties.

Both analyses used the DC technique to identify iron-induced showers. They both used a 'standard' stereoscopic analysis with Monte-Carlo simulation based look-up tables for the energy as described in Section 4.4 to reconstruct the direction and energy of the primary particle. Images containing DC light were identified by looking for pixels with more light than their neighbors close to the reconstructed direction. The amount of DC light was estimated by subtracting the average over the neighbor's signals from the DC pixel. Events with at least two images with DC light were considered further, and the amount of DC light was used to determine the contribution from lighter elements.

Both experiments report on their statistic and systematic uncertainties. The statistic uncertainty was the largest *single* source of uncertainty in both cases. Dominant sources of systematic uncertainty were uncertainties due to atmospheric modeling and due to the hadronic interaction model used in the simulations.

1.5.4 Cosmic Ray Anisotropy

The arrival directions of cosmic rays on the sky are distributed nearly isotropically. Deviations from isotropy on the level of up to 10^{-3} have been measured on both small and large angular scales by many experiments.

Below about 10 GeV per nucleon, cosmic rays are noticeably affected by the solar wind:

The cosmic ray flux undergoes a modulation following the 11-year solar cycle (Olive et al., 2014). They are also deflected by the Earth's magnetic field, leading to an anisotropy and inhomogeneity in the flux. For example, the cosmic ray flux is generally higher near the poles (Olive et al., 2014).

Most recently, IceCube (Achterberg et al., 2006) reported on the anisotropy in the arrival directions of cosmic rays in the southern hemisphere in the energy range from 13 TeV to 5.4 PeV (Aartsen et al., 2016). The dominant contribution comes from a dipole component with energy-dependent amplitude and phase. Projecting the dipole along the right ascension axis, the phase of the dipole shifts from 50° to 270° at energies from 130 TeV to 240 TeV. The amplitude decreases with energy below the shift and increases after the shift, its maximum is on the order of 10^{-3}. In addition to the large scale anisotropy, Ice Cube observes significant contributions down to angular scales below 10°. After subtracting the large-scale contributions, they identify six regions with significant excess of cosmic rays and six regions with a significant deficiency. They do not observe any time-dependence of the anisotropy apart from a slight solar dipole, which does not affect the measurements over long periods of time.

The High Altitude Water Cherenkov (HAWC) Observatory measured the arrival directions of cosmic rays mostly from the northern hemisphere for cosmic rays with median energies of 2 TeV (Abeysekara et al., 2014). After subtracting the large-scale contributions, they identify three regions with significant excess (relative amplitudes of 10^{-4} to 10^{-3}), similar to what had been reported previously.

No significant anisotropy has been observed at higher energies (Maier, 2003; Deligny, 2014; Aab et al., 2015b; Aab et al., 2015a; Abbasi et al., 2014). There are hints for anisotropy at the highest energies, seen both by Auger ($E >$58 EeV) and Telescope Array ($E >$57 EeV). Auger reports no significant correlation between cosmic ray arrival directions and the locations of certain bright AGNs as well as the radio galaxy Centaurus A (Aab et al., 2015b). Telescope Array reports non-significant clustering between arrival directions on angular scales of around 20° as well as a non-significant correlation beteen cosmic ray arrival directions and the large scale structure of the Universe (Abbasi et al., 2014).

1.5.5 Indirect Measurements of Galactic Cosmic Rays

Gamma-Ray Emission from Supernova Remnants

Super-nova remnants are thought to be the main sources of galactic cosmic rays. Many of them have been found to emit non-thermal gamma rays in the GeV to TeV range (Aharonian et al., 2004; Albert et al., 2007a; Acciari et al., 2009; Acero et al., 2015), which indicates the presence of highly energetic charged particles (electrons, protons and/or nuclei). The energy spectrum of the gamma-ray emission can be used to disentangle whether the gamma-ray emission is mainly due to electrons or due to hadrons, and how many electrons respectively hadrons are accelerated in each SNR.

For example, broad-band studies of Tycho's SNR, including TeV-range gamma rays de-

tected by VERITAS, have provided evidence that the gamma-ray emission from this source is mainly due to pion decays, and that the main particles accelerated in this source are protons or nuclei (Slane et al., 2014).

The *Fermi*-LAT experiment (Atwood et al., 2009) has observed evidence for a characteristic spectral feature, the *pion bump*, in the HE gamma-ray spectra of two SNRs (W44 and IC 443) (Ackermann et al., 2013). This indicates that the HE gamma rays are produced in decays of neutral pions. From the shape of the gamma-ray and radio spectra, the *Fermi*-LAT collaboration was able to show that these two SNRs mainly accelerate protons up to several GeV. The electron-to-proton ratio must be 1% or less at $1\,\mathrm{GeV}$.

Electron acceleration in SNRs has also been observed. The HE and VHE gamma-ray emission from RX J1713.7-3946 is dominated by leptonic processes (inverse Compton scattering of ambient photons on relativistic electrons) (Abdo et al., 2011). However, this does not necessarily imply that proton acceleration does not take place as well. Protons could be accelerated and leave the source without much interaction with ambient matter if the density of the ISM around the SNR is low.

The superbubble theory is supported by the detection of gamma rays emitted by cosmic rays in the Cygnus cocoon, an OB association in the Cygnus region (Ackermann et al., 2011).

Diffuse Gamma-Ray Emission

The *Fermi*-LAT has also measured the diffuse gamma-ray emission from the Galaxy due to neutral pion decay as well as inverse Compton scattering and Bremsstrahlung of electrons. (Ackermann et al., 2012). As expected, the diffuse emission traces the distribution of gas in the Galaxy, however, their measurements of the diffuse emission from the outer Galaxy imply a larger galactic halo of cosmic rays than previously thought.

1.5.6 Cosmic-Ray Acceleration in Star-Forming Galaxies

Similar to the diffuse emission from our own Galaxy, we expect other galaxies to emit gamma-ray photons due to the interaction of cosmic rays with the ISM inside those galaxies. Thus, gamma-ray emission from other galaxies can be used to test our understanding of cosmic ray acceleration and propagation, even if individual sources cannot be resolved. As described in Section 1.4.5, it is expected that galaxies with a high rate of star formation have a high density of cosmic rays. These cosmic rays would be mainly confined to the galaxy, but they could produce gamma rays by interacting with the dense dust and gas of the star-forming region, which then would be detected at Earth. The gamma-ray spectrum of theses sources is expected to follow the cosmic-ray spectrum, i.e. a power law with and index of about -2 to -2.5. The higher density of cosmic rays in star forming galaxies, combined with a higher density of the ISM, should lead to a high luminosity in gamma rays.

Gamma-ray emission in the TeV range has been detected from two star-forming galaxies using IACTs, M82 (Acciari et al., 2009) and NGC 253 (Abramowski et al., 2012). While
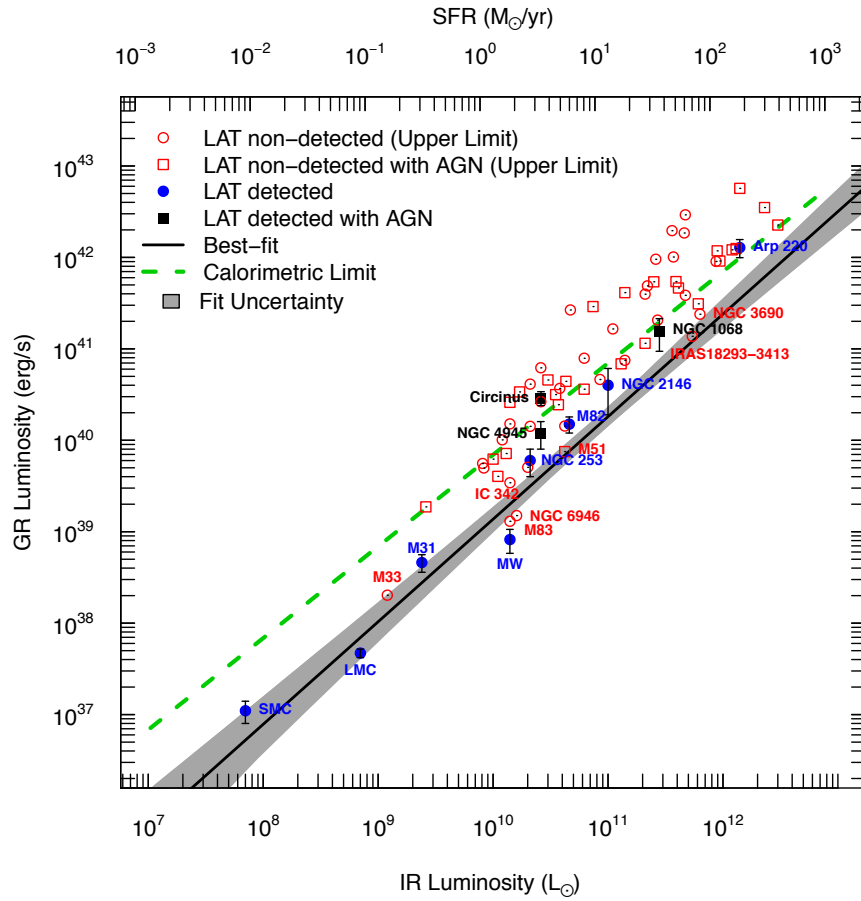
Figure 1.8: Gamma-ray luminosity (measurements and 95 % upper limits) versus star-formation rate as estimated by the infrared luminosity for star-forming galaxies. Plot from Rojas-Bravo & Araya, (2016).

the sample size is not sufficient to test for correlation, models of predominantly hadronic acceleration in SNRs do match the observed spectra (Lacki et al., 2011).

Fermi-LAT has detected gamma-ray emission in the GeV range from seven star-forming galaxies to date, as well as the Milky Way and our closes neighbors: the Large and Small Magellanic Clouds, and the Andromeda Galaxy (M31). The results are shown in Fig. 1.8. The gamma-ray luminosities of this sample correlates well with the star formation rates estimated from the FIR luminosity (Ackermann et al., 2012a; Rojas-Bravo & Araya, 2016). The Circinus galaxy, which also houses an AGN, is found to have a slightly higher gamma-ray luminosity than predicted from the star formation rate in the calorimetric limit, which might be due to a contribution from the AGN (Rojas-Bravo & Araya, 2016). Upper limits derived from non-detected star-forming galaxies do not contradict the derived correlation. Overall, the average measured gamma-ray luminosities imply a calorimetric fraction of $14\,\%$ to $30\,\%$ for galaxies with a star formation rate of $1\,M_\odot\,\mathrm{yr}^{-1}$ to $10\,M_\odot\,\mathrm{yr}^{-1}$, which is low, but consistent with predictions (Rojas-Bravo & Araya, 2016).

IACTs have searched for TeV emission from other star forming galaxies, and set upper limits on the gamma-ray luminosity. In Section 8.3, upper limits on the TeV-range gamma-ray emission from the three galaxies Arp 220, IRAS 17208-0014 and IC 342, derived using data taken by the VERITAS array, will be presented. In the following section, studies of these galaxies by other telescopes will be presented, as well as results on M82, which can be used to estimate the expected TeV flux of the other three galaxies.

M82

M82 is one of two star-forming galaxies which have been detected in the VHE gamma-ray regime. It is located within the local group at a distance of only $3.4\,\mathrm{Mpc}$ (Gao & Solomon, 2004). Its luminosity in the far infrared is about $46 \cdot 10^9 L_\odot$ (Gao & Solomon, 2004), indicating a star formation rate of roughly $5\,M_\odot\,\mathrm{yr}^{-1}$ (Ackermann et al., 2012b). VERITAS detected gamma-ray emission above $700\,\mathrm{GeV}$ from M82 (Acciari et al., 2009). The integral flux above this energy was measured to be $(3.7 \pm 1.0) \cdot 10^{-9}\,\mathrm{m}^{-2}\mathrm{s}^{-1}$. The energy spectrum from $700\,\mathrm{GeV}$ to $5\,\mathrm{TeV}$ is compatible with a power law with index $\gamma = 2.5 \pm 0.6$. M82 has also been detected in HE gamma rays by the *Fermi*-LAT (Abdo et al., 2010).

Lacki et al., (2011) use the measured gamma-ray spectra, compared to predictions given the infrared luminosity or the supernova rate, to derive the calorimeter fraction of M82. They find values of 0.3 to 0.4, with large uncertainties due to uncertainties on, e.g., the supernova rate, supernova acceleration efficiency, and distance to the galaxy.

NGC 253

NGC 253, the Sculptor Galaxy, is the other star-forming galaxy which has been shown to emit VHE gamma rays. It is located in the local group, at a distance of about $2.5\,\mathrm{Mpc}$ from Earth, and has an infrared luminosity of $21 \cdot 10^9 L_\odot$ (Gao & Solomon, 2004). This indicates a star

Reference	E_{min} [GeV]	E_{max} [GeV]	Flux (E_{min} to E_{max}) [m^{-2}s^{-1}]	Index γ
Ackermann et al., (2012a)	0.1	100	$\leq 4.4 \cdot 10^{-5}$	
Peng et al., (2016)	0.2	100	$(1.8 \pm 0.5) \cdot 10^{-5}$	2.35 ± 0.16
Griffin et al., (2016)	0.8	100	$(2.4 \pm 0.9) \cdot 10^{-6}$	2.23 ± 0.46
H.E.S.S. (Cornils, 2006)	1000	—	$\leq 3.3 \cdot 10^{-9}$	
H.E.S.S. (Nedbal, 2008)	1430	—	$\leq 2.5 \cdot 10^{-9}$	

Table 1.4: Measurements of the integral flux and spectral index of Arp 220 in the HE and VHE range. All measurements assume a power-law spectrum $\frac{dF}{dE} = f_0 \cdot \left(\frac{E}{E_0}\right)^{-\gamma}$.

formation rate of about $2\,M_\odot\,yr^{-1}$, a bit lower than M82 (Ackermann et al., 2012b). VHE gamma radiation from NGC 253 was detected by the H.E.S.S. telescopes (Acero et al., 2009; Abramowski et al., 2012). Its flux in the VHE regime was measured to $(5.6 \pm 1.2)\,nm^{-2}s^{-1}$ above 190 GeV, with a spectral index of 2.14 ± 0.35, indicating a calorimetric efficiency of 0.2 to 0.3 (Abramowski et al., 2012). HE gamma-ray emission from NGC 253 has been detected by the *Fermi*-LAT (Abdo et al., 2010)

Arp 220

Arp 220 is considered a very good candidate to search for gamma-ray emission due to its predicted gamma-ray luminosity and small distance to Earth. It is the closest ultra-luminous infrared galaxy (ULIRG) at a redshift of $z = 0.018$ (corresponding to about 75 Mpc, depending on the values of the cosmological parameters used to derive the distance). Arp 220 contains two dense cores (Rangwala et al., 2011), probably resulting from a merger event in the past. There is evidence for an AGN in one of the cores (Rangwala et al., 2011). It has a luminosity in the FIR range of about $1 \cdot 10^{12}$ to $2 \cdot 10^{12} L_\odot$ (Rangwala et al., 2011; Ackermann et al., 2012b) and a super-nova rate of about $(4 \pm 2)\,yr^{-1}$ (Lonsdale et al., 2006). Arp 220 has a very high rate of star formation, on the order of $200\,M_\odot\,yr^{-1}$ as estimated from the FIR luminosity.

Previous observations in the VHE regimes by the IACTs H.E.S.S. (Cornils, 2006; Nedbal, 2008) and MAGIC (Albert et al., 2007b) have not yielded evidence for VHE γ-ray emission from Arp 220. The upper limits derived from those observations are consistent with predictions by theoretical models.

Recently[2], two groups have reported evidence for gamma-ray emission in the high-energy regime, using data recorded by *Fermi*-LAT (Griffin et al., 2016; Peng et al., 2016). The measurement is quite challenging due to the presence of another gamma-ray source (likely CRATES J153246+234400) only $0.5°$ from the location of Arp 220. Griffin et al., (2016) report a tentative detection (4.6σ) of gamma-ray emission from Arp 220 in the energy range from 0.8 GeV to 100 GeV. Peng et al., (2016) report a definite detection (6.3σ in the energy

---

[2] *after* the studies presented in this work had been conducted

range from $0.2\,\text{GeV}$ to $100\,\text{GeV}$. The results from the two groups agree within uncertainties and their best-fit values of the integral flux and the spectral index can be found in Table 1.4. Both groups find a spectral index of about 2.2. Peng et al., (2016) also test for variability, but do not detect any. They conclude that the gamma-ray emission is most likely due to the star-forming activity as described in Section 1.4.5 due to the non-detection of variability, and because the measured flux and index agree with the theoretical predictions. In fact, the gamma-ray luminosity of Arp 220 is slightly larger than the predicted value in the calorimetric limit, but still consistent within the uncertainties (Griffin et al., 2016; Rojas-Bravo & Araya, 2016). This supports the idea that Arp 220 is a complete proton calorimeter (i.e., that the cosmic rays lose nearly all of their energy in interactions within the galaxy, rather than being able to diffuse out of it).

Peng et al., (2016) use the measured gamma-ray flux above $1\,\text{GeV}$ to estimate the acceleration efficiency of SNRs, i.e. the fraction of energy released in the super-nova explosion which eventually ends up in (hadronic) cosmic rays. They assume that Arp 220 is fully calorimetric and that the gamma-ray emission above $1\,\text{GeV}$ is dominated by hadronic processes. Further assuming the canonical value of $1 \cdot 10^{51}\,\text{erg}$ for the mean energy released in a super-nova explosion, and a super-nova rate of $(4 \pm 2)\,\text{yr}^{-1}$, they obtain an acceleration efficiency of $(4.2 \pm 2.6)\,\%$. The dominant uncertainty is due to the uncertainty of the super-nova rate. This result is compatible with what has been found for SNRs in our Galaxy and in the star-forming galaxies M82 and NGC 253.

IRAS 17208-0014

IRAS 17208-0014 is a ULIRG at a distance of about $173.1\,\text{Mpc}$ (Gao & Solomon, 2004). Its infrared luminosity is about $2.3 \cdot 10^{12}\,L_\odot$ and its estimated star formation rate is about $300\,\text{M}_\odot\,\text{yr}^{-1}$, making it a galaxy with one of the highest estimated rates of star formation. IRAS 17208-0014 has not been detected in HE or VHE gamma rays so far.

IC342

IC 342 is a star-forming galaxy at a similar distance as M82 ($3.7\,\text{Mpc}$) and four times lower infrared luminosity (Gao & Solomon, 2004), which puts its estimated star formation rate at $1\,\text{M}_\odot\,\text{yr}^{-1}$ (Ackermann et al., 2012b). It was observed in the VHE range by the Whipple 10m telescope, which did not detect an excess of gamma rays above the background expectations. They derived an upper limit on the gamma-ray flux of $55 \cdot 10^{-9}\,\text{m}^{-2}\text{s}^{-1}$ (99.9% C.L.) above $600\,\text{GeV}$ (Merriman, 2010).

1.6 Interpretations of the Results

Even with the increased precision and energy range over which the cosmic ray spectrum and composition have been measured, no distinct picture of the origin and propagation of

cosmic rays exists. It is believed that most of the galactic cosmic rays are accelerated in the discontinuity shocks of expanding supernova remnants, but this has not been conclusively proven.

Different explanations for the observed spectral features and energy-dependent cosmic ray composition have been proposed. For example, a good overview over different models explaining the *knee* in the spectrum is given by Hörandel, J. R., (2004). There are four categories of mechanism that affect the cosmic ray spectra and composition:

1. Energy limits of the acceleration mechanisms.

2. Energy-dependent leakage from the galaxy.

3. Interactions with interstellar matter, neutrinos, or photons.

4. New physics in high-energy interactions in the atmosphere.

The first two effects are difficult to disentangle from each other. Acceleration requires cosmic rays to be confined inside the accelerator by magnetic fields, and hence the maximum energy should be proportional to the particle's charge. The maximum energy for confinement in the Galaxy is also proportional to the particle's charge for the same reasons. However, neither the magnetic fields inside the sources of cosmic rays nor the Galactic magnetic fields are known with high precision. As long as the details about cosmic ray sources remain unknown, these parameters can be adjusted to reproduce the measured data.

For instance, Gaisser et al., (2013) propose a model that explains the measured data as a superposition of several spectral components with different cutoffs, where each component corresponds to a different source class. No complex propagation effects are needed. To ease computation, the elements are divided into seven groups and only one representative of each group is considered. Each elemental spectrum can then be described by a superposition of four distinct components, each described by a power law with an exponential cutoff. This includes the energy-dependent diffusion coefficient. The cutoff for each component is fixed, the spectral indices and the normalization of each element within each component are left free and fitted to the data. They were able to explain the measured spectra and composition from $Z\cdot200\,\mathrm{GeV}$ to the highest energies using four components with cutoff energies of $Z\cdot120\,\mathrm{TV}$, $Z\cdot4\,\mathrm{PV}$, $Z\cdot1.5\,\mathrm{EV}$ and $Z\cdot40\,\mathrm{EV}$, respectively. In this case, the first component is thought to correspond to supernova remnants. The second component, which would need less than 10% of the power budget of the first component, is thought to be a different type of galactic sources. Both galactic components have contributions from all elemental groups. The third and fourth component are thought to be extra-galactic; the third component contains only protons and iron, the fourth component protons only. The last component is not needed if one assumes a heavy composition at the highest energies. The authors note that the fit results are not unique; the same approach describes the data using only three distinct components with cutoffs at $Z\cdot4\,\mathrm{PV}$, $Z\cdot30\,\mathrm{PV}$ and $Z\cdot2\,\mathrm{EV}$, respectively, and different normalizations/spectral indices.

On the other hand, a different group of authors (Giacinti et al., 2015a; Giacinti et al., 2015b) propose an approach that describes the cosmic ray measurements with only two components (galactic and extra-galactic). The galactic sources are modeled with straight power law spectra. The Galactic magnetic field is modeled in detail and the knee is explained as a result of the rigidity-dependent leakage from the Galaxy. The transition to extra-galactic sources occurs around 200 PeV. The extra-galactic component is dominated by Active Galactic Nuclei in their model, in particular BL Lac objects. They are assumed to produce power law spectra with a cutoff at about 10 EeV.

The third and fourth mechanisms mentioned above are not considered likely explanations for the *knee* in the spectrum anymore. Interactions between cosmic rays in the PeV range and the interstellar medium would produce an excess of lower-energy cosmic rays, which has not been observed (Hörandel, J. R., 2013). However, interactions with the cosmic microwave background may be the cause for the observed cutoff at the highest energies (GZK cutoff or photo-disintegration). Until the sources of extra-galactic cosmic rays are found, it will be difficult to ascertain whether this cutoff is due to properties of the sources or propagation effects.

The last mechanism proposes the existence of yet unobserved, heavy particles which would be produced in interactions between cosmic rays and nuclei in the atmosphere. These particles would either be stable or decay into other new particles or neutrinos, thus reducing the hadronic content of the air showers. In this case, the observed spectral features would not be real, but just apparent changes in the spectrum due to a bias in the energy reconstruction. So far, the LHC experiments have not published any indications of new physics in proton-proton collisions with center-of-mass energies up to 13 TeV, corresponding to a 90 PeV proton colliding with a proton at rest. This makes it unlikely that new physics could explain the *knee* at around 4 PeV.

The non-observation of anisotropy at the highest energies can be used to constrain some combinations of cosmic ray composition, source distribution, and magnetic fields. For example, assuming a proton-dominated composition up to the highest energies, a major contribution from galactic sources above 1 EeV can be excluded because the predicted anisotropy is much higher than what is observed (Aab et al., 2015b; Deligny, 2014). For extra-galactic (proton-)sources, the combinations of source density and magnetic deflection can be constrained (Aab et al., 2015a).

1.7 Motivation for Measuring the Iron Spectrum with VERITAS

As shown before, there are currently many models that describe the origin of cosmic rays and explain the shape of the spectra. To distinguish between them, it is important to measure the spectra and composition at all energies very precisely. For example, AMS has shown that the proton and helium display spectral hardening for energies above 100 GeV resp. 200 GeV,

which could indicate the onset of a new component at a rigidity of 100 GeV. This would correspond to an energy of roughly 2.5 TeV for iron.

The iron spectrum has been measured across all energies; however, the energy range between 10 TeV and 1 PeV is not well covered (see Section 1.5.3). In particular, there is no good measurement of the spectral index in this region.

The DC technique, which identifies heavy nuclei due to the Cherenkov light they emit before starting an air shower, is able to help bridge this "gap". IACTs like VERITAS cannot provide measurements at either 2.5 TeV nor the *iron knee* at above 10 PeV using this technique. However, they can provide good coverage of the intermediate energies (between roughly 10 TeV and 500 TeV). This is important to get a good lever arm for studying the shape/energy of the knee or a possible spectral hardening, and to detect (or exclude) possible other features (deviations from a power law shape) that could give a hint at the sources of cosmic rays.

Due to the larger effective collection area, the measurements have smaller statistical uncertainty than measurements made with satellite or balloon experiments. At the same time, the systematic uncertainties on the measured charge are smaller than for air shower arrays, and dominated by uncertainties in the atmosphere and in the detector modeling rather than uncertainties in the hadronic interaction models.

As mentioned, the DC technique is particularly suited for the study of heavy elements, of which iron is the most abundant in cosmic rays. However, the charge resolution is not good enough to obtain the elemental iron spectrum. The DC technique has already been applied to measure the spectrum of elements between $Z = 25$ and $Z = 28$ (Aharonian et al., 2007). With a larger data set and an improved analysis method, we can extend the energy range and obtain a more precise measurement of the spectral index.

A great benefit of the DC method is that an existing data set can be used. IACTs record tens to hundreds of shower images per second, most of which originate from cosmic rays. These events make up the largest background to for gamma-ray astronomy. Analyzing these events to select iron-induced shower images does not require additional hardware or special detector settings and hence does not take time away from gamma-ray astronomy applications.

2 Atmospheric Properties Affecting the Understanding of Air Showers

It is impossible to precisely describe the development of air showers and emission of Cherenkov light in an analytic way. Instead, Monte-Carlo simulations of air showers, Cherenkov light emission and propagation, and the detector response are used to develop and optimize analysis techniques, calibrate for example the energy response of the detector, and to determine the reconstruction/selection efficiency for signal events. For applications within gamma-ray astronomy, there is a large background of cosmic-ray showers. The background rejection can be optimized and studied on signal-free parts of the sky. For the cosmic-ray analysis presented here, both signal and background showers are distributed nearly isotropically, so simulations are used for both. In either case, the simulations have to be validated against recorded data.

The simulation procedure can be divided into four parts:

1. Development of the air shower.

2. Emission of Cherenkov light.

3. Propagation of the Cherenkov light through the atmosphere and telescope optics.

4. Camera signals and their propagation through the readout electronics.

The first three parts depend on the properties of the atmosphere above the site, which will be discussed in this chapter. The *density profile* of the atmosphere determines the development of the air shower. The intensity and angle of the Cherenkov emission depend on the *refractive index* and the propagation through the atmosphere depends mainly on the *transmission profile* of the atmosphere.

2.1 Density Profiles

In this section, we will first derive atmospheric density profiles for some simplified assumptions, followed by more detailed assumptions which let us derive models valid for the VERITAS site. In all cases, it is assumed that the atmosphere is in hydrostatic equilibrium,

$$\mathrm{d}P = g\rho\mathrm{d}z, \qquad (2.1)$$

where P is the pressure, g the acceleration due to Earth's gravity, ρ the density of air, and z the height above sea level.

2.1.1 The Ideal Gas Atmosphere

Let us first assume that the atmosphere is homogeneous and follows the ideal gas law,

$$P = \frac{\rho RT}{M}, \tag{2.2}$$

with P and ρ as above, R the ideal gas constant $(8.31 \, \mathrm{N\,m\,mol^{-1}\,K^{-1}})$, T the temperature in Kelvin, and M the molar mass (about $0.029 \, \mathrm{kg\,mol^{-1}}$ for air). Combined with Eq. (2.1), the following differential equation for P is obtained:

$$\frac{\mathrm{d}P}{P} = -\frac{gM}{RT}\mathrm{d}z \tag{2.3}$$

Here, M is constant (since the atmosphere was considered to be homogeneous), and we will consider g to be constant as well for now. We will consider first an *isothermal* atmosphere, i.e. $T = T_0$ is constant as well. In that case, Eq. (2.3) can be solved by integrating both sides and one obtains

$$P(z) = P_0 \cdot \exp\left(-\frac{gM}{RT_0} \cdot (z - z_0)\right) \tag{2.4}$$

and

$$\rho(z) = \frac{MP(z)}{RT_0} = \rho_0 \cdot \exp\left(-\frac{gM}{RT_0} \cdot (z - z_0)\right) \tag{2.5}$$

where P_0 is the pressure at the reference level z_0 (e.g., the ground) and $\rho_0 = \frac{MP_0}{RT}$. The expression $\frac{RT_0}{gM}$ has units of length and is referred to as the *scale height*. For $T_0 = 0\,°\mathrm{C}$ the scale height is approximately $8\,\mathrm{km}$. The scale height is proportional to the temperature. For constant ground pressure, a higher temperature will lead to a density profile that is less dense at ground level, but decreases more slowly with increasing height.

Let us now consider an atmosphere with a constant temperature gradient, i.e. $T(z) = T_0 + L(z - z_0)$. In this case, T_0 is the temperature at the reference level z_0 and L is called the *temperature lapse rate*. Again, Eq. (2.3) can be solved by integration and one obtains

$$P(z) = P_0 \cdot \left(\frac{T(z)}{T_0}\right)^{\left(-\frac{gM}{RL}\right)} \tag{2.6}$$

and

$$\rho(z) = \rho_0 \cdot \left(\frac{T(z)}{T_0}\right)^{-\left(1 + \frac{gM}{RL}\right)} \tag{2.7}$$

with $\rho_0 = \frac{MP_0}{RT_0}$.

For the purposes of air shower simulations, we are concerned with the atmospheric profile up to about $100\,\mathrm{km}$ or $120\,\mathrm{km}$ above sea level. Assuming a scale height of $8\,\mathrm{km}$, the density at $120\,\mathrm{km}$ above sea level is only about $3 \cdot 10^{-7}$ of the density at sea level.

In this range, the temperature of the atmosphere takes values between from about $190\,\mathrm{K}$ to $340\,\mathrm{K}$ (NASA et al., 1966), corresponding to scale heights from $5.5\,\mathrm{km}$ to $10\,\mathrm{km}$. The isothermal assumption is too simplistic to model the atmosphere over the full range. However, it can be used to model the atmospheric profile at smaller scales, as well as to get an idea of the overall behavior of the atmospheric properties.

The whole atmosphere may be modeled as set of layers where each layer has either constant temperature or a constant temperature gradient. The parameters P_0, ρ_0, T_0 and z_0 have to be replaced by the pressure, density, temperature, and height at the layer boundaries, and chosen so that there are no discontinuities in pressure/density at the layer boundaries.

2.1.2 US Standard Atmospheres and Supplements

The U.S. committee for the extension of the standard atmosphere (COESA) has accepted a set of atmospheric models that describe atmospheric parameters (e.g., temperature, pressure, density, composition) from the sea level up to $1000\,\mathrm{km}$ for a given geographic latitude and season (NASA et al., 1966; NASA et al., 1976). The models are based on various measurements, including radiosondes, rocketsondes, satellite drag, and others. Each model describes the atmosphere as a set of layers, with smooth transition between the layers. In the region of interest here (below about $120\,\mathrm{km}$), the temperature in each layer is either constant or increases/decreases linearly with height. The mean molecular mass is constant below about $80\,\mathrm{km}$, thus, the expressions derived above apply. The atmospheric profiles are tabulated in the above mentioned publications. The widely used air shower simulation package CORSIKA (Heck et al., 1998) contains several atmospheric profiles corresponding to some of the US standard profiles. This data is also included in the MODTRAN software package (Kneizys et al., 1996; Berk et al., 2006; Anderson et al., 2007; Berk et al., 2008), which was used to derive the optical properties of the atmospheric models (optical index and transmission probabilities).

2.1.3 Atmospheric Profiles for the VERITAS Site

The National Weather Service of the U.S. maintains an upper-air observation program[1], releasing weather balloons with radiosondes from 92 stations in the USA twice a day. This

---

[1]`http://www.ua.nws.noaa.gov/`

includes a station in Tucson, Arizona, close to the location of the VERITAS array. These radiosondes provide measurements of the air pressure, temperature, and humidity up to 30 km or more on some flights. Cleaned data are provided by the University of Wyoming in machine-readable format[2].

Previous studies, using Tucson radiosonde data, showed that the density profile up to 30 km above the VERITAS site displays seasonal variations, causing differences of up to 18 % in the light yield for gamma-ray showers, and that the seasonal averages are not well described by any of the standard atmospheric models described above (Daniel et al., 2008).

Running dedicated simulations for each observing night would require too many computing resources. Also, there is some scattering/measurement uncertainty associated with a single flight. The atmosphere above southern Arizona is quite stable during the winter months and the summer months, respectively. The transition dates shift slightly from year to year: The transition from winter-like months to summer-like months usually happens in April or May. The transition from summer-like to winter-like usually happens in October or November. The VERITAS collaboration uses two dedicated atmospheric profiles to produce gamma-ray shower simulations, which are used to derive the instrument response functions for the VERITAS telescopes for the analysis of gamma-ray data. These profiles describing average conditions at the VERITAS site during the winter (December to February) and the summer (May and September[3]) months. They were derived from the radiosonde measurements and extended above the radiosonde range using the US76 standard profile for the VERITAS summer model, and the mid-latitude winter profile for the VERITAS winter model.

These profiles, shown in Figs. 2.1 and 2.2, were, however, not suitable for the simulation of direct Cherenkov light emitted by hadronic primaries, due to the way that the data points had been averaged. The 'kinks' in the profile, while affecting the predicted emission of DC light, were smoothed out when considering the predicted light yield from air showers, and hence did not affect the gamma-ray simulations.

To remedy this, two new profiles were derived using again the radiosonde measurements (plus the same standard profiles above the balloon range). The winter atmospheric profile was obtained from data taken in December, January, February and March. The summer profile was obtained from data taken in May and September. Transition months were excluded, as were July and August as there are no VERITAS observations during these months due to the summer monsoon.

The averaging procedure has been changed to avoid biases. The averages are now calculated in the following way: First, the desired heights for which the values are to be tabulated are chosen, in this case steps of 1 km starting at 1 km above sea level. Then, tabulated profiles of density and temperature are produced for each radiosonde flight. If there is a measurement available at the desired height, it is used. If there is no measurement available, the values

---

[2]http://weather.uwyo.edu/upperair/sounding.html

[3]Due to monsoon season with heavy rainfall and frequent thunderstorms, VERITAS generally does not take data between June and August. Atmospheric data from those months are not included in the averages

are interpolated from the nearest measurements. The temperature and relative humidity are interpolated linearly, the pressure is interpolated log-linearly (i.e. it is assumed that the pressure follows an approximately exponential profile). No extrapolation is performed below the first or above the last data point of each flight. Then, these tabulated density and temperature are averaged over all flights. For each height, only balloon flights that had data available are used in the averaging procedure.

The density profiles derived in this manner can be seen in Figs. 2.1 and 2.2. The densities are shown as a ratio to a isothermal atmosphere with an arbitrary scale height of 8 km, to enhance differences between the profiles. The mid-latitude winter model and the US 76 model match the data in the 'transition regions' (20 km to 25 km resp. 25 km to 30 km), but not at lower altitudes.

2.2 Components of the Atmosphere

The major constituents of the atmosphere are the dry gases (nitrogen, oxygen, argon) and water vapor. These are sufficient to calculate the pressure/density profiles to the precision needed for the simulation of air showers. In addition, there are trace gases (e.g., ozone, nitrous oxides, carbon monoxide, and carbon dioxide) and aerosols which may affect the optical properties of the atmosphere. However, these trace components can be neglected for other purposes such as determining the density profile.

Due to turbulent mixing, the relative amounts of the dry gases can be considered constant with height up to about 80 km. The dry component of the atmosphere below this height contains 78.08 % nitrogen (N_2), 20.95 % oxygen (O_2), and 0.93 % argon (Ar) by volume, with a mean molecular mass of 28.9645 g mol^{-1}. Above the *turbopause*, the atmosphere cannot be considered homogeneous. Above about 80 km, the atmosphere is so thin that turbulent mixing does not occur and the atmosphere becomes stratified by weight. However, while this effect is necessary to understand the pressure/density profile of the atmosphere at high altitudes, it can be neglected for the purposes of air shower simulations.

Water vapor is present at a varying level in the lower part of the atmosphere, up to a few percent by volume. The scale height of the water vapor component is smaller than that of the dry component, i.e. water vapor is present only below about 25 km (NASA et al., 1966). Water can also be present in the form of aerosol (fog or clouds), which will be treated below.

The amount of water vapor is often specified in terms of the relative humidity, defined as $RH = \frac{P_w}{P_s(T)}$, where P_w is the partial pressure of the water vapor component and P_s is the temperature-dependent pressure of saturated water vapor. P_s is about 23 hPa at 20 °C and increases non-linearly with the temperature, see for example Tetens, (1930) and Buck, (1981).

The molecular mass of water is less than that of the dry components of air. Hence, moist air is lighter than dry air of the same pressure. This effect has to be accounted for when calculating the density. To first order, assuming ideal gases, we have
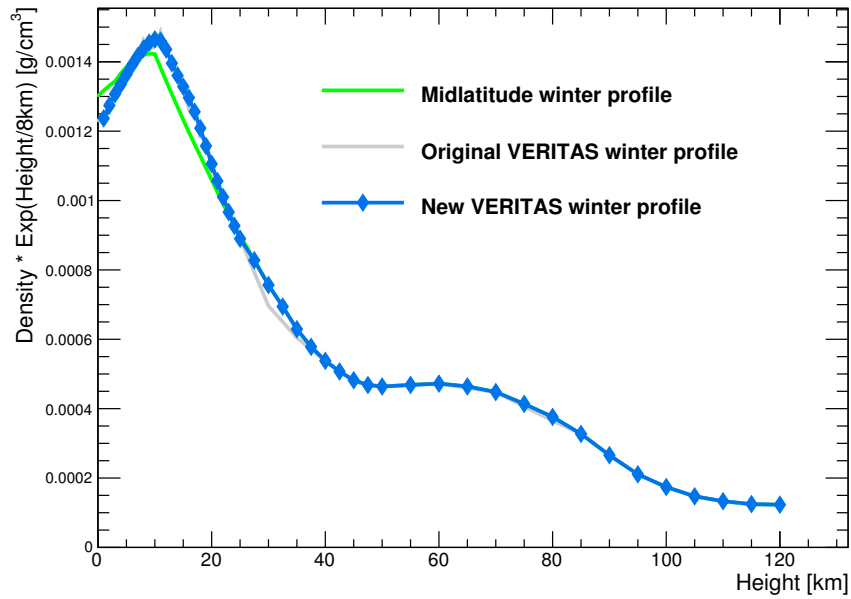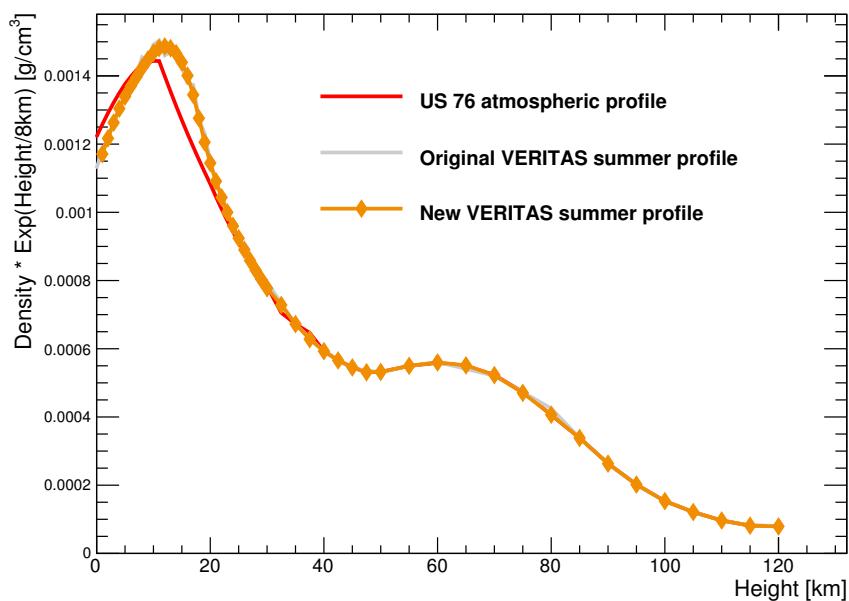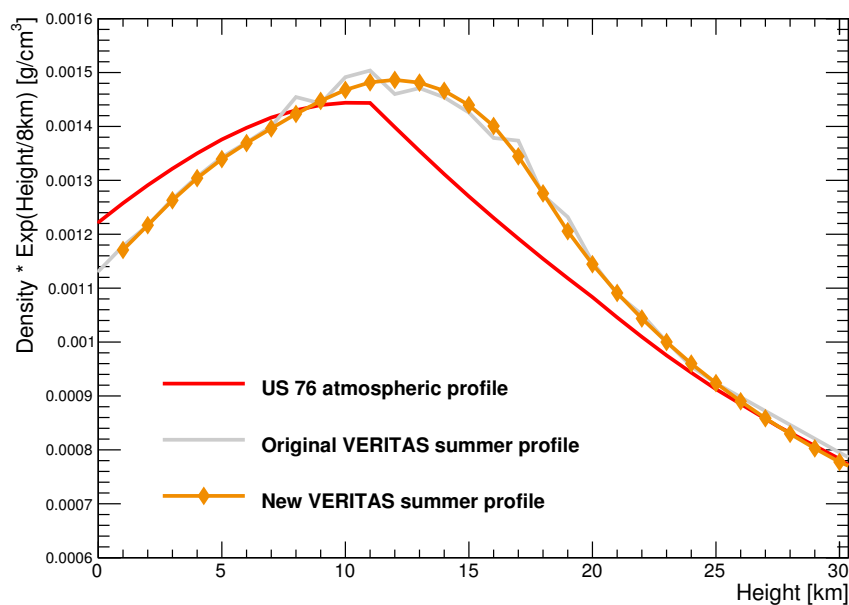
(a) Full profile.
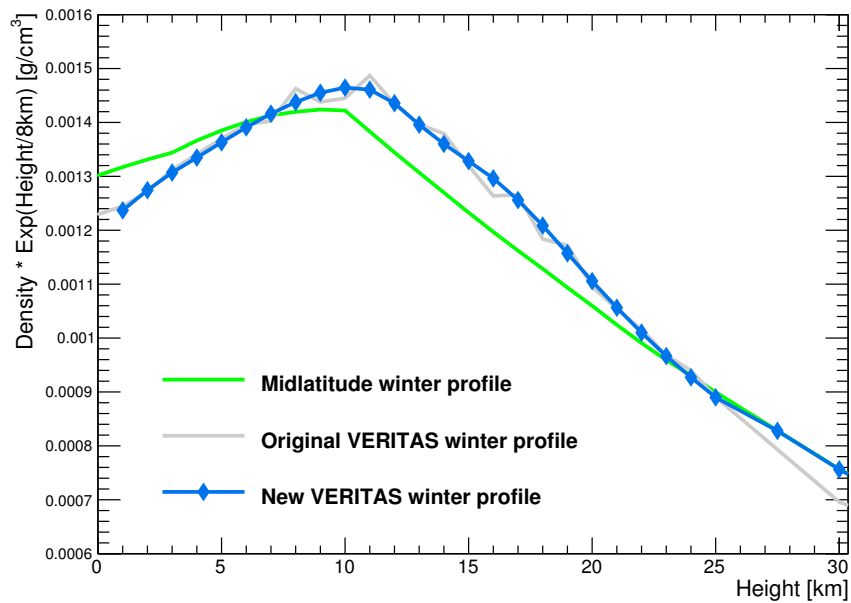
(b) Density profile below 30 km.

Figure 2.1: Density profile of the atmosphere above the VERITAS site, winter months. Blue: New model. Gray: Model previously used by the VERITAS collaboration. Green: mid-latitude winter atmosphere.

(a) Full profile.

(b) Density profile below 30 km.

Figure 2.2: Density profile of the atmosphere above the VERITAS site, summer months. Orange: New model. Gray: Model previously used by the VERITAS collaboration. Red: US standard atmosphere (1976).

$$\begin{aligned}
\rho_{\text{moist}} &= \frac{P_d \cdot M_d + P_w \cdot M_w}{R \cdot T_0} \\
&= \frac{(P - P_w) \cdot M_d + P_w \cdot M_w}{R \cdot T_0} \\
&= \frac{P \cdot M_d}{R \cdot T_0} \cdot \left(1 - \frac{P_w}{P} \cdot e \right),
\end{aligned}$$

where P is the total pressure, P_d and P_w are the partial pressures of the dry components resp. water vapor, M_d and M_w are the average molecular mass of the dry component and the molecular mass of water, respectively, and $e = \frac{M_d - M_w}{M_d} \approx 0.378$.

The relative humidity profile above the VERITAS site as measured by the radiosondes can vary a lot from measurement to measurement. The average typically takes values from 20% to 40% below $10\,\text{km}$ above sea level, and rapidly decreases at higher altitudes. On single flights, the relative humidity can be much higher (up to 100%). However, such a high relative humidity often coincides with the presence of clouds or fog. Under such conditions, VERITAS would either not take data, or the data would be excluded from science analysis[4]. The relative humidity at the VERITAS site is estimated to be below 50% on nights that are relevant for science analysis.

Among the trace gases, the dominant contribution is due carbon dioxide, about $4 \cdot 10^{-3}\%$ by volume in 2016. The steady increase in carbon dioxide does not affect the optical properties of the atmosphere relevant for the study of Cherenkov emission due to air showers. For this purpose, the only important contribution is due to ozone (O_3), which has absorption bands between $200\,\text{nm}$ and $340\,\text{nm}$, affecting the measured Cherenkov spectrum. Ozone is present at the 40 ppb (parts per billion, 10^{-9}) level in unpolluted air at sea level. The ozone concentration near the ground is increased in populated areas due to pollution. Most of the atmospheric ozone, however, is contained in the ozone layer (roughly $20\,\text{km}$ to $40\,\text{km}$ above sea level), where its concentration is actually higher than on the ground.

Aerosols are, by definition, small solid particles or droplets, which form a colloidal mixture with a gas. Atmospheric aerosols can be grouped into solid aerosols (particulate matter such as dust) and liquid droplets (mostly water, in the form of mist, fog, clouds etc). The former will be treated in more details below. The latter are of no importance for the study of air showers with the VERITAS telescopes due to its location in southern Arizona (desert environment, no mist/spray) and due to the fact that no science data is taken under cloudy or foggy conditions.

For modeling particulate matter aerosols, Kneizys et al., (1996) consider four regions/zones in the atmosphere. The boundary altitudes given below refer to the case of a flat terrain at sea level. The real boundary altitudes can be different depending on the topography of the surrounding terrain.

---

[4]Data taken under thin or patchy clouds can still be used to check for the presence of very bright flares, for example, but would not be used in light curves or spectra.

The *boundary* or *mixing layer* extends from the ground to about 2 km above sea level. It is characterized by contributions from surface sources (e.g. dust pickup from the ground, soot from forest fires, and man-made pollutants). The aerosol content in the mixing layer is subject to variations on timescales of days or less due to weather (wind/rain) and diurnal variations in certain pollutants. MODTRAN provides a range of models with different visibility conditions for use in the mixing layer, depending on local conditions.

The *upper tropospheric layer* extends from the top of the mixing layer to about 10 km. It shows large seasonal variations in the aerosol content (the aerosol concentration is highest in summer). MODTRAN provides two models, suitable for spring/summer and fall/winter, respectively.

The aerosol content in the *lower stratosphere* (10 km to 30 km) and the *upper atmosphere* (30 km to 100 km) is (under normal conditions) dominated by meteoritic dust. Volcanic activity can increase the stratospheric aerosols by a factor of ten to a hundred for a few weeks to months after heavy volcanic eruptions.

For the VERITAS atmospheric profiles, the *tropospheric model* with 50 km visibility was chosen for the mixing layer, due to the fact that the VERITAS site is located in a sparsely populated area and data is generally taken under good visibility conditions. For the upper troposphere, the appropriate seasonal model was chosen (fall/winter for the winter atmospheric model, spring/summer for the summer atmospheric model). The background aerosol model was chosen for the lower stratospheric layer. Bernlöhr, (2000) showed that moderate volcanic contributions do not affect the observed Cherenkov spectrum. High volcanic aerosols (from recent eruptions) would affect the observed Cherenkov spectrum by 5 % to 10 %, however, only for emission heights above 20 km.

The presence of water vapor affects the size distribution of some aerosols. Since only the average humidity profile is used for the VERITAS atmospheres, the effect of the changing humidity on the aerosol properties is not included in the simulations.

2.3 The Refractive Index

For visible light, the refractive index n of the atmosphere is close to unity, and slightly wavelength-dependent. The *refractivity* $(n-1)$ is approximately proportional to the *density* of the atmosphere. A correction for water vapor effects has to be included when considering moist air since both the refractive index and the dispersion relation of water vapor differ from dry air. For the VERITAS atmospheric profiles, the expression for the refractive index of the atmosphere from Edlén, (1966), as implemented in the MODTRAN software package, was used. For the studies below, however, an isothermal toy atmosphere and the following expression for the refractive index from Ciddor, (1996) will be used:

$$n = 1 + \frac{\rho_a}{\rho_{axs}} \cdot (n_{axs} - 1) + 1 + \frac{\rho_w}{\rho_{ws}} \cdot (n_{ws} - 1) \,. \tag{2.8}$$

Here, ρ_a and ρ_w refer to the partial densities of the dry components of the atmosphere and water vapor, respectively. n_{axs} and n_{ws} denote the (wavelength-dependent) refractive indices of dry air resp. water vapor at the reference densities ρ_{axs} and ρ_{ws}. See Ciddor, (1996) for details and numerical constants.

According to Ciddor, (1996), the refractive index of dry air also depends on the CO_2 content. However, this dependency is small and the change in atmospheric CO_2 levels is slow enough that this effect will be ignored here. All plots use a CO_2 content of 450 ppb.

Moist air is less dense and has a slightly smaller index of refraction than dry air. Figure 2.3 shows the dependency of the refractive index on the temperature and the relative humidity. The density of the dry components decreases exponentially with the height above sea level. However, the partial density of water vapor to first order depends on the relative humidity and the temperature. Thus, a constant relative humidity would actually lead to an increasing water vapor content at higher altitudes, and an increasing difference in refractivity compared to dry air. However, in a realistic model of the atmosphere, the relative humidity is not constant. In fact, there is virtually no water vapor present above about 25 km above sea level, cf. Section 2.2.

As will be shown later (Fig. 3.4), the change in the angle and intensity of the Cherenkov emission due to water vapor effects is negligible. It is thus not necessary to model the day-to-day variations in the water vapor content to obtain an accurate prediction of the refractive index. The VERITAS atmospheric profiles use the average relative humidity profile from radiosonde measurements in the calculations of the refractive index. Above the balloon altitudes, the relative humidity profiles from the standard atmospheres are used.
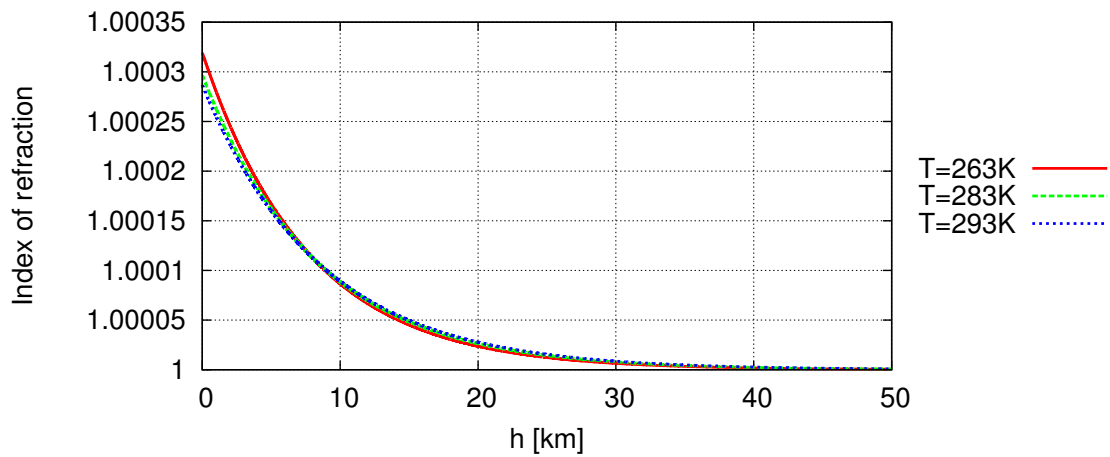
(a) Index of refraction for a wavelength of 300 nm versus altitude, for dry air.
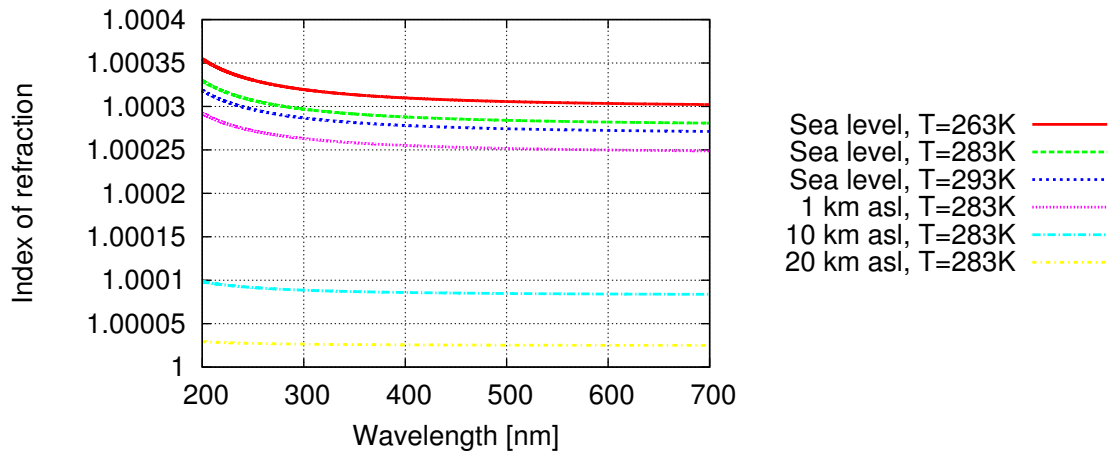
(b) Index of refraction versus wavelength for different altitudes and temperature levels.
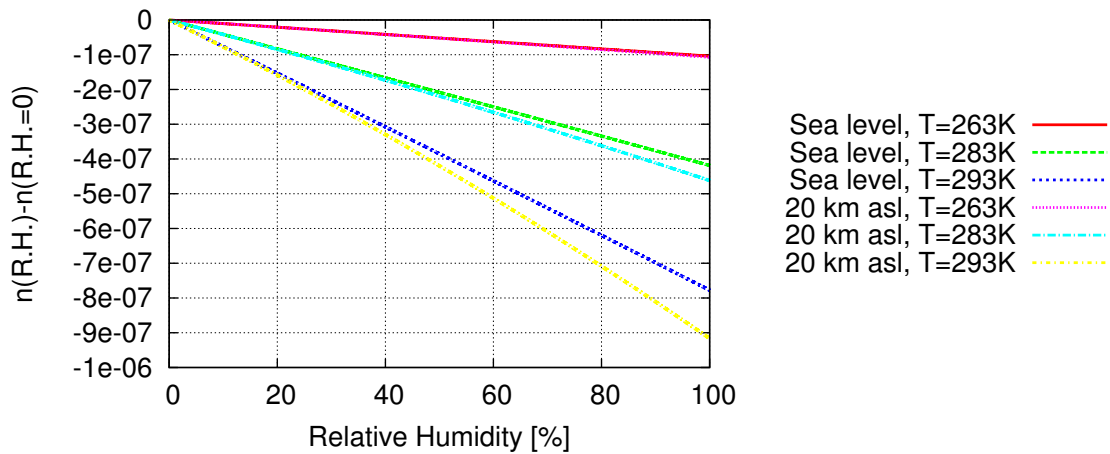
(c) Change of the refractive index with the relative humidity relative to dry air, $\lambda = 300$ nm.

Figure 2.3: Various dependencies of the index of refraction. All cases assume an isothermal atmosphere with $P_0 = 1015.25$ hPa at sea level.
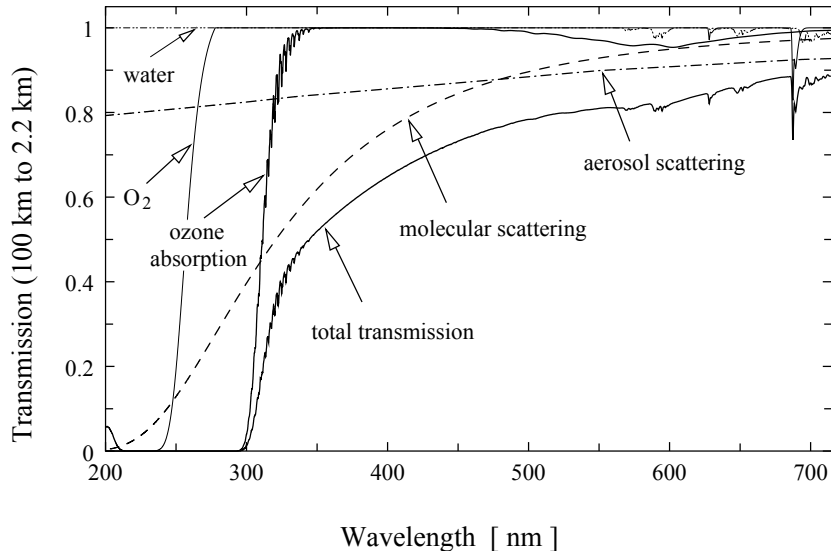
Figure 2.4: Transmission probability for photons from zenith, crossing the entire atmosphere. The transmission probability is higher than this for photons produced in air showers lower down in the atmosphere, and smaller for photons entering at an angle. Plot from Bernlöhr, (2000).

2.4 Transmission Profiles

The three main processes leading to extinction of Cherenkov light in the atmosphere are molecular absorption, molecular (Raleigh) scattering, and aerosol (Mie) scattering. We will here consider the range of wavelengths between 200 nm and 700 nm, which is roughly the range in which Cherenkov telescopes are sensitive. The total transmission probability for a photon crossing the entire atmosphere, as well as the contribution of the different components discussed below, can be found in Fig. 2.4.

The two dominant contributors to molecular absorption are molecular oxygen (O_2) and Ozone (O_3). Oxygen mainly absorbs light with wavelength shorter than 242 nm (Hertzberg continuum). Ozone absorption dominates between about 240 nm and 300 nm. For light emitted high in the atmosphere, virtually all photons with wavelengths below 300 nm are absorbed. Absorption by water vapor is less important for Cherenkov light; there are several H_2O lines above 600 nm but the absorption probability is not as high as for ozone or oxygen.

Scattering on molecules, which are smaller than the wavelengths considered here, can be described by the Rayleigh scattering approach. The scattering probability is proportional to λ^{-4}; molecular scattering dominates the extinction of Cherenkov light between about 300 nm and 450 nm. For the purposes of imaging Cherenkov showers, we can consider all scattered light as *lost*. Rayleigh scattering is almost isotropic, with the scattering angle θ distributed according to $\frac{\mathrm{d}N}{\mathrm{d}\Omega} = \frac{3}{16\pi} \frac{2}{\delta+2} \left((1+\delta) + (1-\delta)\cos^2(\theta)\right) \approx \frac{3}{16\pi}\left(1 + \cos^2(\theta)\right)$, where $\delta \approx 0.029$ in air (Bernlöhr, 2000). More than 99 % of the scattered light is scattered by 5° or more, and would thus arrive outside of current IACT cameras. Double scattering can be neglected because the scattering probability is sufficiently low. For light with a wavelength of 300 nm,

about 60 % is lost by Rayleigh scattering when traversing the entire atmosphere, and the probability decreases with increasing wavelength.

Rayleigh theory does not apply to scattering off larger particles (aerosols). In Mie scattering theory, the scattering probability depends on the size of the scattering particles, and is only weakly dependent on the wavelength. Assuming good visibility conditions, aerosol scattering only affects 10 % to 20 % of the photons between 200 nm and 700 nm. However, this rate increases for adverse conditions such as fog or haze, dust storms etc. The aerosol scattering angle generally peaks in the forward direction, but according to (Bernlöhr, 2000), the amount of scattered light in the camera is still negligible, especially for small distances to the shower core and short integration times, which are used in IACTs.

Not all components of the atmosphere follow the same profiles. For example, water vapor tends to be concentrated within 10 km or 20 km of the ground, while the ozone concentration is highest in the ozone layer, see Section 2.2. While the extinction probability for light traversing the whole atmosphere can be easily measured using stars, this information is not sufficient for calculating the extinction probability for photons emitted by air showers. Bernlöhr, (2000) showed that the simplified approach of assuming that the extinction probability is proportional to the density overestimates the amount of measured Cherenkov light, for the same total extinction probability. For the air shower simulations described here, the MODTRAN software package (Berk et al., 2006; Anderson et al., 2007; Berk et al., 2008; Kneizys et al., 1996) was used to determine the optical index of the atmosphere as well as the extinction probability for light emitted at arbitrary altitudes.

It would be very computationally expensive to follow the path of each Cherenkov photon through the atmosphere separately. Instead, the atmosphere was split into layers of 1 km thickness. MODTRAN was configured to calculate the transmission probability through each layer (depending on the wavelength). For the simulations, it is assumed that each layer is homogeneous so that the transmission probability can be interpolated for arbitrary emission heights down to the detector level.

Most of the Cherenkov light from the extended air showers studied here is emitted roughly 10 km above sea level. Direct Cherenkov light is of course emitted much higher up and for many hadronic showers, there is also a contribution from muons that reach ground level. Fig. 2.5 shows the transmission probability for Cherenkov light through the two atmospheric models for these three cases (Cherenkov emission from primary particles, air showers, and muons close to the ground). For direct Cherenkov light and Cherenkov light from air showers, almost no photons with wavelengths below 300 nm survive, whereas for light emitted from local muons, photons down to 200 nm reach the detector. Assuming a Cherenkov spectrum (emission $\propto \lambda^{-2}$), about 70% of the photons between 200 nm and 700 nm emitted 500 m above the detector level reach the detector, compared to only 38% of the photons emitted 10 km above sea level and 32% of the photons emitted 40 km above sea level.
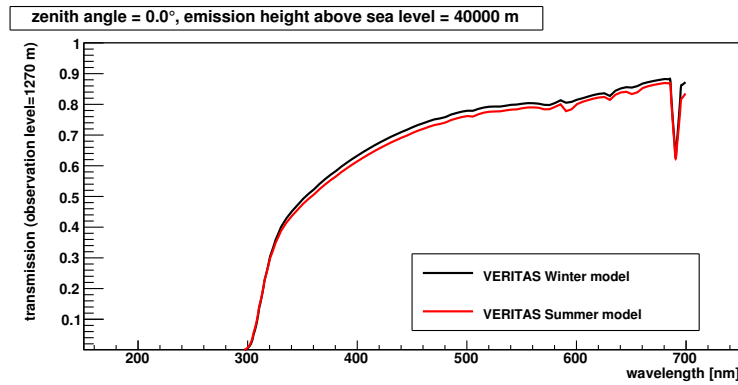
(a) Transmission probability for photons emitted 40 km above sea level (corresponding to direct Cherenkov emission from iron nuclei).
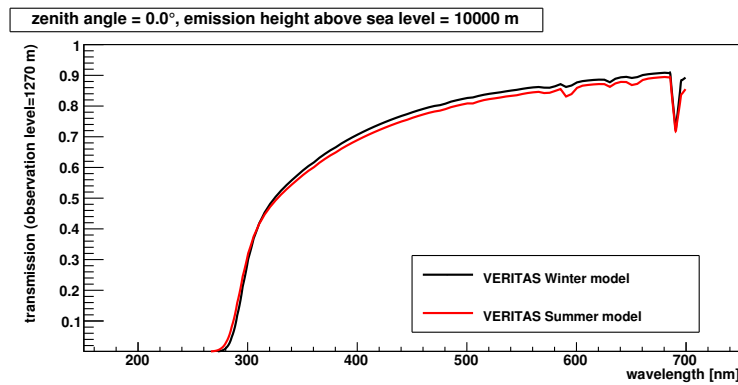
(b) Transmission probability for photons emitted 10 km above sea level (corresponding to Cherenkov emission from air showers).
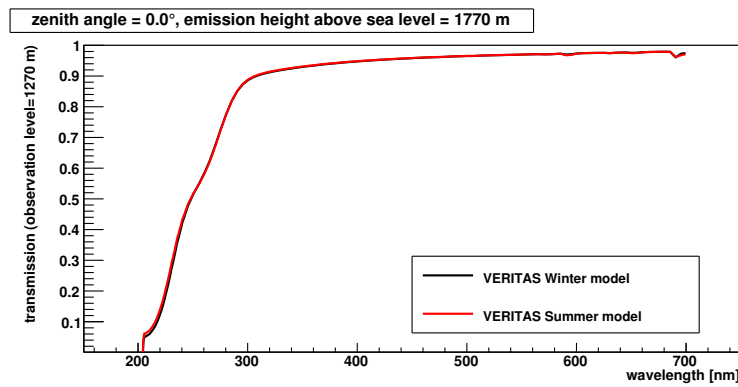
(c) Transmission probability for photons emitted 500 m above the detector level (corresponding to direct Cherenkov emission from muons).

Figure 2.5: Transmission probability for Cherenkov photons for the winter and summer atmospheric models at the VERITAS site.

3 Cherenkov Light Emission in the Atmosphere

3.1 Introduction

The charged components of the shower (electrons, muons, charged pions and protons) radiate Cherenkov light if they are moving faster than the speed of light in their current medium. The amount of Cherenkov light emitted in the wavelength interval $d\lambda$ over the path dx is given by the Frank-Tamm formula (Tamm & Frank, 1937):

$$\frac{d^2N}{dx\,d\lambda} = \frac{2\pi\alpha Z^2}{\lambda^2}\left(1 - \frac{1}{\beta^2 n^2(\lambda)}\right) \tag{3.1}$$

Here, λ is the wavelength of the emitted light, Z is the particle's charge in units of the proton charge, β is its velocity (in natural units), α is the electromagnetic fine structure constant, and $n(\lambda)$ the optical index. Cherenkov light is emitted for all wavelengths for which $\beta \cdot n(\lambda) > 1$. For air, $n < 1$ for hard X-rays and higher energies, which ensures that the amount of emitted Cherenkov light does not diverge (Grieder, 2010).

Cherenkov light is emitted in a cone around the particle's direction of flight. The opening angle θ_c is given by the formula

$$\cos(\theta_c) = \frac{1}{\beta \cdot n(\lambda)} + \frac{E_\gamma}{2\beta E}\cdot\left(1 - \frac{1}{n(\lambda)^2}\right) \approx \frac{1}{\beta \cdot n(\lambda)}, \tag{3.2}$$

where E_γ is the energy of the emitted photon, and E is the energy of the emitting particle. In air, $E_\gamma \lesssim 100\,\text{keV}$ (no Cherenkov emission of X-ray photons), $n \approx 1$, and $E > 20\,\text{MeV}$ at sea level (Grieder, 2010). Thus, the correction term is very small and the approximate expression may be used.

In the atmosphere, Cherenkov light is emitted under small angles. The maximum angle is less than 2 degrees (for a particle with $\beta \approx 1$ near sea level ($n = 1.00028$)). For light emitted higher up in the atmosphere, the maximum opening angle is smaller since the air is less dense there.

As cosmic rays are charged particles themselves, they can also emit Cherenkov light before the first interaction. This *direct Cherenkov* (DC) light can be used to measure the charge of the primary particle, if it can be separated experimentally from the light emitted by the rest of the shower.
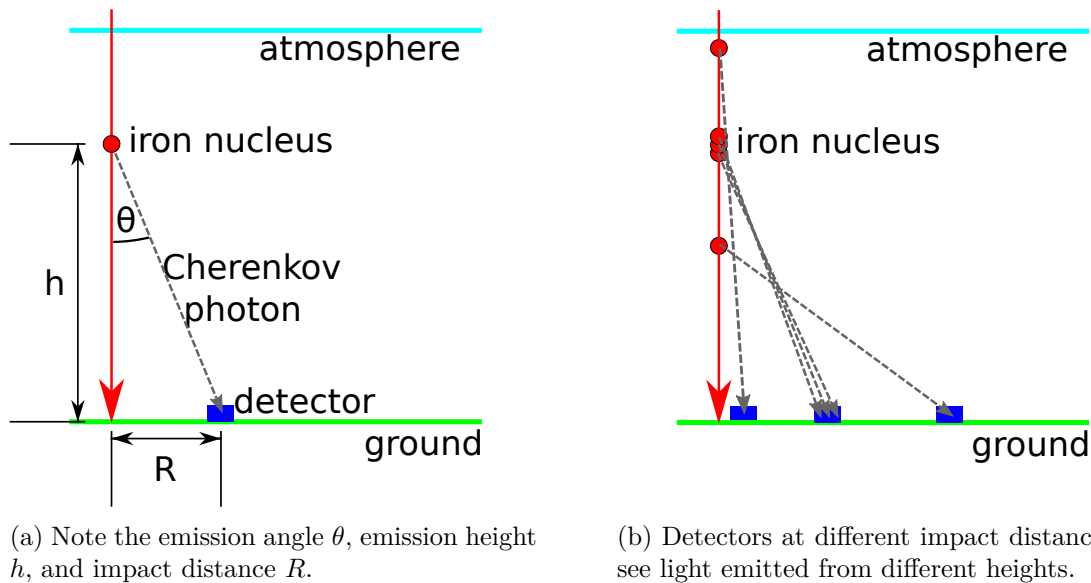
(a) Note the emission angle θ, emission height h, and impact distance R.

(b) Detectors at different impact distances R see light emitted from different heights.

Figure 3.1: Schematics of direct Cherenkov light emission. Not to scale.

3.2 Geometric Properties and Intensity of Direct Cherenkov Light

In the following, I investigate the characteristics of the DC light emitted by iron particles. I used a simplified, isothermal atmospheric profile with $P_0 = 1013.25\,\text{hPa}$, $T = 3\,\text{K}$. The air is assumed to be dry (no water vapor) unless stated otherwise. The density profile and index of refraction were calculated according to Ciddor, (1996).

We consider the Cherenkov light emitted by iron nuclei arriving from zenith. For now, the effect of the Earth's magnetic field are ignored. So are absorption and refraction of Cherenkov light in the atmosphere. For the survival probability study, the interaction length is set to $\chi_0 = 14\,\text{g\,cm}^{-2}$. The detector is located at $H = 1.27\,\text{km}$ above sea level, roughly the elevation of the VERITAS observatory.

Fig. 3.1a shows a schematic view of this setup. It illustrates the definition of the emission height h, the emission angle θ and the impact distance R between the path of the iron nucleus and the Cherenkov photon at ground.

In this model, we assume that the iron nucleus starts 'above' the atmosphere, at $h \to \infty$. As the iron particle descends through the atmosphere, there is a chance that it will interact with a nucleus of the atmosphere and start a shower. The column depth T of the material that the particle has passed is given by

$$T(h) = \int\limits_{h}^{\infty} \rho(h')\mathrm{d}h' = \rho_0 \cdot h_0 \cdot \exp\left(-\frac{h}{h_0}\right)$$

The probability to survive down to height h above sea level is then given by

$$p(h) = \exp\left(-\frac{T(h)}{\chi_0}\right) \tag{3.3}$$

This relation is shown in Fig. 3.2a. Even though in this naive model, the atmosphere extends infinitely far from the Earth's surface, virtually all iron nuclei survive down to about 90 km above sea level, and 90 % of them reach 50 km. The chance to descend to 35 km or below is about 50 %. Only about 10 % of the nuclei reach a height of 25 km above sea level and virtually all of them interact above 15 km above sea level.

Cherenkov light is only emitted when the particle is faster than the local speed of light, i.e. when $\beta \cdot n(h) > 1$. That makes the height at which emission starts very energy dependent. For example, a 500 TeV iron nucleus would start emitting Cherenkov light more than 80 km above sea level, whereas a 20 TeV iron nucleus would only emit Cherenkov light below roughly 34 km above sea level.

Assuming the optical index to be independent of wavelength, we can obtain expressions for the emission angle θ_c and the radius R of the Cherenkov ring at ground from Eq. (3.2), given the refractive index $n(h)$.

$$\theta(h) = \cos^{-1}\left(\frac{1}{\beta \cdot n(h)}\right)$$

and, with basic trigonometry,

$$R(h) = h \cdot \tan(\theta) = h \cdot \sqrt{\beta^2 \cdot n^2(h) - 1}$$

These relations are plotted in Figs. 3.2b and 3.2c. The emission angle is zero when the particle first starts emitting Cherenkov light and continually increases as the particle descends through the atmosphere. The ring radius is zero at first as well and then increases. It has a maximum at around 15 km emission height or 120 m ring radius, depending on the energy. As the particle descends lower in the atmosphere, the ring would become smaller again. However, virtually all iron nuclei would have interacted with a nucleus in the atmosphere and started a shower. If we restrict ourselves to $h > 15$ km, there is a one-to-one mapping between h and R (for a given energy of the iron nucleus), meaning for a given impact distance R between a detector and the path of an iron nucleus, there is only one height h from which the iron nucleus could emit Cherenkov light which hits the detector. Unfortunately, there is no algebraic or trigonometric expression for $h(R)$, however it is implicitly defined as the inverse of $R(h)$. Similarly, there is a well-defined function $\theta(R)$ mapping each impact parameter to one emission angle.

The energy emitted via Cherenkov radiation is given by Eq. (3.1). Integrating over the photon wavelength, it can be used to obtain an expression for N, the number of emitted Cherenkov photons. The integration range corresponds to wavelengths between $\lambda_1 = 200$ nm and $\lambda_2 = 700$ nm as that is the region where Cherenkov radiation is emitted and the PMTs can detect them. The following expression describes the number of photons dN emitted over a short path dh:

$$\frac{dN}{dh} = 2\pi \cdot \alpha \cdot Z^2 \cdot \left(\frac{1}{\lambda_1} - \frac{1}{\lambda_2}\right) \cdot \sin^2(\theta)$$

From this, one can obtain an expression for the intensity of the Cherenkov photons on the ground:

$$
\begin{aligned}
\frac{\mathrm{d}N}{\mathrm{d}A} &= \frac{\mathrm{d}N}{\mathrm{d}h} \cdot \left(\frac{\mathrm{d}h}{\mathrm{d}A} \right) \\
&= \frac{\mathrm{d}N}{\mathrm{d}h} \cdot \left(\frac{2\pi R \mathrm{d}R}{\mathrm{d}h} \right)^{-1} \\
&= \frac{\mathrm{d}N}{\mathrm{d}h} \cdot \frac{1}{2\pi R^2/h - \beta^2 \cdot h^2 \cdot n(h) \cdot \frac{\mathrm{d}n}{\mathrm{d}h}}
\end{aligned}
\tag{3.4}
$$

We are only interested in Cherenkov photons emitted *above* the first interaction, which virtually always occurs above $\approx 15\,\mathrm{km}$. With this restriction ($h > 15\,\mathrm{km}$), we have well-defined expressions for $\theta(R)$ and $h(R)$ and we can thus plot the photon intensity as a function of the impact parameter. This is shown in Fig. 3.2d for four different nucleus energies. For impact parameter zero, the intensity at ground is zero as well and it increases with increasing R (corresponding to lower emission height h). There is an integrable singularity at the maximum radius of the Cherenkov cone. There is a small dependence of the intensity on the energy as well.

Note that some of the photons will be absorbed or scattered in the atmosphere, which is not considered here. Also, the telescopes' mirrors are not perfectly reflective and detectors such as PMTs typically have quantum efficiencies below one, meaning they would not detect all photons. However, IACTs such as VERITAS have mirror areas of about $100\,\mathrm{m}^2$. Such a telescope would pick up 50000 direct Cherenkov photons (pre-extinction) if it were placed at $90\,\mathrm{m}$ impact distance to an iron nuclei. Even assuming 80% extinction losses in the atmosphere, another 50% loss in the optical system (shadowing, mirrors etc) and a quantum efficiency of only 10% (integrated over the full wavelength), we would still expect the telescope to detect about 500 photo-electrons from the direct Cherenkov light, concentrated within about 0.1°. This amount of light is easily detected by today's Cherenkov telescopes.

However, as Fig. 3.2d shows, the amount of direct Cherenkov light depends heavily on the impact distance between the detector and the iron nucleus. To be able to use the DC light to measure the nuclei's charge or to separate heavy and light nuclei, one thus needs to measure the impact position and the energy with high resolution.

The intensity of the direct Cherenkov light is proportional to the square of the nuclear charge, making it particularly suitable for the study of heavy elements, of which iron ($Z = 26$) is the most abundant. Protons ($Z = 1$) and helium ($Z = 2$) emit considerably less than 1% of the amount of DC light compared to iron. Carbon ($Z = 6$) and oxygen ($Z = 8$), the next most abundant elements, emit only about 5% resp. 10% of the DC light that iron emits.
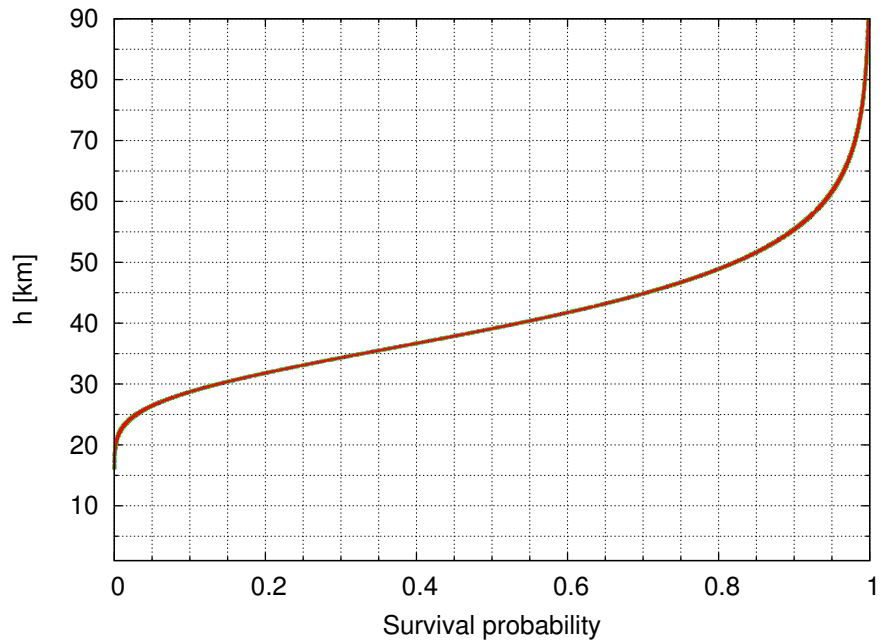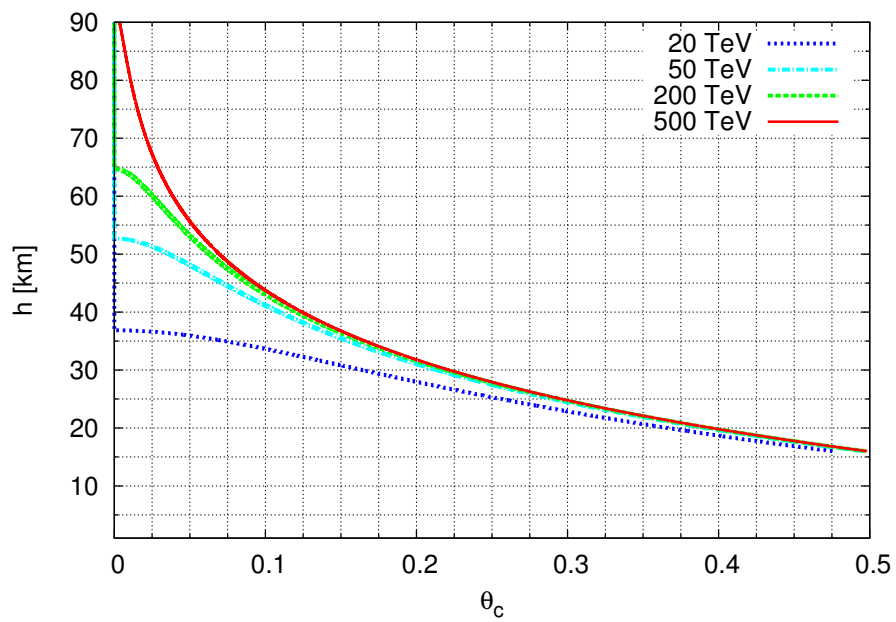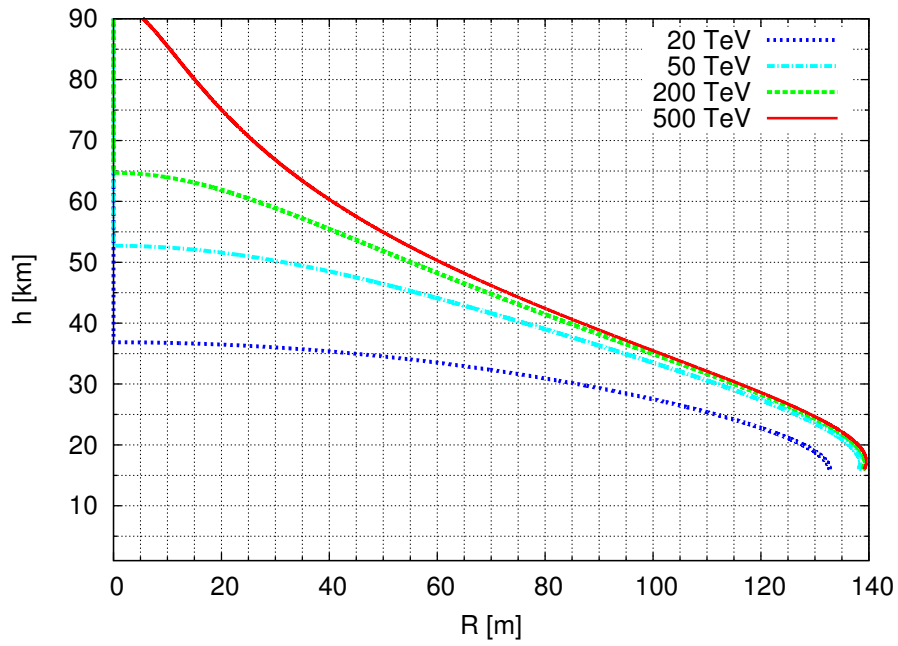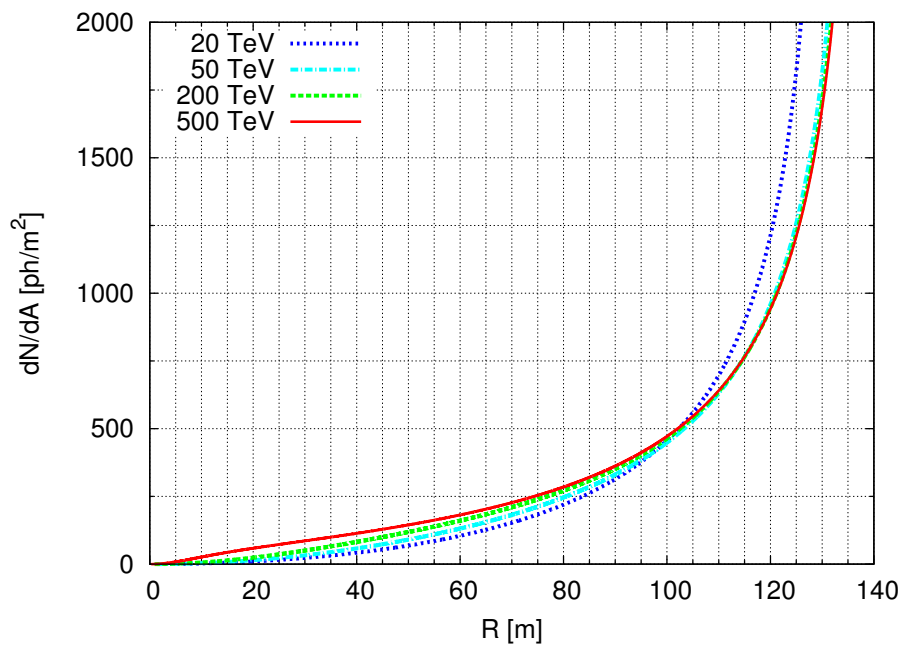
(a) Survival probability for iron nuclei from zenith vs height h in the atmosphere.

(b) Cherenkov light emission angle θ_c in degrees vs height of emission h.

Figure 3.2: Properties of Cherenkov light emitted by iron nuclei in the atmosphere.
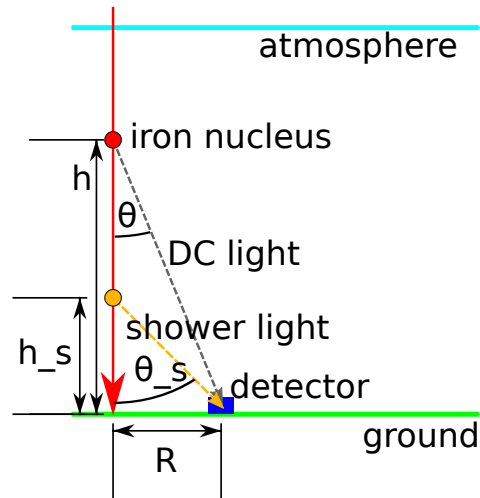
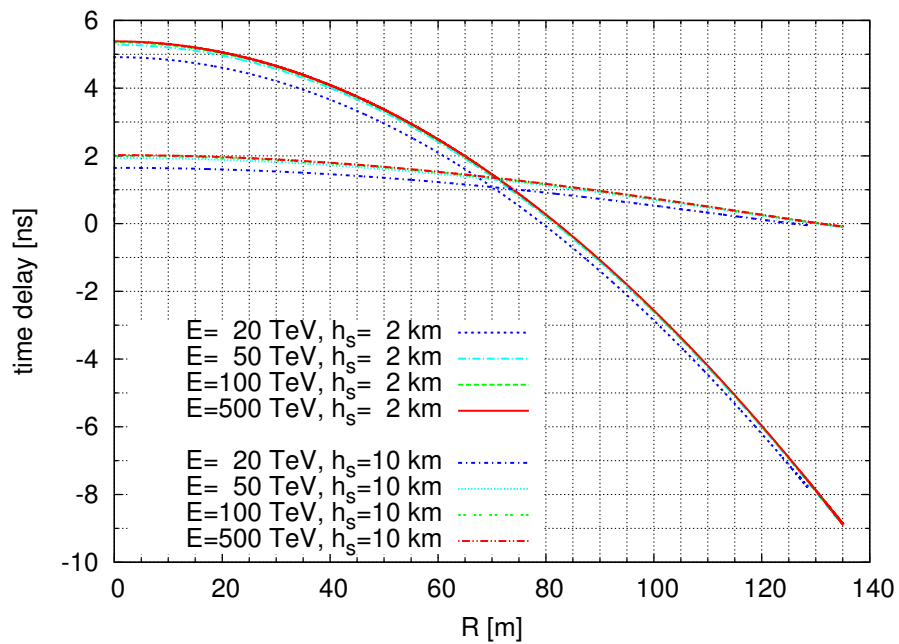(c) Cherenkov light cone radius R on ground vs height of emission h.

(d) Cherenkov light intensity vs light cone radius R on the ground.

Figure 3.2: Properties of Cherenkov light emitted by iron nuclei in the atmosphere, contd.

(a) Schematic depicting the quantities used to derive the timing delay of the direct Cherenkov light compared to the air shower.

(b) Time delay of the direct Cherenkov light compared to light emitted by the air shower at height h_s. For the emission height of the DC light corresponding to a particular core distance R, see Fig. 3.2c.

Figure 3.3: Timing properties of Cherenkov light emitted by iron nuclei in the atmosphere.

3.3 Timing Delay of Cherenkov Light

It has been suggested that timing information can be used to separate the DC light contribution in the camera from the rest of the image (Kieda et al., 2001). In fact, there is a small time delay, which will be investigated in detail in the following paragraphs. The light from the air shower generally arrives at the detector before the DC light.

Excluding scattering and refraction, the travel time for DC light emitted at height h above the ground to the detector is given by the following expression (see also Hammond et al., (1978)):

$$T_{DC} = \int\limits_{0}^{h} \frac{n\left(h'\right)}{c \cdot \cos\left(\theta\right)}\, \mathrm{d}h' \;=\; \frac{\beta \cdot n\left(h\right)}{c} \cdot \left(h + h_0 \cdot \left(n(0) - n\left(h\right)\right)\right)$$

To calculate the arrival time of the light from the air shower, we assume that the nucleus continues to travel downwards with velocity βc until it starts an air shower. We also assume that all particles in the air shower propagate downwards with the same speed. At height h_s, Cherenkov light is emitted from the air shower under an angle $\theta_s = \tan^{-1}\left(\frac{R(h)}{h_s}\right)$ so that it hits the same detector as the DC light. The arrival time of the air showr light is given by the sum of the travel time of the nucleus/shower particles from height h to height h_s and the travel time of the Cherenkov light emitted by the air shower at height h_s:

$$T_s = \frac{h - h_s}{\beta c} + \int\limits_{0}^{h_s} \frac{n\left(h'\right)}{c \cdot \cos\left(\theta_s\right)}\, \mathrm{d}h' \;=\; \frac{h - h_s}{\beta c} + \frac{\sqrt{h_s^2 + R^2}}{c \cdot h_s}\left(h_s + h_0 \cdot \left(n(0) - n(h_s)\right)\right)$$

Recall that R and θ are determined by h and the particle's velocity βc. Thus, for a given energy, we can express the time delay $\Delta T = T_{DC} - T_s$ as a function of the detector offset R. This is shown in Fig. 3.3b for two different shower heights h_s ($10\,\mathrm{km}$ and $2\,\mathrm{km}$). The time delay also slightly depends on the energy of the iron particle, hence it is plotted for four different energies ($20\,\mathrm{TeV}$ to $500\,\mathrm{TeV}$).

The former case corresponds roughly to light emitted from the shower maximum. Here, the time delay is positive, which means that the DC light reaches the detector after the light from the shower. However, the absolute value of the time delay is small (below $2\,\mathrm{ns}$). For an IACT like VERITAS with Davis-Cotton (non-isochronous) optics, this time delay would be very hard to measure, considering that a time spread of about $1.3\,\mathrm{ns}$ is added to the light front due to the mirror structure.

The latter case corresponds to light that is emitted more at the bottom of the air shower. The time delay can be larger in this situation (up to $4.5\,\mathrm{ns}$), but it depends strongly on the distance between the detector and the shower core. For a distance of about $75\,\mathrm{m}$, the DC light and the light from the air shower arrive at the same time. For smaller distances, the

DC light arrives later; for larger distances, the DC light arrives before the light from the air shower. This is consistent with the results of Hammond et al., (1978), who find that shower from the top of the air shower arrives first for core distances greater than 50 m.

## 3.4 Effect of Water Vapor on the Emission of Cherenkov Light

Wet air has a slightly smaller index of refraction than dry air (Ciddor, 1996) and thus the Cherenkov angle and intensity decrease with increasing humidity. This is shown in Fig. 3.4. Neither the Cherenkov emission angle nor the intensity depend strongly on the amount of water vapor present. For example, for Cherenov light emitted 10 km above sea level, increasing the relative humidity from zero to 50 % leads to a decrease in the Cherenkov angle of about 0.001°, less than one tenth of the diameter of a VERITAS pixel. The intensity of Cherenkov light decreases by less than 1 %. At higher emission altitudes, the air pressure drops and the same relative humidity would lead to a larger fraction of water vapor. Hence, the effect increases with altitude. On the other hand, most of the atmospheric water vapor is actually concentrated below 20 km above sea level. Thus, the effect of water vapor on both the direct Cherenkov emission and on the Cherenkov emission from the air shower is small enough to be neglected. The average relative humidity profile is sufficient to obtain realistic values of the index of refraction for the simulation of air showers.

3.5 Dispersion Effects

Up to now, the dispersion (wavelength-dependence on the index of refraction) has been ignored. However, the refractive index is slightly larger for blue and UV light compared to red and orange light. This affects the angle of the Cherenkov light cone, the intensity of the Cherenkov emission, and the travel time of the Cherenkov light. In this section, these effects are investigated. For the plots shown here, the dispersion relation from (Ciddor, 1996) was used. Note that refraction is still ignored, light is assumed to travel in a straight line.

Figure 3.5a shows the Cherenkov angle versus light cone radius on the ground for two different wavelengths. Blue light is actually emitted under a larger angle than red light. This means that the light cone radius for blue DC light is larger than for red light emitted at the same height, or conversely that DC blue light is emitted higher up, and thus under a smaller angle, than red light seen at the same detector. The differences in angle are small, up to 0.15°, which is smaller than the optical PSF of the VERITAS telescopes and can thus be ignored.

Evaluating the effect on the intensity on the Cherenkov light is less straight-forward. Including the dispersion affects both the shape and the normalization of the emitted Cherenkov spectrum. More blue light is emitted than predicted by the simple $1/\lambda^2$ approximation. However, blue light is also emitted at a larger angle and thus spread out over a larger area on the ground, decreasing the intensity. The interplay of those two effects makes numeric inte-
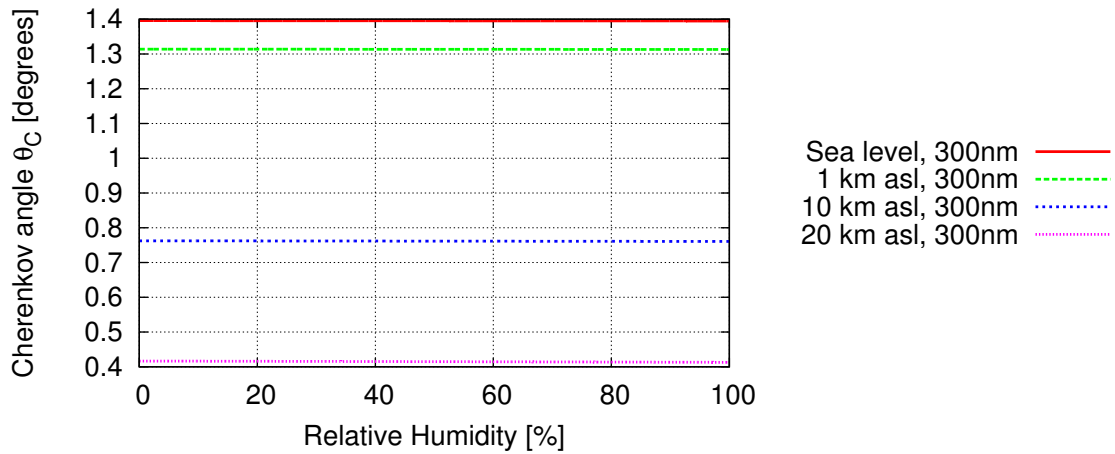
(a) Cherenkov emission angle θ_C versus relative humidity for different emission heights.
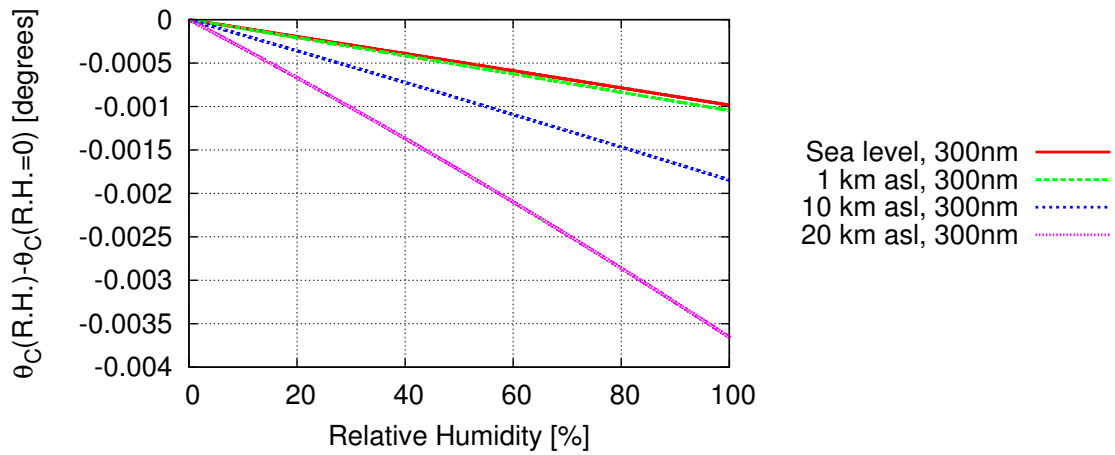
(b) Change in Cherenkov emission angle θ_C relative to dry air for different emission heights.
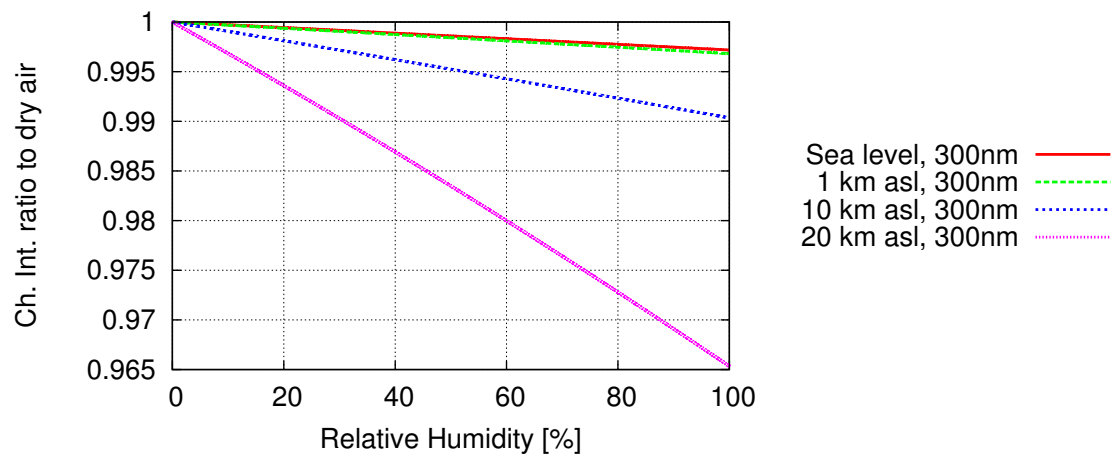

(c) Intensity of Cherenkov emission relative to dry air versus relative humidity for different emission heights.

Figure 3.4: Effects of relative humidity on Cherenkov emission angle and intensity, for a wavelength of 300 nm. Equation 5 from Ciddor, (1996) was used for the index of refraction.

gration impossible. To estimate the effect of the dispersion on the intensity on the ground, the intensity was calculated following Eq. (3.4), for two different wavelengths (300 nm and 600 nm). The results can be seen in Fig. 3.5b. The differences are on the order of 10 % or less for core distances below 120 m, but can become large near the maximum radius. In fact, blue/UV light has a maximum radius that is about 10 m larger than the maximum radius for red/orange light. Note that each intensity curve still assumes a constant index of refraction. Also, no absorption effects are included.

The dispersion also smears out the Cherenkov light front in time. However, the difference in travel time between a photon with wavelength 300 nm and a photon with wavelength 600 nm is well below 1 ns even for DC light emitted several tens of km above the ground. For VERITAS, this delay can be ignored since it is much smaller than the effects of the mirror and the PMT rise time.
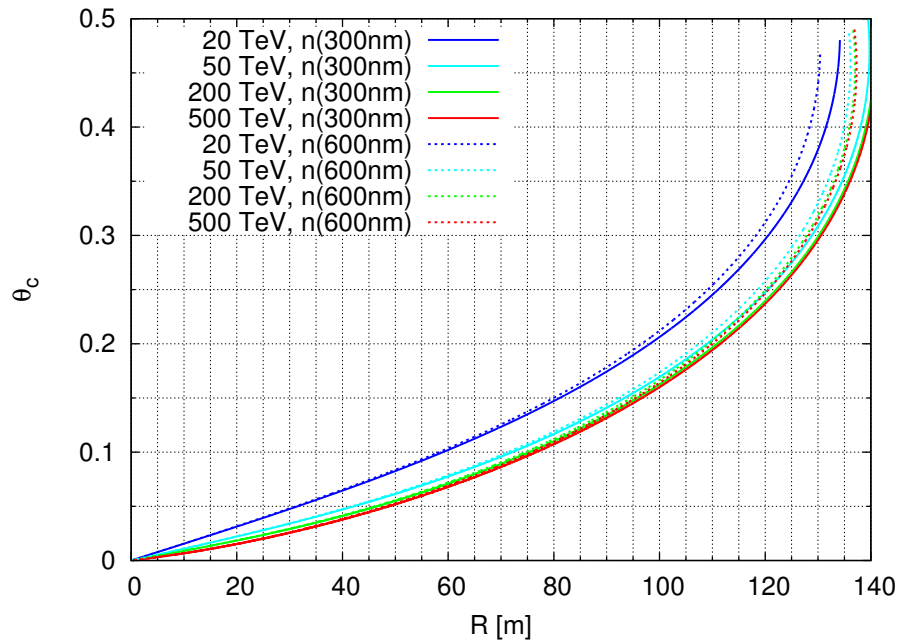
(a) Cherenkov light emission angle θ_c in degrees vs light cone radius R.
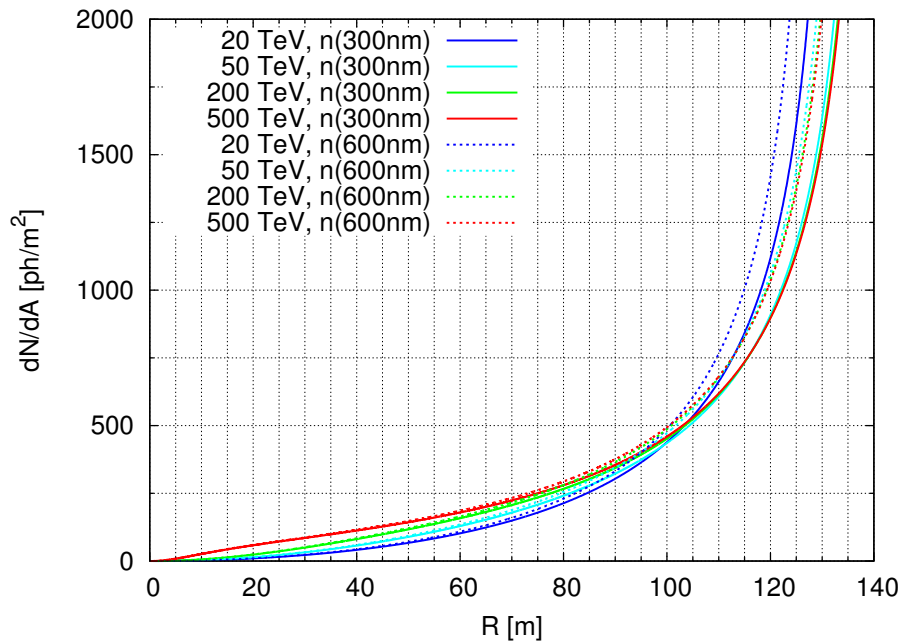
(b) Cherenkov intensity on the ground.

Figure 3.5: Cherenkov emission angle and Cherenkov intensity on the ground for two different wavelengths.

4 The VERITAS Experiment

4.1 Overview

VERITAS[1](Holder et al., 2008; Park et al., 2016), the Very Energetic Radiation Imaging Telescope Array System, is an array of four imaging atmospheric Cherenkov telescopes. It is located at the Fred Lawrence Whipple Observatory in southern Arizona. The telescopes employ a Davis-Cotton optical design. Each telescope has about 350 hexagonal mirror facets with a total area of about $100\,\mathrm{m}^2$, which focus light onto a camera consisting of 499 PMTs. Each PMT with its associated readout electronics is also referred to as a *pixel*.

Since its completion in 2007, the array was upgraded several times. Telescope 1 (T1) was moved to its final position in 2009, increasing the collection area and improving background rejection and angular resolution. The trigger system was updated in 2011. In 2012, the original PMTs were replaced by new ones with a higher quantum efficiency and faster rise time. See Fig. 4.1 for an image of the array in its current layout.

The three different array configurations will be referred to as follows:

- **V4** refers to the array after the fourth telescope was installed, but before the T1 move (September 2007 to July 2009).

- **V5** refers to the improved array layout, before the PMT upgrade (September 2009 to July 2012).

- **V6** refers to the array after the PMT upgrade (September 2012 to present).

4.2 Signal Chain and Readout

The VERITAS cameras consist of 499 PMTs each (Holder et al., 2008; Rajotte, 2014). From the PMT, the signal passes through a pre-amplifier, and is then sent to the ground (trailer) via a coaxial cable. The signal is then split into three copies.

One copy of the signal is amplified further, digitized by a 7-channel FADC with an integration time of $2\,\mathrm{ns}$, and written into a ring buffer. A second copy is de-amplified and fed through a time-delay circuit (low-gain circuit). If the nominal signal is too large (outside the FADC range), the de-amplified copy is also written into the ring buffer, behind the nominal signal.

---

[1]`http://veritas.sao.arizona.edu`

Figure 4.1: The VERITAS array in its current configuration (V6).

Another copy is sent to the level 1 trigger (constant fraction discriminator, CFD). If the signal passes a given threshold, the CFD triggers. If the level 2 trigger (pattern trigger) receives trigger signals from 3 or more neighboring pixels (within a coincidence window of 5 ns), it sends a signal to the level 3 trigger (array trigger). If two or more telescopes trigger at the same time (coincidence window 50 ns), the array is read out. The array trigger generates and event number and time stamp. This information is sent back to the telescopes, triggering each telescope's DAQ (data acquisition) system to read out the ring buffers. Only 16–24 samples are read out, the rest of the information in the ring buffer is lost. If the low gain readout mode was triggered, the look-back time is adjusted accordingly and the de-amplified signal is read out.

The information is collected by the event builders and the harvester. The data taking is divided into runs of 15-30 minutes duration. At the end of each run, the information from all telescopes is collected into one file, which is analyzed later. Other data, such as the trigger rates, currents and voltages in the camera are measured every second and written to a database.

When the ring buffers are read out to record one event, all other information in the buffer is lost and no more data can be saved while the readout is in progress. It takes about 300 µs to read out the ring buffer, during which the telescope is effectively *dead* (if Cherenkov light from a second shower were to hit the telescope within that time, it could not be recorded). Trigger rates during regular data-taking are generally between 200 Hz and 500 Hz, leading to dead time fractions between 6% and 15%. Further *dead time* can occur (more rarely) due to buffer transfers. The live time of the detector needs to be taken into account or the measured fluxes will be underestimated. Two scalars, connected to a 500 MHz clock, are employed to measure the live time of the detector. One scalar counts up every 2 ns, the other one only counts up if the detector is in a non-busy state. The values of the two scalars are written to the data file, so that the live time can be calculated from the ratio of the differences between two consecutive values of the scalar.

4.3 Low Gain Readout Mode

VERITAS uses 8-channel FADCs to digitize the pulses from the PMTs. The dynamical range of these FADCs is too small to satisfactorily cover the full range of pulse amplitudes expected from Cherenkov emission of air showers. Thus, a dedicated readout chain for high-amplitude pulses is employed.

Pulses exiting the PMT pass through the pre-amplifier (still located inside the camera) and are then sent to the FADC boards through coaxial cables. Inside the FADC boards, the pulses are split. One copy is further amplified (by a factor of about 4.85) and passed into the digitizer itself. This *high-gain system* maxes out at pulse amplitudes corresponding to about 120 photo-electrons in the PMT. The second copy is attenuated by a factor of about 0.76 (i.e., the pulses are about 6 times smaller than for the high-gain readout) and passed through a time-delay circuit. If the high-gain readout is saturated or close to saturation, this attenuated copy of the pulse is passed into the FADC and written into the ring buffer behind the first copy. This *low-gain system* saturates for amplitudes corresponding to about 750 photo-electrons. When the ring buffer is read out, the readout window is placed so that the appropriate digitization of the pulse is selected (high gain trace for small amplitudes, low gain trace for large amplitude pulses that saturate the high gain system).

Pulses read out in low gain mode must be corrected for the attenuation occurring in the low gain readout chain. In addition to attenuating the pulse, the delay/attenuation circuit slightly distorts the pulse shape. The pulses read out in low gain mode are broader than the ones read out in high gain mode. In the standard VERITAS analysis, a correction factor is applied to the integrated charge to account for the attenuation of the low gain pulses. Since the pulse shapes differ between high-gain and low-gain mode, this correction factor must depend on the size and placement of the integration window. The methods for deriving this correction factor (also called the *low gain multiplier* are detailed in Section 4.4.2.

The brightest pixels of very bright shower images can also saturate the dynamic range of the low gain readout mode. The response of the delay/attenuation circuit becomes non-linear for nearly saturated and saturated pixels, distorting the pulse shapes more and leading to broader and broader recorded traces. However, due to the finite width of the readout window and the integration window, the pulse will eventually be longer than the integration window and the integrated charge saturates. This non-linear behavior of the camera is matched in simulations to measurements performed in the lab.

4.4 Data Analysis

The VERITAS standard data analysis is described in Daniel et al., (2007). It is divided into several steps. Each run is analyzed separately; only at the very end are the results of multiple runs combined. The reconstruction process is independent of the species of the

primary particle to be selected (e.g. VHE gamma rays or iron), but of course certain tools such as energy look-up tables have to be trained depending on the type of primary particle.

4.4.1 Calibration and Image Cleaning

The FADC pedestal level (the measured signal in the absence of Cherenkov light) and its variance depend on the electronics noise and the night-sky background light (NSB). The pedestals for the high gain readout mode are measured constantly during data-taking: A 1 Hz-scalar triggers a readout every second. As the noise conditions and especially the NSB rate can change during the run, the pedestal level and its variance are determined from these pedestal events in three-minute time slices. The pedestals for the low-gain readout mode are more stable (they only depend on the electronics, not on the NSB). They are measured in special low gain calibration runs.

After pedestal correction, the cameras are flat-fielded to match the relative gains between the pixels. The relative gains are measured each night using special LED flashers which evenly illuminate the camera plane with Cherenkov-like pulses.

Some of the objects targeted for VERITAS observations have bright stars (or planets) in the same field of view. Especially for high elevations and good visibility conditions, the light from such stars can cause elevated currents in the VERITAS PMTs. If the currents are too high, the affected PMTs are switched off to avoid damage to the photo-cathodes or accelerated aging. Disabled pixels are recognized automatically by the analysis software and marked as 'dead'. In addition, some PMTs may have large currents and therefore lots of noise, but still be below the threshold for disabling. These pixels may still be "switched off" in the analysis due to the increased pedestal variations.

Charge integration and stereo reconstructions proceeds in two iterations (double-pass integration). In a first pass, the t_0 value (time at which the signal reaches half its maximum value) is determined for each pixel. The signal is integrated over 6 samples starting one sample before t_0. Image cleaning is applied and the Hillas parameters (see Section 4.4.3) are calculated. Then, t_0 values are projected along the long image axis and fit with a linear function. The value of the fit function at each pixel then determines the start of the integration window for the second pass. All image parameters are re-calculated with the updated integrated charges. The advantage of this double-pass algorithm is that for weak pulses close to the cleaning threshold the fitted t_0 is more accurate than the measured one which is subject to noise fluctuations. Pixels in low-gain readout mode are exempt from the double-pass procedure. After integration, they are scaled to the equivalent high-gain charge (i.e., the charge that would have been measured if the channel had a larger dynamic range and had been read out in high-gain mode).

The image is *cleaned* to remove background noise. Pixels are considered to be part of the image if their integrated charge is larger than five times the pedestal width, or if the integrated charge is larger than 2.5 times the pedestal width *and* one of their neighboring

pixels fulfills the first condition. Only images with four or more pixels are considered for the following reconstruction steps.

4.4.2 Calibration of the Low Gain Readout Mode

In the analysis stage described above, the charge in each pixel is determined by integrating over the recorded trace. In order to reduce fluctuations due to noise, the integration window is usually narrower than the readout window. By default, it is 6 samples wide, about as wide as the Cherenkov pulse recorded by the PMT. This is referred to as the *nominal sumwindow*. Sometimes, the recorded pulse may start only near end of the readout window, in which case the integration window could be truncated (obviously it cannot extend beyond the readout window). This can happen in showers with a large time gradient in the image (readout is triggered by the first set of pixels to pass the trigger threshold). For some of the data recorded by VERITAS, there are also issues with the timing alignment, especially for low gain pulses. For some time, the readout settings were such that the low gain pulses would start only in the middle of the readout window even for events with small time gradients. The possibly truncated window is referred to as the *actual sumwindow* in the following.

Assume VERITAS had an FADC system with a larger dynamic range and could measure both the low gain and high gain pulse for a given injected charge. Neglecting noise, the following would hold:

$$Q = \frac{S_{LG}(sw_{LG})}{c_{LG}(sw_{LG})} = \frac{S_{HG}(sw_{HG})}{c_{HG}(sw_{HG})},$$

where Q is the total deposited charge, c is a gain factor which depends on the readout mode and the length of the sumwindow, and S is the signal summed over a certain sumwindow. $c_{HG}(sw_{HG})$ and $c_{LG}(sw_{LG})$ are constant as long as the readout system is linear.

Rewriting this gives us

$$S_{HG}(sw_{HG}) = \frac{c_{HG}(sw_{HG})}{c_{LG}(sw_{LG})} \cdot S_{LG}(sw_{LG}) =: m(sw_{HG}, sw_{LG}) \cdot S_{LG}(sw_{LG}).$$

This defines the low gain multiplier m, which depends on both sumwindows. It can be thought of as the ratio of the high gain charge that would have been measured in an ideal system with a larger dynamic range to the charge that is measured with the actual FADC system (in low gain mode, with sum window sw_{LG}). This expression is only valid as long as the low gain circuit and readout electronics are in the linear regime. The effect of the pulse distortion in low gain for very large pulses is neglected here, because the non-linear regime is not reached during the calibration runs.

As the true charge Q is unknown, and the DAQ system of VERITAS can only ever readout either the high gain pulse or the low gain pulse, we cannot use one of the equations above

to find the low gain multipliers. VERITAS is conducting dedicated HiLo calibration runs. In those runs, an LED flasher with seven different light levels evenly illuminates the camera. The flasher pulses have a shape similar to the Cherenkov pulses recorded from air showers. Half of the telescope is kept at a reduced voltage, so that the channels there never switch into low gain mode. The average signal in these channels is referred to as *monitor charge* Q_{mon}. Since the flasher delivers the same amount of light to each PMT, the momitor charge is proportional to the true charge seen in each channel in the 'high' half of the camera: $Q_{mon}(sw_{mon}) = \alpha(sw_{mon}) \cdot Q$, with unknown but fixed α.

The pixels in the half of the camera at nominal voltage will be in high gain mode for the lower lightlevels (one to three LEDs) and in low gain mode for the brighter light levels. In both modes, the recorded signal must be proportional to the true charge and hence to the monitor charge:

$$S_{HG}(sw_{HG}) = c_{HG}(sw_{HG}) \cdot Q = c_{HG}(sw_{HG}) \cdot \alpha(sw_{mon}) \cdot Q_{mon},$$

and in low gain mode:

$$S_{LG}(sw_{LG}) = c_{LG}(sw_{LG}) \cdot Q = c_{LG}(sw_{LG}) \cdot \alpha(sw_{mon}) \cdot Q_{mon}.$$

By fitting the slope of the charge recorded in each channel against monitor charge, separately for low gain and high gain, we can determine $c_{HG}(sw_{HG}) \cdot \alpha(sw_{mon})$ and $c_{LG}(sw_{LG}) \cdot \alpha(sw_{mon})$ separately. If we make sure to always integrate the monitor charge over the same window, we can get the ratio

$$m(sw_{HG}, sw_{LG}) = \frac{c_{HG}(sw_{HG})}{c_{LG}(sw_{LG})} = \frac{c_{HG}(sw_{HG}) \cdot \alpha(sw_{mon})}{c_{LG}(sw_{LG}) \cdot \alpha(sw_{mon})}$$

and hence the low gain multipliers for any summation windows sw_{HG}, sw_{LG}. Note that light levels close to the low gain threshold, which have some events in high gain mode and others in low gain mode, should be excluded from the fit.

The sum-window dependent low gain multipliers $m(sw_{HG}, sw_{LG})$ determined in this way are averaged over all pixels in each camera. In data analysis, the integrated charge recorded in low gain mode must be multiplied by the appropriate low gain multiplier to obtain the equivalent charge that would have been recorded by the high gain system if the dynamic range was higher.

4.4.3 Hillas Parameters and Stereo Reconstruction

The second step in the analysis chain is the calculation of the statistical moments of the image. Air shower images in IACT cameras generally have elliptical shapes, and are approximately

described by a two-dimensional Gaussian function. They are thus characterized by the *size s* (sum of the signal in all image pixels), the *centroid* of the image, the direction of the image axes, and the *width w* and *length l* of the image along these axes.

Having images of the same shower in two or more telescopes provides a *stereoscopic* view of the shower, which can be used to reconstruct the arrival direction of the primary particle and the location of the shower core on the ground.

The arrival direction is given by the intersection of the image axes when all camera images are overlaid on top of one another. In the case of more than two images, a weighted average off all intersections is calculated. The reconstruction of the shower core is done in a similar manner in the shower plane (perpendicular to the shower axis). The height of the maximum Cherenkov emission can be estimated from the location of the brightest pixels in each camera.

Only two images are needed to reconstruct the direction, shower core location and maximum emission height. If there are more than two images, these parameters are over-constrained and a weighted average over each pair of telescopes is calculated. χ^2-like parameters are defined to asses the quality of the reconstruction.

This geometric reconstruction algorithm relies on some very general assumptions, but does not require any specific knowledge about the shower development such as the number of particles in the shower or the rate of Cherenkov emission. It assumes that the shower core follows a straight path (the extension of the path of the primary particle), that the shower development is symmetric with respect to rotation around the shower axis, and that the emitted light propagates in a straight line. None of these assumptions is strictly speaking true. The Earth's magnetic field bends the path of charged primary particles and the charged component of the shower, which can lead to asymmetries in the image. Due to the density gradient in the atmosphere, the Cherenkov light is refracted and follows a curved path. However, these effects are small compared to the statistical fluctuations in shower development and Cherenkov light emission.

4.4.4 Energy Reconstruction and Reduced Scaled Parameters

The amount of Cherenkov light produced in an air shower depends on the number of charged particles. The distribution of light on the ground follows a distinct profile (see Fig. 1.3. If the distance of the telescope to the shower core is known, the amount of light (the *size* of the image) can be used to estimate the energy. Look-up tables of the energy versus size and impact distance (and azimuth/zenith angles) are used for this purpose. The energy estimates from the different telescopes are averaged to obtain the event-wise energy estimate. The tables are filled using simulations of air showers. As the air shower development depends on the primary particle, different look-up tables have to be used for the study of gamma-ray and for example iron-induced showers. Each telescope image provides an independent estimate of the energy. For events with more than one image, the energy is over-constrained; a weighted average of the energy estimates and a χ^2-like parameter assessing the reconstruction quality are calculated.

The *width* and *length* of the shower image provide important information regarding the species of the primary particle. The *width* and *length* of an image also depend on the energy (or size) and the impact distance. Hence, it is useful to use quantities like the *mean reduced scaled width* and *length*, which are scaled by the expected values of width and length.

The *reduced scaled width* per image is defined as

$$MSCWT_i = \frac{w_i - \langle w_{MC}(s_i, D_i)\rangle}{\sigma_{MC}^{width}(s_i, D_i)},$$

where w_i, s_i, and D_i are the *width*, *size*, and impact distance of the ith image/telescope, and $\langle w_{MC}(s, D)\rangle$ and $\sigma_{MC}^{width}(s, D)$ are the median and 90 % coverage interval of the distribution of the *width* parameter in simulations for a given *size s* and impact distance D.

The *mean reduced scaled width* is then defined as the weighted mean of the scaled width parameters for all N telescopes that recorded a given event:

$$MSCW = \frac{\sum\limits_{i=1}^{N} MSCWT_i \cdot w_i}{\sum\limits_{i=1}^{N} w_i} \quad \text{with weights} \quad w_i = \left(\frac{\langle w_{MC}(s_i, D_i)\rangle}{\sigma_{MC}^{width}(s_i, D_i)}\right)^2.$$

The *mean reduced scaled length* ($MSCL$) is defined in an analogous manner. The mean reduced scaled parameters have a mean of approximately zero and a 90 % coverage width of 1 for whichever species of particle the look-up tables were filled, and in general have different distributions for other particles. Hence, they can help separate showers induced by different species of primary particles. For example, gamma-ray induced showers tend to be long and narrower than cosmic-ray induced showers. In gamma-ray astronomy, one often selects gamma-ray candidates by requiring the mean scaled width and length to be below certain thresholds. The scaled parameters may also be used as input for a multivariate classifier.

4.4.5 Advanced Analysis Methods

The moment-based stereoscopic reconstruction combined with *size*-based look-up tables for energy reconstruction is widely used and very robust as it does not rely on too many assumptions about the shower physics. However, it has some disadvantages. A lot of information is 'lost' (everything is compressed into few image parameters). Also, the image parameters may be skewed by disabled pixels, and larger images may only be partly inside the camera. These deficiencies can be overcome by interpolating the 'holes' in the camera or extrapolating outside the field of view. However, some model of the image shape is required for that. One either needs to make some very simplifying assumption or include knowledge about the shower physics.

An example for the former approach, which is often used for the analysis of VERITAS data, is simply fitting a 2D Gaussian function to the image. This is somewhat valid for gamma-ray

induced showers as long as not too much of the image is cut off. However, cosmic-ray induced showers are often not well fit by a Gaussian function.

The latter approach includes algorithms where the recorded images are fit to a model (analytic, semi-analytic or based on simulations) of the shower images. Often, event parameters such as the arrival direction or the energy of the primary particle are part of the fit. Such an algorithm was implemented for the reconstruction of iron-induced showers with VERITAS and is described in Section 5.1.

5 Data Analysis Methods

In this chapter, I will describe any new or non-standard data analysis methods that were used to derive the results in Chapters 7 and 8. In particular, I present the template likelihood analysis method for the reconstruction of the primary particle's energy and arrival direction, specifically its application to iron-induced showers, the separation of iron-induced showers from background events, and the calculation of fluxes as well as upper limits on fluxes from event counts.

5.1 Template likelihood analysis

5.1.1 Overview

The stereoscopic analysis based on statistical moments (see Section 4.4) has been used for image reconstruction in gamma-ray astronomy for decades. It is quite robust, but it does not take all available information into account. More advanced techniques are being investigated to improve the performance of the analysis. One of these methods is a template-based likelihood fit, which takes the information from all pixels into account. It was pioneered by the CAT experiment for the reconstruction of gamma-ray induced showers (Le Bohec et al., 1998) and has also been used by other experiments, for example by the H.E.S.S. (Parsons & Hinton, 2014) and VERITAS (Vincent et al., 2016) collaborations. De Naurois & Rolland, (2009) describe a similar method, but use a semi-analytic approach to obtain their models of gamma-ray shower images.

The template likelihood method can also be used to identify and reconstruct cosmic-ray induced events. However, some adaptations have to be introduced. For example, the shower-to-shower fluctuations, which can be neglected for gamma-ray induced showers, should be taken into account when considering cosmic-ray induced showers. In the following, I will describe the template likelihood method and the adaptations made for the reconstruction of iron-induced showers. Earlier versions of this work have been shown in Fleischhack et al., (2016a) and Fleischhack et al., (2015).

For the likelihood fit, one needs a model for the probability distribution of the Cherenkov light intensity in the camera depending on some properties of the primary particle. In the case of the template fit, this model is derived from a set of simulations. A likelihood formula is derived which compares recorded (data) events to the model. Given a particular event, the model parameters are varied to maximize the likelihood. The model parameters which maximize the likelihood are taken as estimates for the true parameters. A goodness-of-fit

Parameter	Number of steps	Step size	First value	Last value
$\log_{10}\left(\frac{E}{\text{TeV}}\right)$	17	0.1	$\log_{10}(10)$	$\log_{10}(500)$
D	31	10 m	0 m	300 m
h	11	–	70 km	22 km
x	300	0.02°	−2°	4°
y	150	0.02°	0°	3°

Table 5.1: Grid parameters for the generation of the image templates. The steps in h are chosen to provide even coverage of the likely first interaction heights. The ith height h_i corresponds to column depth $\chi_i = \lambda \cdot \ln\left(\frac{N-i-\Delta}{N}\right)$ with $\lambda = 13\,\frac{g}{cm^2}$, $N = 11$ and $\Delta = 0.5$ for $i > 0$, h_0 is set to 70 km.

parameter (derived from the final value of the likelihood function) can be used both for quality selection and to separate the desired 'signal' events from the background. For example, it may be used to separate iron-induced showers from those induced by lighter nuclei.

In the present implementation, the model parameters are

- the primary particle's energy E,

- the height h of the first interaction of the primary with an atom in the atmosphere,

- the direction of the primary particle relative to the pointing direction of the telescopes (X_s, Y_s),

- the projected position X_p, Y_p of the shower core on the ground.

The 6-tuple of model parameters describing a given event is abbreviated as

$$\boldsymbol{\Theta} = (E, h, X_p, Y_p, X_s, Y_s).$$

The shape and magnitude of the template image is described by only three parameters (E, h, and the impact distance D between the shower core and the telescope). The remaining three parameters fix the placement and orientation of the image in the camera. This assumes that the optical point spread function (PSF) is constant over the camera, which is not completely true for the VERITAS telescopes. There is also a dependence on the absolute zenith and azimuth angles as well; however, for small zenith angles, the image shape and intensity change slowly with the zenith and azimuth angle, so this was not taken into account here.

5.1.2 Image Template Generation

The distribution of Cherenkov light in the camera is obtained using Monte Carlo simulations of iron-induced showers at a fixed 'grid' in E, h, and impact distance D of the shower core to the telescope, see Table 5.1. Showers are simulated coming from zenith ($Ze = 0$) with the telescopes pointing at zenith as well. See Chapter 2 for more details about the simulations.
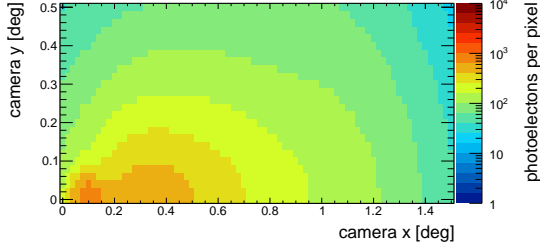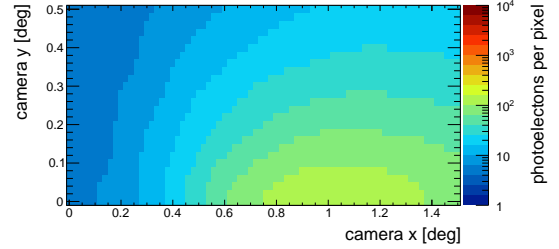
(a) Image template for a first interaction height of 19 km, an energy of 30 TeV and impact distance of 50 m. There is a visible contribution from DC light around (0.1, 0).
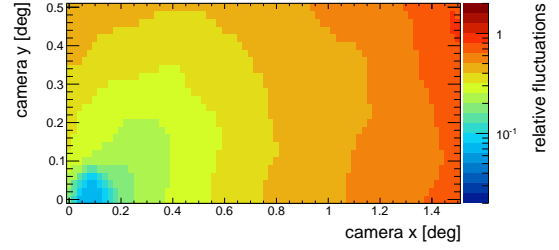
(b) Shower-to-shower fluctuations for a first interaction height of 19 km, an energy of 30 TeV and impact distance of 50 m. The fluctuations are smallest for DC light and very large at the edge of the image.
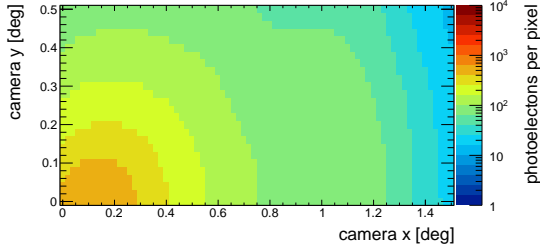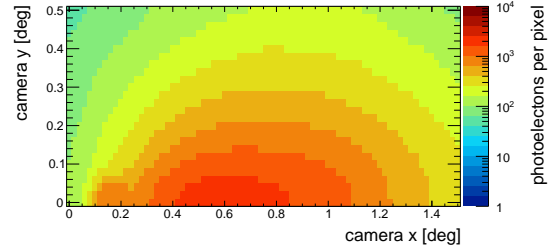
(c) Image template for a first interaction height of 33 km, an energy of 30 TeV and impact distance of 20 m. The shower image is nearly round and there is no discernible contribution from DC light.

(d) Image template for a first interaction height of 33 km, an energy of 30 TeV and impact distance of 200 m. The image is very elongated and there is no contribution from DC light since the impact distance is too large.
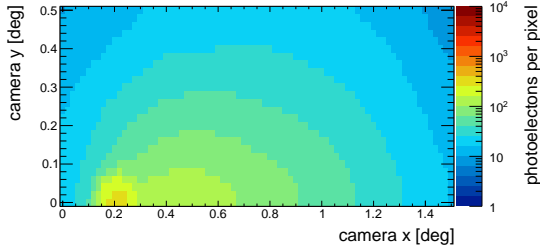
(e) Image template for a first interaction height of 33 km, an energy of 15 TeV and impact distance of 80 m. There is a contribution from DC light about 0.2° offset from the primary direction.

(f) Image template for a first interaction height of 33 km, an energy of 80 TeV and impact distance of 80 m. There is a contribution from DC light about 0.2° offset from the primary direction.

Figure 5.1: Iron shower templates for the VERITAS cameras. All templates were produced for zenith angle 0°. The x-axis is chosen to be the symmetry axis of the image, the y-axis is perpendicular to the x-axis so that (0,0) marks the direction of the primary particle. The color scale corresponds to the number of photo-electrons per camera pixel. To save computing resources, only the top half ($y > 0$) of the images is plotted.

CORSIKA (Heck et al., 1998) is used to simulate shower development and the emission of Cherenkov light. The GrOptics[1] package is used to simulate ray-tracing in the telescope, giving the distribution of Cherenkov light in the camera plane. The VERITAS telescopes all have the same design, so the same templates were used for all telescopes. A correction factor for shadowing is applied to the templates. Photons are integrated over a circular area with radius 0.14°, corresponding to the size of the pixels in the VERITAS camera. The wavelength-dependent mirror reflectivity and PMT quantum-efficiency are taken into account to obtain the expected number of photo-electrons (p.e.) per pixel.

For the generation of the templates, the telescopes are assumed to be pointing in the direction of the shower. Light distributions for different directions in the camera and different core positions are obtained by displacing and rotating the predicted image in the camera. Distributions for arbitrary values of E, h, and D are obtained by interpolating between the grid values.

Figure 5.1 shows some predicted light distribution in the camera for iron showers. In some of the templates, for example Fig. 5.1a, there is a clear contribution from DC light, which can be clearly separated from the rest of the shower by eye. The direct Cherenkov light is emitted at a very small angle high up in the atmosphere, and confined to a region in the camera that is about the same size as a pixel. Not all template images have this contribution. For example, Fig. 5.1d shows a template with a large impact distance, so the detector is outside the Cherenkov cone for DC light for this image. In combination with images taken by the other telescopes, such an image can still help constrain the shower parameters and thus should not be discarded.

### 5.1.3 Template Normalization & Saturated Channels

The templates are produced in units of photo-electrons (p.e.), while the observed signal (integrated charge) is measured in digital counts (dc). The two can be converted into one another since the absolute gain, also referred to as *dc-to-pe ratio*, is known from calibration measurements. This ratio has to be adjusted for the integration window (only part of the pulse is integrated). In addition, a throughput correction factor has to be applied to the templates, accounting for both shadowing (which was not included in the generation of the templates), and the differences in mirror reflectivity between the telescopes. Both these effects are included in the regular detector simulation chain. The correction factor was obtained by comparing simulated shower images (after full detector simulation) to the template prediction, evaluated at the true energy, direction, and core position of the simulated event. The results (after adjusting the template normalization) can be seen in Fig. 5.2.

The reconstructed charge saturates for very bright images. To correct for that, the following piecewise-defined function was fit to the average reconstructed charge $\bar{q}$ as a function of the template prediction s:

---

[1] http://otte.gatech.edu/care/
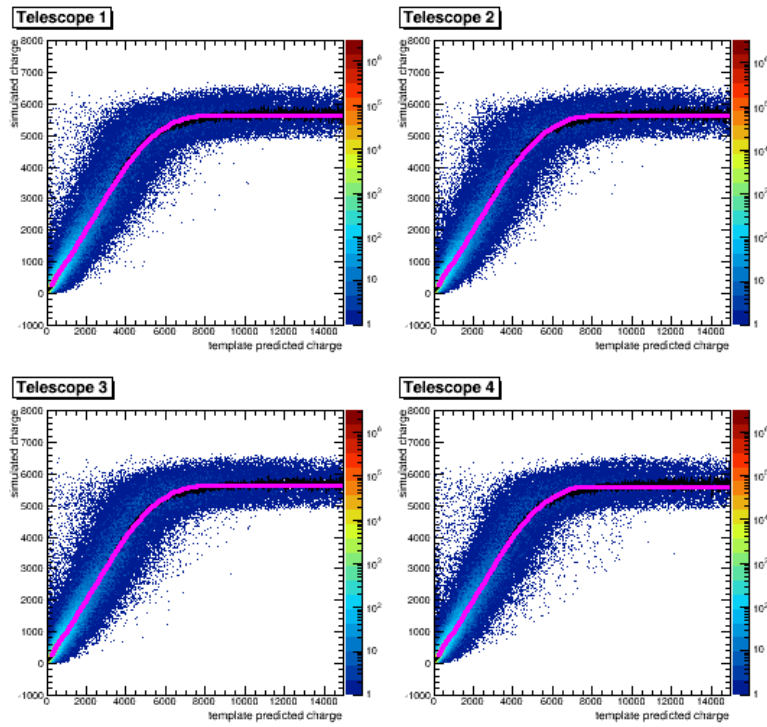
(a) Reconstructed charge versus template predicted charge, without saturation correction.
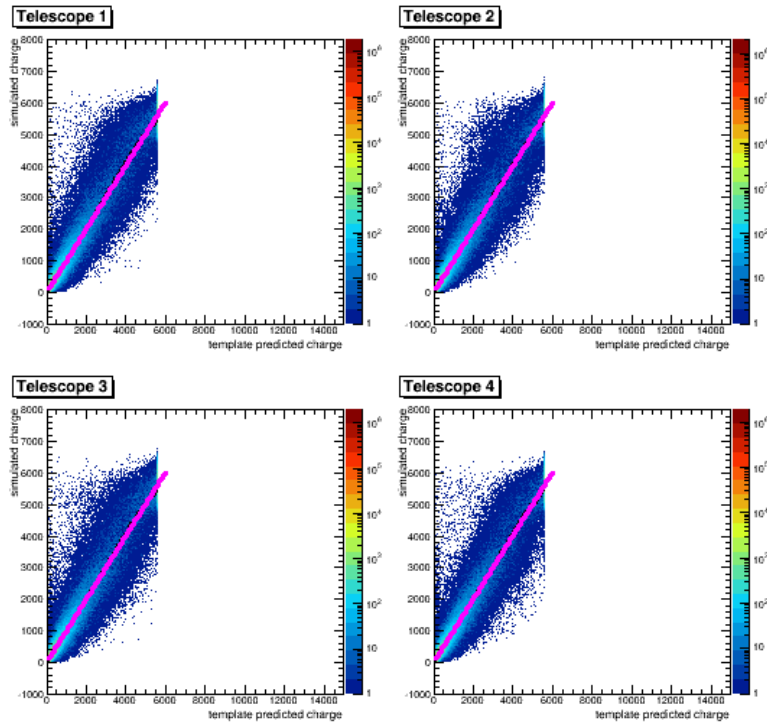
(b) Reconstructed charge versus template predicted charge, saturation correction applied.

Figure 5.2: Validation of the iron tempates using simulated iron shower images. The templates are evaluated at the true event parameters of the simulated events.

$$f(s) = \begin{cases} 2u \cdot (b-a) \cdot s & s \le a \\ u \cdot \left(b^2 - a^2 - (x-b)^2\right) & a \le s \le b \\ u \cdot \left(b^2 - a^2\right) & b \le s \end{cases}$$

This function consists of a linear rise for small pulses, a constant term for large (saturated) pulses, and a quadratic term which smoothly connects the two. After adjusting the template normalization, the slope of the linear term is 1 by definition, and f simplifies to

$$f(s) = \begin{cases} s & s \le a \\ \frac{a+b}{2} - \frac{(x-b)^2}{2(b-a)} & a \le s \le b \\ \frac{a+b}{2} & b \le s \end{cases}$$

As shown in Fig. 5.2, the fit function reproduces the average reconstructed charge sufficiently well. After applying this saturation correction to the predicted template charge, a roughly linear behavior is recovered.

5.1.4 Likelihood fit

Probability distribution for the observed signal in each pixel can be divided into three parts:

1. The distribution of the expected number of photo-electrons per pixel for a shower with a given energy, first interaction height, direction and impact point. This distribution is assumed to be Gaussian. Mean and standard deviation are taken from the templates.

2. The distribution of the actual number of photo-electrons per pixel, given the expected number. This is a Poisson distribution, which can be approximated by a Gaussian for large signals.

3. The distribution of the observed signal (after pedestal correction), converted to units of p.e., given the true number of photo-electrons. This distribution is Gaussian. The mean is given by the true number of photo-electrons. The two main contributions to the variance are the pedestal variance σ_p^2 and the variance in the PMTs' gains σ_e^2. The pedestal variance is mostly due to the night sky background and is measured continuously (see Section 4.4.1). The gain variance is measured by special calibration runs.

Previous implementations of the template likelihood method (Le Bohec et al., 1998; Parsons & Hinton, 2014; Vincent et al., 2016) only took the second two contributions into account, neglecting the shower-to-shower fluctuations. This approach is valid for gamma-ray showers because electromagnetic showers tend to have small shower-to-shower variations once the

differences in the first interaction height have been accounted for. However, hadronic showers tend to form clusters or sub-showers, which lead to larger variation between showers. The relative fluctuations are also different in different parts of the image. For example, if part of the image is dominated by DC light, the fluctuations in that part are typically very low and the overall distribution is dominated by the p.e. counting statistics or by the detector noise. Outside of the central region, the images are dominated by light from sub-showers or muons which reach the ground level.

The probability distribution for the signal in one pixel is a convolution of the three components mentioned above, and is an extension of the distribution used by De Naurois & Rolland, (2009), Parsons & Hinton, (2014), and Vincent et al., (2016). It is given by:

$$P(q|s(\mathbf{\Theta}), \sigma_p, \sigma_e, \sigma_s(\mathbf{\Theta})) = \int \mathrm{d}\mu \; G(\mu|s(\mathbf{\Theta}), \sigma_s(\mathbf{\Theta})) \cdot \sum_n Poi(n|\mu) \cdot G(q|n, \sqrt{\sigma_p^2 + n\sigma_e^2})$$

$$\approx G(q|s(\mathbf{\Theta}), \sigma(\mathbf{\Theta})) \;\; \text{with} \;\; \sigma = \sqrt{\sigma_p^2 + s\left(1 + \sigma_e^2\right) + \sigma_s^2(\mathbf{\Theta})} \quad (5.1)$$

Where

- $\mathbf{\Theta} = (E, h, X_p, Y_p, X_s, Y_s)$ is the (true) set of parameters describing the event.

- $G(x|\mu, \sigma) = \frac{1}{\sigma\sqrt{2\pi}} \cdot \exp\left(-\frac{(x-\mu)^2}{2\sigma^2}\right)$ is the normal distribution with mean μ and width σ.

- $Poi(n|\mu) = \frac{\lambda^k e^{-\lambda}}{k!}$ is the Poisson distribution with mean μ.

- q is the pedestal-corrected integrated charge (converted to units of p.e.).

- $s(\mathbf{\Theta})$ and $\sigma_s(\mathbf{\Theta})$ are the predicted average number of photo-electrons in each pixel and its uncertainty.

- μ is the predicted number of photo-electrons in a given shower, assumed to follow a Gaussian distribution with mean s and width σ_s.

- n is the number of photo-electrons, assumed to follow a Poisson distribution with mean μ.

- σ_e^2 is the variance of the signal (integrated charge) from a single photo-electron.

- σ_p^2 is the variance of the FADC pedestal of the given pixel.

The Gaussian approximation is valid for the images considered here. If the predicted number of photo-electrons is large, the Poisson distribution may be approximated by a Gaussian. Otherwise, the predicted number of photo-electrons is small, which happens at the edges of the images and which means that the shower-to-shower fluctuations dominate the distribution anyway.

The likelihood function describing the likelihood of the primary particle having certain parameters $\mathbf{\Theta}$, given the measured signal q, is given by the same function:

$$L_i(\mathbf{\Theta}|q_i, \sigma_p, \sigma_e) \;=\; P\left(q_i|s_i(\mathbf{\Theta}), \sigma_{p,i}, \sigma_{e,i}, \sigma_{s,i}(\mathbf{\Theta})\right)$$

The product of the single-pixel likelihood functions gives the overall likelihood function for each event. Instead of maximizing the likelihood, one traditionally minimizes its negative logarithm. The log-likelihood function to be minimized is thus given by the sum over the likelihoods of all active pixels:

$$-\ln L(\mathbf{\Theta}) = -\sum_{\text{pixel } i} \ln L_i(\mathbf{\Theta}) = \sum_{\text{pixel } i} \ln P(q_i|s_i(\mathbf{\Theta}), \sigma_i(\mathbf{\Theta})).$$

For real data, the true event parameters $\mathbf{\Theta}$ are unknown. For each measured event, the event parameters $\mathbf{\Theta} = (E, h, X_p, Y_p, X_s, Y_s)$ are adjusted to minimize $-\ln L$:

$$\hat{\mathbf{\Theta}} \text{ such that } \hat{L} := L(\hat{\mathbf{\Theta}}) \geq L(\mathbf{\Theta}) \; \forall \mathbf{\Theta}$$

It can be shown (Behnke et al., 2013) that the parameters $\hat{\mathbf{\Theta}}$ obtained from a maximum-likelihood fit are (in the mathematical sense) consistent estimators for the true values. As the parameter space is quite large, the results of the standard moment-based event reconstruction are used as starting values for the fit. The first interaction height is not determined during the moment-based analysis; a value of 33.3 km, which is close to the median for iron showers, is used instead.

The Levenberg-Marquardt algorithm implemented in the Gnu Scientific Library[2] was used to minimize $-\ln L$. An example of a simulated iron shower image and the best-fit template found by the minimizing algorithm can be seen in Fig. 5.3.

The fitting algorithm returns the final value of the likelihood, the best-fit values of the event parameters and their uncertainties.

Optionally, one or more of the event parameters may be fixed and exempt from the fit. For example, they may be set to the true values (for simulated events) or to the results of the moment-based analysis. In that case, the likelihood fit finds the best-fit set of parameters under the given constraints. Fixing the parameters can be done for debugging purposes. In this work, a large discrepancy was found in the distribution of the λ parameter (which corresponds to the height of the first interaction), when comparing data to the expectation from simulation. Hence, it was decided to exclude λ from the likelihood fit and fix it to the value 5, which corresponds approximately to the true average first interaction height for iron showers. This is discussed further in Section 6.1.

---

[2]http://www.gnu.org/software/gsl/

5.1.5 Average Value of the Likelihood and Goodness of Fit

The calculations in this section roughly follow De Naurois & Rolland, (2009), using the Gaussian approximation for the counting statistics and taking the shower-to-shower fluctuations into account.

In the following, the event parameters $\boldsymbol{\Theta}(E, h, X_p, Y_p, X_s, Y_s)$ are fixed and we will consider the distribution of the values that $l := -2 \ln L$ will take for different events with the same underlying parameters.

First, consider the single-pixel likelihood. As shown above, the signal q_i approximately follows a normal distribution with mean $s_i = s_i(\boldsymbol{\Theta})$ and width $\sigma_i = \sigma_i(\boldsymbol{\Theta})$ as defined before. Thus, we have

$$l_i(q_i) = -2 \ln L_i = \ln \left(2\pi\sigma^2\right) + \frac{(q_i - s_i)^2}{\sigma_i^2}.$$

The average value of l_i over an ensemble of repeated measurements is given by

$$\langle l_i \rangle_{q_i} = \int\limits_{-\infty}^{\infty} \left(\ln\left(2\pi\sigma_i^2\right) + \frac{(q_i - s_i)^2}{\sigma_i^2} \right) \cdot \frac{1}{\sigma_i\sqrt{2\pi}} \cdot \exp\left(-\frac{(q_i - s_i)^2}{2\sigma_i^2} \right) \mathrm{d}q_i$$
$$= \ln\left(2\pi\sigma_i^2\right) + 1,$$

and its standard deviation can be calculated as follows:

$$\left\langle l_i^2 \right\rangle_{q_i} = \int\limits_{-\infty}^{\infty} \left(\ln\left(2\pi\sigma_i^2\right) + \frac{(q_i - s_i)^2}{\sigma_i^2} \right)^2 \cdot \frac{1}{\sigma_i\sqrt{2\pi}} \cdot \exp\left(-\frac{(q_i - s_i)^2}{2\sigma_i^2} \right) \mathrm{d}q_i$$
$$= \left(\ln\left(\sigma_i\sqrt{2\pi}\right) \right)^2 + 2\ln\left(\sigma_i\sqrt{2\pi}\right) + 3$$

$$\sigma_{l_i}^2 = \left\langle l_i^2 \right\rangle_{q_i} - \langle l_i \rangle_{q_i}^2 = 2$$

Assuming there are N active pixels in all telescopes, $l := \sum\limits_i l_i = \sum\limits_i -2\ln L(\boldsymbol{\Theta}|q_i, \sigma_i(\boldsymbol{\Theta}))$ has expectation value

$$\langle l \rangle_q = N \cdot (1 + \ln 2\pi) + \sum_i \ln\left(\sigma_{p,i}^2 + s_i(\boldsymbol{\Theta}) \cdot \left(1 + \sigma_{e,i}^2\right) + \sigma_{s,i}^2(\boldsymbol{\Theta}) \right)$$

and standard deviation $\sigma_l = \sqrt{2N}$.

Note that this is the distribution of the measured likelihood values *under the assumption that the true parameters are known*. In the case of actual measurements, the true parameters are unknown and instead we have to rely on $\hat{\boldsymbol{\Theta}}$ and $\hat{l} = -\ln \hat{L}$. In this case, N is much larger

than the number of free parameters and $\boldsymbol{\Theta}$ is over-constrained. In that case, we can assume that $\hat{\boldsymbol{\Theta}} \approx \boldsymbol{\Theta}$ and that $\hat{l}$ follows a similar distribution as l. In that case, it is apposite to define a goodness-of-fit function as follows:

$$G = \frac{-2 \cdot \ln \hat{L} - \langle l \rangle_q}{\sqrt{2N}}.$$

As long as $\hat{\boldsymbol{\Theta}}$ is a good estimator for $\boldsymbol{\Theta}$, the goodness of fit G has mean 0 and width 1. In practice, since by definition $\hat{l} \leq l$, using $\langle l \rangle$ instead of $\langle \hat{l} \rangle$ slightly overestimates the mean and G will have a mean of slightly less than 0.

In the case of events that were not due to iron-induced showers, we do not expect the probability function derived from iron shower templates to describe the measured charge. For those events, G should tend to much larger values. Hence, G can be used to discriminate between signal and background events.

5.2 Direct Cherenkov Light in the Camera

Direct Cherenkov light (see Chapter 3) provides another method of separating iron-induced showers from those induced by lighter nuclei. As DC light is emitted under a small angle and is concentrated within the area of one pixel in the camera, the idea is to search for pixels that are much brighter than the neighboring pixels.

Similar to Aharonian et al., (2007) and Wissel, (2010), we define the DC quality factor for each pixel as

$$q_{DC} := \frac{I_{pixel}}{\langle I \rangle_{neighbors}},$$

where I is the measured charge/signal in each pixel.

The DC quality is calculated for all pixels within $0.5°$ of the reconstructed direction of the primary. DC light is emitted at angles below $0.3°$ (see Fig. 3.2); however, there is an uncertainty in the direction reconstruction which make it necessary to open the search region a bit. The pixel which has the largest value of the DC quality is called the *DC candidate pixel*. Assuming that the shower image (without the DC contribution) is smooth and has a constant gradient, the contribution of DC light to the DC candidate pixel can be estimated as

$$I_{DC} = I_{pixel} - \langle I \rangle_{neighbors}.$$

The DC contribution must be larger than 0 for the DC candidate.

The same search is also conducted in the best-fit template image. If the template has a DC candidate pixel at the same location as the recorded image, that pixel is called the *DC pixel.*

There are two advantages to requiring the template to have a DC candidate pixel in the same place as the real image. First, it cuts down on false positives (some hadronic showers have clumpy images due to the shower structure or due to statistical fluctuations). Second, such a requirement also removes some misreconstructed events (where the best-fit template actually does not describe the true event parameters properly).

However, requiring at least one image to have a DC pixel also removes a lot of iron events. For example, the shower core could have been in a position where no telescope was able to detect the direct Cherenkov light.

An example for a simulated event with a DC pixel can be seen in Fig. 5.3.

Neglecting absorption in the atmosphere, the DC intensity I_{DC} is proportional to the ratio of the number of emitted Cherenkov photons N_{DC} and the distance D between telescope and shower core: $I_{DC} \propto \frac{N_{DC}}{D}$. The number of emitted Cherenkov photons is approximately proportional to $Z^2 \cdot \sin \theta_c \cdot \Delta h$, where Z is the charge number of the emitting particle, Δh the length of the path segment over which the DC light is visible from the detector, and θ_C is the Cherenkov angle, which can be approximated by the angular distance Δ_{DC}^{dir} between the DC pixel and the reconstructed direction.

Following Rolf Bühler, (2005) and neglecting the dependence on Δh, the (non-normalized) *reconstructed charge,*

$$Z_{\text{reco}} = \frac{\sqrt{I_{DC} \cdot D}}{\sin \Delta_{DC}^{dir}},$$

is thus approximately proportional to the charge number of the emitting particle. For events with more than one DC candidate pixel, the average reconstructed charge $\langle Z_{\text{reco}} \rangle$ is defined as the simple average over the images which include a DC contribution.

Due to the uncertainties in measuring Δ_{DC}^{dir} and D as well as the neglected absorption in the atmosphere and dependence on Δh, the distribution of $Z_mathrmreco$ is actually quite wide and cannot be used to determine the primary particle's charge on its own. However, it can be used as input for a multivariate classifier.

5.3 Decision Trees and Random Forests

Decision trees are decision-making algorithms similar to flow-charts[3]. They can be represented by a *binary tree* (a connected, a-cyclic graph with one distinguished *root* vertex, in which each *internal* node has exactly two children). In a *decision* tree, each internal node corresponds to a binary condition or yes/no question, and each of the two vertices pointing
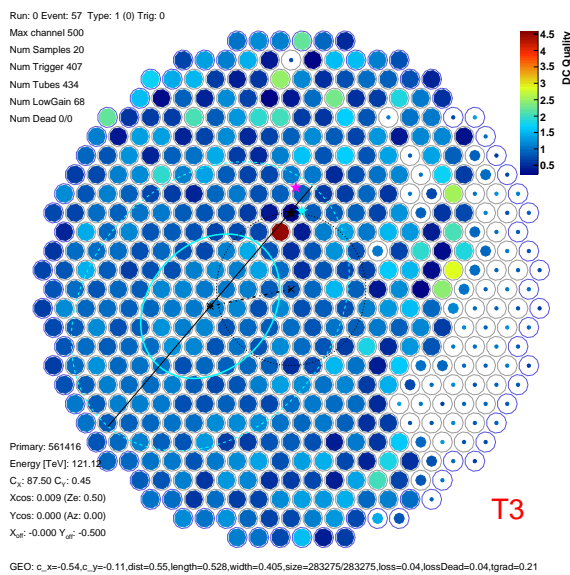
---

[3]See Hoecker et al., (2007) for more information about decision trees and the training thereof.
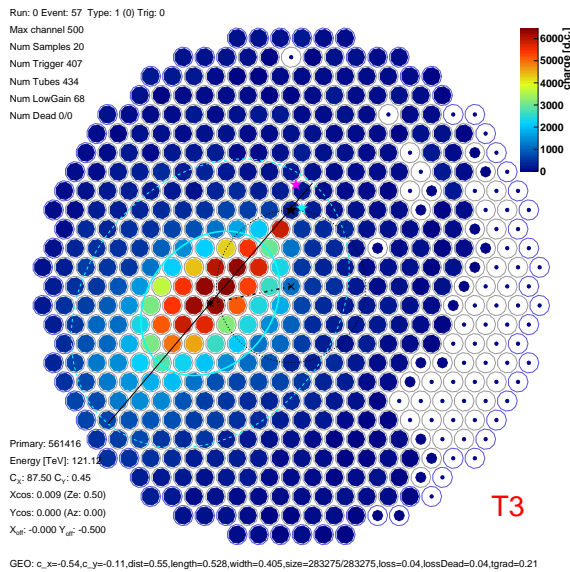
(a) Integrated charge per pixel.
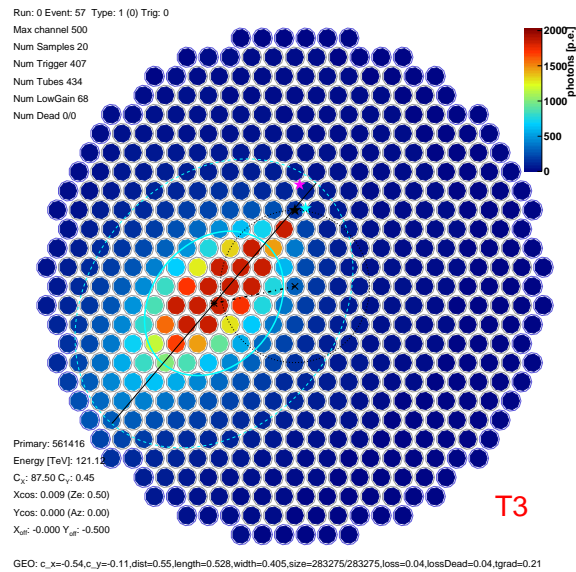
(b) Best-fit image template.

(c) DC quality factor for the simulated image.

Figure 5.3: Simulated 121 TeV iron shower image in one of the VERITAS telescopes. There is a visible contribution from DC light. Black star: true shower direction. Pink star: shower direction reconstructed by the moment analysis. Cyan star: shower direction reconstructed by the template analysis.
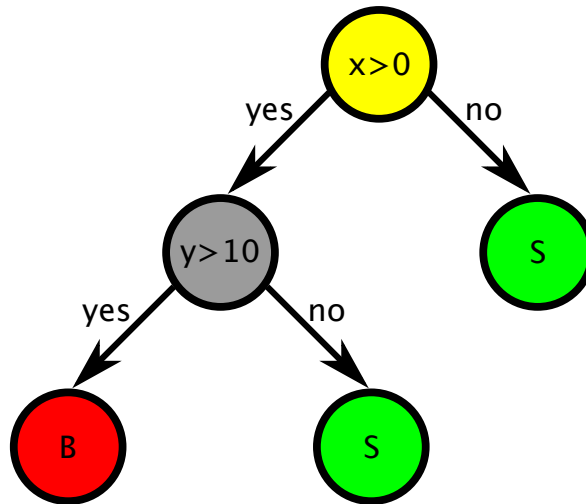
Figure 5.4: Decision tree (schematic) with two internal nodes and three leaves. The root node is colored yellow, signal leaves are colored green and background leaves are colored red.

to the child nodes corresponds to a yes or no. To traverse the tree, one starts at the root and follows the path indicated by each question. The *leaves* (external vertices) of the tree correspond to a global yes/no answer.

In physics, decision trees are often used as binary classifiers, for example to separate *signal* events from *background* events. In this case, the events are characterized by a set of parameters and the yes/no questions are Boolean functions of these parameters. The leaves are labeled either *signal* or *background* and events are assigned the class of the leaf they end up in. An example for a decision tree on two variables can be seen in Fig. 5.4. Decision trees are often used to combine multiple weak classifiers into one stronger one. In Section 5.4, I will show how decision trees can be trained to separate iron-induced showers from showers induced by lighter elements based on several image parameters.

Decision trees can be constructed manually, or they can be *trained* to produce optimal separation on a labeled training sample, often obtained from simulations. To reduce computing complexity, the conditions are typically restricted to the form $P > c$, where P is one of the event parameters and c is a constant. Optimal separation is defined by some cost function; a common cost function is the *Gini*-index. The *Gini*-index[4] for node n is defined as

$$Gini(n) = p_n \cdot (1 - p_n),$$

where $p_n = \frac{S_n}{S_n + B_n}$ is the *purity* (ratio of signal events S_n to background events B_n) in node n. The tree is trained recursively, starting at the root node with the full training sample. Consider node n with child nodes n_l and n_r. First, the combination of cut variable and cut threshold is found that maximizes the expression $G := G_n - G_{n_l} - G_{n_r}$. If $G_{max} > 0$, the

---

[4]To be consistent with the general definition of the *Gini*-index, the formula should be $2 \cdot p_n \cdot (1 - p_n)$, however that does not make a difference for the minimization procedure described here.

corresponding cut is assigned to node n. The sample is split according to that cut and the procedure is repeated for n_l and n_r with the partial samples. Otherwise, the n is made a leaf node; it is declared a *signal* node if $p_n > 0.5$ and a background node otherwise.

Trees trained in this manner tend to classify the events in the training sample very well, but are unstable (small changes in the training sample can change the entire structure of the tree) and prone to over-training (the tree recognizes small structures due to statistical fluctuations in the training sample which do not exist in the real sample). There are several ways to combat over-training; for example by restricting the depth of the tree, or by requiring a minimum number of events in each leaf. However, these restrictions can degrade the performance of the tree. Also, a single decision tree is inflexible; there is no way to change the efficiency/background rejection after training. If one wants, for example, a less sensitive tree with better background suppression, one would have to redo the training with a different distribution of signal and background events in the training sample.

There are several extensions of the decision tree that provide more stable and flexible classifiers that are less sensitive to over-training. They rely on training not just one tree, but a *forest* (ensemble of trees). The global response is then given as the (weighted) average over the tree responses, often re-scaled to give a value between -1 (background-like) and $+1$ (signal-like). To recover a binary classifier, one has to define a threshold on the global forest response above which an event will be classified as signal. The forest provides a more flexible classifier because the threshold can be changed to obtain the desired efficiency or background rejection. Also, the global forest response provides additional ways to asses the validity of the classifier. To check for over-training, one can compare the distribution of the forest response on signal/background events for the training sample and an independent test sample. A difference in the distributions indicates over-training. Additionally, one can compare the distributions for data and the training (or test) sample, re-weighted to the appropriate number of signal and background events. A mismatch between the distributions can indicate that the training sample was not chosen well or that the simulations used for the training do not describe the real data properly.

With the method described above, a given training sample will always produce the same tree. To obtain an ensemble of trees, one therefore has to change the training sample or the training algorithm. The *random forest* algorithm (Breiman, 2001) introduces two such changes. First, in each training step, instead of testing all input parameters to find the optimum cut, only a random subset of the input parameters are considered. This random selection is re-done for each training step. Secondly, each tree is trained on a random sub-sample of events from the training sample. Events may be sampled with or without replacement. The number of input parameters considered in each training step and the number of events in each sub-sample are parameters of the algorithm that can be selected by the user.

There are other methods that yield an ensemble of decision trees. One other very common classifier is an ensemble of *boosted decision trees* (BDTs). In this case, the full sample is used

to train each tree. However, the events are re-weighted in each step, with events that were previously misclassified being assigned higher weights.

5.4 Signal/background Separation with Random Forests

Even with the requirement that a DC candidate pixel is found in the template and in the image at the same location, requiring a DC pixel does not remove all of the background from lighter particles. To obtain better separation between signal and background, 15 parameters are combined into one random forest classifier (Albert et al., 2008). The classifier is trained on the simulations described in Chapter A using the TMVA software package (Hoecker et al., 2007). TMVA implements random forests as a special case of the boosted decision tree classifier[5]. The training is performed only on events with a successful template fit and at least one image with a DC pixel.

The input parameters are:

- mean scaled width ($MSCW$)

- mean scaled length ($MSCL$)

- χ^2 from the fit of a constant energy to all telescope images ($\log_{10}(\chi_E^2)$)

- The height of the maximum of the Cherenkov emission from the geometric reconstruction ($EmissionHeight$)

- χ^2 from the fit of a constant maximum height to all telescope pairs ($\log_{10}(\chi_H^2)$)

- The $size$ of the second brightest image ($\log_{10}(size2nd)$)

- The distance between the shower core and the array center ($\sqrt{XP^2 + YP^2}$)

- The energy uncertainty from the look-up table analysis dES

- The fit goodness parameter from the likelihood fit, using all image pixels ($GoodnessImg$)

- The uncertainty of the energy resulting from the likelihood fit $frogsEnergyerr$

- The height of the first interaction determined by the likelihood fit λ

- The uncertainty of the height of the first interaction from the likelihood fit $Lambdaerr$

- The number of images that had a DC pixel (N_{DC})

- The sum of the DC quality factors from all images that had a DC pixel ($\sum q_{DC}$)

- The sum of the DC contributions from all images that had a DC pixel ($\sum I_{DC}$)

---

[5]Sampling with replacement (referred to as *bagging* in TMVA) is implemented by assigning each event a random weight, distributed according to a Poisson distribution.
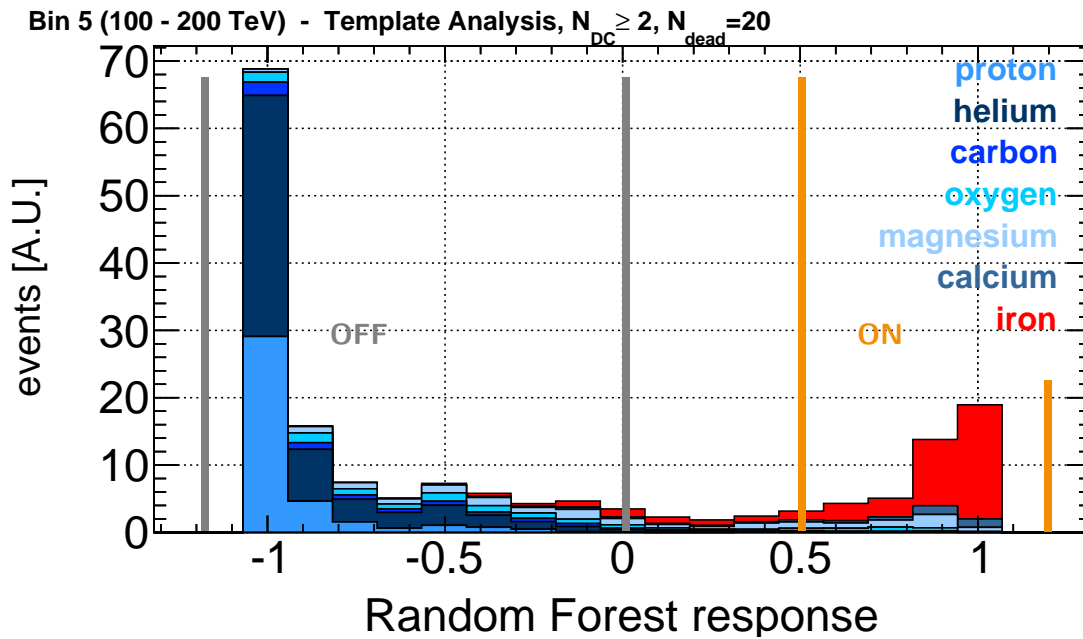
Figure 5.5: Response of the random forest classifier in the first energy bin from 100 TeV to 200 TeV. *ON* and *OFF* regions have been marked.

- The average reconstructed charge $\langle Z_{\mathrm{reco}} \rangle$

The classification is done in 5 bins of energy. The bin limits are approximately 20 TeV, 30 TeV, 50 TeV, 100 TeV, 200 TeV, 500 TeV. Half of the events are used for training, the other half for validation.

The random forest classifier returns values between -1 and 1, with the background distribution peaking at lower values and the signal distribution at higher values. For this case, there is still significant overlap between the distributions (see Section 6.2.5) so that a simple cut is not able to remove all of the background.

5.5 Background Estimation from Random Forest Response

There is some overlap between the distributions of the random forest response for signal and background, but the distributions have very different shapes. In gamma-ray astronomy, one can use off-source observations to estimate the remaining background in such a case. However, the cosmic ray flux is nearly isotropic and there are no iron-free regions of the sky. Thus, the signal and background contributions have to be estimated from the shape of the random forest response of the data.

The algorithm that was used is similar to the 'matrix method' in high-energy particle physics (Behnke et al., 2013) or to the 'template background estimate' (Rowell, 2003) in

gamma-ray astronomy. The difference to applications in gamma-ray astronomy is that for cosmic rays, the directional information is less important.

We define non-overlapping ON and OFF intervals in the random forest response (cf. Fig. 5.5), where the ON interval is signal-dominated and the OFF interval is background-dominated. The thresholds are later optimized for good performance. We then define the ON ratio α and the OFF ratio β both for signal and background:

$$\alpha_s = \frac{N_{on}^{signal}}{N^{signal}} \qquad\qquad \alpha_b = \frac{N_{on}^{bg}}{N^{bg}}$$
$$\beta_s = \frac{N_{off}^{signal}}{N^{signal}} \qquad\qquad \beta_b = \frac{N_{off}^{bg}}{N^{bg}}$$

These ratios must be obtained from simulations due to the lack of a clean iron/iron-free data sample.

When a measurement is performed, we measure a certain number N^{data} of events passing the pre-cuts. We are interested in how many of the data counts are contributed by signal (N_s) and background (N_{bg}) respectively, where $N^{data} = N_s + N_{bg}$.

The number of signal counts can be determined as follows. First, the number of data events N_{on}^{data} and N_{off}^{data} falling into the ON and OFF regions are measured. We must have

$$N_{on} = \alpha_s \cdot N_s + \alpha_b \cdot N_b$$
$$N_{off} = \beta_s \cdot N_s + \beta_b \cdot N_b.$$

As long as the two equations are linearly independent, meaning that $\alpha_s \cdot \beta_b - \alpha_b \cdot \beta_s \neq 0$, this system of equations can be solved for the number of signal events N_s:

$$N_s = \frac{1}{\beta_s} \cdot \frac{N_{on} - \frac{\alpha_b}{\beta_b} \cdot N_{off}}{\frac{\alpha_s}{\beta_s} - \frac{\alpha_b}{\beta_b}}$$

Assuming that N_{on} and N_{off} are large, they follow approximately Gaussian distributions and their uncertainties are given by $\Delta N_{on} = \sqrt{N_{on}}$ resp. $\Delta N_{off} = \sqrt{N_{off}}$. Assuming the ratios α and β are known from simulations with negligible uncertainty, we can estimate the uncertainty on N_s as

$$\Delta N_s = \sqrt{\left(\frac{\partial N_s}{\partial N_{on}^{data}} \cdot \Delta N_{on}^{data}\right)^2 + \left(\frac{\partial N_s}{\partial N_{on}^{data}} \cdot \Delta N_{on}^{data}\right)^2}$$

$$= \left(\frac{\beta_b}{\alpha_s \cdot \beta_b - \alpha_b \cdot \beta_s}\right) \cdot \sqrt{N_{on} + \frac{\alpha_b^2}{\beta_b^2} N_{off}}.$$

Note that for $\alpha_s \cdot \beta_b - \alpha_b \cdot \beta_s \approx 0$, i.e. when the relative contributions to the ON and OFF regions are about the same for signal and background, the uncertainty can get very large. This happens when the ON and OFF regions are poorly chosen or when the classifier is so bad that its response is distributed very similarly for the signal and background samples.

5.6 Flux Estimation (Isotropic Case)

The number of signal events N_s alone is not a physical quantity that can be easily compared to other results. Instead, we are typically interested in the cosmic ray *flux* or the *energy spectrum*. Assuming a fully efficient detector covering an area A with field of view $\Delta\Omega$ and taking data over a time ΔT, the (isotropic and homogeneous) particle flux $\frac{\mathrm{d}N}{\mathrm{d}A\mathrm{d}\Omega\mathrm{d}t}$ can be estimated as

$$F = \frac{\mathrm{d}N}{\mathrm{d}A\mathrm{d}\Omega\mathrm{d}t} \approx \frac{N_s}{A \cdot \Delta\Omega \cdot \Delta T}$$

For this formula to apply, $\Delta\Omega$ must be small and define a connected field of view around the line of sight, and the area A must be measured perpendicular to the line of sight.

To determine the differential flux $\frac{\mathrm{d}F}{\mathrm{d}E}$, one just needs to restrict the signal count to a small energy bin $\left(E - \frac{\delta E}{2}, E + \frac{\delta E}{2}\right)$ and divide by the bin width:

$$f(E) = \frac{\mathrm{d}F}{\mathrm{d}E} = \frac{\mathrm{d}N}{\mathrm{d}A\mathrm{d}\Omega\mathrm{d}t\mathrm{d}E} = \frac{N_s\left(E - \frac{\delta E}{2}, E + \frac{\delta E}{2}\right)}{A \cdot \Delta\Omega \cdot \Delta T \cdot \Delta E}$$

The factor $G = A \cdot \Delta\Omega$ is called the *geometric factor*.

In the case of a non-ideal detector, the detection efficiency has to be taken into account. For IACTs, the overall efficiency ε is the product of three separate factors:

- The trigger efficiency (fraction of events that have enough light to trigger the array readout)

- The reconstruction efficiency (fraction of triggered events that are reconstructed successfully and that pass reconstruction quality cuts)

- The analysis efficiency (fraction of reconstructed events that pass analysis cuts aimed at suppressing background, for example the random forest pre-selection cuts).

The efficiency ε depends on the particle's energy E, its core position on the ground (x_p, Y_p), the offset from the camera center (X_s, Y_s), the level of noise l (especially noise from the night sky background), and the pointing direction (Ze,Az) of the telescopes.

The geometric factor G must be replaced by an *effective* geometric factor that takes this efficiency into account:

$$G_{eff}(E, Ze, Az, l) = \int\limits_A \int\limits_{\Delta\Omega} \epsilon(X_p, Y_p, X_s, Y_s, E, Ze, Az, l) \mathrm{d}X_s \mathrm{d}Y_s \mathrm{d}X_p \mathrm{d}Y_p$$

Simulations are used to evaluate the efficiency. Instead of finding an analytic expression for efficiency with all its non-trivial dependencies on the energy, core position etc, it is common to just solve the integral via Monte-Carlo integration. In a given (small) energy bin around the energy E, N_{sim} events are simulated, scattered uniformly over an area A_{sim} and the solid angle $\delta\Omega_{sim}$. The pointing direction of the telescopes and the noise level are kept fixed. A_{sim} and $\Delta\Omega_{sim}$ have to be large enough to cover the full area/solid angle over which the efficiency is larger than 0. For IACT analysis, this usually corresponds to a scattering radius of several hundred meters in the shower plane and several degrees on the sky. The detector response including the trigger is part of the simulation. The triggered events are fed through the same analysis software as data even and the number of reconstructed events N_{rec} is counted. The effective geometric factor is then given by

$$G_{eff}(E, Ze, Az, l) = \frac{N_{rec}}{N_{sim}} \cdot A_{sim} \cdot \Delta\Omega_{sim}.$$

The geometric factor has to be calculated for each pointing direction and noise level. Usually, a fixed grid in Ze, Az, and l is used. If the detector configuration was changed during data taking, the effective geometric factor is determined separately for each configuration.

The effective geometric factor can depend strongly on the energy, especially close to the energy threshold. One usually chooses larger energy bins for data than for the calculation of G_{eff} from simulation. Therefore, it is helpful to use a *spectral weighted* geometric factor for the flux calculation. Here, one has to assume that the true spectral shape $f_{true}(E)$ is known. For cosmic rays, the spectrum can be described by a power law: $f_{true}(E) \propto E^{-\gamma}$. The normalization is not important here because it cancels out. The spectral weighted geometric factor is then given by

$$G_w(\gamma, Ze, Az, l) = \frac{\int\limits_{\mathrm{bin}} G_{eff}(E, Ze, Az, l) \cdot f_{true}(E) \mathrm{d}E}{\int\limits_{\mathrm{bin}} f_{true}(E) \mathrm{d}E}$$

The residual dependence on γ is small for use cases in gamma-ray astronomy and astro-

particle physics, because the observed energy spectra tend to be power laws with spectral indices between -1.5 and -4.5. To measure the spectral index, one calculates the differential flux for a reasonable assumption of the spectral index and performs a power law fit to the spectrum. The spectral index determined from the fit result is used to re-calculate G_w for the next step. The process is repeated until the assumed and fitted spectral index agree within the statistical uncertainty of the fit. If the index does not converge, the spectrum probably deviates significantly from a power law.

The pointing directions and noise level and hence G_w change over time. The observations are split into N time bins with duration Δt_i, over which the observing conditions are nearly constant. For VERITAS, each observing run of 20 to 30 minute duration may be chosen as a single time bin, but sometimes it is necessary to split the runs further. The number of signal events N_s^i and the effective geometric factor G_i are determined for each time bin. The average flux is then given as

$$F = \frac{\sum\limits_{i=0}^{N} N_s^i}{\sum\limits_{i=0}^{N} \left(\Delta T_i \cdot G_i \right)}$$

Note that this expression is only valid if the flux can be assumed to be constant in time. Otherwise, the observed average flux of course depends on the observing times.

5.7 Gamma-Ray Point Source Analysis

Eventdisplay[6], one of the two VERITAS data analysis packages, was used for the search for gamma-ray emission from star-forming galaxies, see Chapter 8. The standard VERITAS data analysis is described in Daniel et al., (2007). In this subsection, I will discuss some aspects of the analysis relevant for the estimation of the flux (and upper limits on the flux) of gamma-ray point sources.

5.7.1 Background Estimation from Off-Source Counts

Except for observations of the Galactic center region, diffuse gamma-ray emission is negligible in the VHE regime. For the star-forming galaxies studied in this work, the dominant contribution to the background after gamma-ray selection cuts is due to cosmic ray events, whose arrival directions are distributed nearly isotropically. Thus, simultaneous off-source data from the same field of view as the source can be used to estimate the remaining background in the source region (Fomin et al., 1994). When possible, this approach is preferred over the method described in Section 5.5 because it does not rely on simulations of the background.

---

[6]https://znwiki3.ifh.de/CTA/Eventdisplay%20Software

For the study presented here, data were taken in *wobble* mode, with the center of the camera offset from the source by $0.5°$. The source region or ON region is then defined as a circular region, centered on the source position, with a radius of $0.09°$ (comparable to the angular resolution for gamma rays). For the background estimate, six circular OFF regions were used with the same radius and the same offset from the camera center as the source region. The acceptance of the VERITAS camera has been found to be radially symmetric, so the background rate is expected to be the same for each region. In the ON region, there may be an additional (unknown) contribution from signal events.

The actual event counts in the ON and OFF regions after gamma-ray selection cuts and possible cuts on the reconstructed energy, N_{ON} and N_{OFF}, are expected to follow Poissonian distributions with mean values $\lambda_{ON} = N_S + N_B$ and $\lambda_{OFF} = \frac{N_B}{\alpha}$, where N_S (N_B) corresponds to the expected number of signal (background) events in the ON region, and $\alpha = \frac{1}{6}$ is the ratio between the area of the ON and OFF regions.

Given the event counts N_{ON} and N_{OFF}, the statistical significance of the signal is evaluated according to Eqn. 17 in Li & Ma, (1983). The threshold for a significant detection is set at the customary value of 5σ.

5.7.2 Flux Estimation (Point Source)

Given a significant excess, the best estimate for the number of signal events in the ON region is given by $\widehat{N_S} = N_{\mathrm{ON}} - \alpha \cdot N_{\mathrm{OFF}}$ (Li & Ma, 1983). and the flux is then estimated as $\widehat{F} = \frac{\widehat{N_S}}{A_{\mathrm{eff}} \cdot T}$, where A_{eff} is the effective collection area of the array, weighted according to the energy spectrum and T is the observing time after corrections for dead time due to detector readout. The effective collection area takes into account the efficiencies of the trigger system, reconstruction algorithm, and gamma-ray selection cuts as well as losses due to mis-reconstruction of the arrival direction. This expression is can be used for point sources and sources with an extension smaller than the field of view of the instrument.

If no significant excess over the background expectation is found, an upper limit on the number of source counts, N_S^{UL}, is calculated following the formalism of Rolke et al., (2005) method 4 (background from sidebands, known efficiency $\tau = \frac{1}{\alpha}$) and reported at 99% confidence level. The upper limit on the flux is then given by $F^{\mathrm{UL}} = \frac{N_S^{\mathrm{UL}}}{A_{\mathrm{eff}} \cdot T}$.

5.7.3 Expected Flux Limits

Eventdisplay provides several sets of gamma-ray selection cuts, optimized for different source strengths and spectral indices. The energy threshold for the calculation of the flux (or upper limits) can be set independently of the cuts, although a lower limit on the energy threshold is defined by the reconstruction algorithm and selection cuts. It is necessary to compare the sensitivity of the different cut sets and to chose the optimal energy threshold in an un-biased way. *Expected limits*, calculated under the assumption that there is no source as described

below, are used for this purpose. These only depend on the background counts, which have smaller statistical fluctuations that the ON counts.

Given the number of background events (above a certain energy threshold) N_{OFF} and the ON/OFF ratio α, the best estimate for the background rate N_B is $\widehat{N_B} = \alpha \cdot N_{\text{OFF}}$. Assuming there is no gamma-ray source ($N_S = 0$), the number of ON events follows a Poissonian distribution with mean N_B.

To calculate the expected limits, I perform toy Monte-Carlo experiments in which I draw ON and OFF events according to Poissonian distributions with mean parameters $\lambda_{ON} = N_B$ and $\lambda_{OFF} = \frac{N_B}{\alpha}$. For each draw, the upper limit on the signal events according to (Rolke et al., 2005) is calculated. The expected limit on the signal count is then given by median of the distribution of limits over a large number (typically 100000) random draws. The 1σ and 2σ error bars are derived from the 2.5 %, 16 %, 84 %, and 97.5 % quantiles of the distribution. The expected limits on the flux are calculated in the same way as described above.

These expected limits and their associated uncertainties provide an estimate on the mean value and on the statistical fluctuations to expect on the actual upper limits. In roughly 95 % of all observations of non-sources, the upper limit derived from background counts should be within the 2σ band around the expected limit. The actual limit can be lower than the expected limit due to downward fluctuation of the background.

6 Performance and Validation of the Analysis Methods

6.1 Fit of the First Interaction Height

The λ parameter, which corresponds to the height of the first interaction, is the only fit parameter for which there is no starting value available in data, because it is not determined by the moment-based analysis. Thus, the allowed range for the minimizer had to be left open to cover the full phase space. Accordingly, the λ parameter was least constrained by the fit. It also only had a weak correlation to the true value for iron simulations, and was very unstable when changing the random seed for the minimizer algorithm. All other fit values (energy, direction, and core position) were well correlated with the true values for iron simulations, as well as when repeating the template fit with a different random seed.

Additionally, the distribution of the best-fit results for λ showed a peak around $\lambda \approx 0$. This peak is more pronounced in data events, but can also be seen in the lambda distributions for simulations. This pull towards $\lambda \approx 0$ is unexpected: The λ distribution is expected to be uniform by definition for iron showers. Lighter elements have a smaller cross section for interacting with air nuclei, and hence penetrate deeper into the atmosphere, corresponding to larger values of λ.

No cause for the peak at $\lambda \approx 0$ was found. Neither was it possible to match the extent of the peak seen in data in the simulations, e.g. by introducing a deliberate mis-match between the template normalization and the simulated telescope throughput.

Finally, it was decided to fix λ during the likelihood fit rather than fitting it to the recorded image. For this, the value of $\lambda = 5$ was chosen because it approximates the median of the true λ values for iron showers. Accordingly, λ and *lambdaErr* were removed from the list of input variables to the Random Forest classifier.

6.2 Instrument Response

The instrument response was evaluated on simulated iron showers. The effective collection area is plotted against the reconstructed energy, whereas the energy bias, energy resolution, angular resolution, and core resolution are plotted against the true energy. Angular resolution and core resolution refer to the 68 % containment radius. The energy resolution refers to the
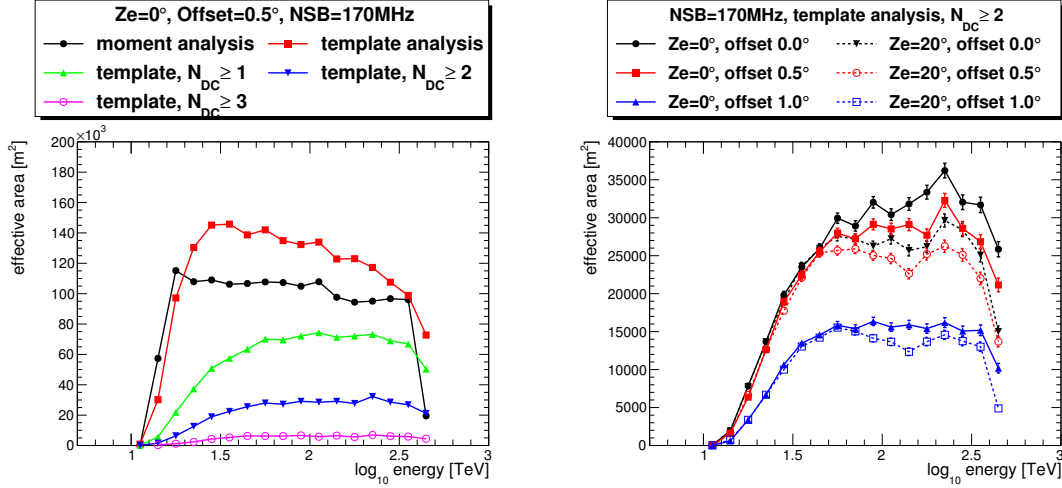
(a) Effective collection area for different cut sets.
(b) Effective collection area for different zenith angles and offsets from the camera center

Figure 6.1: Effective collection area versus energy.

68 % containment interval around the median. Unless otherwise mentioned, all azimuth directions were combined to produce the plots shown.

The instrument response was evaluated for the *moment-based analysis* with basic cuts on the reconstruction quality (as a baseline) as well as for the *template analysis*. The following quality cuts were applied:

Active telescopes: At least tree triggering telescopes.

Reconstruction: Successful reconstruction of the event direction/core position, energy, and mean scaled width/length.

Image brightness: At least two images with a *size* (total signal) of 8 kd.c. or more.

Core position: Reconstructed core position less than 350 m from the array center and less than 180 m from the closest telescope.

Event direction: Reconstructed direction less than 1.25° from the camera center.

Reconstructed energy: At least 10 TeV (minimum template energy).

Goodness-of-fit: Image goodness between −99 to 1000, background goodness between −20 to 20 (*template* reconstruction only).

DC pixel candidates: For the nominal analysis, at least two images must have a DC pixel candidate. Other values of $N_{DC}^{\min}$ were also tested (*template* reconstruction only).

6.2.1 Effective Collection Area

Figure 6.1 shows the effective collection area for the moment-based analysis and the template-based analysis with different requirements on the number of DC pixel candidates. The peak effective area is about $1.5 \cdot 10^5 \, \mathrm{m}^2$ for the template-based analysis compared to about $1.1 \cdot 10^5 \, \mathrm{m}^2$ for the moment-based analysis. This might be surprising, since only events passing the moment-based analysis are considered by the template analysis. However, the template-based analysis has a better core and angular resolution (see next subsection), so that more events pass the requirements on the core position and the reconstructed direction. Also, the bias in the energy reconstruction (see below) could cause the same events to be reconstructed at different energies.

Requiring at least one DC pixel candidate reduces the effective collection area above $100 \, \mathrm{TeV}$ by about a factor of two, and even more for lower energies. Requiring at least two DC pixel candidates leads to another reduction by a factor of two, for a peak collection area of about $3 \cdot 10^4 \, \mathrm{m}^2$.

Energy bias and energy resolution for the nominal analysis (template analysis, ≥ 2 DC pixel candidates) were evaluated for different zenith angles ($0°$, $20°$) and offsets from the camera center ($0°$, $0.5°$, $1°$). There is no strong dependence on the zenith angle, however, the effective collection area does drop off closer to the edge of the allowed region of the camera. Dependence on night sky background noise level and azimuth of the shower direction were also tested and no strong dependence was found for dark sky conditions.

There is a statistical uncertainty on the effective area, due to the limited statistics of the simulations. This uncertainty is below $10 \, \%$ for all energies.

6.2.2 Energy Bias and Resolution

The energy bias and energy resolution were evaluated for the moment-based analysis as well as the template analysis with different cuts on the minimum number of DC pixel candidates. The results can be found in Fig. 6.2. In all cases, there is a large positive bias (i.e. the reconstructed energy is too large) close to the energy threshold ($10 \, \mathrm{TeV}$). This just happens due to the energy cut: Of all events with a true energy of $10 \, \mathrm{TeV}$, only those with reconstructed energy above $10 \, \mathrm{TeV}$ will pass the selection.

For events with a true energy above $50 \, \mathrm{TeV}$, the moment-based analysis has an energy bias of $-20 \, \%$ and the template analysis has an energy bias of $-10 \, \%$. The reason for this offset is unclear. It is possible that fixing the λ parameter can introduce an energy bias for the template analysis. Requiring one or more DC pixel candidates leads to a positive energy bias. This is probably a selection effect: Events with a large reconstructed energy are more likely to have DC emission in the template.

The energy resolution, shown in Fig. 6.3 is definitely improved by the template analysis ($17 \, \%$ to $27 \, \%$) compared to the moment-based analysis ($13 \, \%$ to $35 \, \%$). Requiring one or more DC pixel candidates further improves the resolution as mis-reconstructed events are
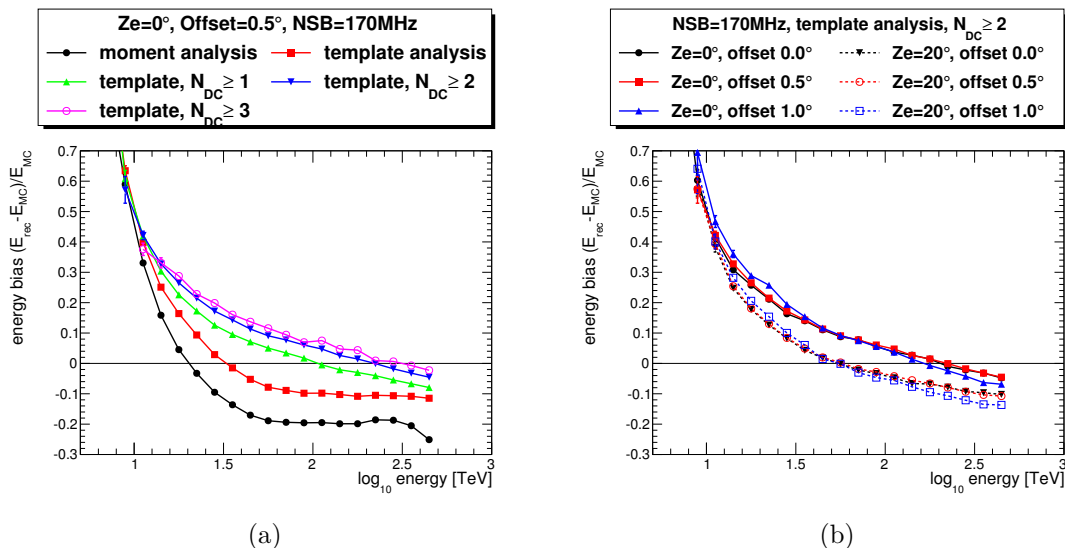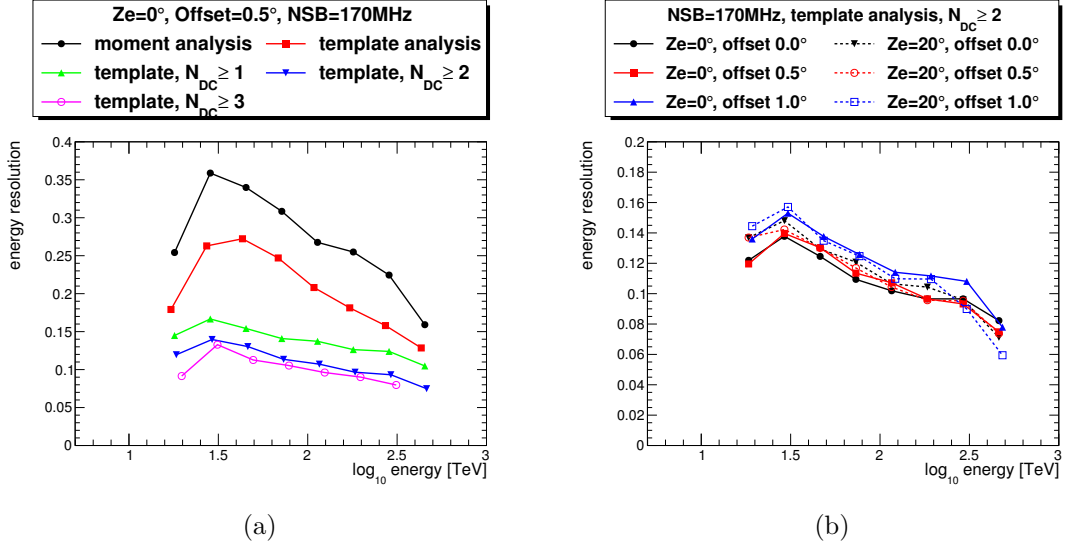
Figure 6.2: Energy bias (median) versus energy (a) for different cut sets; (b) for different zenith angles and offsets from the camera center.

removed. Mis-reconstructed events would not have the DC pixel in the same position in the template and the recorded image, and hence are unlikely to pass the minimum DC pixel candidate requirements. Requiring at least two DC pixel candidates decreases the energy resolution below 15 %.

Energy bias and energy resolution were also evaluated for different zenith angles ($0°$, $20°$) and offsets from the camera center ($0°$, $0.5°$, $1°$). No strong dependence on the offset was found. The energy bias does depend on the zenith angle: Showers at $20°$ zenith angle have about 10 % lower reconstructed energy compared to showers from zenith. This is explained by the fact that the templates used for the energy reconstruction were all generated at $0°$ zenith angle. Showers from a larger zenith angle develop slightly higher in the atmosphere and thus have less light and seem to be less energetic. The energy resolution does not depend on the zenith angle. Dependence on night sky background noise level and azimuth of the shower direction were also tested and no strong dependence was found for dark sky conditions.

The energy-dependence of the energy bias is slightly worrying, because it could affect the measured spectral index. This is explored further in Section 7.3.1.

6.2.3 Angular Resolution and Core Position Resolution

The reconstruction of the core position and the event direction are not of immediate importance since the iron flux is isotropic (especially at the size scale of the VERITAS field of view). However, a good resolution is needed to ensure that the DC candidate has been correctly identified. The core resolution and angular resolution are shown in Figs. 6.4 and 6.5. The template analysis shows a greatly improved core resolution compared to the moment-based analysis. Requiring one or more DC pixel candidates further improves the resolution since
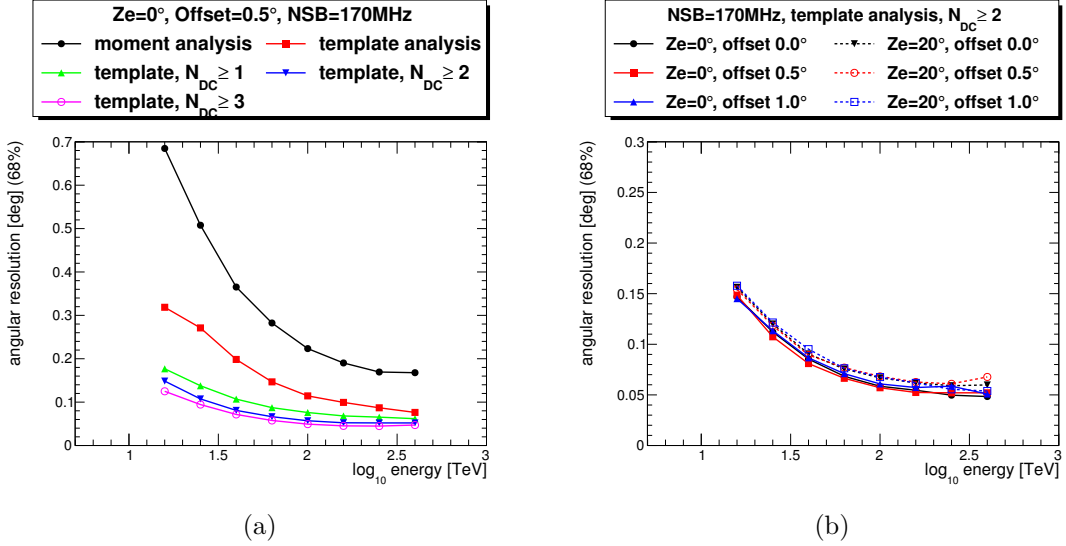
Figure 6.3: Energy resolution (68 % containment interval) versus energy (a) for different cut sets; (b) for different zenith angles and offsets from the camera center.

mis-reconstructed events are removed. For events with two or more DC candidate pixels (nominal cuts), the angular resolution is below 0.15° for energies above 20 TeV (which corresponds approximately the size of the VERITAS PMTs), and below 0.1° for energies above 30 TeV. This means we can be confident that the template-based analysis has identified the correct DC pixel candidates. The angular resolution depends only weakly on the zenith angle (it is about 0.01° worse for showers with a zenith angle of 20° compared to showers from zenith) and does not depend on the offset from the camera center.

Reconstructing the correct core position improves the separation between signal and background, because the intensity of the DC light depends on the distance from the shower core. Again, the template analysis improves the core resolution compared to the moment-based analysis. Requiring one or more DC pixel candidates further improves the core resolution. For showers from zenith, the core position is determined to 25 m or better for energies above 20 TeV and to 10 m or better for energies above 65 TeV. For showers with a zenith angle of 20°, the core resolution is worse by about 4 m.

Dependence of both angular resolution and core resolution on the night sky background noise level and azimuth of the shower direction were also tested and no strong dependence was found for dark sky conditions.

6.2.4 Number of Direct Cherenkov Pixel Candidates

The number of images with a DC pixel candidate, N_{DC} is a good discriminating variable. The distribution of N_{DC} for cosmic-ray simulations can be found in Fig. 6.6. For lower energies ($E < 50$ TeV), requiring two or more DC candidate pixels suppresses most of the background due to light and medium elements (hydrogen to oxygen). Heavier elements (represented here
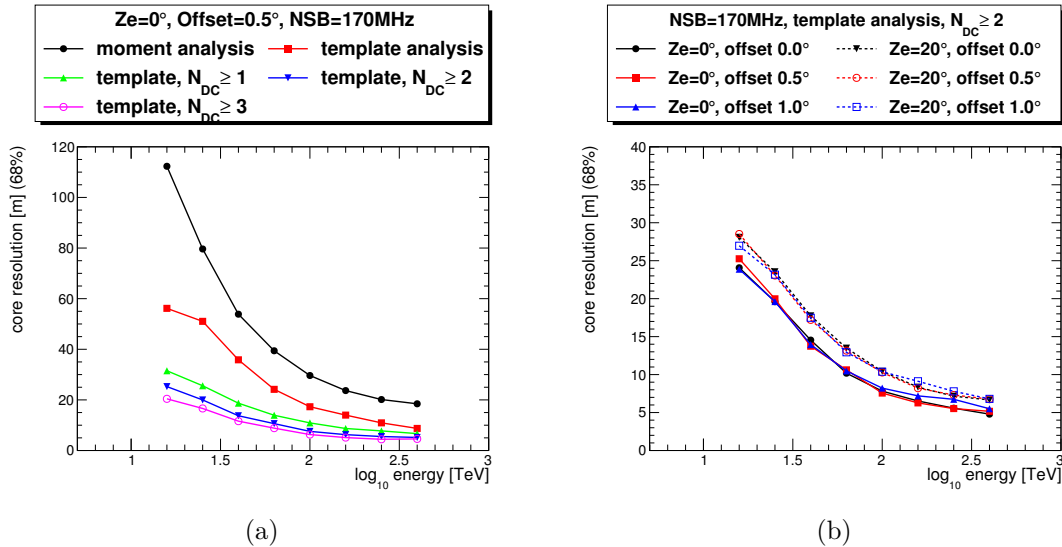
Figure 6.4: Core position resolution (68 % containment radius) versus energy (a) for different cut sets; (b) for different zenith angles and offsets from the camera center.

by magnesium and calcium) do emit real direct Cherenkov light themselves and are thus not suppressed by the requirement. For higher energies, there is also some contribution from light elements even when applying the $N_{DC} \geq 2$ requirement. Requiring more DC pixel candidates would further improve the purity of the sample, but at the cost of lowered statistics. It was decided to require $N_{DC} > 2$ for the final analysis.

6.2.5 Random Forest Performance

The random forest classifiers were trained as described in Section 5.4. Events were binned in five energy bins for the training, with bin limits at 20 TeV, 32 TeV, 50 TeV, 100 TeV, 200 TeV, 500 TeV. Table 6.1 shows the importance of each input variable depending on the energy bin. The *variable importance* is defined as the fraction of nodes in the random forest that apply a selection on a particular variable, weighted with the separation power of that selection. For low energies, the DC contribution $\sum I_{DC}$ and the average reconstructed charge $\langle Z_{\mathrm{reco}} \rangle$ are the most important input variables. For high energies, the goodness-of-fit and the uncertainty on the energy reconstruction by the likelihood fit are the best classifiers. The mean scaled width has good separation power in all energy bins.

For comparison between data and simulations as well as for the measurement of the iron spectrum, the first two energy bins were each split in two, giving a total of seven energy bins with bin limits at 20 TeV, 25 TeV, 32 TeV, 40 TeV, 50 TeV, 100 TeV, 200 TeV, 500 TeV. Figure 6.7 shows the distribution of the random forest response on an independent test sample, weighted to the expectations for data. For energies below 100 TeV, the random forests are very efficient at suppressing backgrounds due to light and medium elements and even magnesium. Calcium, the heaviest representative in the simulated background sample,

Figure 6.5: Angular resolution (68 % containment radius) versus energy (a) for different cut sets; (b) for different zenith angles and offsets from the camera center.

is not as well separated. For $E > 100$ TeV, there is also some magnesium remaining in the signal-like region. The light backgrounds are still well separated even at the highest energies.

The OFF interval was chosen to be $[-1.2, 0]$ and the ON interval as $[0.5, 1.2]$. The signal and background efficiencies (cf. Section 5.5) for the ON and the OFF cuts were evaluated for the signal and background samples and can be found in Table 6.2.

Figure 6.7 also shows that the shape of the random forest response is different for the different elements that make up the background sample. Such differences can also be seen in the distributions of the random forest input parameters (cf. Section C.3). It stands to reason that it would be possible to perform a cosmic ray composition measurement with a dedicated analysis trained to reconstruct the primary species rather than just separate iron from the other elements. However, as the template likelihood reconstruction uses templates generated for iron showers, the energy bias for the background samples is very large. Dedicated templates would be needed to perform a proper composition measurement, and this idea is not pursued any further in the current context.

6.3 Comparison of Different Interaction Models

To test the dependency of the analysis results on the hadronic interaction model, a second set of simulations was performed, using the Sibyll 2.1 interaction model (Engel, 1999) instead of QGSjet II-03, which was used for the nominal simulations. Due to the computing resources required, it was not possible to produce a full set of simulations. Instead, showers due to protons, helium, and iron nuclei were simulated and the resulting images analyzed as before, using templates, look-up tables, and random forest classifiers trained on QGSjet simulations.

The distributions of some event parameters can be seen in Section B.1. The Sibyll sample
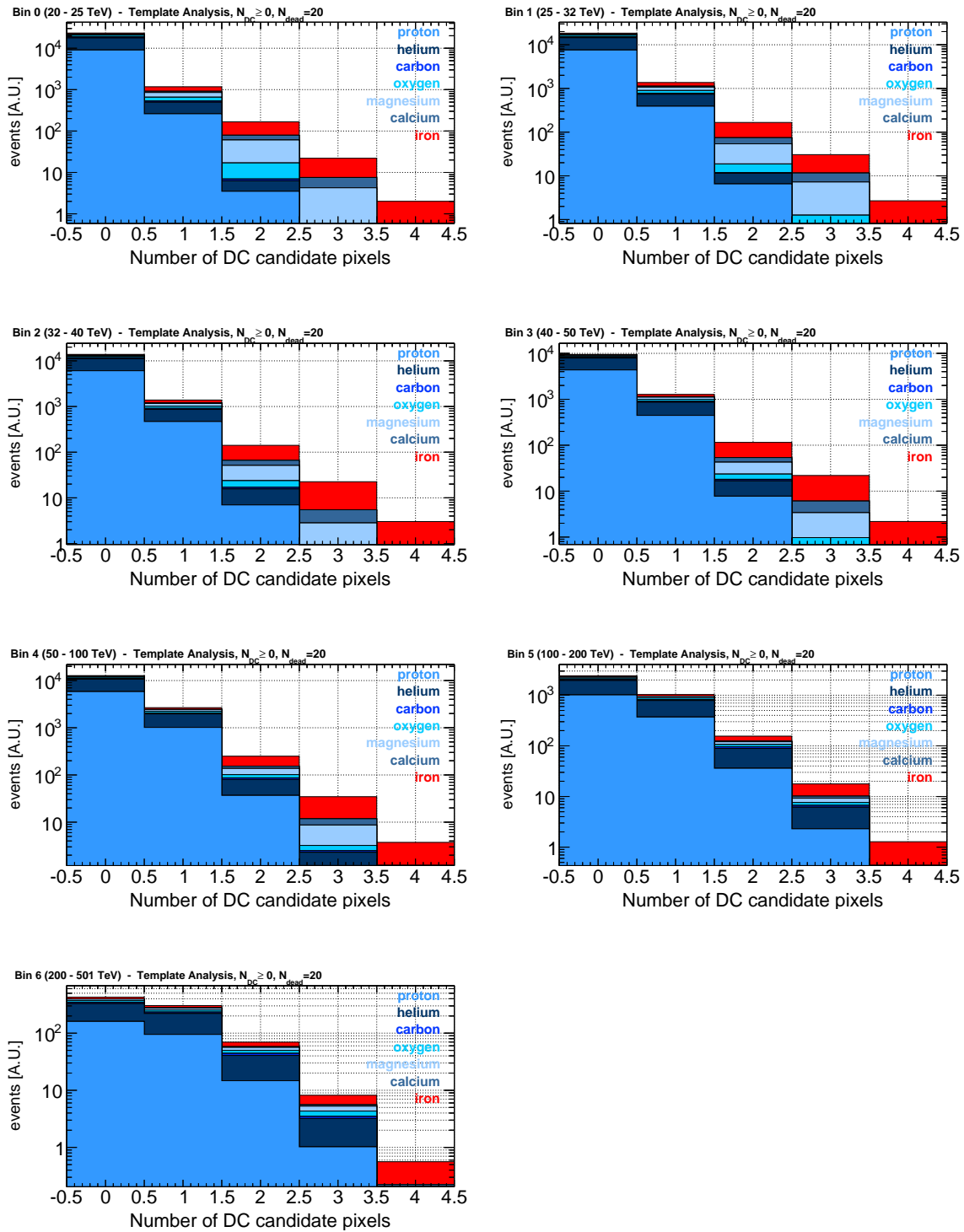
Figure 6.6: Number of images with a DC pixel candidate per event for simulations.
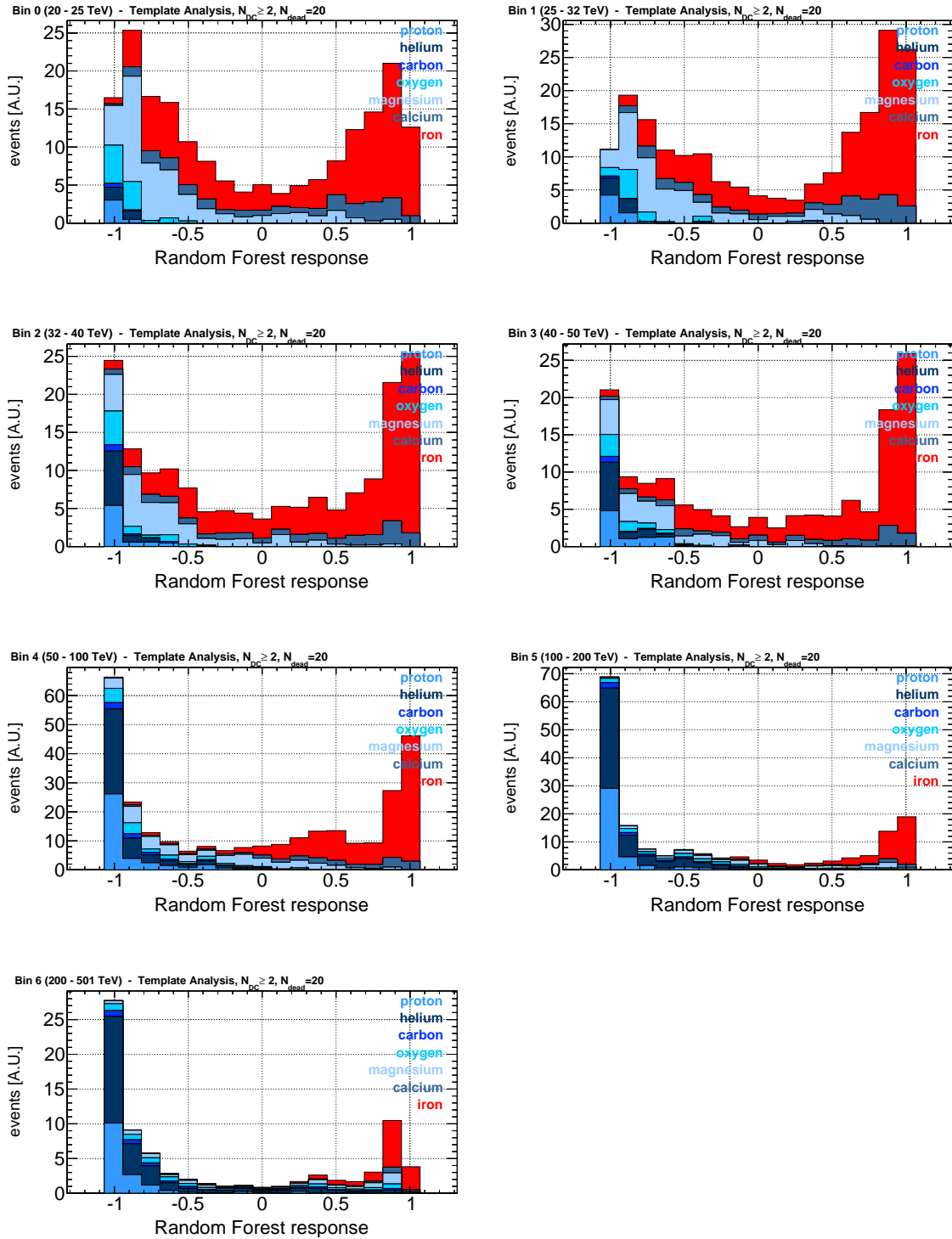
Figure 6.7: Response of the Random Forest classifier, trained on events with at least two DC pixel candidates, for simulations.

Variable	Bin 0	Bin 1	Bin 2	Bin 3	Bin 4
dES	0.019	0.014	0.005	0.002	0.001
$EmissionHeight$	0.067	0.019	0.005	0.003	0.002
$Energyerr$	0.027	0.037	**0.170**	**0.305**	**0.369**
$GoodnessImg$	0.027	0.005	0.079	**0.210**	**0.284**
$\log_{10}(\chi_E^2)$	0.005	0.003	0.005	0.001	0.001
$\log_{10}(\chi_H^2)$	0.014	0.003	0.002	0.009	0.003
$\log_{10}(size2nd)$	0.027	0.025	0.005	0.005	0.019
$MSCL$	0.016	0.037	0.044	0.012	0.002
$MSCW$	**0.102**	**0.157**	**0.240**	**0.275**	**0.227**
$\sqrt{XP^2 + YP^2}$	0.009	0.010	0.004	0.003	0.008
$\sum I_{DC}$	**0.262**	**0.258**	0.123	0.031	0.003
N_{DC}	0.009	0.005	0.015	0.035	0.041
$\sum q_{DC}$	0.049	0.102	0.083	0.046	0.008
$\langle Z_{\mathrm{reco}} \rangle$	**0.366**	**0.327**	**0.220**	0.063	0.032

Table 6.1: Importance of the input variables for the Random Forest classifiers. For each training energy bin, the three most important input variables have been marked in bold.

Bin	α_s	α_b	β_s	β_b	r_s	r_b
0	0.519	0.130	0.382	0.784	1.36	0.166
1	0.658	0.173	0.263	0.742	2.51	0.233
2	0.597	0.113	0.258	0.807	2.31	0.140
3	0.640	0.102	0.243	0.845	2.64	0.121
4	0.708	0.0644	0.0841	0.862	8.42	0.075
5	0.838	0.0646	0.0798	0.907	10.51	0.071
6	0.842	0.0987	0.0722	0.831	11.66	0.119

Table 6.2: Signal and Background efficiencies for the random forest classifier, per energy bin. See Section 5.5 for variable definitions.

has on average 10 % to 20 % more iron showers per energy bin than the QGSjet sample. The images tend to be a bit narrower and shorter (smaller $MSCW$ and $MSCL$) and have a larger reconstructed charge number.

These differences lead to differences in the random forest response distribution, which in turn changes the signal/background efficiencies. The efficiencies derived for the Sibyll simulations (still using QGSjet for the medium to heavy background elements, carbon to calcium) can be found in Table 6.3. Table 6.4 shows the ratio of the number of events per energy bin passing the quality cut and the $N_{DC} \geq 2$ requirement in the Sibyll and QGSjet samples.

Bin	α_s	α_b	β_s	β_b	r_s	r_b
0	0.521	0.1312	0.371	0.783	1.41	0.168
1	0.665	0.1645	0.249	0.765	2.67	0.215
2	0.633	0.1186	0.233	0.797	2.72	0.149
3	0.677	0.0965	0.207	0.853	3.27	0.113
4	0.674	0.0593	0.105	0.871	6.39	0.068
5	0.764	0.0613	0.126	0.912	6.08	0.067
6	0.788	0.0886	0.101	0.841	7.78	0.105

Table 6.3: Signal and Background efficiencies for the random forest classifier, evaluated on Sibyll simulations of protons, helium, and iron, per energy bin. See Section 5.5 for variable definitions.

Bin	R_{H}	R_{He}	R_{Fe}
0	*1.14	*0.42	1.20
1	*1.52	*0.63	1.16
2	*0.89	*0.73	1.20
3	*1.30	*0.88	1.16
4	1.13	1.20	1.10
5	1.13	1.08	1.10
6	1.14	1.14	1.03

Table 6.4: Ratio of the number of Sibyll-generated events with successful template reconstruction and at least two DC candidate pixels to the number of QGSjet II-03 generated events with the same requirements, per energy bin, for protons (H), helium (He), and iron (Fe). The values marked with an asterisk (*) refer to bins in which the results are not statistically significant due to the small number of surviving events.

6.4 Comparison of Data and Simulations

To validate the simulations, the distributions of several image parameters were compared between data and Monte-Carlo based simulations. Seven representative elements (H, He, C, O, Mg, Ca, Fe) were simulated and weighted to the expectations according to the spectra from Hörandel, J. R., (2003). See Chapter A for more details.

Simulations of iron showers with zenith angles of $0°$ and $20°$ in *wobble* mode (fixed offsets between shower direction and camera center) were used to derive lookup tables for energy reconstruction and mean scaled parameters. Simulations of all seven elements with zenith angle $0°$ in *diffuse* mode (random arrival directions within the camera) were used to train the random forest classifier, and to compare data and simulations. Half of the events were used for training, the other half for comparison.

The data set consists of 210 VERITAS runs with average zenith angles of $10°$ or less, taken between September 2009 and March 2012[1]. All runs were taken during 'winter' atmospheric conditions, clear skies, and no or low levels of moonlight. The night-sky background noise distribution in simulations was chosen to match the distribution in data.

In this section, a selection of data/MC comparison plots is shown. The full sample of plots can be found in Chapter C. Data is binned according to reconstructed energy[2].

6.4.1 Standard Analysis and its Parameters

Some parameters of the moment-based analysis are plotted in Section C.1. Generally, the shape of the distributions agrees well between data and simulations, but the normalization does not: There are 10% to 20% more data events than expected. For the highest energies, there is a significant difference in the shapes of the MSCW and MSCL distributions.

6.4.2 Template Analysis and its Parameters

After fixing the λ parameter, the results of the template likelihood analysis agree reasonably well with the data. There is one issue in particular with the number of DC candidate pixels. Independently of the normalization, the ratio of events with one or fewer DC pixel candidates to events with two or more DC candidate pixels differs between simulations and data.

For the sample of events with two or more DC candidate pixels, the simulations agree with the data, cf. Section C.3.

---

[1]after the T1 relocation and before the camera upgrade.

[2]Since the energy reconstruction is calibrated for iron showers, the reconstructed energy is generally much larger than the true energy for showers induced by light CRs such as protons and helium.

7 The Cosmic Ray Iron Spectrum

In this chapter, I will apply the template likelihood reconstruction method and the Random Forest classifiers described in Chapter 5 to VERITAS data and derive the energy spectrum of iron nuclei in cosmic rays. I will also list potential sources of the systematic uncertainty and evaluate their effect on the measured energy spectrum.

7.1 Data Selection

For this study, VERITAS data were selected according to the following requirements:

1. Detector configuration: Only data runs recorded between September 2009 and May 2012 were used. This correspnds to the *V5* period (after the T1 relocation, before the camera upgrade). Before the T1 relocation, the effective collection area of the array was much smaller, and in the data taken after the camera upgrade, there are issues with the PMTs and the signal chain being saturated by DC light.

2. Season: Only data runs recorded in winter-like months were used. Most of the available data was taken in winter, so it was decided to drop the summer data to reduce computing time (including summer data would have meant simulating twice the number of air showers).

3. Data quality: Only data runs taken under nominal observing conditions, with all four telescopes active, no hardware issues, and under clear, moonless skies were used.

4. Elevation: Only runs with an average elevation above $80°$ were used.

There were 210 data runs which pass all criteria, corresponding to $71\,\mathrm{h}$ livetime. The data were calibrated and analyzed following the procedures described in Section 4.4 and Chapter 5.

Bin	E_{min} [TeV]	E_{max} [TeV]	E_c [TeV]	N_{tot}	N_{on}	N_{off}	N_s	differential flux $\frac{\mathrm{d}N}{\mathrm{d}E\mathrm{d}A\mathrm{d}t\mathrm{d}\Omega}$ [cm^{-2} s^{-1} TeV^{-1} sr^{-1}]
0	20	25.1	22.4	192	75	102	127 ± 19	$(5.78 \pm 0.88) \cdot 10^{-6}$
1	25.1	31.6	28.2	189	76	105	86.3 ± 15.2	$(2.08 \pm 0.36) \cdot 10^{-6}$
2	31.6	39.8	35.5	171	51	103	65.3 ± 13.0	$(1.02 \pm 0.20) \cdot 10^{-6}$
3	39.8	50.1	44.7	147	45	95	54.9 ± 11.2	$(6.08 \pm 1.23) \cdot 10^{-7}$
4	50.1	100.	70.8	337	67	229	71.1 ± 11.8	$(1.52 \pm 0.25) \cdot 10^{-7}$
5	100.	200.	141.3	197	41	141	37.2 ± 7.8	$(4.03 \pm 0.84) \cdot 10^{-8}$
6	200.	500.	316.2	65	13	48	8.76 ± 4.44	$(3.12 \pm 1.56) \cdot 10^{-9}$

Table 7.1: Results of the energy-binned iron analysis. For each bin, E_c corresponds to the logarithmic bin center. N_{tot} is the total number of data events surviving the analysis cuts. N_{on} and N_{off} are the number of counts in the ON region (signal-like events) resp. OFF region (background-like events) in the RF response. N_s is the estimated number of iron events and $\frac{\mathrm{d}N}{\mathrm{d}E\mathrm{d}A\mathrm{d}t\mathrm{d}\Omega}$ the estimated differential flux.

7.2 Results

The events passing the analysis cuts were binned in energy and fed into the random forest discriminant. Table 7.1 lists the total number of events, the estimated number of iron events, and the differential flux for each energy bin. The spectral points are plotted in Figs. 7.1 and 7.2. The spectrum is well-fit by a power law of the shape:

$$\frac{\mathrm{d}N}{\mathrm{d}E\mathrm{d}A\mathrm{d}t\mathrm{d}\Omega} = f_0 \cdot \left(\frac{E}{E_0}\right)^{-\gamma}. \tag{7.1}$$

All points were included in the fit, covering the energy range from 20 TeV to 500 TeV. The normalization energy was chosen to be $E_0 = 50$ TeV. The best-fit parameter values were: $f_0 = (4.82 \pm 0.98) \cdot 10^{-7}$ cm^{-2} s^{-1} TeV^{-1} sr^{-1} and $\gamma = 2.82 \pm 0.30$.

These results are compatible within the statistic uncertainties with previous measurements of the iron spectrum using the direct Cherenkov technique (Aharonian et al., 2007; Wissel, 2010), but extend the measured spectrum to higher energies.
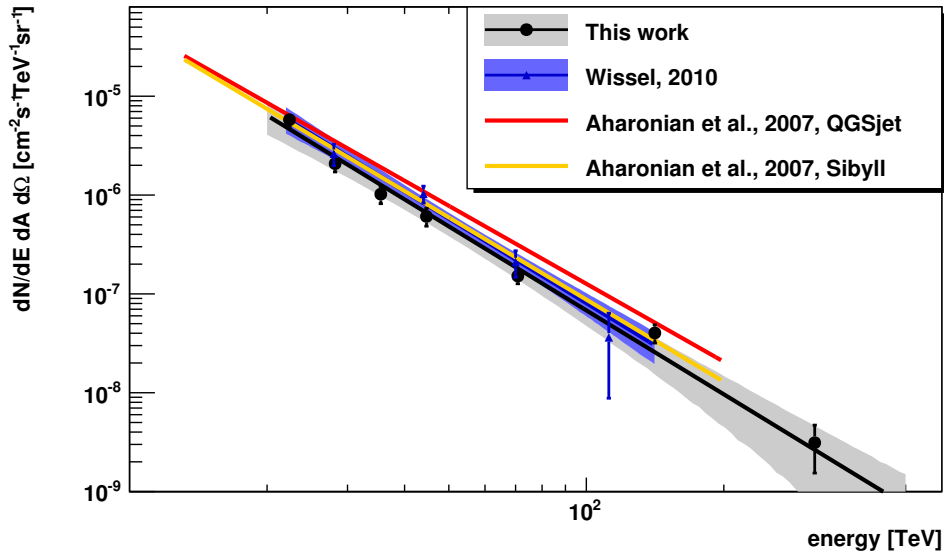
Figure 7.1: The energy spectrum of cosmic-ray iron nuclei as measured by the VERITAS experiment, compared to previous measurements by IACTs.
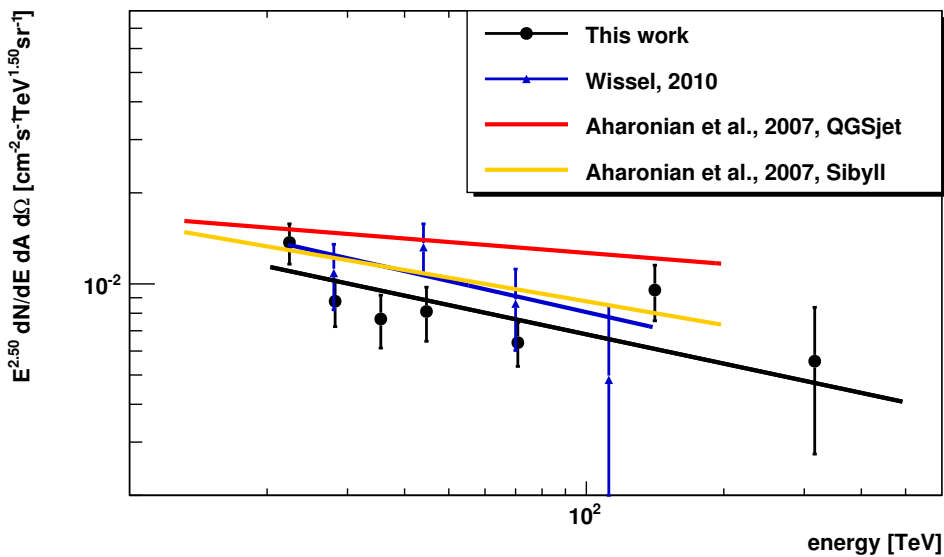
Figure 7.2: The energy spectrum of cosmic-ray iron nuclei as measured by the VERITAS experiment, compared to previous measurements by IACTS. Same data as in Fig. 7.1. The differential flux has been multiplied by $E^{2.5}$ to improve the visual clarity.
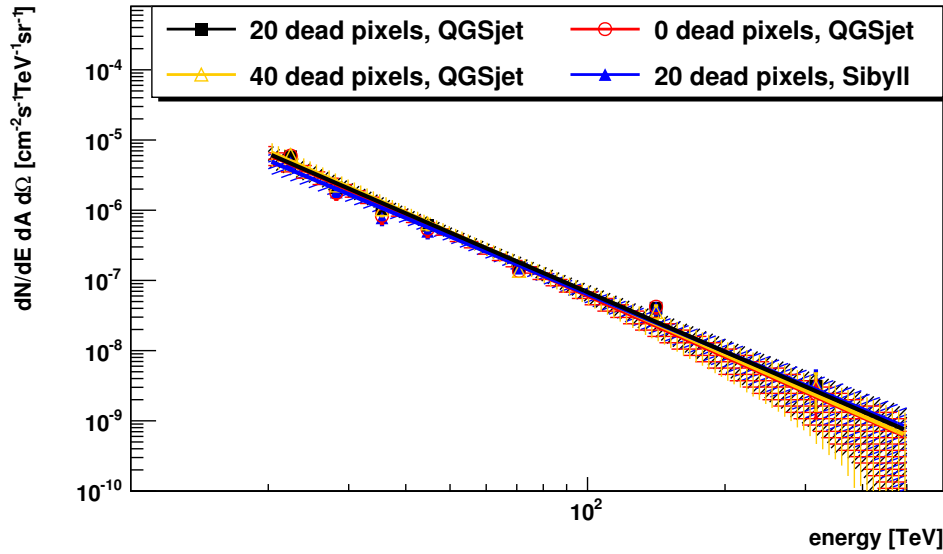
Figure 7.3: Effects of the number of simulated dead channels and on the hadronic interaction model on the cosmic-ray iron spectrum.

Simulations	N_{dead}	f_0 [$\mathrm{cm^{-2}\,s^{-1}\,TeV^{-1}\,sr^{-1}}$]	γ
QGSjet	0	$(4.48 \pm 0.91) \cdot 10^{-7}$	2.88 ± 0.29
QGSjet	**20**	$(4.82 \pm 0.98) \cdot 10^{-7}$	2.82 ± 0.30
QGSjet	40	$(4.88 \pm 1.02) \cdot 10^{-7}$	2.89 ± 0.31
Sibyll	20	$(4.22 \pm 0.82) \cdot 10^{-7}$	2.72 ± 0.28

Table 7.2: Effects of the number of simulated dead channels and on the hadronic interaction model on the cosmic-ray iron spectral fit parameters. In all cases, the spectrum is well described by a power law (see Eq. (7.1)) with $E_0 = 50\,\mathrm{TeV}$.

7.3 Sources of Systematic Uncertainty

7.3.1 Energy Bias

Atmosphere & Detector Model

There are numerous systematic uncertainties associated with the atmospheric model and the detector simulation. These uncertainties are common with the gamma-ray analysis; it is assumed here that they have the same effect on the iron spectrum as on the gamma-ray spectrum.

The effect of the variability of the atmosphere was assessed by simulating gamma-ray showers with atmospheric models corresponding to a particularly warm and a particularly cold week of all winter seasons from 2009 to 2012. The resulting showers were analyzed with the nominal lookup tables and were found to have an energy scale shifted by $\pm 10\,\%$ compared to nominal.
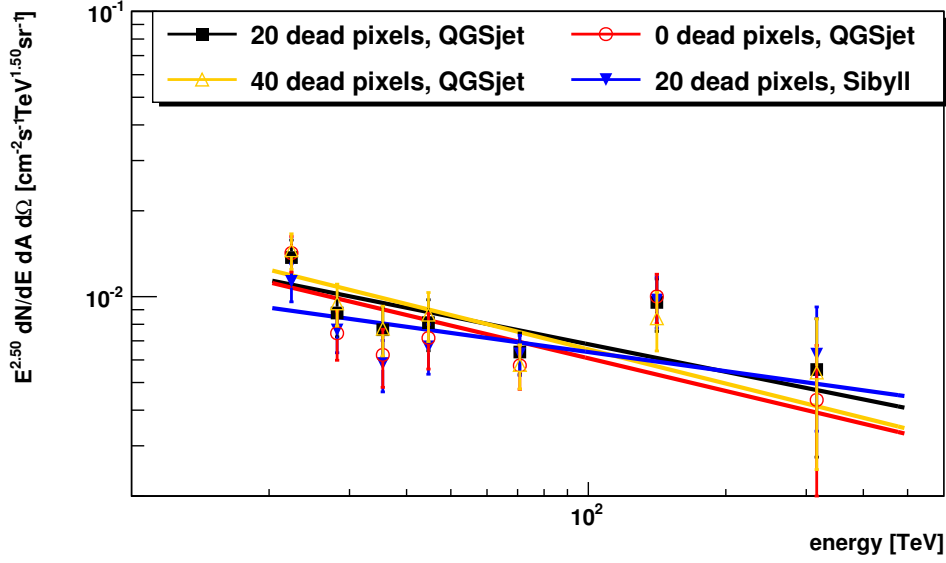
Figure 7.4: Effects of the number of simulated dead channels and on the hadronic interaction model on the cosmic-ray iron spectrum. The differential flux has been multiplied by $E^{2.5}$ to improve the visual clarity.

It is estimated that variations in the aerosol content can shift the energy by another $\pm 10\%$ independently of the variations in the density profile.

The dominant uncertainties related to the detector model are due to the mirror reflectivity. The reflectivity changes over time: Mirrors age and get dusty as they are in use. VERITAS mirrors are washed several times per season and batches of mirrors are removed for re-coating and replaced by freshly coated ones, restoring the reflectivity to the original levels. The average reflectivity over the 3-year time period in question is used for the simulations. The variation in reflectivity has been estimated to affect the energy scale by $\pm 10\%$. Other sources of uncertainty are due to the quantum efficiency of the PMTs, the collection efficiency of the first dynode in the PMT, the efficiency of the light cones, the modeling of the pulse shape, and the shadowing of the camera by the telescope structure. Altogether, the uncertainties listed here lead to a $\pm 20\%$ systematic uncertainty on the energy scale.

For a power law spectrum, a constant bias of the energy scale would not affect the measured spectral index, just the normalization. Let E be the true energy and $E_{\text{rec}} = (1 + b) \cdot E$ the reconstructed energy, where b is the constant bias. Then $E = \frac{E_{\text{rec}}}{1+b}$ and $\frac{dE}{dE_{\text{rec}}} = \frac{1}{1+b}$. Let the true spectrum be a power law with normalization constant N_0 at energy E_0 and index γ: $\frac{dN}{dE} = N_0 \cdot \left(\frac{E}{E_0}\right)^{-\gamma}$. Then the reconstructed spectrum is given by

$$\begin{aligned}
\frac{\mathrm{d}N}{\mathrm{d}E_{\mathrm{rec}}} &= \frac{\mathrm{d}N}{\mathrm{d}E} \cdot \frac{\mathrm{d}E}{\mathrm{d}E_{\mathrm{rec}}} \\
&= N_0 \cdot \left(\frac{E_{\mathrm{rec}}}{E_0 \cdot (1+b)} \right)^{\gamma} \cdot \frac{1}{1+b} \\
&= (1+b)^{\gamma-1} \cdot N_0 \cdot \left(\frac{E}{E_0} \right)^{\gamma}
\end{aligned}$$

For example, a $20\,\%$ uncertainty on the energy bias would leads to a $40\,\%$ uncertainty on the spectral normalization for a spectral index of 2.82.

It is also estimated that there is a systematic uncertainty on the spectral index of ± 0.2 due to these effects.

Energy Bias of the Template Analysis

If the energy bias is not constant, the measured spectral shape can be affected. In this case, the energy bias is approximately linear in $\log(E)$: $E_{\mathrm{rec}} = E \cdot \left(1 + b \cdot \log \left(\frac{E}{E_0'} \right) \right)$ for some normalization energy E_0' and linear term b. For example, the energy bias for iron showers with $0°$ $(20°)$ zenith angle approximately follows this log-linear relationship with $b = -0.2$ and $E_0' = 200\,\mathrm{TeV}$ $(50\,\mathrm{TeV})$, see Fig. 6.2.

In this case, there is no closed expression for $E\,(E_{\mathrm{rec}})$. However, we can write

$$\begin{aligned}
\frac{\mathrm{d}N}{\mathrm{d}E_{\mathrm{rec}}} &= \frac{\mathrm{d}N}{\mathrm{d}E} \cdot \frac{\mathrm{d}E}{\mathrm{d}E_{\mathrm{rec}}} \\
&= \frac{\mathrm{d}N}{\mathrm{d}E} \cdot \left(\frac{\mathrm{d}E_{\mathrm{rec}}}{\mathrm{d}E} \right)^{-1} \\
&= \frac{\mathrm{d}N}{\mathrm{d}E} \cdot \left(1 + b + b \cdot \log \left(\frac{E}{E_0} \right) \right)^{-1}
\end{aligned}$$

This function can be plotted by using E as a parameter and expressing both E_{rec} and $\frac{\mathrm{d}N}{\mathrm{d}E_{\mathrm{rec}}}$ in terms of E. See Fig. 7.5 for an example. The true spectrum was chosen as a power law with normalization constant $N_0 = 1$, normalization energy $E_0 = 50\,\mathrm{TeV}$, and index $\gamma = 2.5$.

The resulting reconstructed spectra are fit well by a power law with index $\gamma' = 2.6$ and normalization constant 1.45 (1.25) over the energy range considered here. The reconstructed spectrum is softer than the true spectrum by about $\Delta\gamma \approx 0.1$.

For a log-linear energy bias as described here, the shift in the measured spectral index depends on the linear term b, while the shift in the normalization depends on the energy at which the bias vanishes.

For the analysis presented here, the effect of the energy bias is partially mitigated by the effective area, which is determined according to the *reconstructed* energy, not the true energy. To be conservative, we still estimate that the energy bias due to the analysis method results in a systematic uncertainty of $^{+0}_{-0.1}$ on the spectral index and $^{+0\,\%}_{-30\,\%}$ on the normalization.
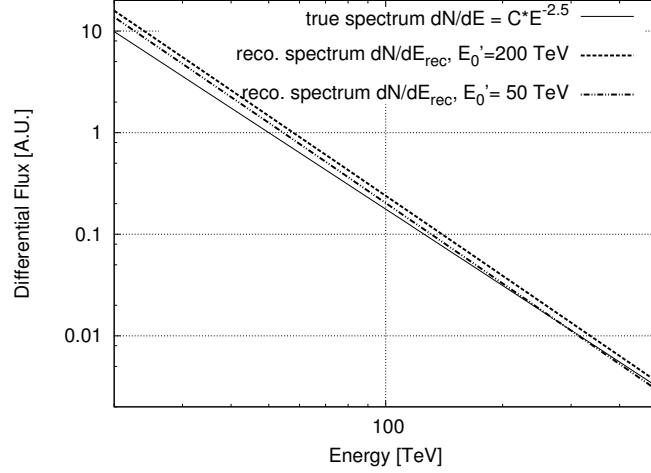
Figure 7.5: Toy study to estimate the effect of a log-linear energy bias on the reconstructed spectrum. See text for details.

7.3.2 Dead Pixels in the Camera

Pixels in the VERITAS camera may be turned off either temporarily (high currents due to bright starlight) or for a longer time (broken PMTs/cables, issues with the FADC channel). These pixels are not used in the analysis and this can affect image parameters such as the *length* and *width*. Also, the identification of DC pixel candidates is affected: If the DC light lands on a 'dead' pixel, the correct DC pixel candidate cannot be identified. In the data set studied here, the number of dead pixels per camera ranged from 6 to 49 per camera, with an average of 18 dead pixels per camera. In the simulations used for the nominal analysis (training and evaluation of random forests, calculation of effective areas), 20 pixels were turned off per camera. The entire procedure was repeated with 0 and 40 dead pixels per camera in the simulation (look-up tables were not changed). The resulting energy spectra are plotted in Figs. 7.3 and 7.4 adn the results of the spectral fit can be found in Table 7.2. The effect on the energy spectrum is smaller than the statistical uncertainty of the fit. The normalization changes by $\leq 7\%$ and the index by ≤ 0.07. We use these values as a conservative estimate of the systematic uncertainties due to the number of dead channels.

7.3.3 Hadronic Interaction Model

Due to the large computing requirements, it was not possible to re-do all simulations with a different interaction model. Instead, a *Sibyll*-based spectrum was calculated as follows. First, in the BDT testing sample (used to determine the ON/OFF ratios), the proton, helium, and iron samples were replaced with simulations based on Sibyll, and new ON/OFF ratios were calculated (cf. Table 6.3). Second, the effective areas used in each energy bin were adjusted by the ratio of the number of Sibyll events passing the cuts over the number of QGSjet events passing cuts (c.f. Table 6.4). The resulting spectrum can be seen in Figs. 7.3 and 7.4.

Cause	Effect on N_0	Effect on γ
Atmosphere + detector model	$\pm 40\,\%$	± 0.2
Dead pixels	$\pm 7\,\%$	± 0.07
Intrinsic energy bias	$^{+0\,\%}_{-30\,\%}$	$^{+0.0}_{-0.1}$
Effective area	$\pm 10\,\%$	—
Interaction Model	$\pm 12\,\%$	± 0.1
Remaining Background	$^{+0\,\%}_{-15\,\%}$	—
Total	$^{+44\,\%}_{-55\,\%}$	$^{+0.23}_{-0.25}$

Table 7.3

The index is harder than the nominal spectrum by about 0.1 and the normalization is lower than the nominal spectrum by about $12\,\%$. We estimate the uncertainty due to the hadronic interaction model to be $\Delta\gamma = \pm 0.1$ and $\Delta f_0 = \pm 12\,\%$.

7.3.4 Effective Area

As described in Section 6.2.1, the effective collection area is determined from Monte-Carlo simulations. A statistical uncertainty on the effective area exists due to limited shower statistics. It is below $10\,\%$ for all energy bins. To be conservative, we estimate a $10\,\%$ systematic uncertainty on the flux normalization due to this effect.

7.3.5 Remaining Background

Elements up to chromium ($Z = 24$) were accounted for in the background sample. According to Hörandel, J. R., (2003), manganese ($Z = 25$) has a flux of about $10\,\%$ of the iron flux in the energy range under study here, and nickel ($Z = 28$) has a flux of about $7\,\%$ of the iron flux. All other elements can be neglected ($< 1\,\%$ of the iron flux). Assuming that showers induced by manganese and nickel have similar properties as iron does, the measured 'iron' flux may be contaminated by up to $15\,\%$ Manganese and Nickel. This is assigned as an additional systematic uncertainty.

7.3.6 Combined Systematic Uncertainty

All sources of systematic uncertainty investigated here are listed again in Table 7.3. They are independent of each other and can be added in quadrature. The resulting final measurement of the parameters of the cosmic ray iron spectrum are thus:

$$f_0 = \left(4.82 \pm 0.98(\text{stat.})^{+2.12}_{-2.65}(\text{syst.})\right) \cdot 10^{-7}\,\text{cm}^{-2}\,\text{s}^{-1}\,\text{TeV}^{-1}\,\text{sr}^{-1}$$

$$\gamma = 2.82 \pm 0.30(\text{stat.}) \pm^{+0.23}_{-0.25}(\text{syst.})$$

7.4 Conclusion

I have presented a novel method for the reconstruction of cosmic-ray induced showers, and applied this method to the measurement of the energy spectrum of iron nuclei in cosmic rays. The measured spectrum between 20 TeV to 500 TeV is well described by a power law and agrees with previous measurements within the statistic and systematic uncertainties.

There were two main innovations with respect to previous measurements of the iron spectrum using direct Cherenkov light: the template likelihood method to reconstruct the energy and arrival direction of the primary particle, and the random forest classifier for signal/background separation and estimation of the signal content. The template reconstruction led to an improved energy resolution as well as improved identification of direct Cherenkov pixels. Using a random forest classifier meant that I was able to retain more signal events while still suppressing most of the background.

The combination of template reconstruction and random forest classifier is especially useful for the identification of iron nuclei with energies of several hundred TeV. At these energies, light from the air shower starts to 'drown out' the direct Cherenkov light, making it harder to rely on the direct Cherenkov emission to identify heavy elements. Here, other quantities such as the goodness-of-fit from the template reconstruction, can really improve background rejection. With the increased statistics and the improved background rejection above 100 TeV, I was able to extend the energy range of the measurement up to 500 TeV, with no measurable deviation from a power law spectrum.

The template likelihood reconstruction, and especially its application to cosmic-ray analyses, is still very new. Several issues with the template reconstruction remain. However, this study does present a viable *proof-of-concept* which shows that this method is promising and should definitely be considered for future studies.

The most pressing problem with the template likelihood fit is certainly the reconstruction of the first interaction height. This parameter was the least constrained in the fit (it is somewhat degenerate with the primary energy) and was not stable against changes in the random seed used for the minimization algorithm. In addition, the distribution of the best-fit first interaction height in simulations did not match data. In this study, the issue was fixed by fixing the first interaction height during the likelihood fit. This improved the agreement between data and simulations, but worsened the energy resolution.

The other issue is the energy bias, in particular the energy dependence of the energy bias, especially when requiring one or more direct Cherenkov pixels. If the energy bias changes with energy, it can distort the measured spectrum.

Last but not least, the analysis presented here relies heavily on simulations for reconstruction, signal/background separation, and estimation of the remaining background. It was attempted to mitigate the latter by using the ratio of signal-like to background-like events in data to estimate the number of signal and background events. This approach does not rely

on the total normalization of the background in simulations, but does require correct relative normalization of the background samples.

In spite of these issues, the dominant sources of uncertainty on the iron spectrum are ones that are common to the gamma-ray analyses: the variations of atmospheric conditions and detector properties (e.g., change of mirror reflectivity over time). This could only be improved by modeling the atmosphere over shorter time scales, and simulating showers with a lot of different atmospheric conditions.

7.5 Outlook

The measurement of the iron spectrum, as presented here, provides a *proof-of-concept* for the template likelihood analysis combined with a random forest classifier. Further developments are needed to utilize the full potential of this method.

Certainly, the issues with the template likelihood analysis described above will have to be investigated and resolved. The energy bias, which is likely caused by selection effects, may be mitigated by employing an unfolding algorithm. The fit of the first interaction height could be stabilized by improving the minimization algorithm, or maybe some other way of estimating the first interaction height could be found and used as a starting value for the fit. The measurement of the first interaction height, if made to work, was a very important reason for developing the template likelihood reconstruction method for cosmic-ray showers because it will eventually enable us to measure the cosmic-ray/air cross sections independently of accelerator experiments.

Going one step further, it should be possible to extend the template likelihood method to also reconstruct the 'species' of the primary particle. The simultaneous fit of the primary charge/mass, energy, and first interaction height, coupled with other image parameters such as width/length and possible direct Cherenkov emission, would enable us to measure the energy-dependent composition (or charge-dependent energy spectra) of cosmic rays, as well as to validate (or invalidate) the predictions of hadronic interaction models.

Improvements in experimental technology will further extend the energy range of cosmic ray measurements. For example, the new gamma-ray observatory CTA (Actis et al., 2011), currently being built at two sites in Chile and Spain, will feature two arrays that are larger than any current instruments, Cherenkov telescopes with three different mirror sizes, better optical resolution and smaller pixels. The large sized telescopes will collect more light than the VERITAS telescopes, which should help extend cosmic ray measurements to lower energies. CTA can improve upon the measurements presented here in several ways. For example, with a better optical resolution and smaller pixels, it will be easier to separate the direct Cherenkov contribution from the shower light because there will be less 'contamination' in the DC pixel. The large number of small sized telescopes will help collect more events, which should improve measurements at higher energies. One caveat that needs to be made is that the direct Cherenkov method can not readily be extended to lower or much higher

energies. For example, for iron below 20 TeV, there is a large chance that the nucleus will interact before it starts emitting Cherenkov light. For energies above 800 TeV or so, it will be impossible to pick out the DC component from the rest of the shower (the exact limit depends on the detector configuration). However, as has been shown in this study, it is possible to achieve good charge identification by using other parameters, such as the shower shape or the goodness-of-fit. In fact, relying mostly on shower shape parameters and goodness-of-fit, one could extend the analysis to larger zenith angles, for which the emission of DC light is less probable, and thus further increase the statistics at high energies.

In the end, an improved measurement of the iron spectrum with better energy resolution and finer spectral points would be very interesting. While the heavy knee at ~ 100 PeV is out of reach for IACTs, with a better energy reconstruction we should be able to see features in the spectra, such as the hardening above 200 GeV nucleon^{-1}, as observed by CREAM and other experiments.

8 Limits on the Gamma-Ray Emission from Star-Forming Galaxies

In this chapter, VERITAS observations of the three star-forming galaxies Arp 220, IRAS 17208-0014 and IC 342 are presented. No excess in gamma-ray like events over the background expectation is found and upper limits on the gamma-ray flux are derived. The results shown here are an updated version of the study presented it the International Cosmic Ray Conference 2015 (Fleischhack et al., 2016b). The results presented here include an additional three hours of data taken on IRAS 17208-0014 in 2015.

8.1 Estimation of the Expected Flux

8.1.1 VHE-FIR correlation

So far, only two star forming galaxies have been detected in VHE gamma rays: M82 (Acciari et al., 2009) and NGC 253 (Abramowski et al., 2012). This sample size is too small to investigate the possible correlation between gamma-ray luminosity and star formation rate. However, assuming that this correlation exists, we can estimate the expected gamma-ray flux of other star-forming galaxies, given the measured VHE flux F^{VHE} of a star-forming galaxy as well as the star formation rates and luminosity distances D_{L}. In the following, the luminosity in the far infra-red, L^{FIR}, is used as a proxy for the star formation rate (cf. Section 1.4.5). Out of the two star-forming galaxies detected at very high energies, M82 has a slightly larger calorimetric fraction (Lacki et al., 2011). Thus, the VHE gamma-ray flux of M82 as measured by VERITAS is used for the extrapolation.

Assuming a simple linear relationship between the far infrared (FIR) and VHE regime, we obtain

$$F^{\mathrm{VHE}} = \frac{L^{\mathrm{FIR}}}{D_L^2} \cdot \frac{D_{L,\mathrm{M82}}^2 \cdot F_{\mathrm{M82}}^{\mathrm{VHE}}}{L_{\mathrm{M82}}^{\mathrm{FIR}}}.$$

Using this relation, the expected VHE flux has been calculated for the three galaxies Arp 220, IRAS 17208-0014, and IC 342 and are listed in Table 8.1. These numbers are meant to provide a very rough estimate of the VHE gamma-ray flux. In particular, the linear relationship only holds as long as all galaxies have a similar calorimetric efficiency. M82 has been estimated to have a calorimetric efficiency of 0.3 to 0.4 (Lacki et al., 2011). If Arp 220

indeed has a calorimetric efficiency of close to unity, which now seems likely given the Fermi detection (Griffin et al., 2016; Rojas-Bravo & Araya, 2016), then its flux could be enhanced by a factor of 2 to 3 compared to Table 8.1. The same is true for IRAS 17208-0014, which also has a very high ISM density. IC 342, on the other hand, has a lower star formation rate and probably has a similar calorimetric efficiency to M82.

An additional source of uncertainty comes in due to the uncertainty on the measured VHE flux from M82. The 30% uncertainty on the normalization and the ±0.6 uncertainty on the index lead to an uncertainty of 37% on the prediction of the flux from Arp 220.

8.1.2 Spectral Extrapolation

As Arp 220 has been detected in HE gamma rays, we can extrapolate the measurements of the HE gamma-ray flux to estimate the flux in the VHE regime, assuming a power-law energy spectrum $\frac{\mathrm{d}F}{\mathrm{d}E} = f_0 \cdot \left(\frac{E}{E_0}\right)^{-\gamma}$. The integral flux $F(E_1 < E < E_2)$ in the energy range $E1 - E2$ is then given by

$$F(E_1 < E < E_2) = \frac{E_0 f_0}{\gamma - 1} \left(\left(\frac{E_1}{E_0}\right)^{1-\gamma} - \left(\frac{E_2}{E_0}\right)^{1-\gamma} \right) \approx \frac{E_0 f_0}{\gamma - 1} \left(\frac{E_1}{E_0}\right)^{1-\gamma}.$$

The approximation holds for $\gamma > 1$ and $E_1 \ll E_2$.

From this, we find

$$F(E > E_{\mathrm{VHE}}) \approx F(E > E_{\mathrm{HE}}) \cdot \left(\frac{E_{\mathrm{VHE}}}{E_{\mathrm{HE}}}\right)^{1-\gamma}$$

The extrapolation of the *Fermi*-LAT measurements to the flux above 500 GeV is given in Table 8.1, assuming the nominal values of the flux normalization and spectral index. Taking the full range of uncertainties into account, we obtain a range of $1 \cdot 10^{-10}\,\mathrm{m}^{-2}\mathrm{s}^{-1}$ to $2 \cdot 10^{-9}\,\mathrm{m}^{-2}\mathrm{s}^{-1}$ from extrapolating the measurement of Peng et al., (2016), and a range of $3 \cdot 10^{-11}\,\mathrm{m}^{-2}\mathrm{s}^{-1}$ to $4 \cdot 10^{-8}\,\mathrm{m}^{-2}\mathrm{s}^{-1}$ from extrapolating the measurement of Griffin et al., (2016).

8.1.3 Theoretical Models of Arp 220

The ultra-luminous infrared galaxy (ULIRG) Arp 220, has been the subject of intense modeling effort by several groups (Lacki et al., 2010; Torres, 2004; Yoast-Hull et al., 2015; Torres & Domingo-Santamaría, 2005). All predict a power-law energy spectrum with an index of approximately 2.2 in the VHE range, with a possible cutoff at a few TeV due to absorption. However, there is less agreement on the normalization. The predictions if the total flux above 500 GeV range from $5 \cdot 10^{-11}\,\mathrm{m}^{-2}\mathrm{s}^{-1}$ to $4 \cdot 10^{-9}\,\mathrm{m}^{-2}\mathrm{s}^{-1}$, cf. Table 8.2. It should be noted that Torres, (2004) originally predicted a slightly higher flux of $8\,\mathrm{nm}^{-2}\mathrm{s}^{-1}$ above 500 GeV, but now consider this too high because the parametrization of the inelastic proton cross sec-

Object	$\mathbf{D_L}$ [kpc]	$\mathbf{L}_{8-1000\mu m}$ [$10^{10} \cdot L_\odot$]	$\mathbf{E}_{min}$ [GeV]	Flux ($\mathbf{E} > \mathbf{E}_{min}$) [m^{-2}s^{-1}]
M82	3.4	4.6	700	$(3.7 \pm 1.0) \cdot 10^{-9}$
IC342	3.7	1.4	500	$1.6 \cdot 10^{-9}$
Arp 220	74.7	140	500	$4 \cdot 10^{-10}$
IRAS 17208-0014	173	230	600	$1 \cdot 10^{-10}$
Arp 220, extrapolating Peng et al., (2016)			500	$5 \cdot 10^{-10}$
Arp 220, extrapolating Griffin et al., (2016)			500	$1.1 \cdot 10^{-9}$

Table 8.1: Predictions for the VHE flux of three starburst galaxies, based on the VHE flux of M82 (Acciari et al., 2009) and on the HE flux of Arp 220. Luminosity distances L_D and FIR luminosities L_{FIR} are taken from Ackermann et al., (2012b). A common spectral index of -2.5 was assumed for all sources, consistent with the M82 measurements and the expectations for other star forming galaxies. For the extrapolation of the Arp 220 flux, the measured spectral index was used.

Reference	$\mathbf{E}_{min}$ [GeV]	$\mathbf{E}_{max}$ [GeV]	Flux ($\mathbf{E}_{min}$ to $\mathbf{E}_{max}$) [m^{-2}s^{-1}]
LTQ, increased wind, B-field	500	—	* $4 \cdot 10^{-9}$
LTQ, standard parameters	500	—	* $1.5 \cdot 10^{-9}$
TD, Blattnig pp cross section	500	—	$8 \cdot 10^{-9}$
TD, Aharonian pp cross section	500	—	$2 \cdot 10^{-9}$
YGH, most optimistic	500	3000	$2 \cdot 10^{-10}$
YGH, most pessimistic	500	3000	$5 \cdot 10^{-11}$

Table 8.2: Predictions for the integral flux of Arp 220 in the VHE range. LTQ refers to Lacki et al., (2010), TD to Torres & Domingo-Santamaría, (2005), and YGH to Yoast-Hull et al., (2015). The two values marked with an asterisk (*) were interpolated from the predictions of the fluxes above 300 GeV and above 1 TeV, assuming a power-law spectrum.

Source	Observing period [MJD]	Livetime [h]	Mean zenith angle [°]
Arp 220	$55978 - 56046$	31	16
IRAS 17208-0014	$55678 - 57168$	17	34
IC342	$55528 - 55572$	3	37

Table 8.3: Overview over VERITAS data analyzed for this study.

tion they used over-estimated the amount of high-energy pions that were produced. This prediction is still included in the table to show the magnitude of this effect: The predictions from an updated model of proton-proton interactions are lower by a factor of four.

8.2 VERITAS Observations and Data Analysis

The VERITAS data sets that were analyzed for this study are summarized in Table 8.3. All data were taken in *wobble* mode, with the tracking position offset from the targets by 0.5°, and after the T1 relocation. The data set on Arp 220 comprises 31 h, taken in February – April 2012, before the camera upgrade. The data set on IRAS 17208-0014 comprises 17 h. The majority (14 h) were taken between April 2011 and March 2012, also before the camera upgrade. An additional 3 h were taken in May 2015. The IC 342 data set comprises 3 h taken between November 2010 and January 2011. Only data taken under clear sky conditions, no or low moonlight, and with all four telescopes operating were selected.

All data were analyzed with the *eventdisplay* package by the author, using the Hillas-based standard analysis. As is customary in the VERITAS collaboration, independent secondary analyses were conducted with the *VEGAS* package, which confirmed the results presented here.

Eventdisplay provides instrument response functions for several sets of gamma/hadron separation cuts, optimized for different source strengths/spectral shapes. For this analysis, two sets of box cuts (*moderate* and *hard*) were used. Box cuts apply requirements on the mean scaled parameters (width and length) independently. The main difference between the cut sets is the cut on the *size* (total signal): *moderate* cuts require at least two images with a *size* of at least 400 d.c. (600 d.c.) before (after) the camera upgrade, whereas *hard* cuts require at least two images with a *size* of at least 1000 d.c. (1400 d.c.) before (after) the camera upgrade.

The *size* cut affects the energy threshold of the analysis as well as the signal and background rates. Hard cuts give the best background suppression, but at the cost of a low signal rate and high energy threshold. Thus, they are most appropriate for sources with hard spectra (index of -2.5 or harder) or long exposures on weak sources. Soft cuts (not used for this study) give the lowest possible energy threshold, at the cost of a large background rate. They are appropriate for very soft sources and/or short exposures on bright sources, for which

Source	E_{min} [GeV]	N_{ON}	N_{OFF}	α	$A_{eff} \cdot T$ [m² s]	Flux ($E > E_{min}$) [m⁻²s⁻¹]
Arp 220	500	45	282	0.17	$8.35 \cdot 10^9$	$\leq 2.24 \cdot 10^{-9}$
IRAS 17208-0014	600	16	124	0.17	$4.76 \cdot 10^9$	$\leq 1.82 \cdot 10^{-9}$
IC 342	500	37	174	0.18	$940 \cdot 10^6$	$\leq 27.6 \cdot 10^{-9}$

Table 8.4: Upper limits (99% confidence level) on the integral flux from the three star-forming galaxies studied here. A power law spectrum with an index of $\gamma = 2.5$ has been assumed for all sources.

background suppression is not critical. Moderate cuts provide a reasonable compromise between good background suppression and a low energy threshold.

For the flux estimates, the radius of the signal region was chosen to be 0.09°, corresponding to the expected angular resolution. See Section 5.7 for more details about the analysis, particularly the flux estimation and the estimation of the expected limits.

8.3 Results

Data taken on the three star-forming galaxies were analyzed with two cut sets (moderate and hard box cuts). None of the objects showed a significant excess of gamma-ray like events above the background expectation. Skymaps showing the excess event count (difference between signal and background expectations) and the significance of these excesses in the field of view can be found in Figs. D.1, D.3 and D.5 in the appendix. All distributions are compatible with the background-only hypothesis.

As no evidence for gamma-ray emission was found, upper limits on the flux were derived. First, *expected* upper limits were calculated from the background counts for different energy thresholds to find the cut set and energy threshold that give the most sensitive limits compared to the flux estimates. Note that the energy threshold for the flux calculation is limited by the analysis energy threshold, which depends on the cut set and the zenith angle under which the observations were taken.

The expected upper limits can be found in Figs. D.2, D.4 and D.6 in the appendix. All limits were evaluated under the assumption of a power law energy spectrum with index 2.5. Hard cuts provide slightly more sensitive limits on Arp 220 and IRAS 17208-0014 compared to moderate cuts, while for IC 342 the difference is negligible due to the smaller exposure. Choosing a larger energy threshold for the flux estimate does not improve the sensitivity. Thus, the upper limits were finally evaluated for hard cuts for Arp 220 and IRAS 17208-0014 and for moderate cuts for IC 342. The energy thresholds were 500 GeV for Arp 220 and IC 342 and 600 GeV for IRAS 17208-0014. The upper limits can be found in Table 8.4.

8.3.1 Uncertainties

Two sources of uncertainty will be taken into account here: The shape of the source spectrum and the detector response (energy scale/effective collection area).

The shape of the source spectrum affects VERITAS' effective collection area. Since no VHE gamma-ray emission was measured, the source spectrum is a priori unknown. However, it is expected that the gamma-ray emission from star forming galaxies follows the cosmic-ray spectrum (Lacki et al., 2011; Torres & Domingo-Santamaría, 2005; Lacki et al., 2010; Torres, 2004). Accordingly, the gamma-ray emission is expected to follow a power law with an index of 2 to 2.5. There can be deviations from this power-law behavior due to absorption in the host galaxy or by the extra-galactic background light (EBL), which would soften the spectra at the highest energies. Due to the relatively small distances, EBL absorption can be neglected in the VERITAS energy range (below some tens of TeV). Absorption in the host galaxy can lead to a cut-off at a few TeV.

VERITAS's spectral weighted effective collection area increases for harder sources. Accordingly, the limits presented here assume a spectral index of -2.5, at the softer end of the expectations. A harder index would imply a larger effective area, and thus more constraining limits for the same event counts.

If there were indeed a cutoff, we would over-estimate the effective collection area. For example, Yoast-Hull et al., (2015) predict a cutoff in the emission from Arp 220 for energies above 2 TeV to 5 TeV. For an energy threshold of 500 GeV and a spectral index of -2.5 (-2.0), only 13 % (25 %) of the gamma-ray photons would have energies above 2 TeV and could potentially be affected by absorption. The presence of such a cutoff would affect the upper limit by less than 25 %.

The uncertainty on the VERITAS energy scale is about 20 %. The main contributions to this uncertainty arise from variations in the atmospheric density and aerosol profiles, mirror degradation, and uncertainty on the PMT quantum efficiency. For a spectral index of -2.5, a 20 % uncertainty on the threshold energy corresponds to an uncertainty of 30 % on the integral flux.

8.4 Summary and Conclusions

It is expected that star-forming galaxies emit gamma-ray photons up to very high energies, and that the gamma-ray luminosity is correlated with the rate of star formation and thus the infrared luminosity. This is supported by the detections of M82 and NGC 253 in the VHE regime and of several star-forming galaxies, most recently Arp 220, in the HE regime, support this idea.

VERITAS searched for gamma-ray emission above 500 GeV from the three galaxies Arp 220, IRAS 17208-0014, and IC 342. No gamma-ray emission was detected and the derived
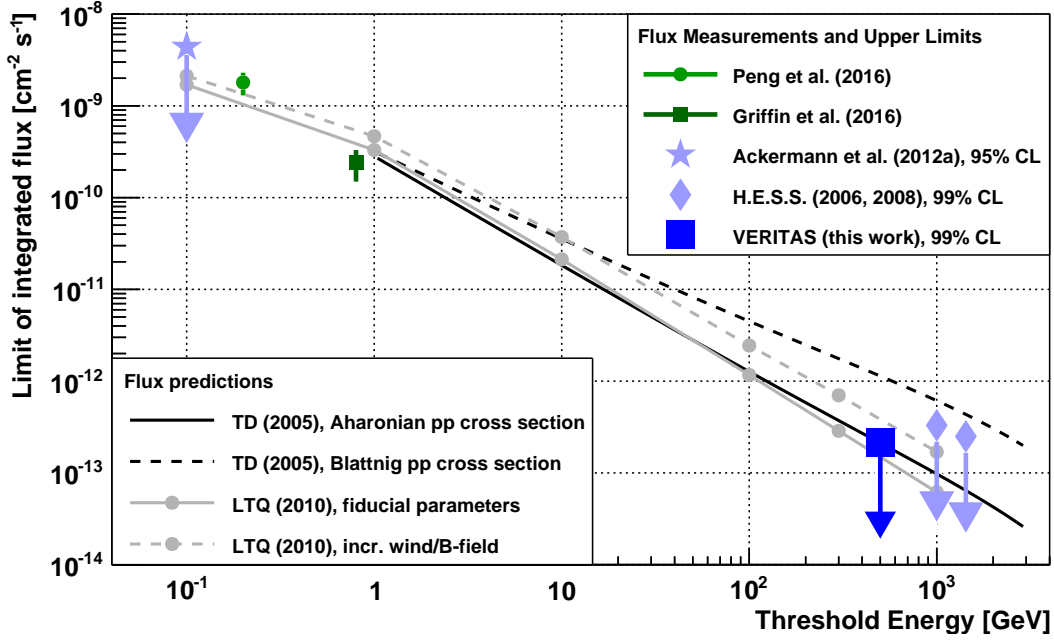
Figure 8.1: Upper limits and measurements of the gamma-ray flux from Arp 220 for different energy thresholds, compared to predictions from theoretical models. LTQ refers to Lacki et al., (2010), TD to Torres & Domingo-Santamaría, (2005). The H.E.S.S. limits are from Cornils, (2006) and Nedbal, (2008).

upper limits can be compared to the expected fluxes. For all three source, the limits presented here are more constraining than earlier limits found in literature.

For IRAS 17208-0014 and IC 342, there are no firm predictions for the expected gamma-ray flux. The upper limits derived from VERITAS are larger than the rough estimates presented here by about an order of magnitude. Much larger exposures would be needed to either detect the sources or constrain any modeling effort.

For Arp 220, there have been several modeling efforts leading to a large range of flux predictions, cf. Fig. 8.1 and Section 1.4.5. The recent detections using *Fermi*-LAT data (Peng et al., 2016; Griffin et al., 2016) are compatible with the predictions of Torres & Domingo-Santamaría, (2005) and Lacki et al., (2010) and at the high end of the predictions by Yoast-Hull et al., (2015). The VERITAS upper limits presented here are fully compatible with the predictions by Yoast-Hull et al., (2015) and with the fiducial model of Lacki et al., (2010). We can exclude the alternative model of Lacki et al., (2010) (with increased wind and increased magnetic field compared to the fiducial model) at the 99 % confidence level, even taking systematic uncertainties into account. However, these predictions were based on a simplified model which was created to fit several galaxies over a range of starforming rates and densities and was never meant to precisely model the emission from Arp 220.

The prediction by Torres & Domingo-Santamaría, (2005) seems unlikely to be true, but cannot be excluded at the 99 % confidence level. The VERITAS limits are also compatible

with the extrapolations from the detections in the HE regime. They are compatible with the full range of uncertainties given by Peng et al., (2016). They are also compatible with the results of Griffin et al., (2016) assuming that the spectral index is not harder than -2.0.

Given the recent detection in the HE regime, it is very likely that Arp 220 also emits in the VHE range (as the produced gamma-ray spectrum is expected to follow a power law and the galaxy is mostly transparent to gamma rays below a few TeV). However, as not even a hint for emission was seen in more than 30 hours of VERITAS data, a much larger exposure would be needed to detect a statistically significant excess. If the flux was at the level of the HE detections, we would need about 500 h to 2 kh to detect a statistically significant excess with the current detector configuration. This would require a large fraction of VERITAS' yearly observation time, and is thus not being pursued at this time. Future instruments with larger collection areas are needed to either detect emission from Arp 220, or firmly constrain the existing models.

A Simulation Parameters

A.1 Air Shower Development

The *CORSIKA* software (Heck et al., 1998) with the *bernlohr* package (Bernlöhr, 2008) is used to simulate the shower development and the emission of Cherenkov light. Performing these two steps at the same time is beneficial because it reduces the overhead due to disk input/output. Some details about the configuration of CORSIKA are given in Table A.1. CORSIKA takes as input an atmospheric profile (see Section 2.1.3), magnetic field strength and inclination at the telescope site, and the locations of the telescopes. The output file contains information about all Cherenkov photons which reach one of the telescopes. For the studies presented here, absorption in the atmosphere or at the mirrors was not handled in CORSIKA. This improves the processing time and retains the flexibility to change the atmospheric extinction model later.

To read out the binary files produced by CORSIKA and output them in a text format that can be used as input for the next stage, the corsikaIOreader[1] is used. Atmospheric extinction is also applied during this step. See Section 2.4 for more details about the extinction profiles.

A.2 Detector Simulation

The detector simulation proceeds in two steps. First, GrOptics[4] is used for ray tracing within the telescope and to apply the mirror efficiencies. GrOptics uses the ROBAST(Okumura et

---

[1] https://wiki-zeuthen.desy.de/CTA/CorsikaIOreader
[2] Ostapchenko, 2006b; Ostapchenko, 2006a.
[3] Bass et al., 1998; Bleicher et al., 1999.
[4] http://otte.gatech.edu/care/

Option	Value
Version	CORSIKA 6.990
High energy hadronic interaction model	QGSJET II.3[2]
Low energy hadronic interaction model	URQMD 1.3cr[3]
Detector geometry	non-flat (volume detector)

Table A.1: Some of the relevant options used to compile CORSIKA for the studies presented here.

Element range Z	Group Norm. f_{100}	Representative Element	Z	Norm. of Representative f_{100}	Index γ
1	$3.55 \cdot 10^{-7}$	H	1	$3.55 \cdot 10^{-7}$	2.66
$2-4$	$4.58 \cdot 10^{-7}$	He	2	$4.40 \cdot 10^{-7}$	2.58
$5-7$	$6.04 \cdot 10^{-8}$	C	6	$5.07 \cdot 10^{-8}$	2.66
$8-11$	$9.77 \cdot 10^{-8}$	O	8	$6.85 \cdot 10^{-8}$	2.68
$12-19$	$1.00 \cdot 10^{-7}$	Mg	12	$4.20 \cdot 10^{-8}$	2.64
$20-24$	$2.40 \cdot 10^{-8}$	Ca	20	$5.85 \cdot 10^{-9}$	2.70
$25-28$	$1.61 \cdot 10^{-7}$	Fe	26	$1.35 \cdot 10^{-7}$	2.59

Table A.2: Flux normalization for signal and background simulations. Simulations are performed for representative elements only and weighted to the total flux of the represented range. The simulations are weighted to an energy spectrum $\frac{\mathrm{d}N}{\mathrm{d}E} = f_{100} \cdot \left(\frac{E}{100\,\mathrm{TeV}} \right)^{-\gamma}$, where the normalization f_{100} at $100\,\mathrm{TeV}$ is given in units of $\mathrm{m}^{-2}\,\mathrm{s}^{-1}\,\mathrm{sr}^{-1}\,\mathrm{TeV}^{-1}$.

al., 2016) software as the ray-tracing engine. CARE[4] is used to simulate the generation of pulses in the photo-multiplier tubes and the digitization of these signals.

A.3 Signal and Background Samples

For the study presented here, the *signal* is chosen to be iron-induced showers. The background is made up of all the other elements which contribute to the cosmic ray spectrum. To simplify computations, the elements were divided into groups and the most abundant element of each group was selected to represent that group. Air shower simulations were produced for each representative element. The simulations were then normalized according to the expected flux from all the elements in that group. The fluxes for protons and helium were taken from CREAM measurements from $2.5\,\mathrm{TeV}$ to $250\,\mathrm{TeV}$ (Yoon et al., 2011). The fluxes of the lighter elements were taken from Hörandel, J. R., (2003) and extrapolated to $500\,\mathrm{TeV}$ assuming a power-law spectrum. To ease the calculations, a common spectral index of -2.7 was assigned to all background samples. The list of representative elements and their normalization can be found in Table A.2. Heavier elements than Nickel were neglected because their combined abundance is less than 5% of the abundance of iron at $100\,\mathrm{TeV}$. Iron contributes 85% of the flux in the last bin.

B Systematic Differences Between Interaction Models

B.1 Template Analysis Parameter Distributions
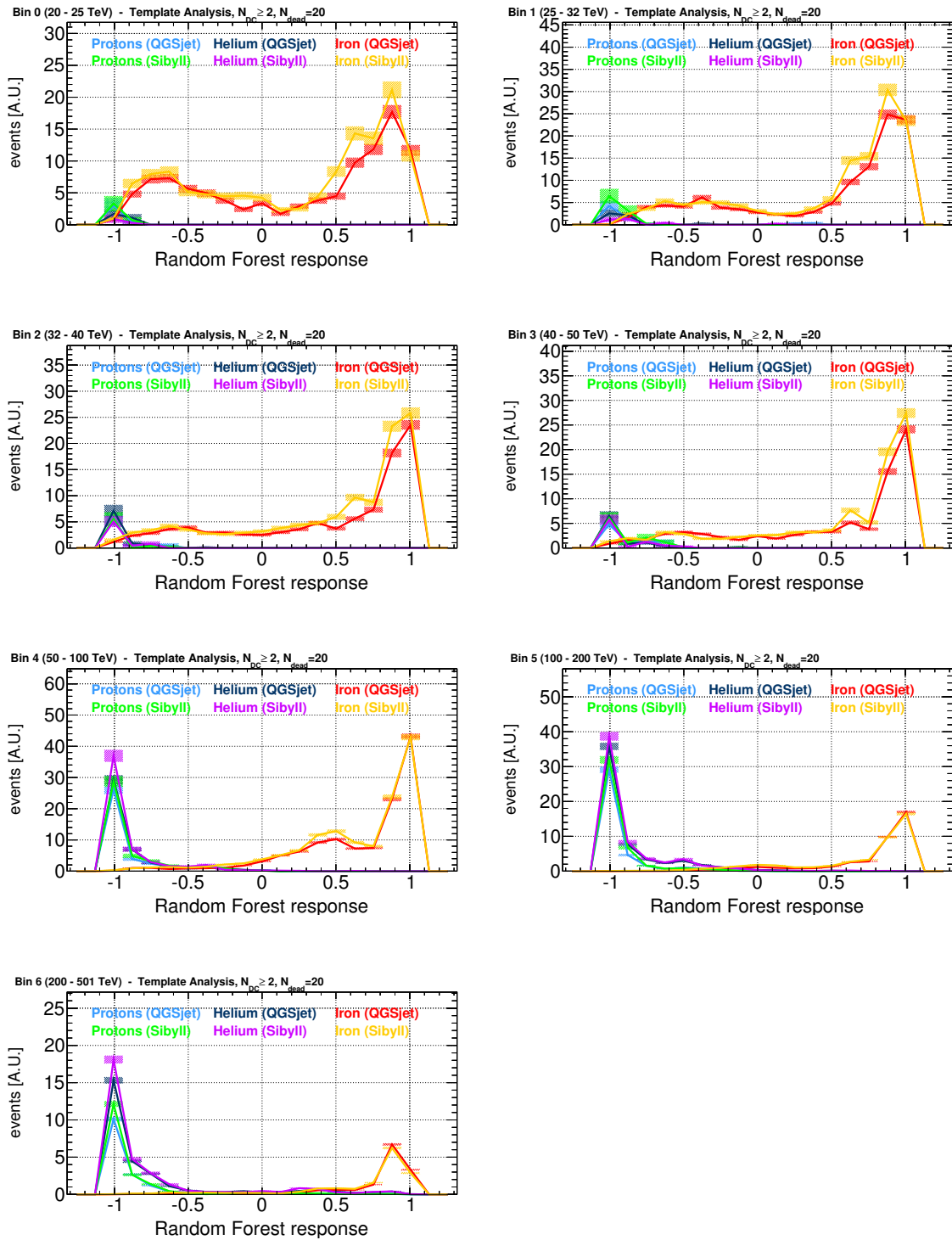
Figure B.1: Random Forest classifier response for different hadronic interaction models.
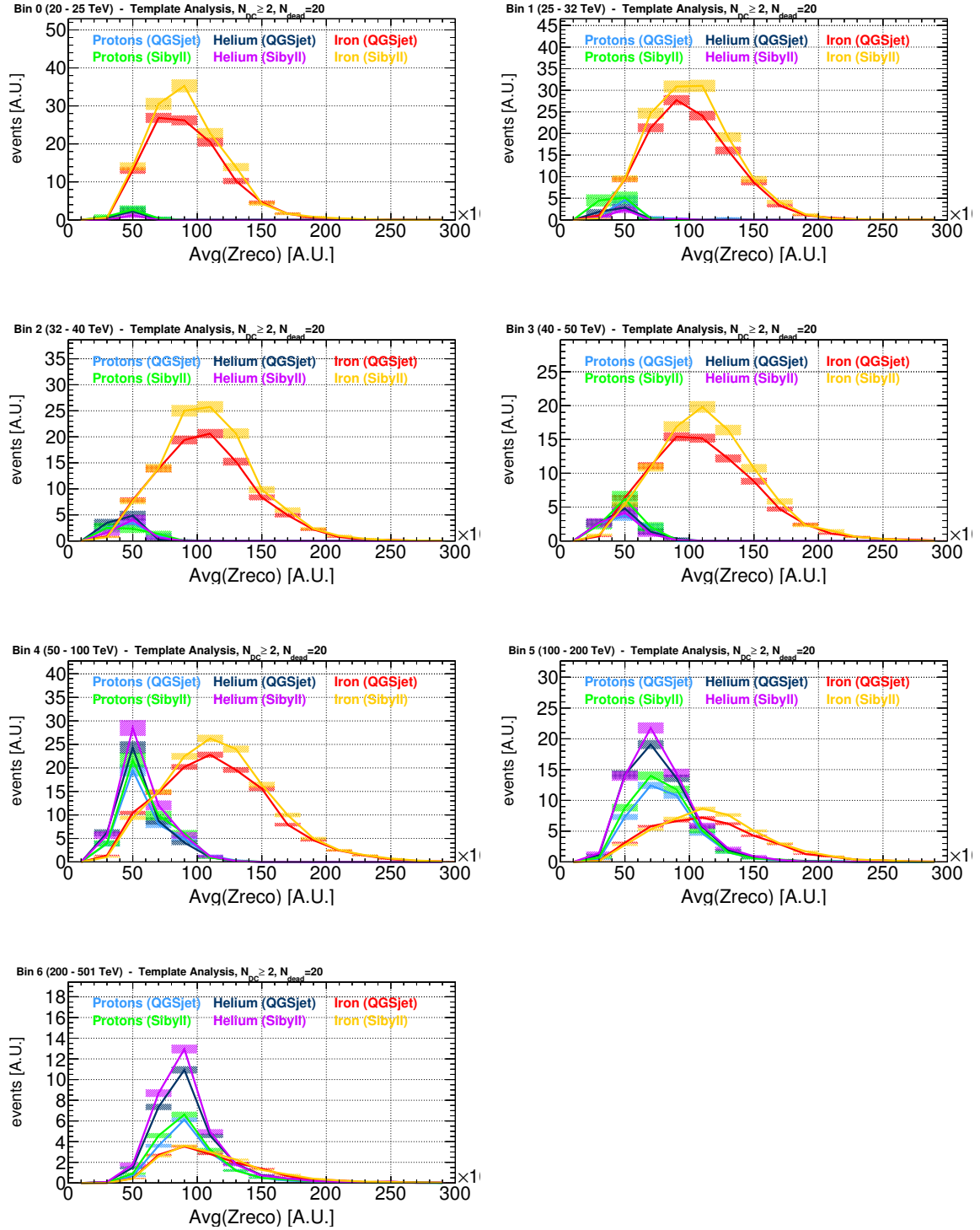
Figure B.2: Reconstructed charge distribution for different hadronic interaction models.
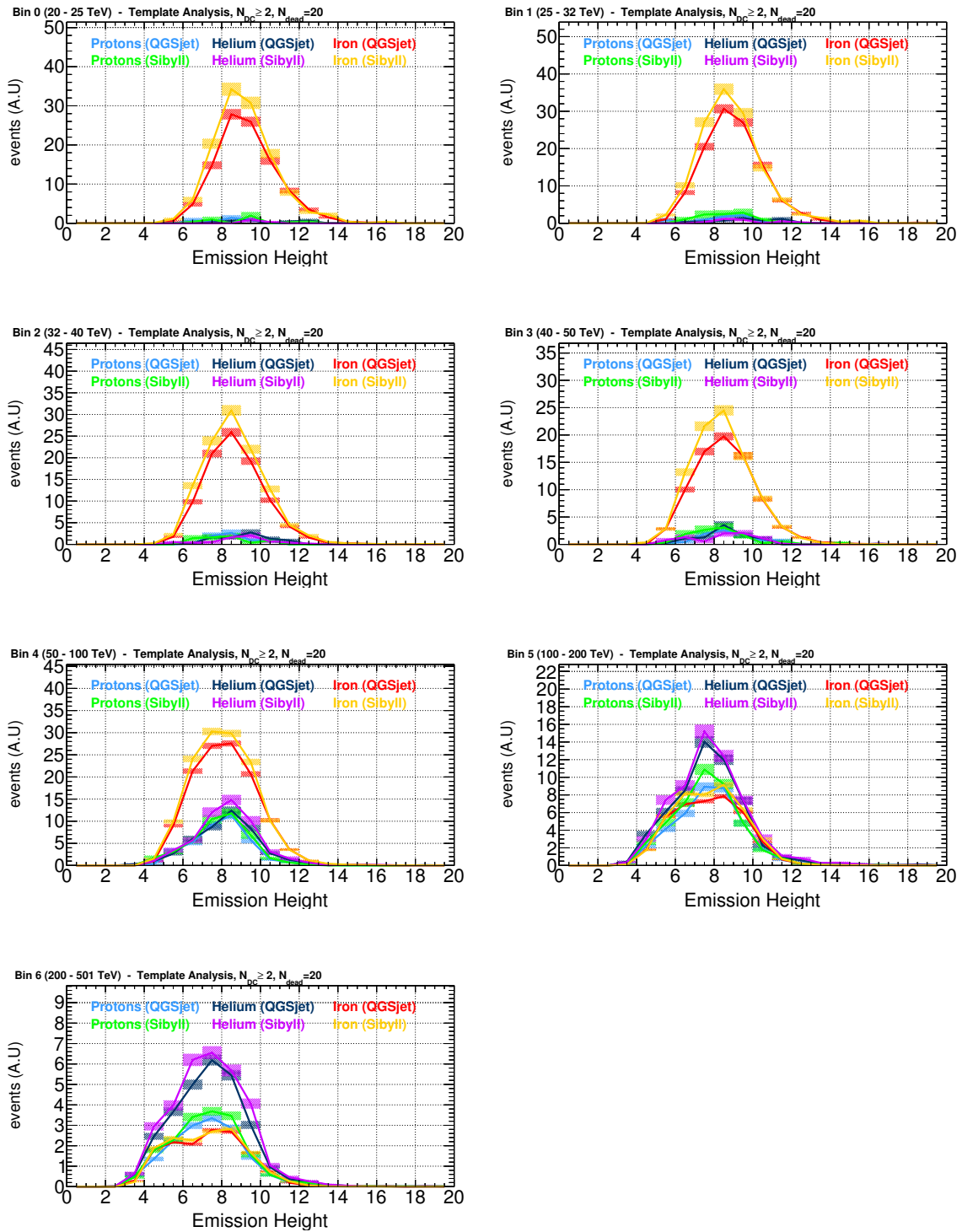
Figure B.3: Distribution of the height of maximum Cherenkov emission for different hadronic interaction models.
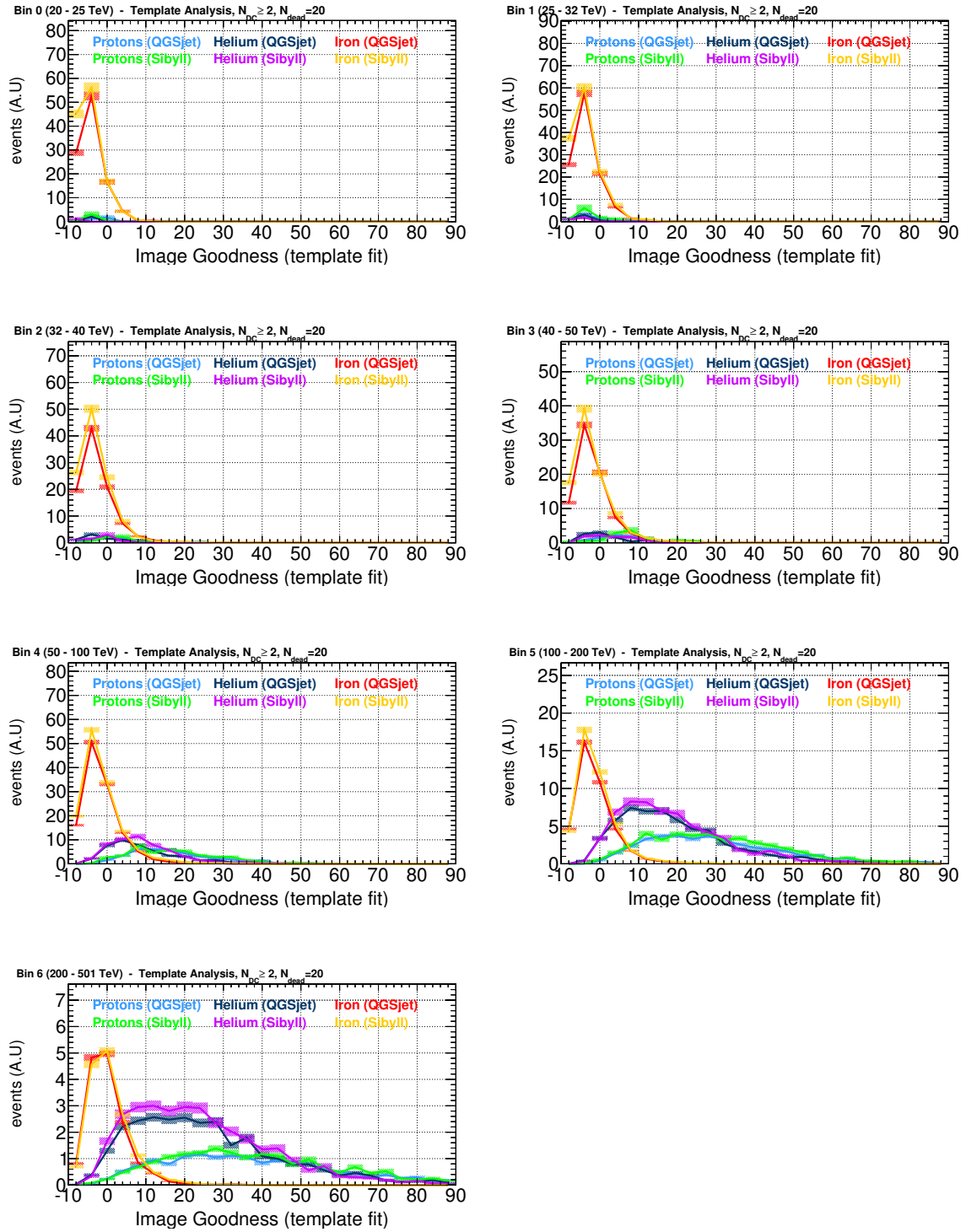
Figure B.4: Goodness-of-fit distribution for different hadronic interaction models.
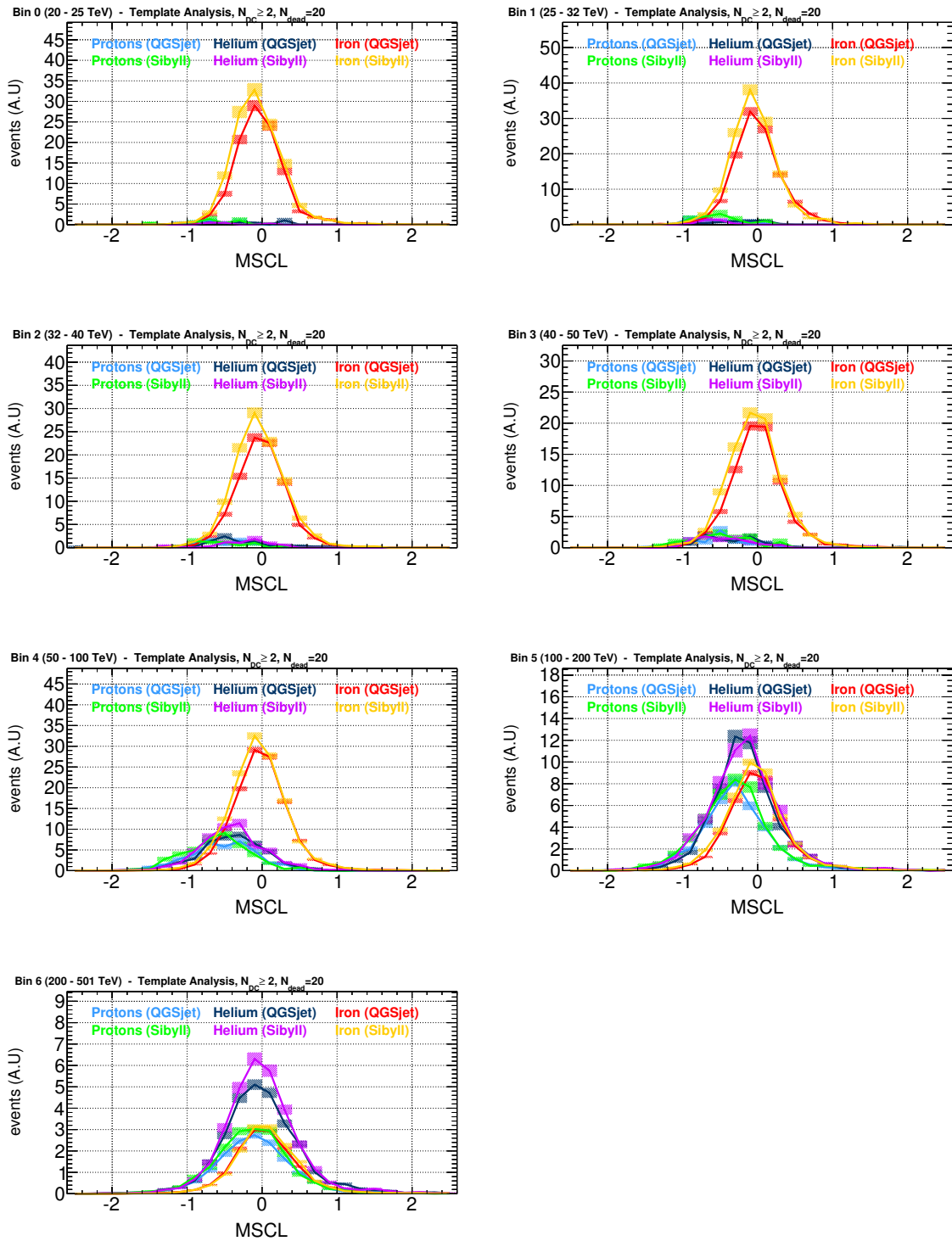
Figure B.5: Mean scaled width distribution for different hadronic interaction models.
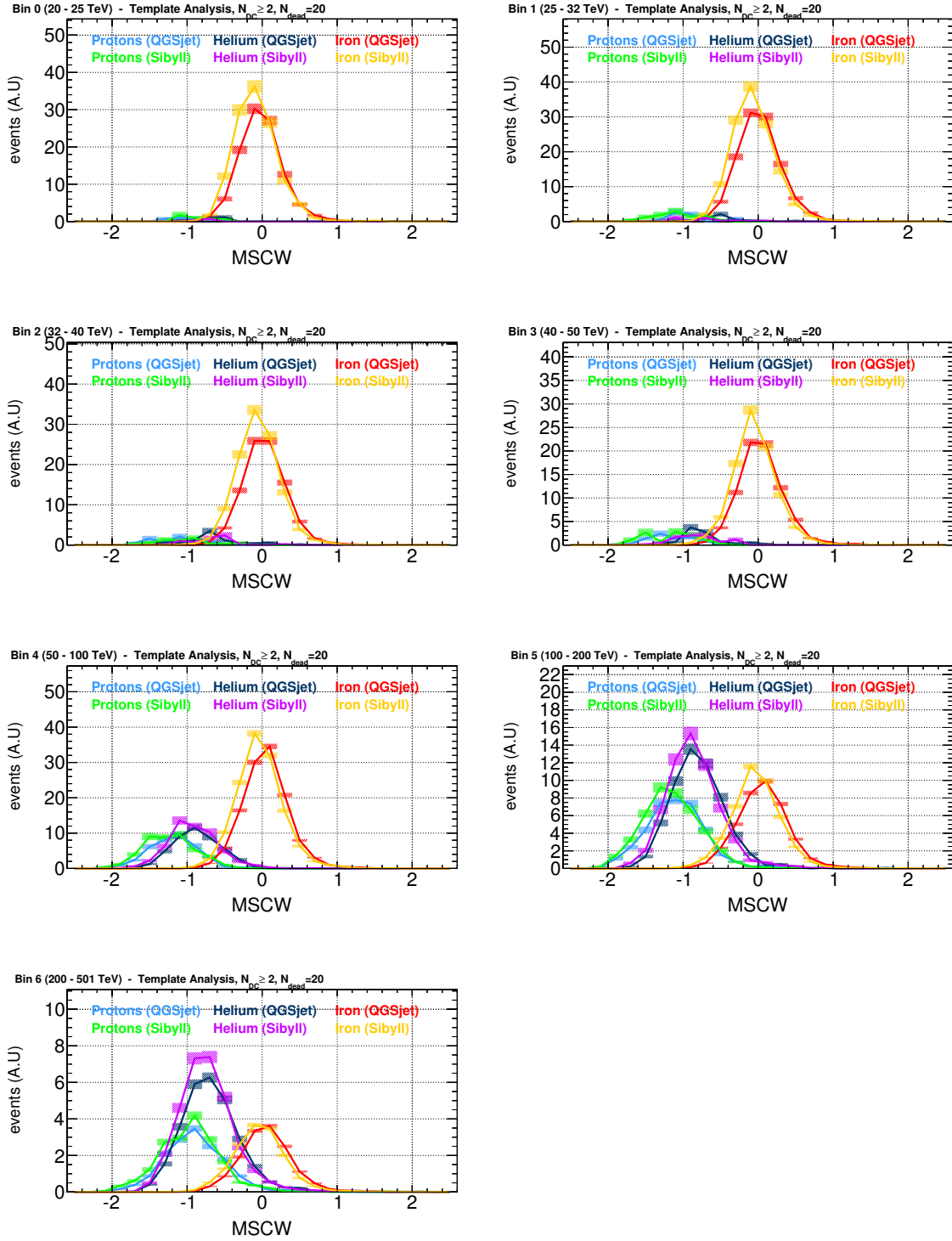
Figure B.6: Mean scaled length distribution for different hadronic interaction models.

C Comparison between Data and Simulations

C.1 Moment-Based Analysis
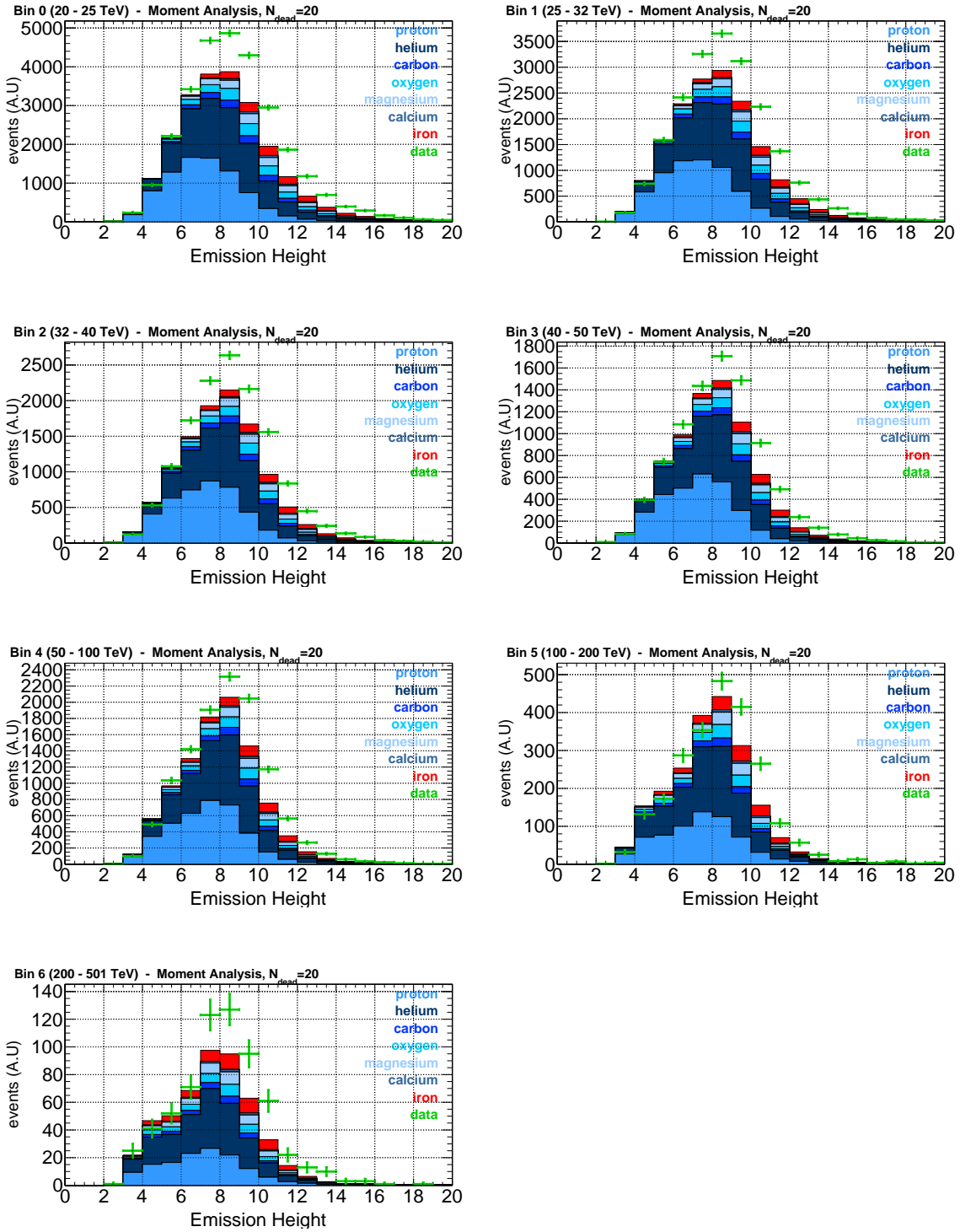
Figure C.1: Distribution of the height of maximum Cherenkov emission.
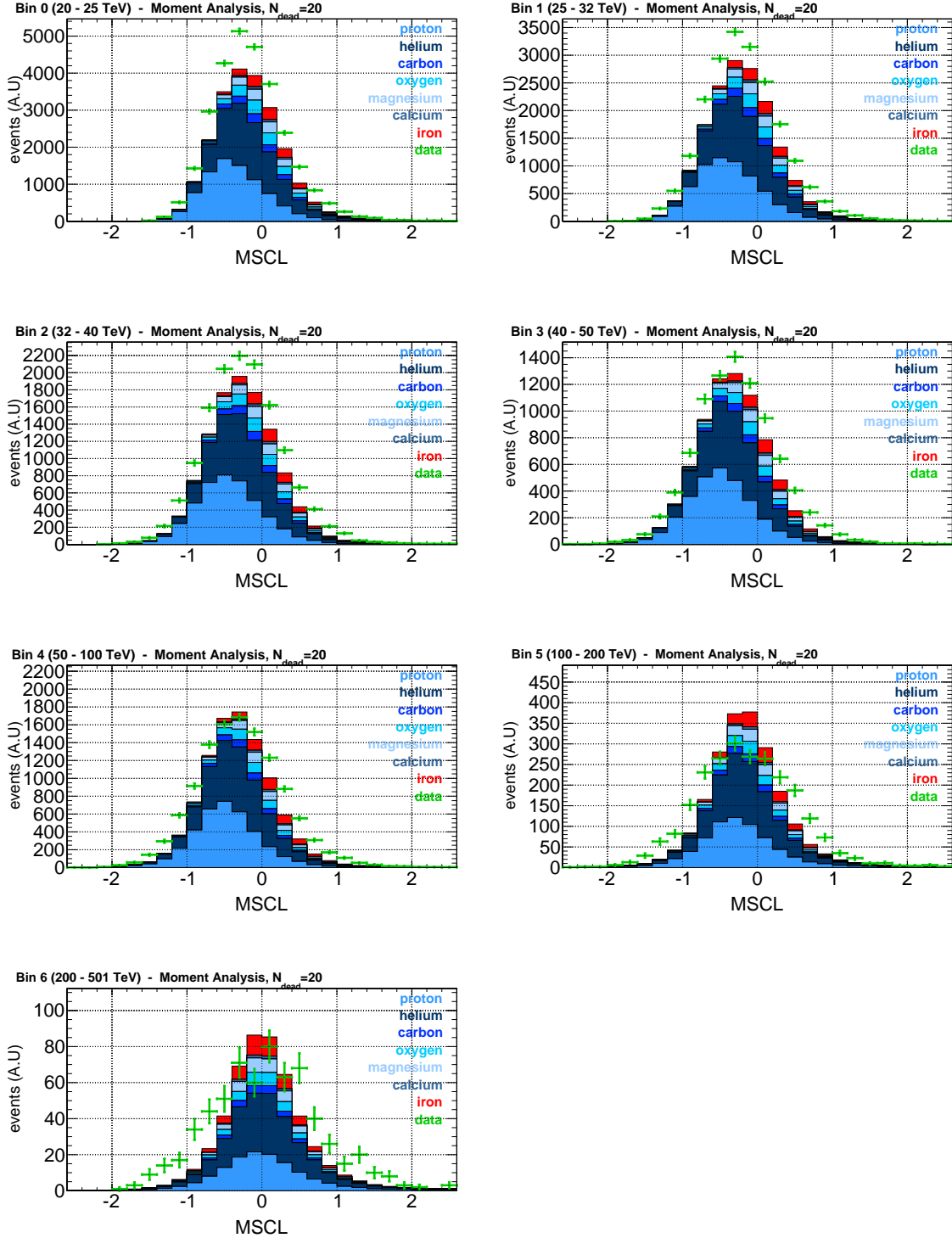
Figure C.2: Distribution of the mean scaled length.
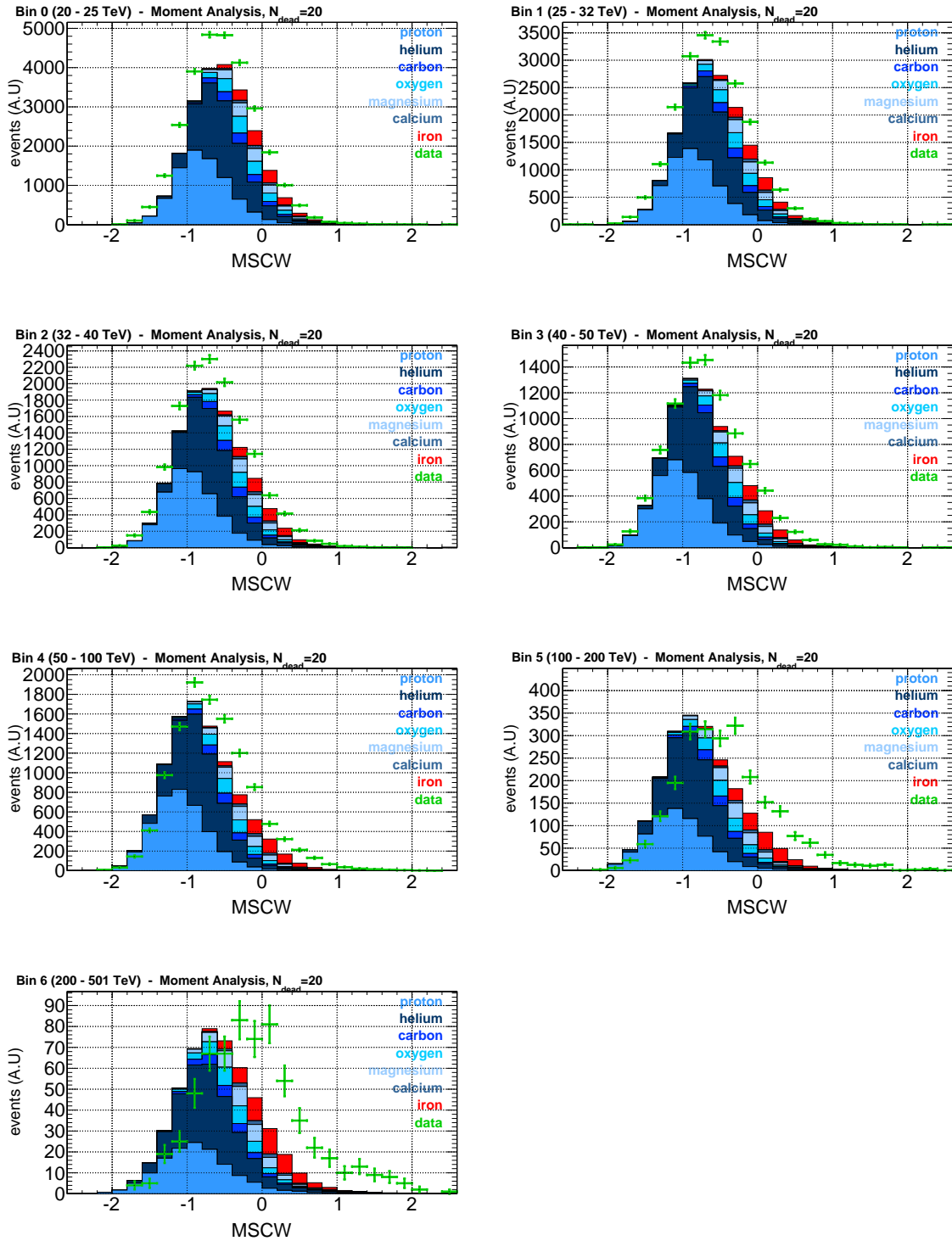
Figure C.3: Distribution of the mean scaled width.

C.2 Template Analysis
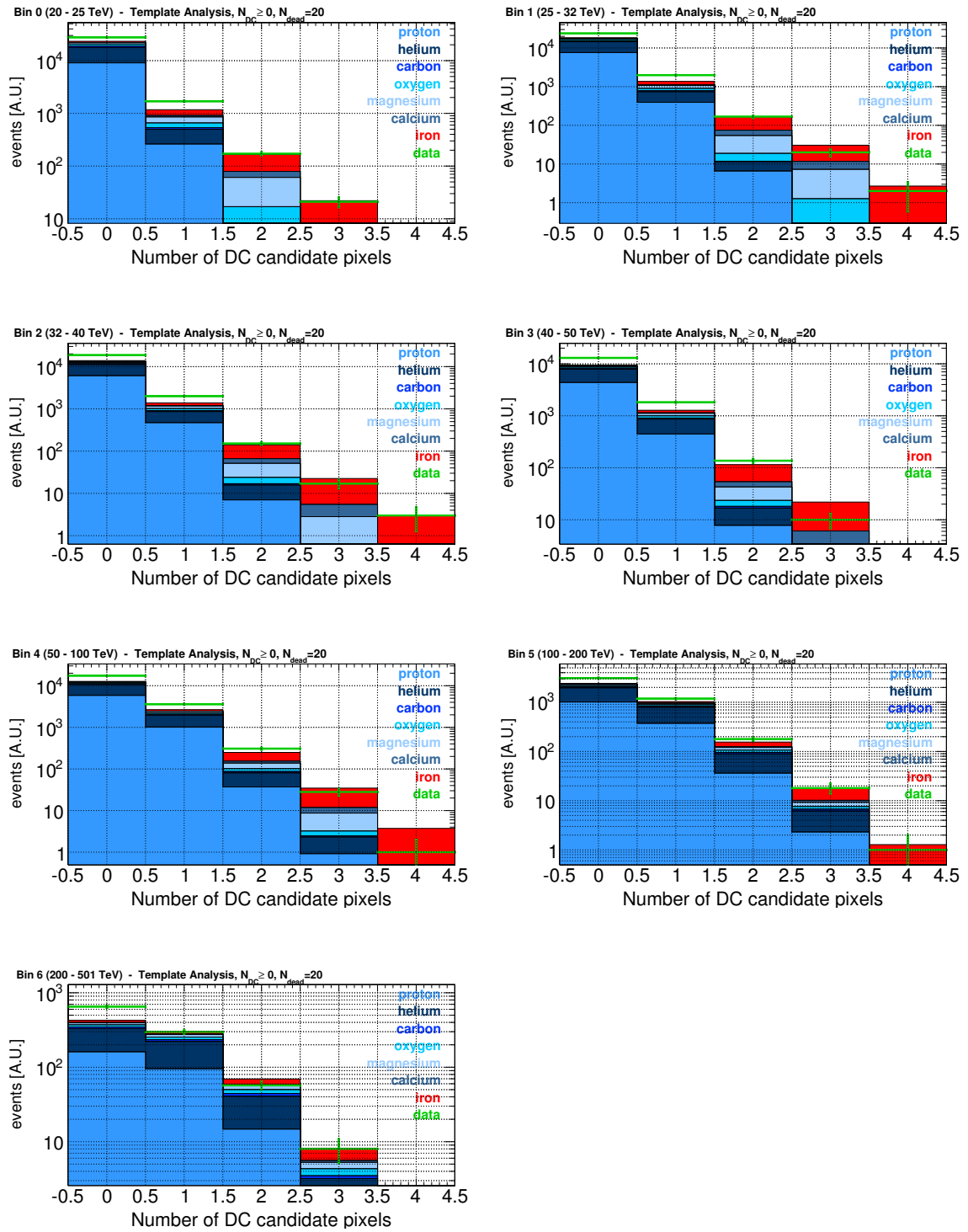
Figure C.4: Distribution of the number of images with a DC candidate pixel per event.

C.3 Template Analysis — Two or More DC Pixel Candidates
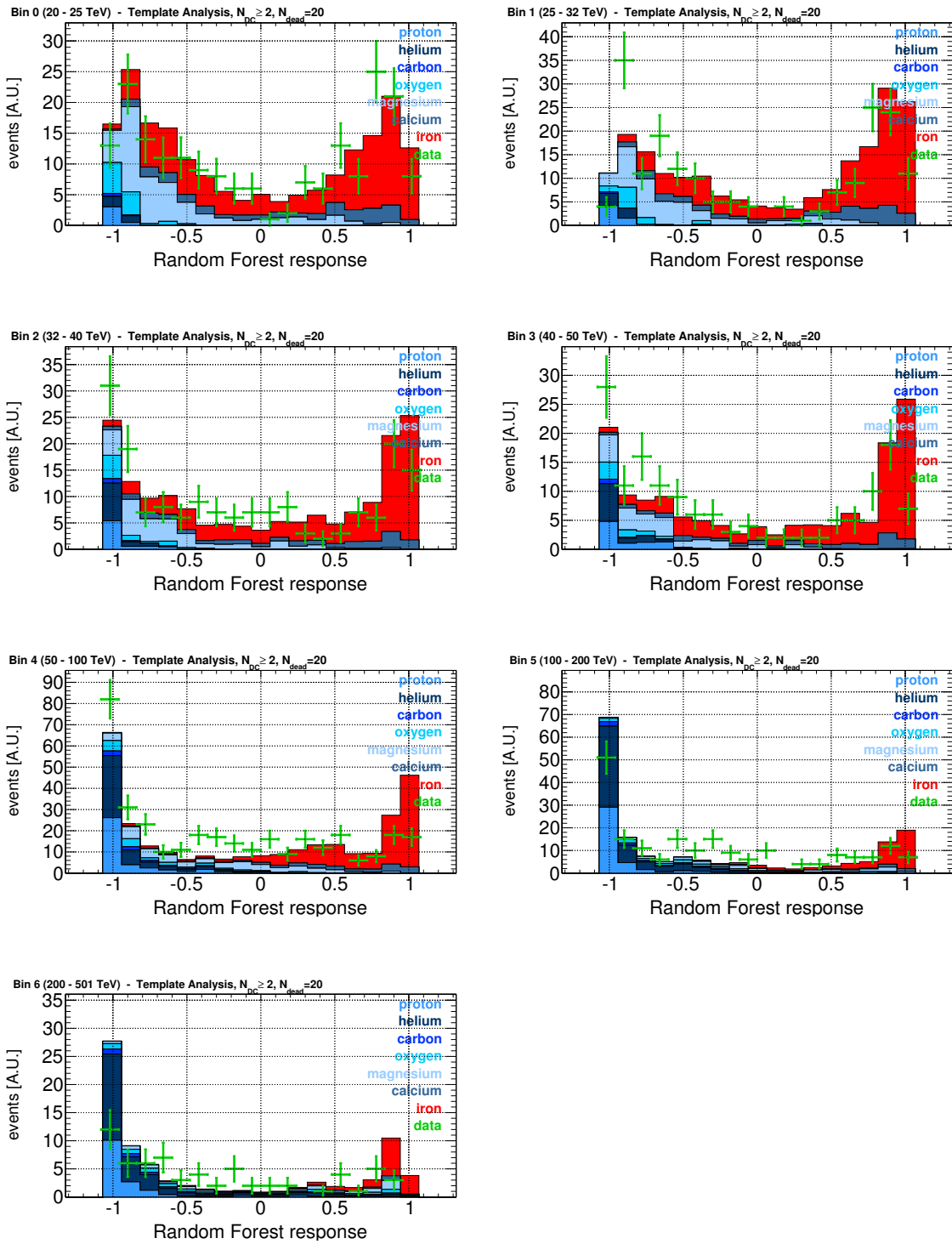
Figure C.5: Response of the Random Forest Classifier.
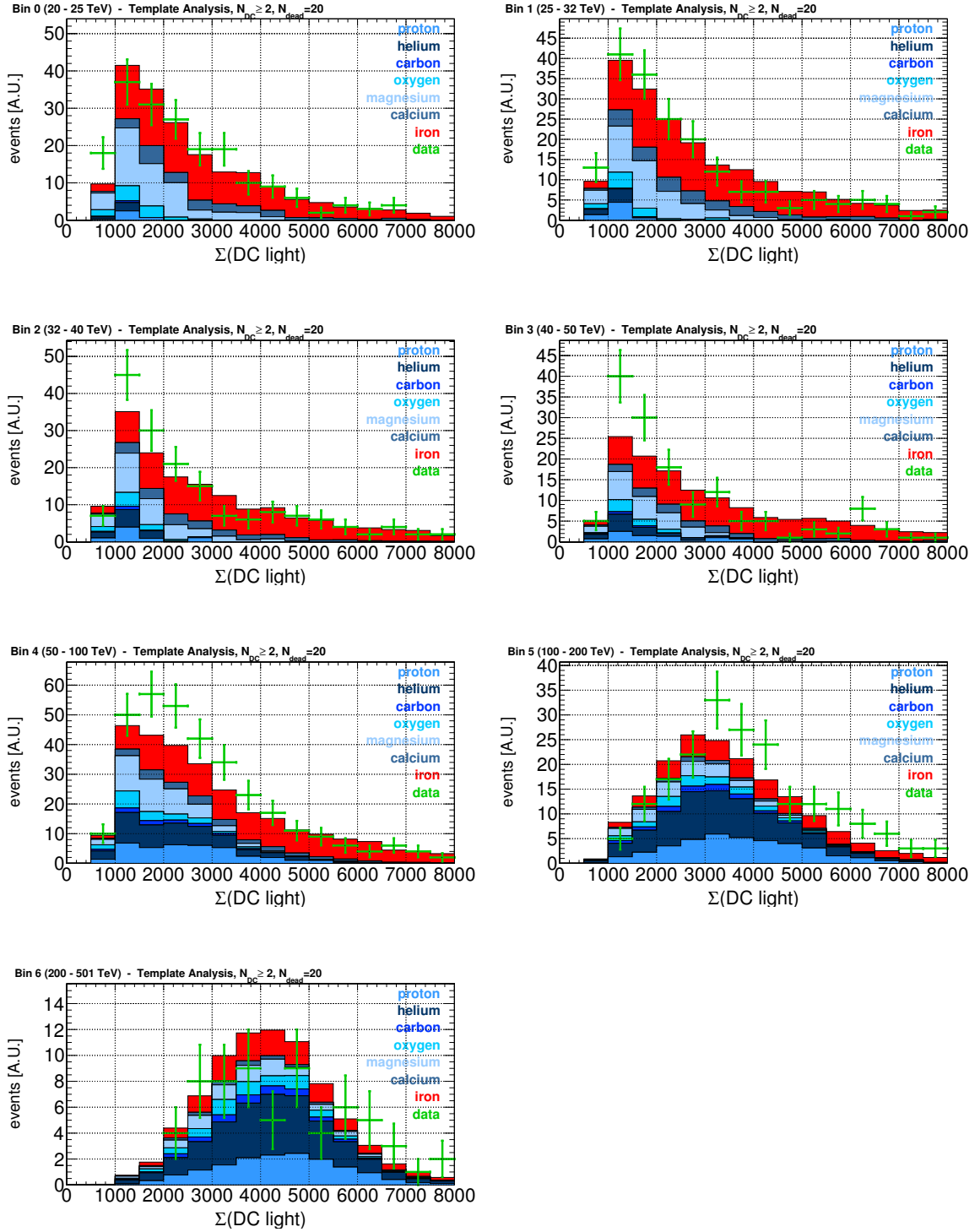
Figure C.6: Distribution of the sum of the contributions from DC light.
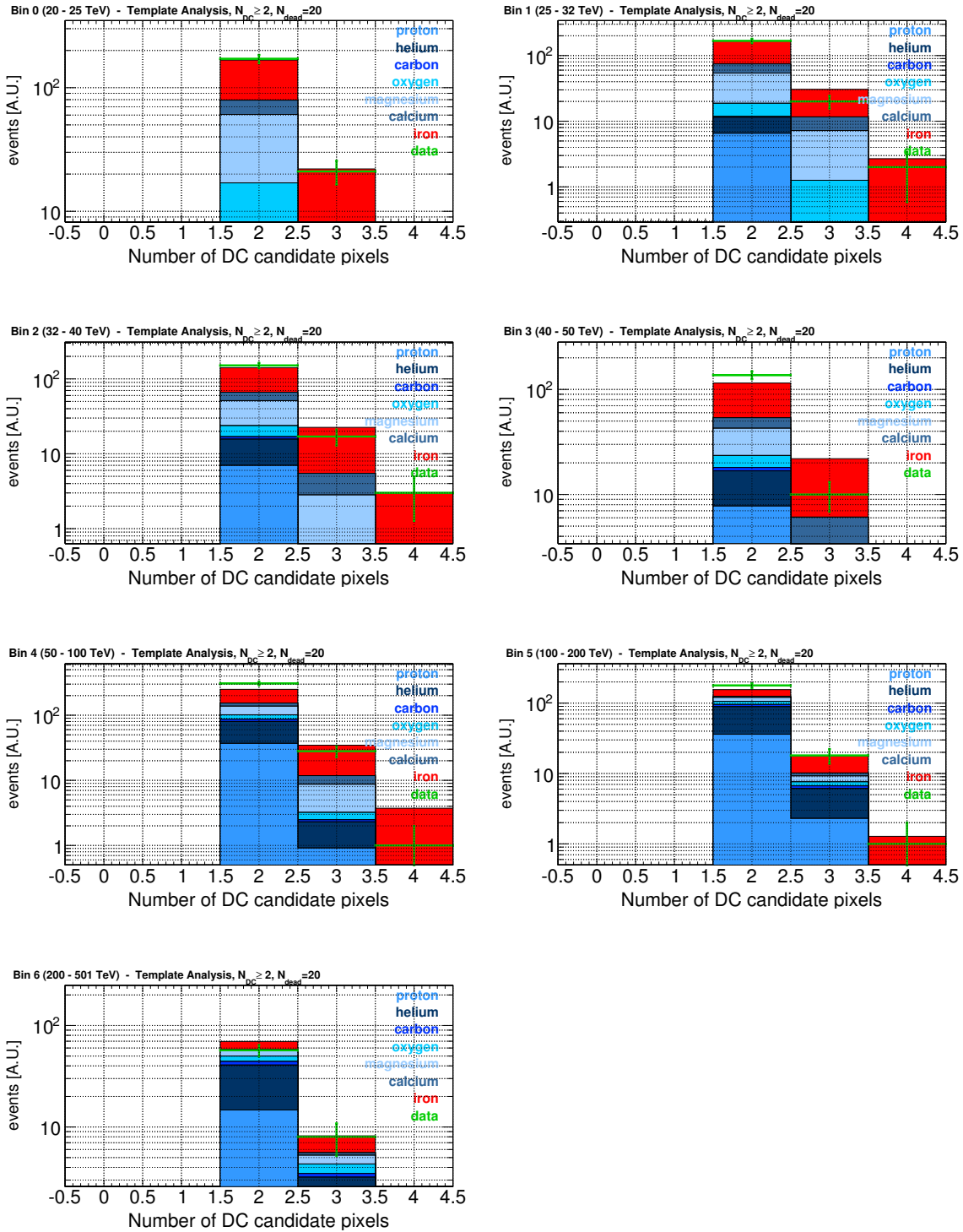
Figure C.7: Distribution of the number of images with a DC candidate pixel per event.
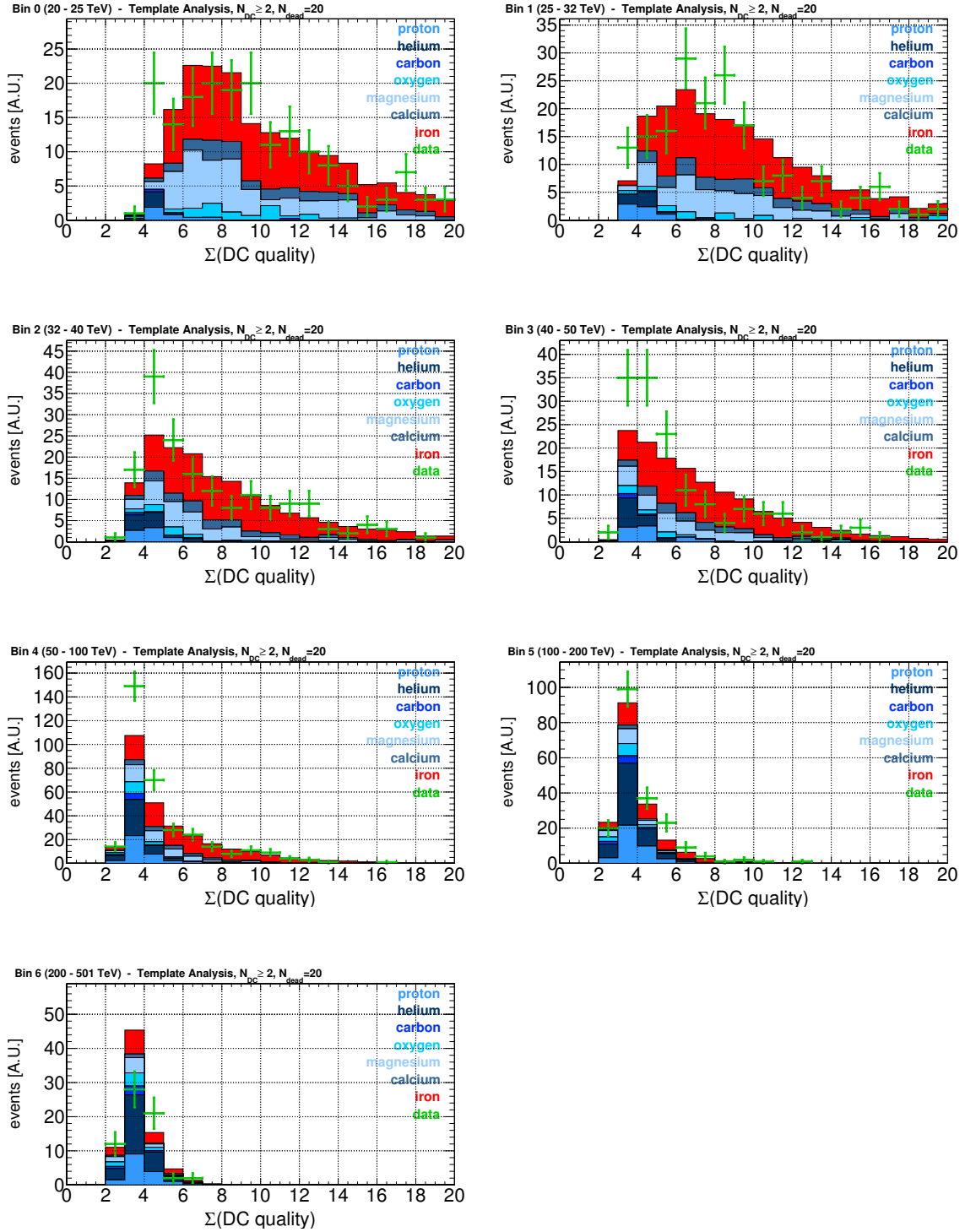
Figure C.8: Distribution of the sum of the DC quality factors.
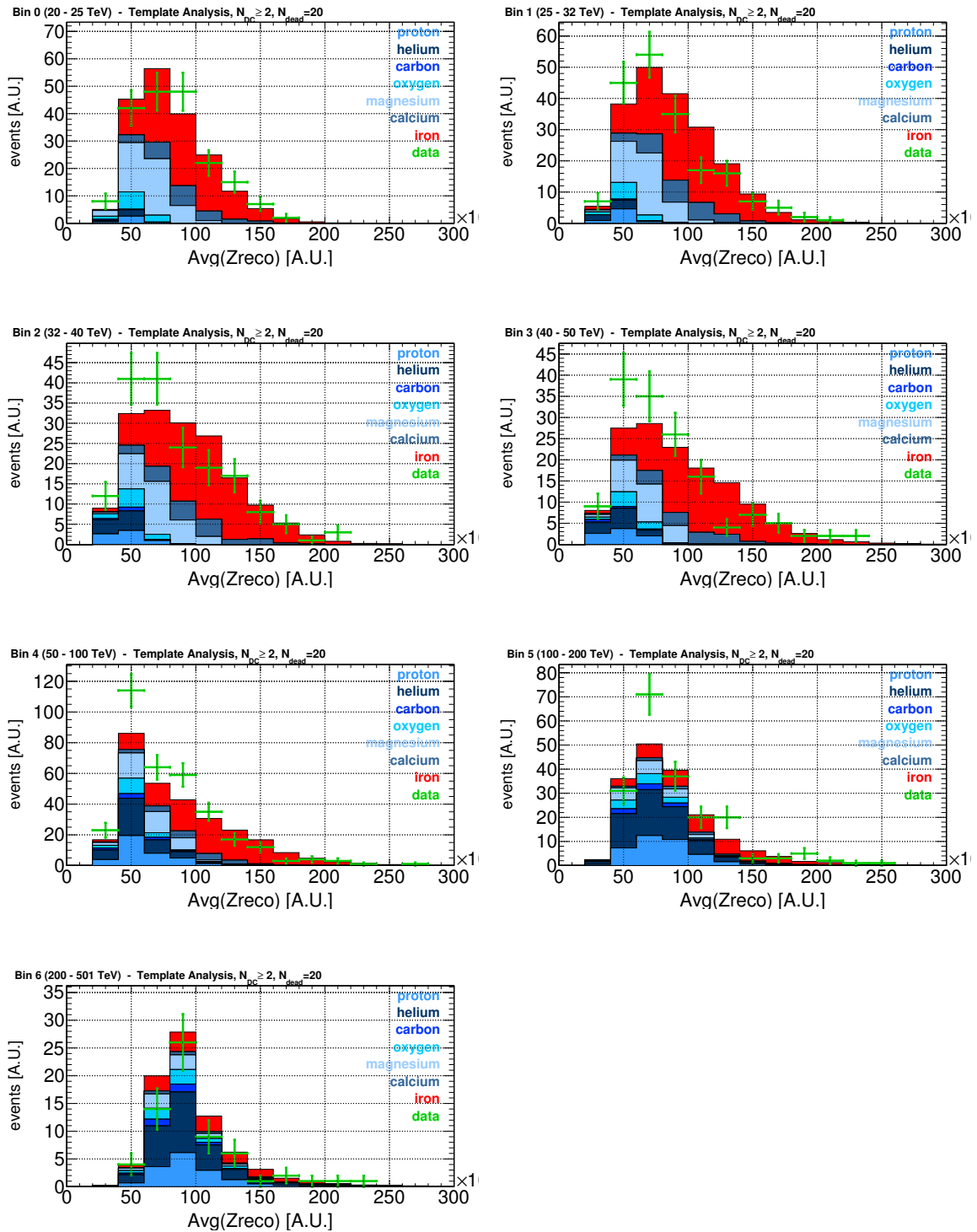
Figure C.9: Distribution of the average reconstructed charge.
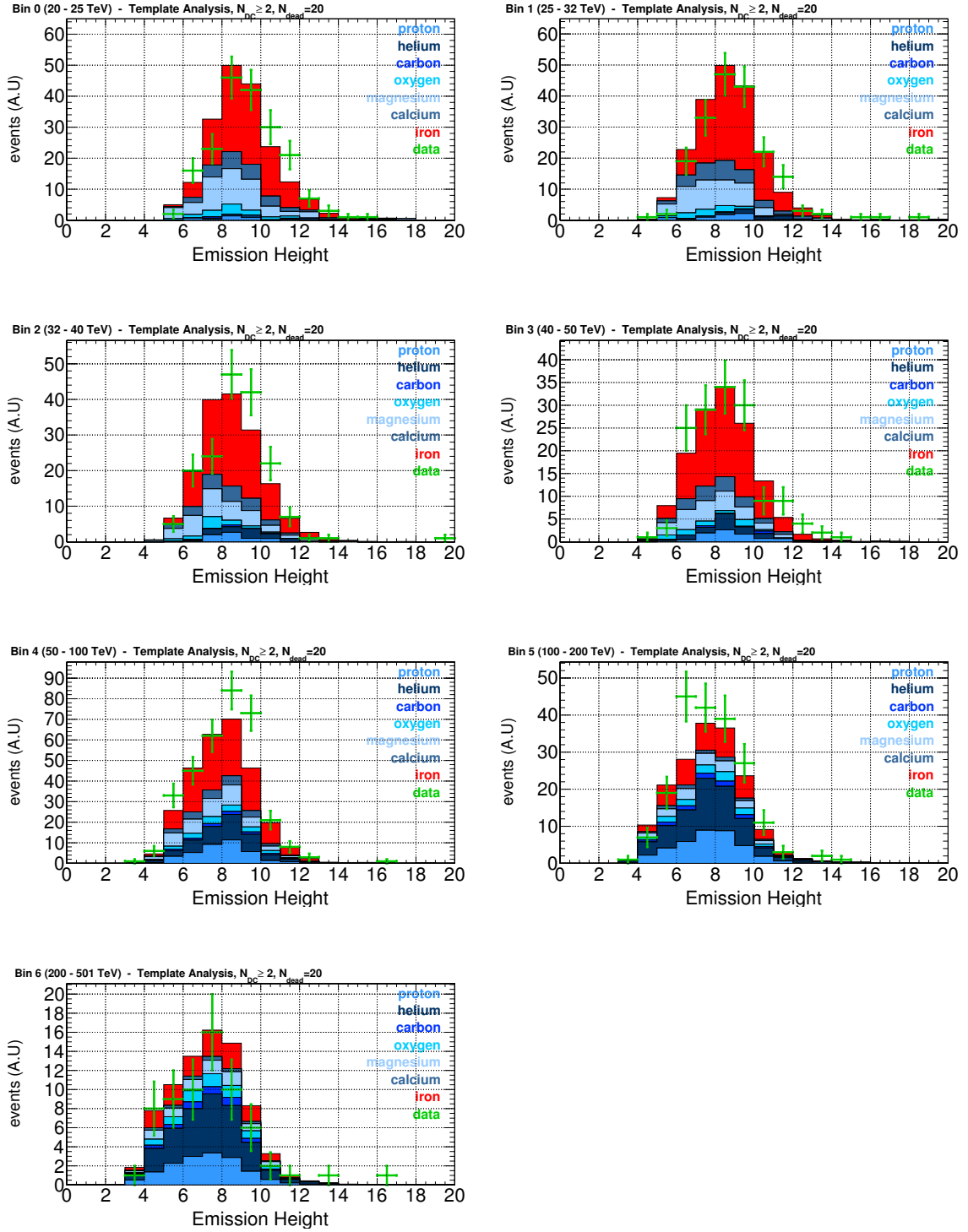
Figure C.10: Distribution of the height of maximum Cherenkov emission.
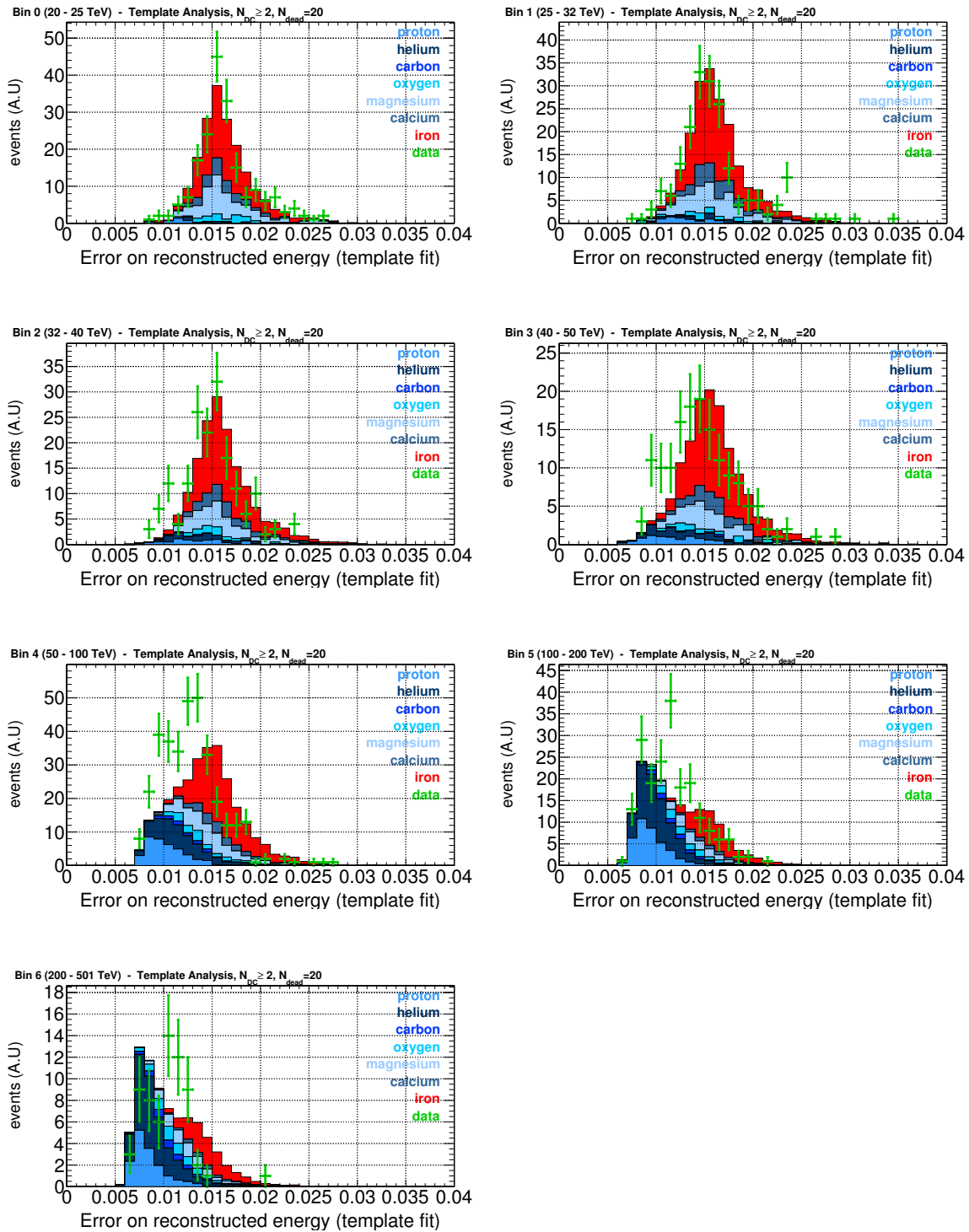
Figure C.11: Distribution of the error on the fitted energy.
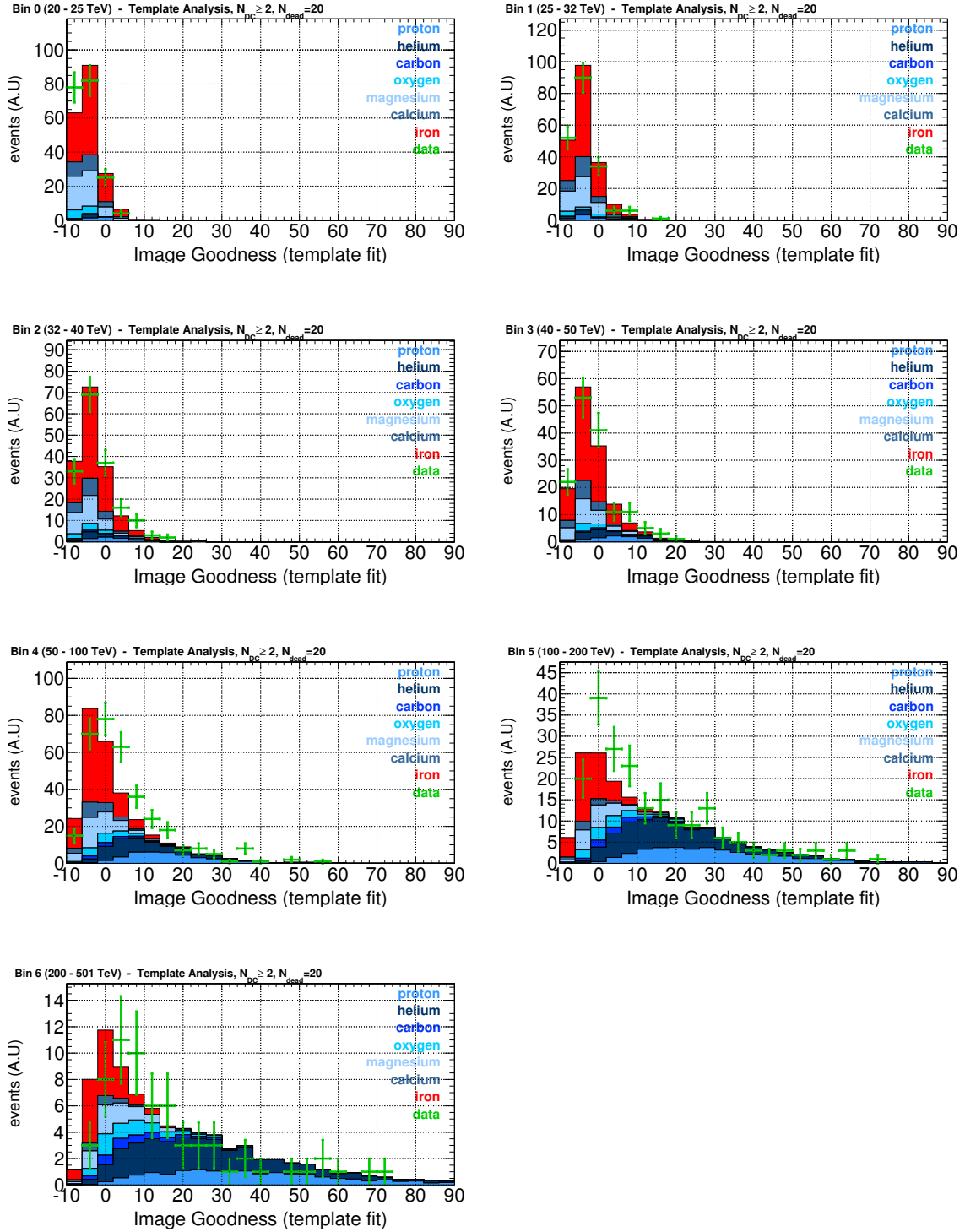
Figure C.12: Distribution of the goodness-of-fit.
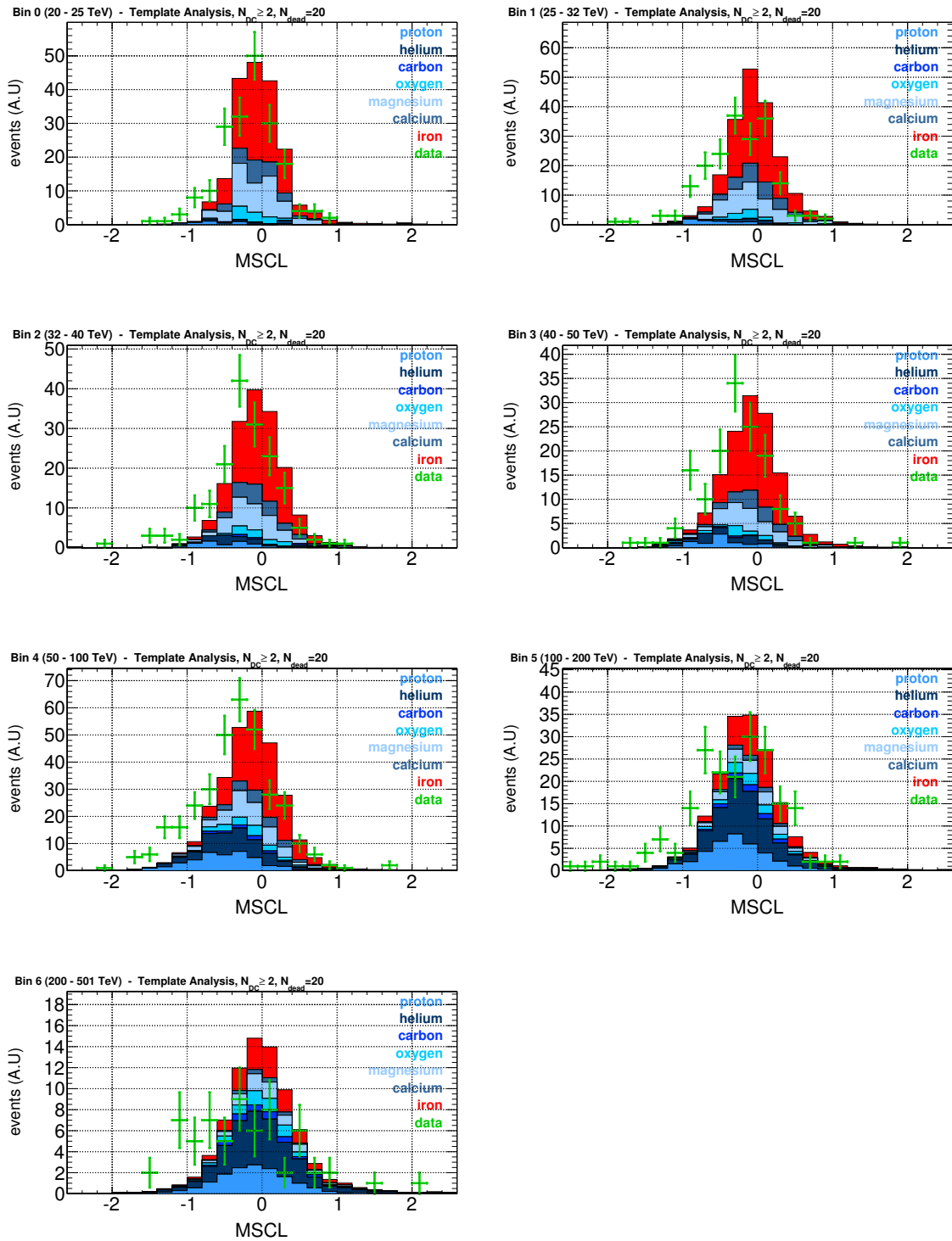
Figure C.13: Distribution of the mean scaled length.
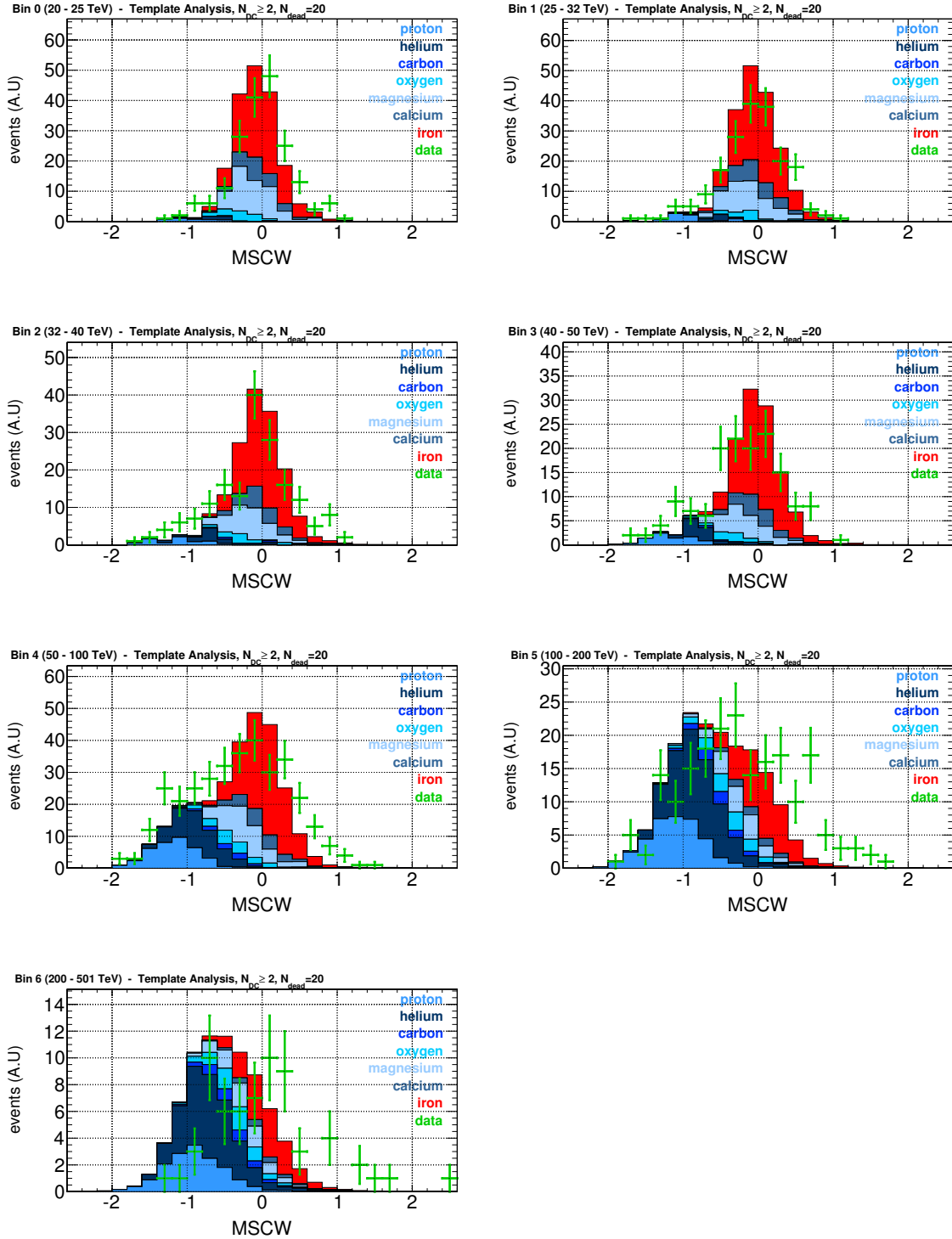
Figure C.14: Distribution of the mean scaled width.

D Sky Maps and Expected Limits for Star Forming Galaxies

D.1 Arp 220

(a) Excess events, hard cuts

(b) Significance, hard cuts

(c) Excess events, moderate cuts

(d) Significance, moderate cuts
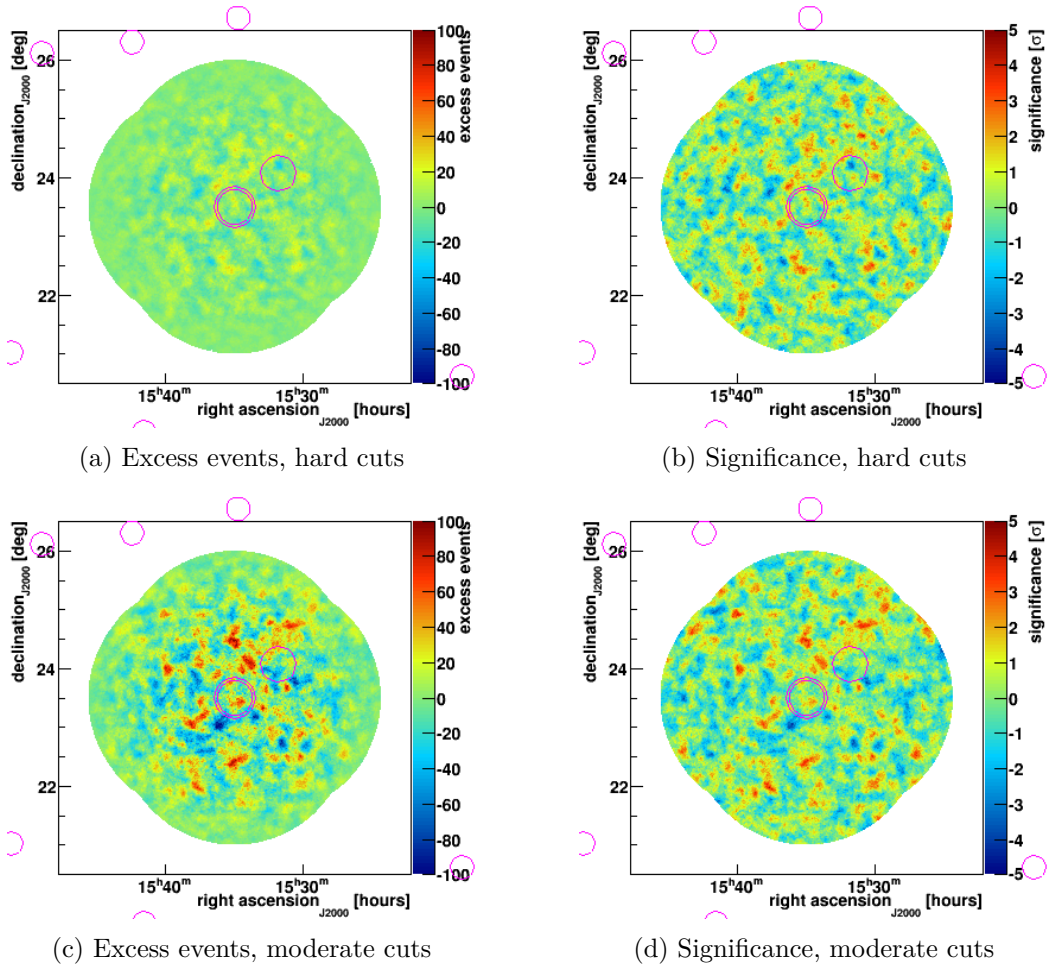
Figure D.1: Skymaps showing the number of excess events (difference between signal counts and background expectation) and the significance of the excess after Li & Ma, (1983) around the location of Arp 220. The distributions are compatible with the background-only hypothesis. The pink circles correspond to regions excluded from background estimation due optically bright stars.
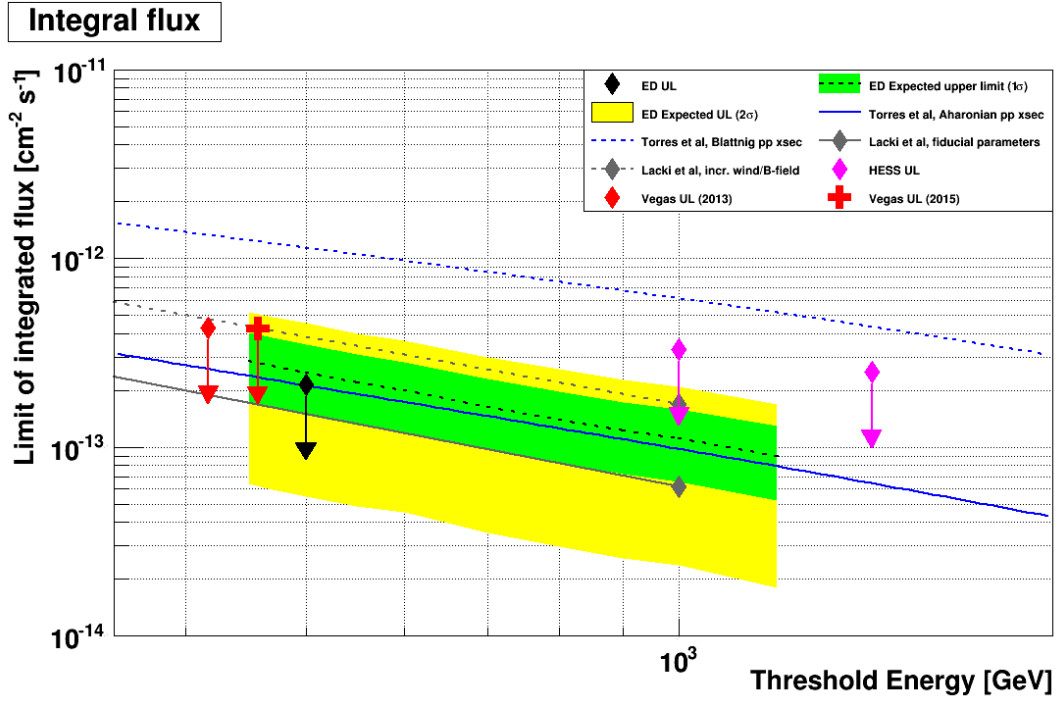
(a) Hard cuts
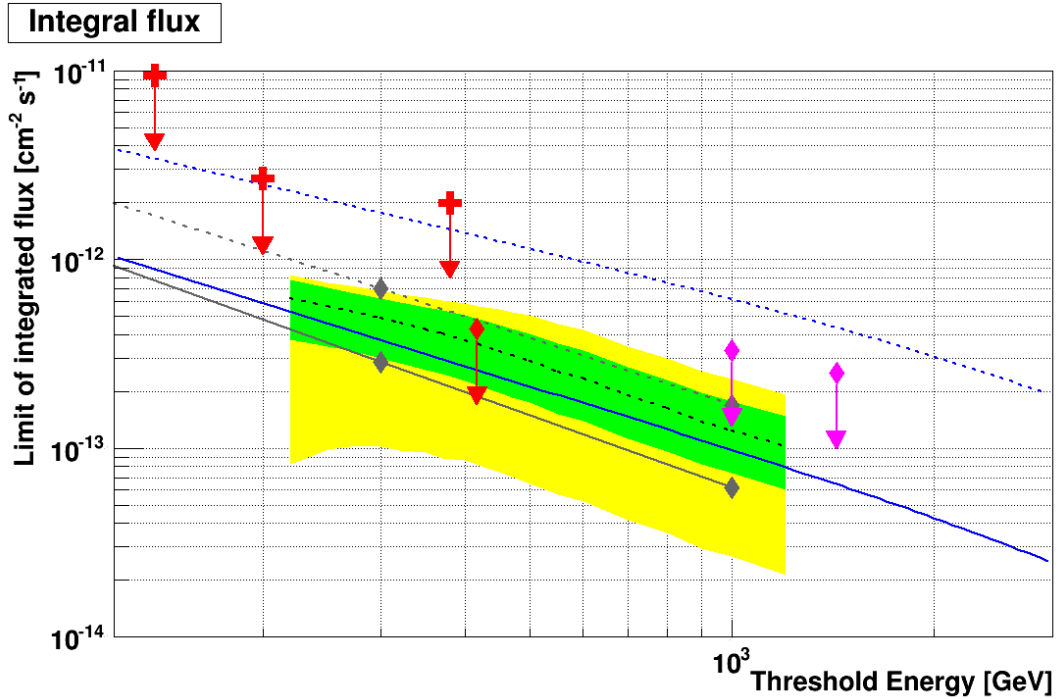
(b) Moderate cuts

Figure D.2: Expected and actual upper limits on the integral gamma-ray flux from Arp 220, compared to model predictions. See Table 8.2 for references on the models and Table 1.4 for references on the H.E.S.S. results. The red (VEGAS) limits were obtained with an independent analysis of the same data set, as a cross check. In this study ("ED"), no upper limits were calculated for moderate cuts, because the expected limits showed that hard cuts were more sensitive.

D.2 IRAS 17208-0014

(a) Excess events, hard cuts

(b) Significance, hard cuts

(c) Excess events, moderate cuts

(d) Significance, moderate cuts
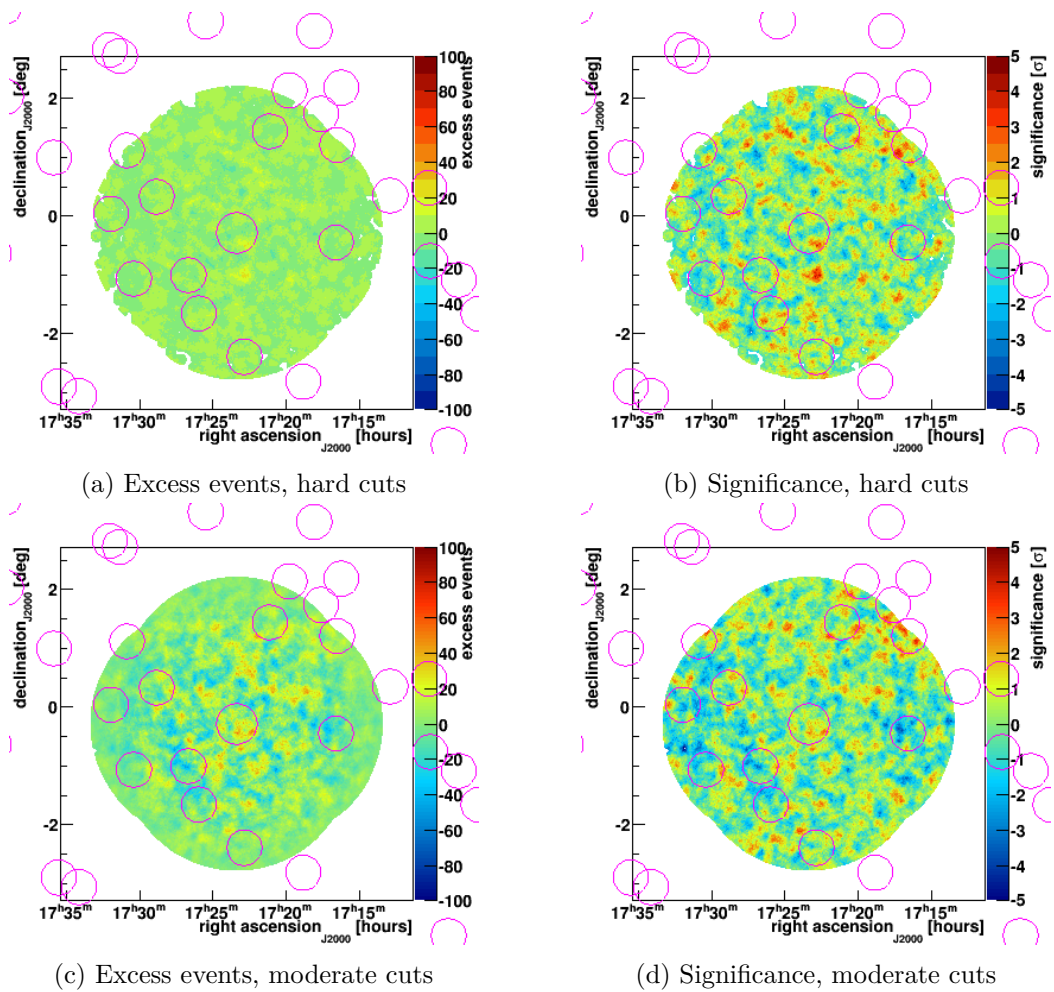
Figure D.3: Skymaps showing the number of excess events (difference between signal counts and background expectation) and the significance of the excess after Li & Ma, (1983) around the location of IRAS 17208-0014. The distributions are compatible with the background-only hypothesis. The pink circles correspond to regions excluded from background estimation due optically bright stars.
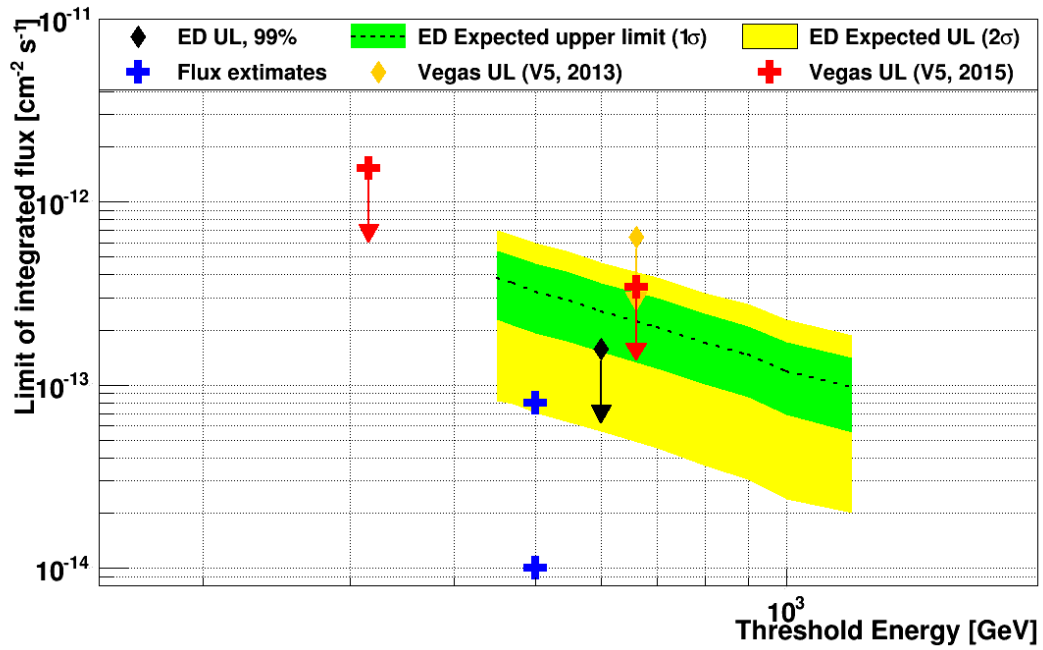
(a) Hard cuts
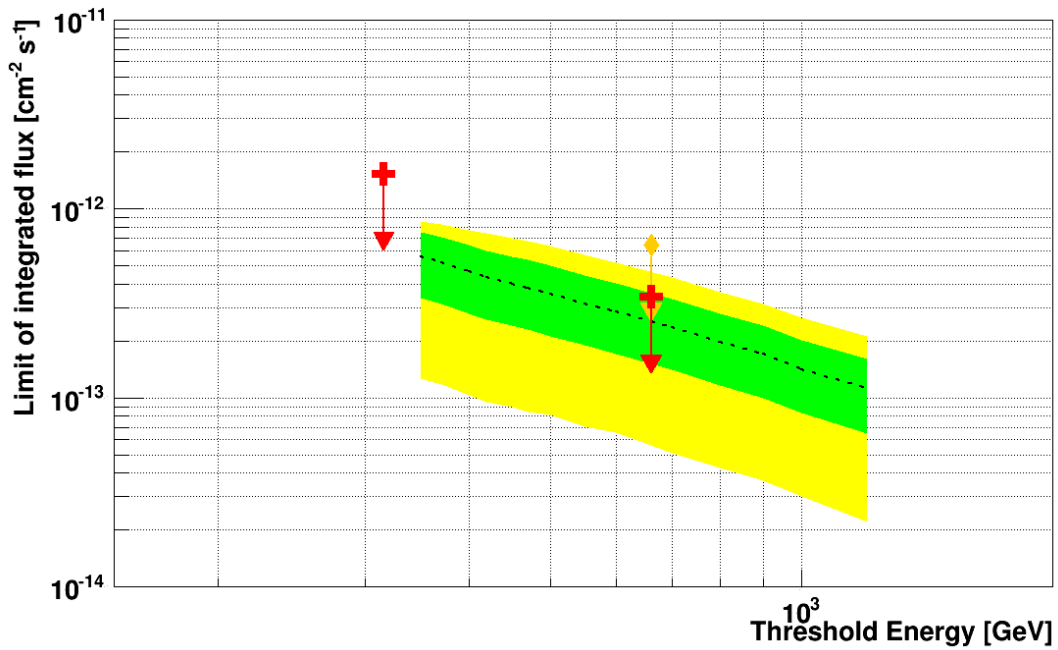
(b) Moderate cuts

Figure D.4: Expected and actual upper limits on the integral gamma-ray flux from IRAS 17208-0014. See Table 8.1 for an explanation of the flux estimates. The VEGAS limits were obtained with an independent analysis of the same data set, as a cross check. In this study ("ED"), no upper limits were calculated for moderate cuts, because the expected limits showed that hard cuts were more sensitive.

D.3 IC 342

(a) Excess events, hard cuts

(b) Significance, hard cuts

(c) Excess events, moderate cuts

(d) Significance, moderate cuts
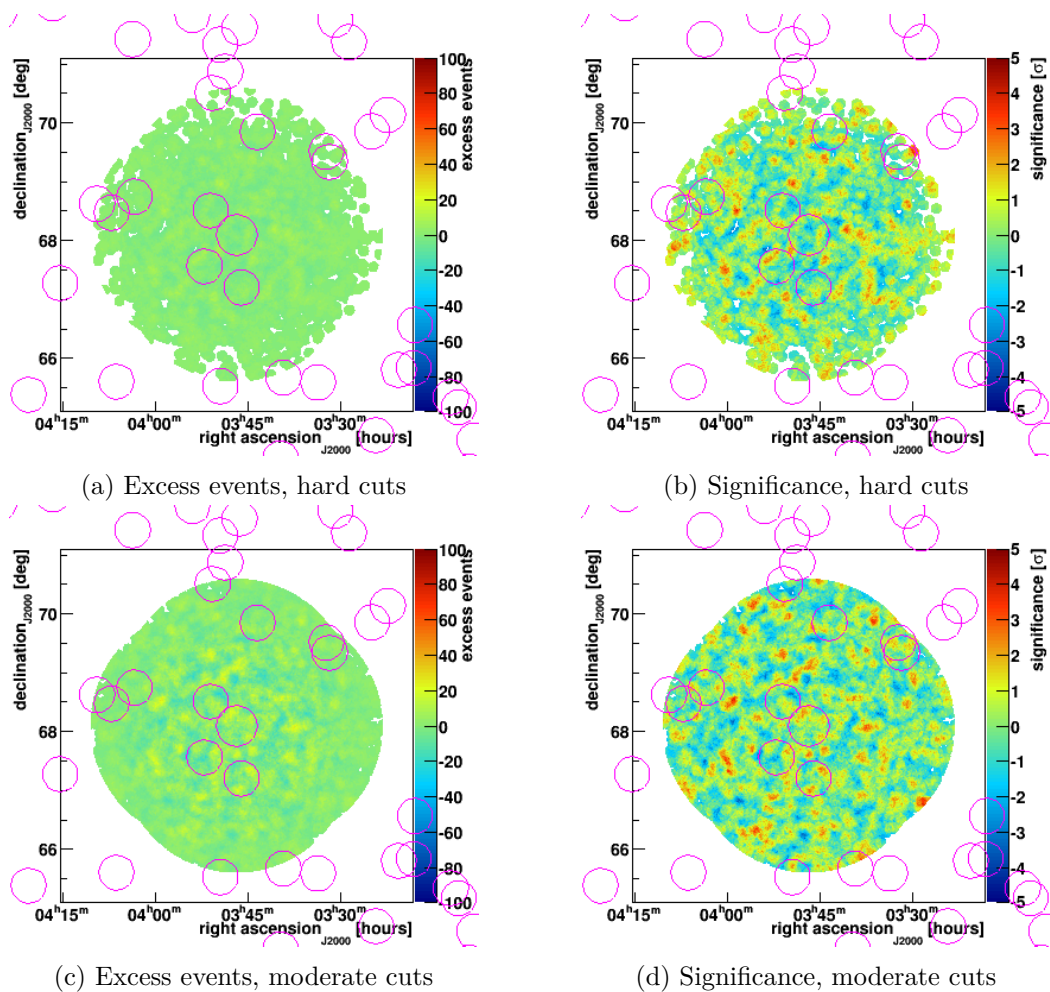
Figure D.5: Skymaps showing the number of excess events (difference between signal counts and background expectation) and the significance of the excess after Li & Ma, (1983) around the location of IC 342. The distributions are compatible with the background-only hypothesis. The pink circles correspond to regions excluded from background estimation due optically bright stars.
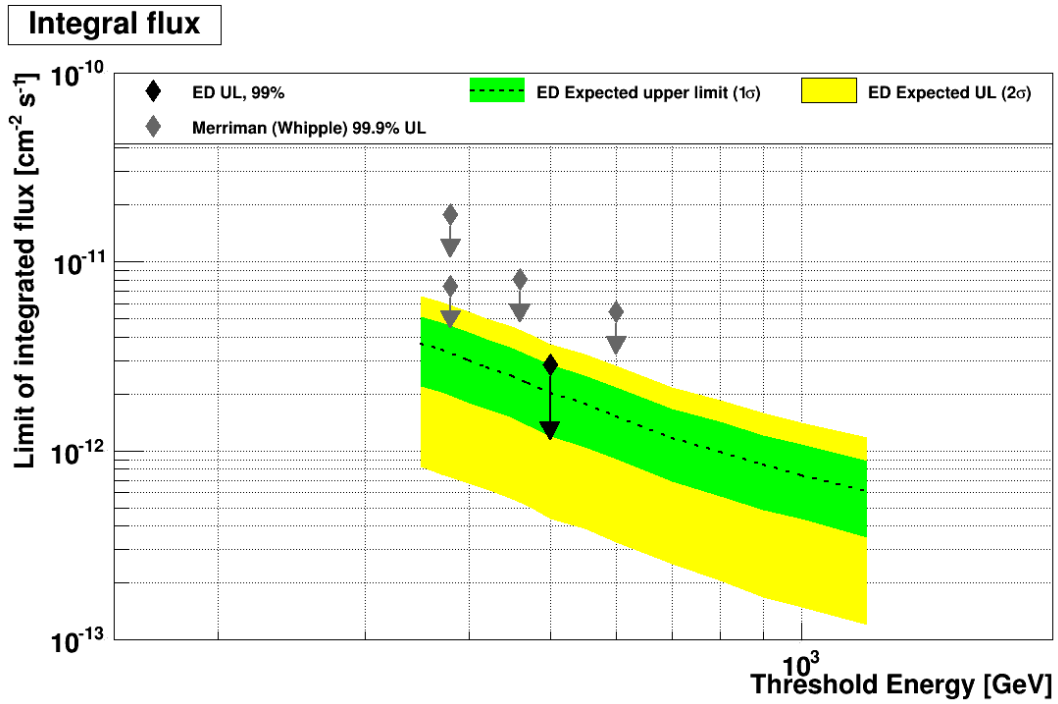
(a) Moderate cuts
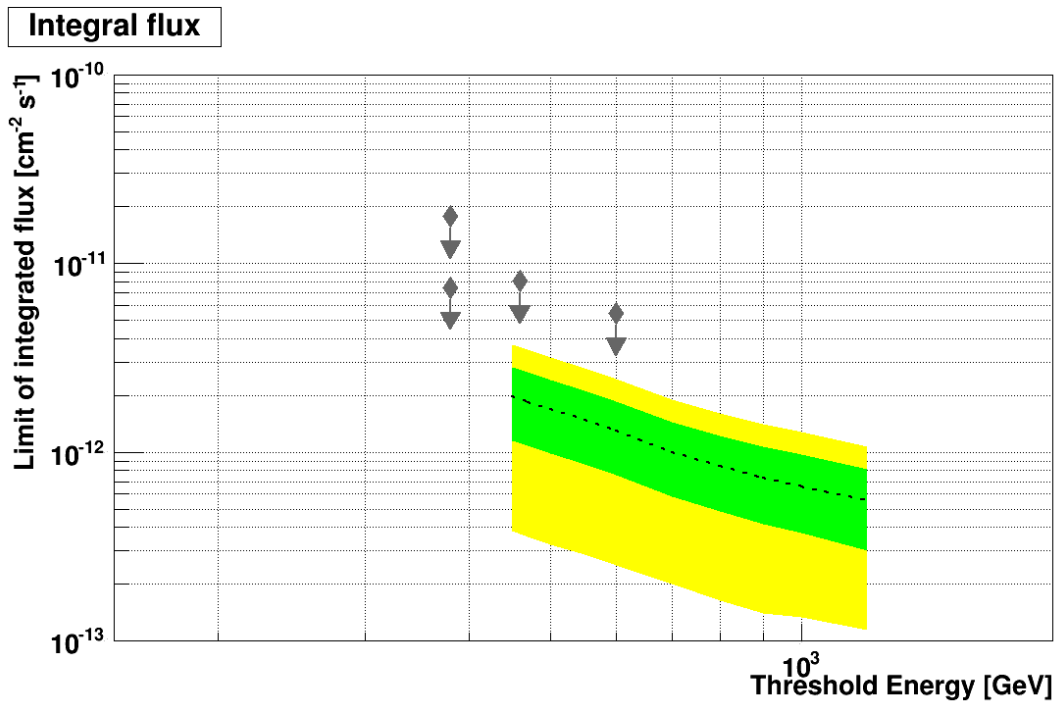
(b) Hard cuts

Figure D.6: Expected and actual upper limits on the integral gamma-ray flux from IC 342. See Merriman, (2010) for details on the Whipple results. In this study ("ED"), no upper limits were calculated for hard cuts due to the high energy threshold.

Bibliography

Aab, A. et al. (2014). "Depth of maximum of air-shower profiles at the Pierre Auger Observatory. II. Composition implications". In: *Phys. Rev.* D90.12, p. 122006.

Aab, A. et al. (2015a). "Search for patterns by combining cosmic-ray energy and arrival directions at the Pierre Auger Observatory". In: *Eur. Phys. J.* C75.6, p. 269.

– (2015b). "Searches for Anisotropies in the Arrival Directions of the Highest Energy Cosmic Rays Detected by the Pierre Auger Observatory". In: *Astrophys. J.* 804.1, p. 15.

Aartsen, M. G. et al. (2016). "Anisotropy in Cosmic-ray Arrival Directions in the Southern Hemisphere Based on six Years of Data From the Icecube Detector". In: *Astrophys. J.* 826.2, p. 220.

Abbasi, R. U. et al. (2014). "Study of Ultra-High Energy Cosmic Ray composition using Telescope Array's Middle Drum detector and surface array in hybrid mode". In: *Astropart. Phys.* 64, pp. 49–62.

Abdo, A. A. et al. (2010). "Detection of Gamma-Ray Emission from the Starburst Galaxies M82 and NGC 253 with the Large Area Telescope on Fermi". In: *Astropart. Journal Letters* 709, pp. L152–L157.

Abdo, A. A. et al. (2011). "Observations of the Young Supernova Remnant RX J1713.7-3946 with the Fermi Large Area Telescope". In: *Astrophys. J.* 734, 28, p. 28.

Abeysekara, A. U. et al. (2014). "Observation of Small-scale Anisotropy in the Arrival Direction Distribution of TeV Cosmic Rays with HAWC". In: *The Astrophysical Journal* 796.2, p. 108. URL: http://stacks.iop.org/0004-637X/796/i=2/a=108.

Abraham, J. et al. (2004). "Properties and performance of the prototype instrument for the Pierre Auger Observatory". In: *Nucl. Instrum. Meth.* A523, pp. 50–95.

Abramowski, A. et al. (2012). "Spectral Analysis and Interpretation of the γ-Ray Emission from the Starburst Galaxy NGC 253". In: *The Astrophysical Journal* 757, 158, p. 158.

Abreu, P. et al. (2012). "Measurement of the Cosmic Ray Energy Spectrum Using Hybrid Events of the Pierre Auger Observatory". In: *Eur. Phys. J. Plus* 127, p. 87.

Abu-Zayyad, T. et al. (2013). "The surface detector array of the Telescope Array experiment". In: *Nucl. Instrum. Meth.* A689, pp. 87–97.

Acciari, V. A. et al. (2009). "A connection between star formation activity and cosmic rays in the starburst galaxy M82". In: *Nature* 462, pp. 770–772.

Acciari, V. A. et al. (2009). "Observation of Extended Very High Energy Emission from the Supernova Remnant IC 443 with VERITAS". In: *The Astrophysical Journal Letters* 698.2, p. L133. URL: http://stacks.iop.org/1538-4357/698/i=2/a=L133.

Acero, F. et al. (2009). "Detection of Gamma Rays from a Starburst Galaxy". In: *Science* 326, p. 1080.

Acero, F. et al. (2015). "The 1st Fermi Lat Supernova Remnant Catalog". In:

Achterberg, A. et al. (2006). "First Year Performance of The IceCube Neutrino Telescope". In: *Astropart. Phys.* 26, pp. 155–173.

Ackermann, M. et al. (2011). "A Cocoon of Freshly Accelerated Cosmic Rays Detected by Fermi in the Cygnus Superbubble". In: *Science* 334.6059, pp. 1103–1107. URL: http://science.sciencemag.org/content/334/6059/1103.

Ackermann, M. et al. (2012). "Fermi-LAT Observations of the Diffuse γ-Ray Emission: Implications for Cosmic Rays and the Interstellar Medium". In: *Astrophys. J.* 750, 3, p. 3.

Ackermann, M. et al. (2012a). "GeV Observations of Star-forming Galaxies with the Fermi Large Area Telescope". In: *The Astrophysical Journal* 755.2, p. 164. URL: http://stacks.iop.org/0004-637X/755/i=2/a=164.

Ackermann, M. et al. (2012b). "GeV Observations of Star-forming Galaxies with the Fermi Large Area Telescope". In: *The Astrophysical Journal* 755.2, p. 164. URL: http://stacks.iop.org/0004-637X/755/i=2/a=164.

Ackermann, M. et al. (2013). "Detection of the Characteristic Pion-Decay Signature in Supernova Remnants". In: *Science* 339.6121, pp. 807–811. URL: http://science.sciencemag.org/content/339/6121/807.

Actis, M. et al. (2011). "Design concepts for the Cherenkov Telescope Array CTA: an advanced facility for ground-based high-energy gamma-ray astronomy". In: *Experimental Astronomy* 32, pp. 193–316.

Aguilar, M. et al. (2015a). "Precision Measurement of the Helium Flux in Primary Cosmic Rays of Rigidities 1.9 GV to 3 TV with the Alpha Magnetic Spectrometer on the International Space Station". In: *Phys. Rev. Lett.* 115 (21), p. 211101. URL: http://link.aps.org/doi/10.1103/PhysRevLett.115.211101.

Aguilar, M. et al. (2015b). "Precision Measurement of the Proton Flux in Primary Cosmic Rays from Rigidity 1 GV to 1.8 TV with the Alpha Magnetic Spectrometer on the International Space Station". In: *Phys. Rev. Lett.* 114 (17), p. 171103. URL: http://link.aps.org/doi/10.1103/PhysRevLett.114.171103.

Aharonian, F. A. et al. (2004). "High-energy particle acceleration in the shell of a supernova remnant". In: *Nature* 432, pp. 75–77.

– (2007). "First ground based measurement of atmospheric Cherenkov light from cosmic rays". In: *Phys.Rev.* D75, p. 042004.

Ahn, H. S. et al. (2007). "The Cosmic Ray Energetics And Mass (CREAM) instrument". In: *Nuclear Instruments and Methods in Physics Research Section A: Accelerators, Spectrometers, Detectors and Associated Equipment* 579.3, pp. 1034 –1053. URL: http://www.sciencedirect.com/science/article/pii/S0168900207010194.

Ahn, H. S. et al. (2009). "Energy Spectra of Cosmic-ray Nuclei at High Energies". In: *Astropart. Journ.* 707, pp. 593–603.

Albert, J. et al. (2007a). "Discovery of VHE Gamma Radiation from IC443 with the MAGIC Telescope". In: *Astrophys. J.* 664, pp. L87–L90.

– (2007b). "First Bounds on the Very High Energy γ-Ray Emission from Arp 220". In: *The Astrophysical Journal* 658.1, p. 245. URL: http://stacks.iop.org/0004-637X/658/i=1/a=245.

– (2008). "Implementation of the Random Forest Method for the Imaging Atmospheric Cherenkov Telescope MAGIC". In: *Nucl. Instrum. Meth.* A588, pp. 424–432.

Anderson, G. et al. (2007). *Reformulated atmospheric band model method for modeling atmospheric propagation at arbitrarily fine spectral resolution and expanded capabilities*. US Patent App. 11/398,696. URL: http://www.google.com/patents/US20070027664.

Antoni, T et al. (2003). "The cosmic-ray experiment {KASCADE}". In: *Nuclear Instruments and Methods in Physics Research Section A: Accelerators, Spectrometers, Detectors and Associated Equipment* 513.3, pp. 490 –510. URL: http://www.sciencedirect.com/science/article/pii/S016890020302076X.

Apel, W. D. et al. (2013). "KASCADE-Grande measurements of energy spectra for elemental groups of cosmic rays". In: *Astropart. Phys.* 47, pp. 54–66.

Apel, W. et al. (2010). "The KASCADE-Grande experiment". In: *Nuclear Instruments and Methods in Physics Research Section A: Accelerators, Spectrometers, Detectors and Associated Equipment* 620.2–3, pp. 202 –216. URL: http://www.sciencedirect.com/science/article/pii/S0168900210007734.

Atwood, W. B. et al. (2009). "The Large Area Telescope on the Fermi Gamma-ray Space Telescope Mission". In: *Astrophys. J.* 697, pp. 1071–1102.

Baerwald, P., Bustamante, M. & Winter, W. (2015). "Are gamma-ray bursts the sources of ultra-high energy cosmic rays?" In: *Astropart. Phys.* 62, pp. 66–91.

Bass, S. et al. (1998). "Microscopic models for ultrarelativistic heavy ion collisions". In: *Progress in Particle and Nuclear Physics* 41, pp. 255 –369. URL: http://www.sciencedirect.com/science/article/pii/S0146641098000581.

Behnke, O. et al. (2013). *Data analysis in high energy physics: a practical guide to statistical methods*. Weinheim: Wiley-VCH. URL: https://cds.cern.ch/record/1517556.

Berk, A. et al. (2006). "MODTRAN5: 2006 update". In: *Algorithms and Technologies for Multispectral, Hyperspectral, and Ultraspectral Imagery XII*. Vol. 6233. Proc. SPIE, 62331F–62331F–8. URL: http://dx.doi.org/10.1117/12.665077.

Berk, A. et al. (2008). *Band model method for modeling atmospheric propagation at arbitrarily fine spectral resolution*. US Patent 7,433,806. URL: http://www.google.de/patents/US7433806.

Bernlöhr, K. (2000). "Impact of atmospheric parameters on the atmospheric Cherenkov technique". In: *Astropart. Phys.* 12, pp. 255–268.

– (2008). "Simulation of Imaging Atmospheric Cherenkov Telescopes with CORSIKA and sim_telarray". In: *Astropart. Phys.* 30, pp. 149–158.

Blasi, P. (2013). "The Origin of Galactic Cosmic Rays". In: *Astron. Astrophys. Rev.* 21, p. 70.

Bleicher, M et al. (1999). "Relativistic hadron-hadron collisions in the ultra-relativistic quantum molecular dynamics model". In: *Journal of Physics G: Nuclear and Particle Physics* 25.9, p. 1859. URL: http://stacks.iop.org/0954-3899/25/i=9/a=308.

Böttcher, M. et al. (2013). "Leptonic and Hadronic Modeling of Fermi-Detected Blazars". In: *Astrophys. J.* 768, p. 54.

Breiman, L. (2001). "Random Forests". In: *Machine Learning* 45.1, pp. 5–32. URL: `http://dx.doi.org/10.1023/A:1010933404324`.

Buck, A. L. (1981). "New Equations for Computing Vapor Pressure and Enhancement Factor." In: *Journal of Applied Meteorology* 20, pp. 1527–1532.

Buitink, S. et al. (2016). "A large light-mass component of cosmic rays at $10^{17} - 10^{17.5}$ electronvolts from radio observations". In: *Nature* 531, pp. 70–73.

Bykov, A. M. & Toptygin, I. N. (2001). "A Model of Particle Acceleration to High Energies by Multiple Supernova Explosions in OB Associations". In: *Astronomy Letters* 27, pp. 625–633.

Bykov, A. et al. (2012). "Particle Acceleration in Relativistic Outflows". In: *Space Science Reviews* 173.1, pp. 309–339. URL: `http://dx.doi.org/10.1007/s11214-012-9896-y`.

Cerutti, B. et al. (2014). "Three-dimensional relativistic pair plasma reconnection with radiative feedback in the Crab Nebula". In: *Astrophys. J.* 782, p. 104.

Ciddor, P. E. (1996). "Refractive index of air: new equations for the visible and near infrared". In: *Appl. Opt.* 35.9, pp. 1566–1573. URL: `http://ao.osa.org/abstract.cfm?URI=ao-35-9-1566`.

Cornils, R. (2006). "Alignment and imaging function of the HESS reflectors and study of the ultraluminous infrared galaxy Arp 220 with the HESS telescope system". PhD thesis. Universität Hamburg.

Daniel, M. et al. (2007). "The VERITAS standard data analysis". In: *Proceedings of the 30th International Cosmic Ray Conference*. Vol. 3, pp. 1325–1328.

– (2008). "Application of radiosonde data to VERITAS simulations". In: *Proceedings of the 30th International Cosmic Ray Conference*, pp. 1329–1332.

De Naurois, M. & Rolland, L. (2009). "A high performance likelihood reconstruction of -rays for imaging atmospheric Cherenkov telescopes". In: *Astroparticle Physics* 32.5, pp. 231 – 252. URL: `http://www.sciencedirect.com/science/article/pii/S0927650509001364`.

Deligny, O. (2014). "Large-Scale Distribution of Arrival Directions of Cosmic Rays Detected at the Pierre Auger Observatory Above 10 PeV". In: *J. Phys. Conf. Ser.* 531, p. 012002.

Donnelly, J. (1999). "New Results on the Relative Abundance of Actinides in the Cosmic Radiation". In: *Proceedings of the 26th International Cosmic Ray Conference*. Vol. 3, p. 109.

Edlén, B. (1966). "The Refractive Index of Air". In: *Metrologia* 2.2, p. 71. URL: `http://stacks.iop.org/0026-1394/2/i=2/a=002`.

Engel, R. (1999). "Air Shower Calculations With the New Version of SIBYLL". In: *International Cosmic Ray Conference* 1, p. 415.

Fermi, E. (1949). "On the Origin of the Cosmic Radiation". In: *Phys. Rev.* 75 (8), pp. 1169–1174. URL: `http://link.aps.org/doi/10.1103/PhysRev.75.1169`.

Fleischhack, H. et al. (2015). "A template method for measuring the iron spectrum in cosmic rays with Cherenkov telescopes". In: *Journal of Physics: Conference Series.* Proceedings

of the 24th European Cosmic Ray Symposium (ECRS2014). Vol. 632. 1, p. 012009. URL: http://stacks.iop.org/1742-6596/632/i=1/a=012009.

– (2016a). "A template method for measuring the iron spectrum in cosmic rays with Cherenkov telescopes". In: *Proceedings of the 34th International Cosmic Ray Conference*.

– (2016b). "Upper limits on the VHE γ-ray flux from the ULIRG Arp 220 and other galaxies with VERITAS". In: *Proceedings of the 34th International Cosmic Ray Conference*.

Fomin, V. P. et al. (1994). "New methods of atmospheric Cherenkov imaging for gamma-ray astronomy. I. The false source method". In: *Astroparticle Physics* 2, pp. 137–150.

Gaisser, T. K., Stanev, T. & Tilav, S. (2013). "Cosmic Ray Energy Spectrum from Measurements of Air Showers". In: *Front. Phys. China* 8, pp. 748–758.

Gao, Y. & Solomon, P. M. (2004). "The Star Formation Rate and Dense Molecular Gas in Galaxies". In: *The Astrophysical Journal* 606.1. This was the basis of the 2012 fermi paper, p. 271. URL: http://stacks.iop.org/0004-637X/606/i=1/a=271.

Giacinti, G., Kachelrieß, M. & Semikoz, D. (2015a). "Escape model for Galactic cosmic rays and an early extragalactic transition". In: *Phys. Rev.* D91.8, p. 083009.

Giacinti, G. et al. (2015b). "Unified model for cosmic rays above 10^{17} eV and the diffuse gamma-ray and neutrino backgrounds". In: *Phys. Rev.* D92.8, p. 083016.

Greisen, K. (1966). "End to the Cosmic-Ray Spectrum?" In: *Phys. Rev. Lett.* 16 (17), pp. 748–750. URL: http://link.aps.org/doi/10.1103/PhysRevLett.16.748.

Grieder, P. K. F. (2010). *Extensive Air Showers. High Energy Phenomena and Astrophysical Aspects - A Tutorial, Reference Manual and Data Book*. Berlin Heidelberg: Springer-Verlag.

Griffin, R. D., Dai, X. & Thompson, T. A. (2016). "Constraining Gamma-Ray Emission from Luminous Infrared Galaxies with Fermi-LAT; Tentative Detection of Arp 220". In: *The Astrophysical Journal Letters* 823.1, p. L17. URL: http://stacks.iop.org/2041-8205/823/i=1/a=L17.

Hammond, R. T. et al. (1978). "Čerenkov radiation in large cosmic-ray air showers". In: *Il Nuovo Cimento C* 1.4, pp. 315–334. URL: http://dx.doi.org/10.1007/BF02525044.

Heck, D. et al. (1998). "CORSIKA: a Monte Carlo code to simulate extensive air showers". In: *Wissenschaftliche Berichte Forschungszentrum Karlsruhe* (FZKA 6019).

Hess, V. F. (1912). "Über Beobachtungen der durchdringengen Strahlung bei sieben Freiballonfahrten". In: *Physikalische Zeitschrift* 13, pp. 1084–1091.

Hoecker, A. et al. (2007). "TMVA - Toolkit for Multivariate Data Analysis". In: *Proceedings of the 11th International Workshop on Advanced computing and analysis techniques in physics research (ACAT 2007)*. PoS ACAT, p. 040.

Holder, J. et al. (2008). "Status of the VERITAS Observatory". In: *Proceedings of the 4th Heidelberg International Symposium on High Energy Gamma-Ray Astronomy (2008)*. Vol. 1085. American Institute of Physics Conference Series, pp. 657–660.

Hörandel, J. R. (2003). "On the knee in the energy spectrum of cosmic rays". In: *Astropart. Phys.* 19, pp. 193–220.

Hörandel, J. R. (2004). "Models of the knee in the energy spectrum of cosmic rays". In: *Astroparticle Physics* 21, pp. 241–265.

– (2005). "Overview on direct and indirect measurements of cosmic rays - Some thoughts on Galactic cosmic rays and the knee". In: *Int. J. Mod. Phys.* A20, pp. 6753–6764.

– (2013). "The composition of cosmic rays at the knee". In: *American Institute of Physics Conference Series*. Ed. by J. F. Ormes. Vol. 1516. American Institute of Physics Conference Series, pp. 185–194.

Huege, T. (2016). "Radio detection of cosmic ray air showers in the digital era". In: *Phys. Rept.* 620, pp. 1–52.

Kachelrieß, M. (2008). *Lecture notes on high energy cosmic rays*. Prepared for the 17th Jyvaskyla Summer School.

Kampert, K.-H. & Unger, M. (2012). "Measurements of the cosmic ray composition with air shower experiments". In: *Astroparticle Physics* 35.10, pp. 660 –678. URL: http://www.sciencedirect.com/science/article/pii/S0927650512000382.

Keilhauer, B. et al. (2013). "Nitrogen fluorescence in air for observing extensive air showers". In: *European Physical Journal Web of Conferences*. Vol. 53. European Physical Journal Web of Conferences, p. 01010.

Kennicutt Jr., R. C. (1998). "The Global Schmidt law in star forming galaxies". In: *Astrophys. J.* 498, p. 541.

Khan, E. et al. (2005). "Photodisintegration of ultra-high-energy cosmic rays revisited". In: *Astropart. Phys.* 23, pp. 191–201.

Kieda, D. B., Swordy, S. P. & Wakely, S. P. (2001). "A high resolution method for measuring cosmic ray composition beyond 10 TeV". In: *Astroparticle Physics* 15.3, pp. 287 –303. URL: http://www.sciencedirect.com/science/article/pii/S0927650500001596.

Kneizys, F. et al. (1996). *The MODTRAN 2/3 Report and LOWTRAN 7 MODEL. Contract F19628-91-C-0132*. MODTRAN Report. Phillips Laboratory, Geophysics Directorate.

Lacki, B. C. et al. (2011). "On the GeV and TeV Detections of the Starburst Galaxies M82 and NGC 253". In: *The Astrophysical Journal* 734, 107, p. 107.

Lacki, B. C., Thompson, T. A. & Quataert, E. (2010). "The Physics of the Far-infrared-Radio Correlation. I. Calorimetry, Conspiracy, and Implications". In: *The Astrophysical Journal* 717.1, p. 1. URL: http://stacks.iop.org/0004-637X/717/i=1/a=1.

Lagage, P. O. & Cesarsky, C. J. (1983). "The maximum energy of cosmic rays accelerated by supernova shocks". In: *Astronomy and Astrophysics* 125, pp. 249–257.

Le Bohec, S. et al. (1998). "A new analysis method for very high definition Imaging Atmospheric Cherenkov Telescopes as applied to the CAT telescope". In: *Nuclear Instruments and Methods in Physics Research Section A: Accelerators, Spectrometers, Detectors and Associated Equipment* 416.2 - 3, pp. 425 –437. URL: http://www.sciencedirect.com/science/article/pii/S0168900298007505.

Li, T.-P. & Ma, Y.-Q. (1983). "Analysis methods for results in gamma-ray astronomy". In: *Astrophys. J.* 272, pp. 317–324.

Longair, M. S. (2011). *High energy astrophysics; 3rd ed.* Cambridge: Cambridge Univ. Press. URL: https://cds.cern.ch/record/1368238.

Lonsdale, C. J. et al. (2006). "VLBI Images of 49 Radio Supernovae in Arp 220". In: *Astrophys. J.* 647, pp. 185–193.

Maier, G. (2003). "Suche nach Anisotropie in der kosmischen Strahlung mit dem KASCADE Experiment". Doktorarbeit. Universität Karlsruhe (TH).

McGuire, R. & Rosenvinge, T. von (1984). "The energy spectra of solar energetic particles". In: *Advances in Space Research* 4.2, pp. 117 –125. URL: http://www.sciencedirect.com/science/article/pii/0273117784903016.

Merriman, A. (2010). "Search for very high energy Gamma radiation from the Starburst Galaxy IC 342". MA thesis. Galway-Mayo Institute of Technology. URL: http://hdl.handle.net/10759/313435.

Mewaldt, R. et al. (2001). "Radioactive Clocks and Cosmic-ray Transport in the Galaxy". In: *Space Science Reviews* 99.1, pp. 27–39. URL: http://dx.doi.org/10.1023/A:1013868225842.

NASA et al. (1966). *U.S. Standard Atmosphere Supplements.* U.S. committee for the extension of the standard atmosphere (COESA), Environmental Science Service Administration, National Aeronautics and Space Administration, United States Air Force. Washington, D.C.

NASA et al. (1976). *U.S. Standard Atmosphere.* National Ocean, Atmospheric Administration, National Aeronautics, and Space Administration, United States Air Force. Washington, D.C.: U.S. Government Printing Office.

Nedbal, D. (2008). "A Study of Very High Energy Gamma-Ray Emission from Extragalactic Objects with H.E.S.S. " PhD thesis. Universität Heidelberg.

Okumura, A., Noda, K. & Rulten, C. (2016). "ROBAST: Development of a ROOT-based ray-tracing library for cosmic-ray telescopes and its applications in the Cherenkov Telescope Array". In: *Astroparticle Physics* 76, pp. 38–47.

Oliva, A. & the AMS Collaboration (2016). "Precision Measurement of Boron to Carbon Flux Ratio in Cosmic Rays with energies from 0.5 GeV/n to 1 TeV/n with the Alpha Magnetic Spectrometer on the International Space Station". In: *Proceedings of the 34th International Cosmic Ray Conference (ICRC 2015)*. PoS(ICRC2015)265.

Olive, K. A. et al. (2014). "Review of Particle Physics". In: *Chin. Phys.* C38, p. 090001.

Ostapchenko, S. (2006a). "Nonlinear screening effects in high energy hadronic interactions". In: *Phys. Rev. D* 74 (1), p. 014026. URL: http://link.aps.org/doi/10.1103/PhysRevD.74.014026.

– (2006b). "On the re-summation of enhanced pomeron diagrams". In: *Physics Letters B* 636.1, pp. 40 –45. URL: http://www.sciencedirect.com/science/article/pii/S0370269306003261.

Parizot, E. et al. (2004). "Superbubbles and energetic particles in the galaxy. 1. Collective effects of particle acceleration". In: *Astron. Astrophys.* 424, pp. 747–760.

Park, N. et al. (2016). "Performance of the VERITAS experiment". In: *Proceedings of the 34th International Cosmic Ray Conference (ICRC 2015)*. PoS(ICRC2015)771.

Parsons, R. & Hinton, J. (2014). "A Monte Carlo template based analysis for air-Cherenkov arrays". In: *Astroparticle Physics* 56, pp. 26 –34. URL: http://www.sciencedirect.com/science/article/pii/S0927650514000231.

Peng, F.-K. et al. (2016). "First detection of GeV emission from an ultraluminous infrared galaxy: Arp 220 as seen with the Fermi Large Area Telescope". In: *Astrophys. J.* 821.2, p. L20.

Piran, T. (2004). "The physics of gamma-ray bursts". In: *Rev. Mod. Phys.* 76, pp. 1143–1210.

Pohl, M. (1994). "On the predictive power of the minimum energy condition. 2: Fractional calorimeter behaviour in the diffuse high energy gamma emission of spiral galaxies". In: *Astron. Astrophys.* 287, pp. 453–462.

Ptuskin, V. S. et al. (1993). "Diffusion and drift of very high energy cosmic rays in galactic magnetic fields". In: *Astronomy and Astrophysics* 268, pp. 726–735.

Rajotte, J.-F. (2014). "Upgrade and performance of the VERITAS telescope array". In: *Nuclear Instruments and Methods in Physics Research Section A: Accelerators, Spectrometers, Detectors and Associated Equipment* 766. Proceedings of the Eighth International Workshop on Ring Imaging Cherenkov Detectors (RICH2013), pp. 61 –64. URL: http://www.sciencedirect.com/science/article/pii/S0168900214004884.

Rangwala, N. et al. (2011). "Observations of Arp 220 Using Herschel-SPIRE: An Unprecedented View of the Molecular Gas in an Extreme Star Formation Environment". In: *Astrophys. J.* 743, 94, p. 94.

Rojas-Bravo, C. & Araya, M. (2016). "Search for gamma-ray emission from star-forming galaxies with Fermi LAT". In:

Rolf Bühler (2005). "Detektion schwerer Kerne in der kosmischen Höenstrahlung mit HESS". Diplomarbeit. Ruprecht-Karls-Universitẗ Heidelberg. URL: http://www.rolfbuehler.net/files/dipl_buehler_rolf.pdf.

Rolke, W. A., López, A. M. & Conrad, J. (2005). "Limits and confidence intervals in the presence of nuisance parameters". In: *Nuclear Instruments and Methods in Physics Research A* 551, pp. 493–503.

Rowell, G. P. (2003). "A new template background estimate for source searching in TeV gamma-ray astronomy". In: *Astron. Astrophys.* 410, p. 389.

Schure, K. M. & Bell, A. R. (2013). "Cosmic ray acceleration in young supernova remnants". In: *Mon. Not. Roy. Astron. Soc.* 435, p. 1174.

Silberberg, R. & Tsao, C. H. (1990). "Spallation processes and nuclear interaction products of cosmic rays". In: *Phys. Rept.* 191, pp. 351–408.

Slane, P. et al. (2014). "A CR-hydro-NEI Model of the Structure and Broadband Emission from Tycho's Supernova Remnant". In: *The Astrophysical Journal* 783.1, p. 33. URL: http://stacks.iop.org/0004-637X/783/i=1/a=33.

Strong, A. W. et al. (2010). "Global Cosmic-ray-related Luminosity and Energy Budget of the Milky Way". In: *The Astrophysical Journal Letters* 722.1, p. L58. URL: http://stacks.iop.org/2041-8205/722/i=1/a=L58.

Tamm, I. & Frank, I. (1937). "Coherent Radiation of Fast Electrons in a Medium". In: *Doklady Akad. Nauk SSSR* 14, p. 107.

Tanaka, H (2005). "A detailed study on nuclear composition of primary cosmic rays around the knee with GRAPES-3". In: *Proceedings of the 29th International Cosmic Ray Conference (ICRC 2005)*. Vol. 6. URL: `http://www.icrr.u-tokyo.ac.jp/can/icrc2005/Proceedings/Vol-16/16209-jap-tanaka-H-abs1-he12-oral.pdf`.

Telezhinsky, I., Dwarkadas, V. & Pohl, M. (2012). "Particle spectra from acceleration at forward and reverse shocks of young Type Ia Supernova Remnants". In: *Astroparticle Physics* 35.6, pp. 300 –311. URL: `http://www.sciencedirect.com/science/article/pii/S0927650511001885`.

Tetens, O. (1930). "Uber einige meteorologische begriffe". In: *Z. Geophys.* 6, pp. 297–309. URL: `http://ci.nii.ac.jp/naid/10003553214/en/`.

Ting, S. (2013). "The Alpha Magnetic Spectrometer on the International Space Station". In: *Proceedings of the IVth International Conference on Particle and Fundamental Physics in Space*. Vol. 243-244. Nuclear Physics B - Proceedings Supplements, pp. 12 –24. URL: `http://www.sciencedirect.com/science/article/pii/S0920563213005525`.

Tinyakov, P. (2014). "Latest results from the Telescope Array". In: *Proceedings of the 4th Roma International Conference on Astroparticle Physics*. Vol. 742. Nuclear Instruments and Methods in Physics Research Section A: Accelerators, Spectrometers, Detectors and Associated Equipment, pp. 29 –34. URL: `http://www.sciencedirect.com/science/article/pii/S0168900213014587`.

Tomassetti, N. & Oliva, A. (2015). "Identification of Light Cosmic-Ray Nuclei with AMS-02". In: *Proceedings of the 33rd International Cosmic Ray Conference (ICRC2013)*. URL: `http://www.cbpf.br/~icrc2013/papers/icrc2013-0896.pdf`.

Torres, D. F. (2004). "Theoretical Modeling of the Diffuse Emission of Gamma Rays from Extreme Regions of Star Formation: The Case of ARP 220". In: *The Astrophysical Journal* 617, pp. 966–986.

Torres, D. F. & Domingo-Santamaría, E. (2005). "Some Comments on the High Energy Emission from Regions of Star Formation Beyond the Galaxy". In: *Modern Physics Letters A* 20, pp. 2827–2843.

Tsuneta, S. (1996). "Structure and Dynamics of Magnetic Reconnection in a Solar Flare". In: *Astrophys. J.* 456, p. 840.

Vincent, S. et al. (2016). "A Monte Carlo template-based analysis for very high definition imaging atmospheric Cherenkov telescopes as applied to the VERITAS telescope array". In: *Proceedings of the 34th International Cosmic Ray Conference (ICRC 2015)*. PoS(ICRC2015)844.

Wissel, S. (2010). "Observations of Direct Cerenkov Light in Ground-based Telescopes and the Flux of Iron Nuclei at TeV Energies". PhD thesis. University of Chicago.

Yoast-Hull, T. M., Gallagher III, J. S. & Zweibel, E. G. (2015). "Cosmic Rays, Gamma-Rays, & Neutrinos in the Starburst Nuclei of Arp 220". In: *ArXiv e-prints* 453.1, pp. 222–228. URL: `http://mnras.oxfordjournals.org/content/453/1/222.abstract`.

Yoon, Y. S. et al. (2011). "Cosmic-ray Proton and Helium Spectra from the First CREAM Flight". In: *The Astrophysical Journal* 728.2, p. 122. URL: http://stacks.iop.org/0004-637X/728/i=2/a=122.

Zatsepin, G. T. & Kuz'min, V. A. (1966). "Upper Limit of the Spectrum of Cosmic Rays". In: *Soviet Journal of Experimental and Theoretical Physics Letters* 4, p. 78.

List of Figures

List of Tables

Selbständigkeitserklärung

Hiermit erkläre ich, die Dissertation selbstständig und nur unter Verwendung der angegebenen Hilfen und Hilfsmittel angefertigt zu haben.

Ich habe mich nicht anderwärts um einen Doktorgrad in dem Promotionsfach beworben und besitze keinen entsprechenden Doktorgrad.

Die Promotionsordnung der Mathematisch-Naturwissenschaftlichen Fakultät, veröffentlicht im Amtlichen Mitteilungsblatt der Humboldt-Universität zu Berlin Nr. 126/2014 am 18. 11. 2014, habe ich zur Kenntnis genommen.

Berlin, den 29. September 2016   Henrike Fleischhack

Acknowledgments

I would like to thank:

- My supervisor, Gernot Maier, for tremendous support and advice over the last four years.

- My other committee members: Thomas Lohse, Markus Risse, Marek Kowalski, and Achim Peters.

- My former office mates Anna and Lucie for tea, cookies, and ice cream.

- Maria, Lucie, Nathan, and especially Anna, for proof-reading and constructive criticism.

- Stephane, for introducing me to FROGS.

- Jamie, for making me analyze the Death Star Galaxy.

- (Former and current) colleagues in Zeuthen, for fruitful discussion and advice: Heike, Gareth, Stefan, Rolf, Moritz, Iftach, Orel.

- My fellow VERITASians for helpful comments, advice, support with the simulations, and teaching me about the instrument. Special thanks to Andrew, Ben, David, David, Jamie, Nahee, Nepomuk, Pascal, Reshmi, and Scott.

- David Kieda, Simon Swordy, and Scott Wakely, for inventing Direct Cherenkov light in the first place.

- My family and friends for their continued support.

- Everyone I forgot.